

**Quantitative Imaging of Mitochondrial and Synaptic Function in the
Human Brain with ^{18}F -BCPP-EF, ^{11}C -SA-4503, and ^{11}C -UCB-J**

Author:

Ayla Mansur

Supervisors:

Prof. Roger N. Gunn

Dr. Ilan E. Rabiner

A thesis submitted in fulfilment of the requirements

for the degree of

Doctor of Philosophy

IMPERIAL COLLEGE LONDON

Division of Brain Sciences

October 29, 2020

Declaration of Authorship

I, Ayla Mansur, declare that this thesis titled, “Quantitative Imaging of Mitochondrial and Synaptic Function in the Human Brain with ^{18}F -BCPP-EF, ^{11}C -SA-4503, and ^{11}C -UCB-J” and the work presented in it are my own. I confirm that:

- This work was done wholly or mainly while in candidature for a research degree at this University.
- Where I have consulted the published work of others, this is always clearly attributed.
- Where I have quoted from the work of others, the source is always given.
- With the exception of such quotations, this thesis is entirely my own work.
- I have acknowledged all main sources of help.
- Where the thesis is based on work done by myself jointly with others, I have made clear exactly what was done by others and what I have contributed myself.

‘The copyright of this thesis rests with the author and is made available under a Creative Commons Attribution Non-Commercial No Derivatives licence. Researchers are free to copy, distribute or transmit the thesis on the condition that they attribute it, that they do not use it for commercial purposes and that they do not alter, transform or build upon it. For any reuse or redistribution, researchers must make clear to others the licence terms of this work.’

Acknowledgments

This thesis would not have been possible without the guidance and support of my supervisors, Professor Roger N. Gunn and Dr. Ilan E. Rabiner. Your enthusiasm for the project, patience and continuous mentorship were integral to the successful completion of this very challenging and rewarding piece of work. Thank you for giving me this opportunity and for being there for me every step of the way.

I owe a great deal of gratitude to the analysis team at Invicro, who supported me through every challenge, and were there to teach and guide me whenever I needed. Graham Searle, Gaia Rizzo and Alex Whittington, thank you so much for all of your help over the years. I could not have done this without you.

In addition, a big thank to my friends Lysia Demetriou and Zina Chatzidimitriadou for their continual moral support, advice and friendship. Thank you for always listening and for saying the right thing to keep me going.

Finally, I would like to thank my husband Moritz, brothers Selim and Eren, and my parents for their everlasting encouragement, love and support.

Abstract

The 'Molecular Imaging of Neurodegenerative Disease: Mitochondria, Associated Proteins & Synapses' (MIND-MAPS) Consortium was formed to investigate three potential molecular markers of the mitochondrial/endoplasmic reticulum/synaptic axis dysfunction associated with neurodegeneration using positron emission tomography (PET) in the healthy human brain as well as across a number of neurodegenerative diseases.

Mitochondrial complex-I (MC-I), sigma 1 receptor (S1R) and synaptic vesicle protein 2A (SV2A) can be quantified using PET radioligands ^{18}F -BCPP-EF, ^{11}C -SA-4503 and ^{11}C -UCB-J, respectively, provided these ligands are selective for their targets, have suitable kinetics and produce a signal that can be analysed using an appropriate tracer kinetic model. The main contribution of this thesis was the identification and development of a set of optimal tracer kinetic models and PET image derived outcome measures for each of these radioligands to be implemented across the MIND-MAPS cohorts.

The work presented on ^{18}F -BCPP-EF (Chapter 4) was the first published quantification of this ligand in the human brain, and showed that the volume of distribution (V_T), the V_T normalised by the free plasma fraction (f_p) and the distribution volume ratio (DVR) derived using either multilinear analysis 1 (MA1) or the two-tissue compartment model (2TC) can be reliably used to quantify MC-I with good reproducibility. The work presented on ^{11}C -SA-4503 (Chapter 5) established MA1 as the optimal kinetic model for the quantification of S1R in the healthy human brain using either V_T or V_T/f_p as outcome measures. Some of the drawbacks of the ligand including unreliable metabolite measurements and associated high intersubject variability of the outcome measures were elucidated and improvements suggested. The characterisation of

^{11}C -UCB-J (Chapter 6) supported previous literature results by showing that the 1TC model is the optimal compartmental model to estimate V_T with time stability results showing that scan time could be reduced to 60 minutes. V_T/f_p , DVR-1 (BP_{ND} =binding potential) and semiquantitative outcome measure SUVr-1 derived from a 20 minute static PET scan were also established as reliable outcome measures, adding confidence to the excellence of ^{11}C -UCB-J as a tool for quantifying SV2A, and its suitability for regular use in clinical settings.

In addition to establishing the appropriate tracer quantification methods, an investigation on the effects of healthy ageing on MC-I, S1R and SV2A (Chapter 7) demonstrated that there is age-related reduction of MC-I in the caudate as well in SV2A in both the caudate and thalamus regions, while S1R is mostly stable with age in healthy individuals.

Altogether, the work presented in this thesis generated the optimal set of tracer kinetic modelling pipelines and outcome measures for the quantification of ^{18}F -BCPP-EF, ^{11}C -SA-4503 and ^{11}C -UCB-J in humans, allowing for the implementation of consistent analytical methods across MIND-MAPS cohorts to enable the study of changes in the mitochondrial/endoplasmic reticulum/synaptic axis in ageing and neurodegeneration.

List of Abbreviations

CT	Computerised Tomography
MRI	Magnetic Resonance Imaging
PET	Positron Emission Tomography
SUV	Standardised Uptake Value
SUVr	Standardised Uptake Value ratio
TAC	Time Activity Curve
ROI	Region of Interest
RF	Radio Frequency
FID	Free Induction Decay
BBB	Blood Brain Barrier
1TC	One-Tissue Compartment
2TC	Two-Tissue Compartment
SRTM	Simplified Reference Tissue Model
MA1	Multilinear Analysis 1
RSS	Residual Sum of squares
AIC	Akaike Information Criterion
PPF	Plasma Parent Fraction
POB	Plasma Over Blood
S1R	Sigma 1 Receptor
MC-I	Mitochondrial Complex I
SV2A	Synaptic Vesicle Protein 2A
NDD	Neurodegenerative Disease
ER	Endoplasmic Reticulum
OXPHOS	Oxidative Phosphorylation
ETC	Electron Transport Chain
ROS	Reactive Oxygen Species
ATP	Adenosine Triphosphate
MAM	Mitochondria-Associated Membrane
UPR	Unfolded Protein Response
AD	Alzheimer's Disease
PD	Parkinson's Disease
Aβ	Amyloid- β
NHP	Nonhuman Primate
TRV	Test-Retest Variability
aTRV	Absolute Test-Retest Variability
ICC	Interclass Correlation
PSF	Point Spread Function
PVC	Partial Volume Correction

***This list only includes abbreviations that are used frequently in this document.**

Table of Contents

1	<i>Neuroimaging</i>	13
1.1	Positron Emission Tomography	14
1.1.1	PET Signal Generation and Detection.....	14
1.1.2	Data Acquisition, Corrections and Image Reconstruction.....	16
1.1.3	Dynamic vs. Static PET Scans.....	18
1.2	Magnetic Resonance Imaging	19
1.2.1	MRI Physics.....	19
1.2.2	T1 weighted MRI images.....	21
1.3	Quantification Methods in PET	22
1.3.1	Time-Activity Curve and Region of Interest Generation.....	22
1.3.2	Basic Pharmacokinetics.....	24
1.3.3	Compartmental Models.....	25
1.3.4	Simplified Reference Tissue Model.....	30
1.3.5	Graphical Analysis.....	31
1.3.6	PET Outcome Measures.....	32
1.3.7	Parametric images.....	35
1.3.8	Parameter Estimation and Model Selection.....	36
1.4	Characteristics of Ideal PET Tracers	37
1.5	Conclusion	38
2	<i>PET Biomarkers of Neurodegeneration</i>	40
2.1	Pathophysiology of Neurodegeneration	41
2.1.1	Mitochondrion, endoplasmic reticulum and cellular stress response in NDD.....	42
2.1.2	Mitochondrion, Endoplasmic reticulum and Cellular Stress Response in Ageing.....	45
2.1.3	Synapses in Neurodegeneration and Ageing.....	46
2.2	Current PET Biomarkers of Neurodegenerative Disease	47
2.2.1	FDG-PET.....	47
2.2.2	Amyloid PET.....	48
2.2.3	Tau PET.....	48
2.2.4	TSPO Imaging.....	49
2.2.5	DAT imaging.....	50
2.3	MIND-MAPS Consortium	51
2.3.1	Mitochondrial complex-I (MC-I).....	52
2.3.2	Sigma-1 Receptor (S1R).....	52
2.3.3	Synaptic Vesicle protein 2A (SV2A).....	53
2.4	Aims and Outline	54
3	<i>Data Processing Pipelines and Datasets</i>	56
3.1	MRI Data	57
3.1.1	Image Acquisition and Processing.....	57
3.2	PET Data	59
3.2.1	Image acquisition.....	59

3.2.2	Image processing	59
3.2.3	Blood data acquisition and arterial input function modelling	62
3.2.4	Kinetic Analysis and Model Selection	65
3.2.5	Time stability analysis	66
3.2.6	Parametric map generation	66
3.3	Datasets.....	67
3.3.1	MIND-MAPS Healthy Volunteer Cohort.....	67
3.3.2	¹⁸ F-BCPP-EF Test-retest cohort	69
4	<i>Quantification and kinetic modelling of ¹⁸F-BCPP-EF</i>	71
4.1	Background and Study Overview	72
4.2	Tracer uptake and distribution.....	72
4.3	Determining the optimum arterial plasma input function	73
4.3.1	Modelling the plasma over blood (<i>POB</i>) data.....	74
4.3.2	Modelling the plasma parent fraction (<i>PPF</i>) data.....	74
4.4	Determining the optimum tissue kinetic model for ¹⁸F-BCPP-EF	77
4.5	Investigation of the centrum semiovale as a pseudo reference region	79
4.5.1	Estimation of ¹⁸ F-BCPP-EF V_{ND} from NHP data.....	80
4.5.2	Assessment of SUVr-1 as an outcome measure	83
4.5.3	Assessment of tracer delivery effects on SUVr and DVR	85
4.6	Time stability analysis.....	85
4.7	Evaluating the test-retest reliability of ¹⁸F-BCPP-EF	87
4.8	Parametric V_T Images.....	92
4.9	Conclusion	94
5	<i>Quantification and kinetic modelling of ¹¹C-SA-4503</i>	95
5.1	Background and Study Overview	96
5.2	Tracer uptake and distribution.....	97
5.3	Determining the optimum arterial plasma input function	97
5.3.1	Modelling the plasma over blood (<i>POB</i>) data.....	97
5.3.2	Modelling the plasma parent fraction (<i>PPF</i>) data.....	99
5.4	Determining the optimum tissue kinetic model for ¹¹C-SA-4503.....	102
5.4.1	Comparison of metabolite corrected vs. uncorrected results	104
5.5	Time stability analysis of ¹¹C-SA-4503	105
5.6	Parametric V_T Images.....	107
5.6.1	MA1	107
5.6.2	One TC	110
	111
5.7	Conclusion	111
6	<i>Quantification and kinetic modelling of ¹¹C-UCB-J</i>	113
6.1	Background and Study Overview	114

6.2	Literature Review of ^{11}C-UCB-J Quantification.....	114
6.3	Tracer Uptake and distribution	116
6.4	Determining the optimum arterial plasma input function	117
6.4.1	Modelling plasma over blood (POB) data.....	117
6.4.2	Modelling plasma parent fraction (PPF) data.....	118
6.5	Determining the optimum tissue kinetic model for ^{11}C-UCB-J.....	119
6.6	Assessment of SUVr-1 as an outcome measure	121
6.7	Time stability analysis.....	122
6.8	Parametric V_T Images.....	124
6.9	Conclusion	125
7	<i>Assessment of Healthy Ageing Effects on MC-I, S1R and SV2A quantification.....</i>	127
7.1	Background.....	128
7.2	Study Overview	130
7.2.1	Hypotheses	130
7.3	Methods	131
7.3.1	Derivation of PET outcome measures	132
7.3.2	Evaluation of age and gender effects	132
7.3.3	Correcting for partial volume effects.....	133
7.4	Results.....	134
7.4.1	Age effects on volume	135
7.4.2	Age and gender effects on ^{18}F -BCPP-EF	136
7.4.3	Age and gender effects on ^{11}C -SA-4503.....	139
7.4.4	Age and gender effects on ^{11}C -UCB-J.....	140
7.5	Discussion.....	142
7.5.1	Choice of outcome parameters	143
7.5.2	Age Effects	143
7.5.3	Gender Effects	147
7.6	Conclusion	147
8	<i>Conclusions, Limitations and Future Work.....</i>	149
	<i>Bibliography.....</i>	155
	<i>Appendix A.....</i>	176
	<i>Appendix B.....</i>	177
	<i>Appendix C.....</i>	178

Figures Index

Figure #	Figure Description	Page #
1.1	Positron annihilation and coincidence detection	15
1.2	Representative dynamic PET series	18
1.3	MRI signal generation and T1-weighted structural MRI scans	20
1.4	Representative time-activity curves	23
1.5	The basic compartmental configuration	25
1.6	Arterial input function	26
1.7	One-tissue compartmental model, two-tissue compartmental model and simplified reference tissue model	31
2.1	Diagram of processes involved in neurodegenerative pathophysiology	41
2.2	Cross-talk between mitochondrion and ER in the regulation of cellular stress responses	43
2.3	Core ageing processes act both downstream and upstream of NDD pathologies	45
2.4	The mitochondrial/ER/synaptic Axis	51
3.1	MRI data processing pipeline	58
3.2	PET data processing pipeline	60
3.3	Diagram of types of motion and motion parameters	61
3.4	Derivation of arterial input function	63
3.5	Example chromatogram data	65
4.1	^{18}F -BCPP-EF PET and MR images from a representative subject	73
4.2	Fits of the 'constant' POB model to ^{18}F -BCPP-EF plasma/blood data	75
4.3	Fits of the 'sigmoid' PPF model to ^{18}F -BCPP-EF metabolite data	76
4.4	^{18}F -BCPP-EF regional 1TC, 2TC and MA1 model fits for representative regions	77
4.5	Centrum semiovale placement within a white matter mask.	79
4.6	Lassen plots demonstrating rotenone blockade of MC-I in 4 monkeys	82
4.7	Boxplot demonstrating baseline NHP and human V_T data	82
4.8	Correlation between ^{18}F -BCPP-EF SUV_{r-1} and $\text{DVR}-1$	84
4.9	Average time stability plots of ^{18}F -BCPP-EF V_T and SUV_{r-1}	85
4.10	Regional time stability plots of ^{18}F -BCPP-EF V_T	86
4.11	Individual MR and SUV images of test and retest ^{18}F -BCPP-EF scans	89
4.12	Bland-Altman plots test-retest derived PET outcome measures	91
4.13	Correlation between TAC derived and parametric ^{18}F -BCPP-EF V_T	92
4.14	Parametric ^{18}F -BCPP-EF V_T images	93
5.1	^{11}C -SA-4503 PET and MR images from a representative subject	96
5.2	Fits of the 'exponential approaches to constant' POB model to ^{11}C -SA-4503 plasma/blood data	98
5.3	Original and modified ^{11}C -SA-4503 PPF model fits and inter-subject variability in resulting V_T estimates	99
5.4	^{11}C -SA-4503 chromatogram data and the effect of background noise on the variance of PPF	101
5.5	^{11}C -SA-4503 regional 1TC, 2TC and MA1 model fits for representative regions	103
5.6	Correlation between metabolite corrected and uncorrected ^{11}C -SA-4503 V_T	104
5.7	Regional time stability plots of ^{11}C -SA-4503 V_T	106

5.8	Average time stability plots of $^{11}\text{C-SA-4503}V_T$	107
5.9	Correlation between MA1 TAC derived and MA1 parametrically derived $^{11}\text{C-SA-4503}V_T$	107
5.10	Parametric $^{11}\text{C-SA-4503}V_T$ images	108
5.11	Correlation between MA1 TAC derived and 1TC parametrically derived $^{11}\text{C-SA-4503}V_T$	111
6.1	$^{11}\text{C-UCB-J}$ PET and MR images from a representative subject	116
6.2	Fits of the 'constant' POB model to $^{11}\text{C-UCB-J}$ plasma/blood data	117
6.3	Fits of the 'sigmoid' PPF model to $^{11}\text{C-UCB-J}$ metabolite data	118
6.4	$^{11}\text{C-UCB-J}$ regional 1TC, 2TC and MA1 model fits for representative regions	120
6.5	Correlation between $^{11}\text{C-UCB-J}$ DVR-1 and SUVR-1	122
6.6	Average time stability plots of $^{11}\text{C-UCB-J}V_T, K_1$ and SUVR-1	123
6.7	Correlation between TAC derived and parametric $^{11}\text{C-UCB-J}V_T$ and K_1	124
6.8	Parametric $^{11}\text{C-UCB-J}V_T$ images	125
7.1	Application of the Muller-Gartner PVC method to PET data	134
7.2	Correlation between $^{18}\text{F-BCPP-EF}$ outcome measures and age	137
7.3	Gender differences in age effect on $^{18}\text{F-BCPP-EF}V_T$ in the caudate	138
7.4	Correlation between $^{11}\text{C-SA-4503}V_T$ and age in the substantia nigra and amygdala	140
7.5	Correlation of $^{11}\text{C-UCB-J}V_T$ with age and $^{11}\text{C-UCB-J}BP_{ND}$ with age in the brainstem, caudate and thalamus	142

Tables Index

Table #	Table Description	Page #
1.1	List of pharmacokinetic parameters	24
3.1	Demographic information of MIND-MAPS healthy cohort	68
3.2	Injection parameters and f_p measurements of MIND-MAPS healthy cohort	69
3.3	Demographic information of ^{18}F -BCPP-EF test-retest cohort	70
3.4	Injection parameters and f_p measurements of ^{18}F -BCPP-EF test-retest cohort	70
4.1	^{18}F -BCPP-EF derived regional PET outcome measures	78
4.2	V_T data from baseline/ post-rotenone monkey and baseline human ^{18}F -BCPP-EF scans	80
4.3	Summary of regional DVR – 1, SUVR – 1 and K_1 values for ^{18}F -BCPP-EF (n=30)	83
4.4	Table of correlation results between ^{18}F -BCPP-EF SUVR -1 values with DVR – 1 derived for 8 SUVR time windows (12 ROIs, 30 subjects).	84
4.5	^{18}F -BCPP-EF derived regional test-retest PET measures	90
4.6	Test-retest reproducibility of ^{18}F -BCPP-EF outcome measures	90
5.1	^{11}C -SA-4503 derived regional PET outcome measures	102
5.2	1TC parametric images derived using a range of k_2 min constraints and correlations between parametric 1TC results and TAC derived MA1 results for each k_2	109
6.1	Regional breakdown of model selection based on AIC and identifiability	119
6.2	^{11}C -UCB-J derived regional PET outcome measures	121
6.3	Table of correlation results between ^{11}C -UCB-J SUVR -1 values with DVR – 1 derived for 8 SUVR time windows (13 ROIs, 24 subjects).	121
7.1	MINDMAPS Healthy Ageing Cohort – Summary of Demographic Information, Injection Parameters and f_p	131
7.2	Summary of regional volumetric and PET outcome measures	135
7.3	Table of correlation results between age and regional volumes (Vol_{ROI})	136
7.4	Table of correlation results between age and ^{18}F -BCPP-EF PET outcome measures	136
7.5	Gender differences in ^{18}F -BCPP-EF PET outcome measures	138
7.6	Table of correlation results between age and ^{11}C -SA-4503 PET outcome measures	139
7.7	Gender differences in ^{11}C -SA-4503 PET outcome measures	140
7.8	Table of correlation results between age and ^{11}C -UCB-J PET outcome measures	141
7.9	Gender differences in ^{11}C -UCB PET outcome measures	142
8.1	Summary of optimal blood and tissue kinetic modelling methods and outcome measures	149

1 Neuroimaging

Since the emergence of molecular imaging towards the end of the 20th century, a number of non-invasive neuroimaging modalities have been developed to study the structure and function of the human brain. Neuroimaging techniques can be divided along the lines of whether they measure structure or function. Structural imaging techniques including computerised-tomography (CT) and magnetic resonance imaging (MRI) enable the study of brain structure and anatomy, whereas functional imaging methods such as functional MRI and positron emission tomography (PET) allow for the direct measurement of biological targets and neural activity. Often structural and functional imaging modalities are used in complement to make use of their respective strengths and compensate for each other's weaknesses (Hirsch, Bauer, & Merabet, 2015; M. Wu & Shu, 2018).

The work presented here utilises both PET and MRI to study molecular targets and processes of the brain with high sensitivity. This chapter outlines the principles underlying PET (Section 1.1) and MRI imaging (Section 1.2) and describes the ways in which they can be used to quantify specific molecular targets (Section 1.3). The chapter is concluded with a summary of the ideal characteristics to look for when evaluating the suitability of a brain PET tracer (Section 1.4).

1.1 Positron Emission Tomography

PET is a nuclear imaging modality that allows for the visualization and measurement of physiological and pathological processes in vivo. The acquisition of a PET scan of the brain involves injecting a subject with a radioactively labelled tracer, or 'radiotracer', designed to bind to a specific target of interest. The local concentration of a tracer in a target region can be quantified with the use of tracer kinetic modelling methods (Morris, Endres, Schmidt, et al., 2004). This allows PET to be employed in evaluating the distribution of novel PET imaging agents, studying the effectiveness of new therapies and potential applications in detecting disease status and characterising disease severity.

This section provides a basic overview of some of the physical principles behind the generation and detection of a PET signal, followed by an explanation of the steps leading to the construction of a PET image. The mathematical methods used to extract spatiotemporal information pertaining to a tracer in a subject's brain are explained.

1.1.1 PET Signal Generation and Detection

In order to acquire a PET scan, a subject is horizontally placed into a PET scanner which consists of multiple rings of photon detectors surrounding a bore. As mentioned earlier, as a first step, a positron emitting tracer is injected into the bloodstream of the subject. The unstable nature of the radioisotope (commonly ^{18}F Fluorine, ^{13}N Nitrogen, ^{11}C Carbon or ^{15}O Oxygen) used to label the tracer causes it to undergo radioactive decay, specifically positron (β^+) decay. As depicted in Figure 1.1 A, the radioisotope undergoing β^+ decay results in the conversion of the nucleus' proton into a neutron to reach a more stable state, in turn emitting a positron and a neutrino (Saha, 2016). The positron (e^+) then interacts with a nearby electron (e^-) of an atom inside the subject's body leading to an annihilation process that produces two 511 keV photons, or gamma rays (γ), which lie approximately 180° apart (Saha, 2016).

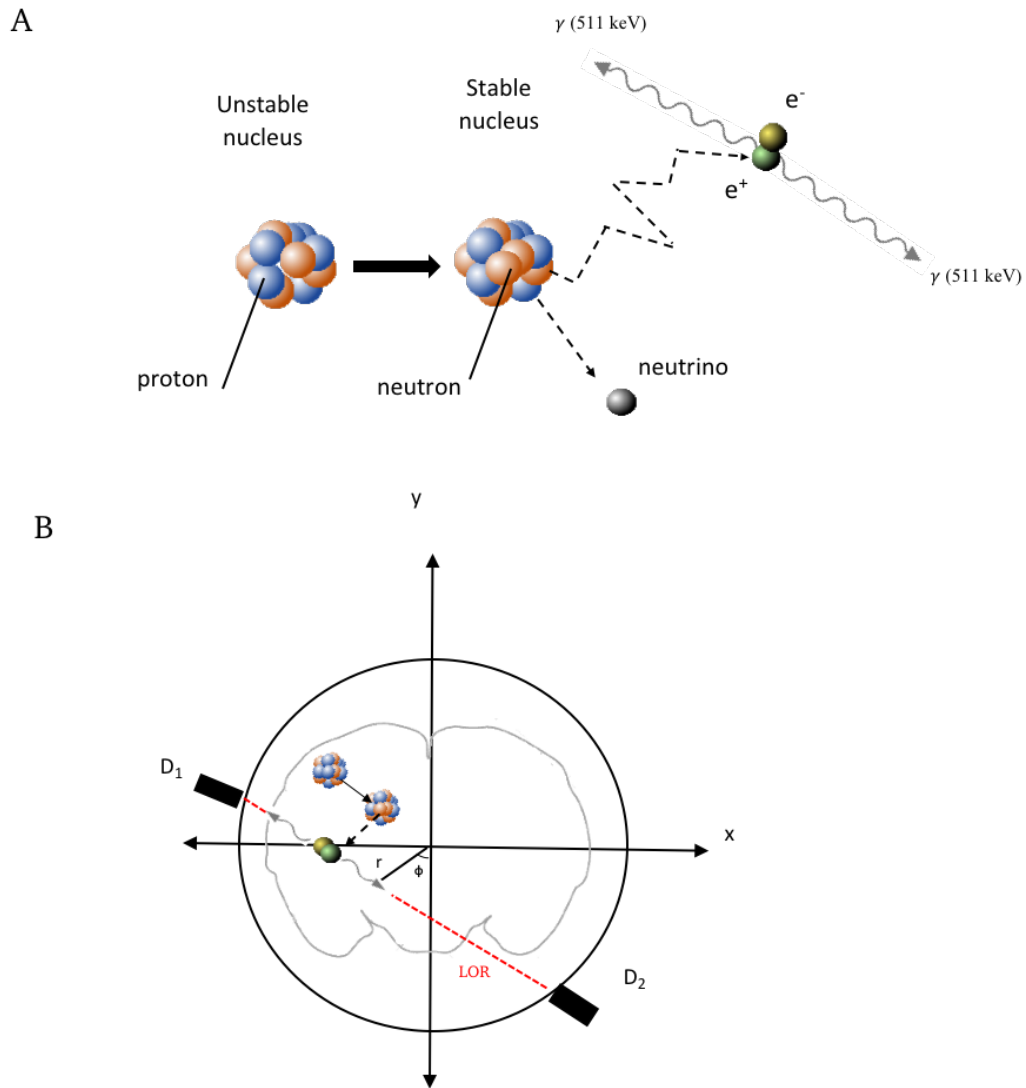


Figure 1.1 **A** An unstable radioisotope nucleus undergoes β^+ decay releasing a positron which annihilates with a nearby electron resulting in the production of two antiparallel γ photons. **B** Two γ photons originating from the same annihilation event are detected by a pair of opposite ring detectors (D_1 , D_2) within a certain ‘coincidence’ window.

When a pair of gamma rays originating from the same annihilation arrive simultaneously at two detectors (D_1 and D_2 in Figure 1.1 B), a ‘coincidence event’ occurs. Coincidence events that result from annihilation processes along a straight line connecting two detectors, i.e., the line of response (LOR – represented by the red dotted line in Figure 1.1 B), are considered ‘true’ coincidence events if they are recorded within a certain coincidence timing window. Coincidence events that do not fit this criterion do not provide the information necessary to

localize the annihilation process and need to be corrected for in the case that they do get detected (Saha, 2016).

1.1.2 Data Acquisition, Corrections and Image Reconstruction

In most modern scanners, raw PET data are recorded as list mode data (a list of individual coincidence events), which are then sorted and stored in two-dimensional (2D) datasets known as a sinogram. Briefly, each coincidence event detected lies along a LOR whose location in the x-y plane can be redefined in terms of a set of (r, ϕ) coordinates where r is the distance of the LOR from the centre of the scan field and ϕ is the angle between r and the scan field's vertical axis (Figure 1.1 B). The 2D mapping of LORs from all detector pairs with different r distances and ϕ angles form a sinogram such that in its final form, each LOR corresponds to a pixel in the sinogram where the total number of counts in each pixel represents the number of coincidence events detected during the chosen frame time along that LOR (Saha, 2016). The final sinograms are then used to generate images through the process of PET image reconstruction.

Various sources of measurement error come into play both during the generation of a PET signal as well as during the construction of a sinogram. These should be corrected prior to the images being reconstructed from the sinogram in order to maximise signal to noise and minimise any impact on the accuracy of measurements derived from PET images. The sources of error to be corrected for include physical variation in detectors that result in nonuniform raw data, photon attenuation, random and scattered coincidence detection (events that are not 'true' coincidence events) and dead time loss (Saha, 2016). The attenuation of photons occurs due to their absorption in body tissue, with photons in the centre of the body undergoing the most attenuation. Attenuation correction is typically done by performing a computed tomography (CT) scan prior to the PET scan from which an attenuation factor for each pixel can be

calculated and later applied to the PET data. Scattering, which occurs when either one or both annihilation photons change direction and lose energy after interacting with matter, also needs to be corrected for as it reduces image contrast and resolution. There are various methodologies used for scatter correction (reviewed in Zaidi and Montandon 2007), and most modern scanners have these correction methods built in.

Another important source of error attributed to the poor spatial resolution of PET cameras are partial volume effects which result in blurred images and a reduction in the apparent radioactivity in a region (Erlandsson, Buvat, Pretorius, et al., 2012; Hoffman, Huang, & Phelps, 1979). The reader is referred to Jomaa et al. for a detailed review of post-reconstruction partial volume correction (PCV) methods (Jomaa, Mabrouk, & Khelifa, 2018).

Once the necessary corrections pertaining to the sources of measurement error mentioned above have been applied to the sinogram data, the sinogram is sampled and reconstructed back into a 2D image using analytical algorithms such as filtered back-projection or iterative reconstruction (Saha, 2016). Modern PET scanners consist of multiple stacked detector rings to increase sensitivity and enable sampling from many angles. The 2D images reconstructed for each detector ring are stacked together to create a 3D image that represents the full spatial distribution of radioactivity concentration in a single frame.

Finally, voxel intensities of a reconstructed PET image are calibrated to reflect absolute units of radioactivity concentration (e.g. kBq/ml). Calibration procedures involve scanning a phantom containing a known amount of activity to derive a scanner specific calibration factor (Meikle & Badawi, 2006). It is also necessary to derive an accurate calibration factor for the well counters that count the amount of radioactivity in the blood samples acquired during a PET scan (Meikle & Badawi, 2006), so that these may be related to the PET image values.

Together with the aforementioned corrections, calibration provides PET with the ability to accurately and precisely map the radiotracer concentration, making it a truly quantitative technique.

1.1.3 Dynamic vs. Static PET Scans

PET scans can be acquired to generate either static or dynamic data. Static scans are acquired over one time frame from which a single 3D image is generated as described in the previous section. A static scan represents the average radioactivity over the course of the acquisition, providing a single estimate of tracer uptake and is usually quantified in terms of the standard uptake value (SUV), which is a semi-quantitative measure of uptake normalised to injected activity and body weight and is calculated as

$$SUV = \frac{Act}{IA/BW} \quad \text{Equation 1.1}$$

where, Act is the measured radioactivity concentration (kBq/ml), IA is the injected radioactivity (MBq) and BW is the subject's bodyweight (kg), resulting in SUV having units of g/ml.

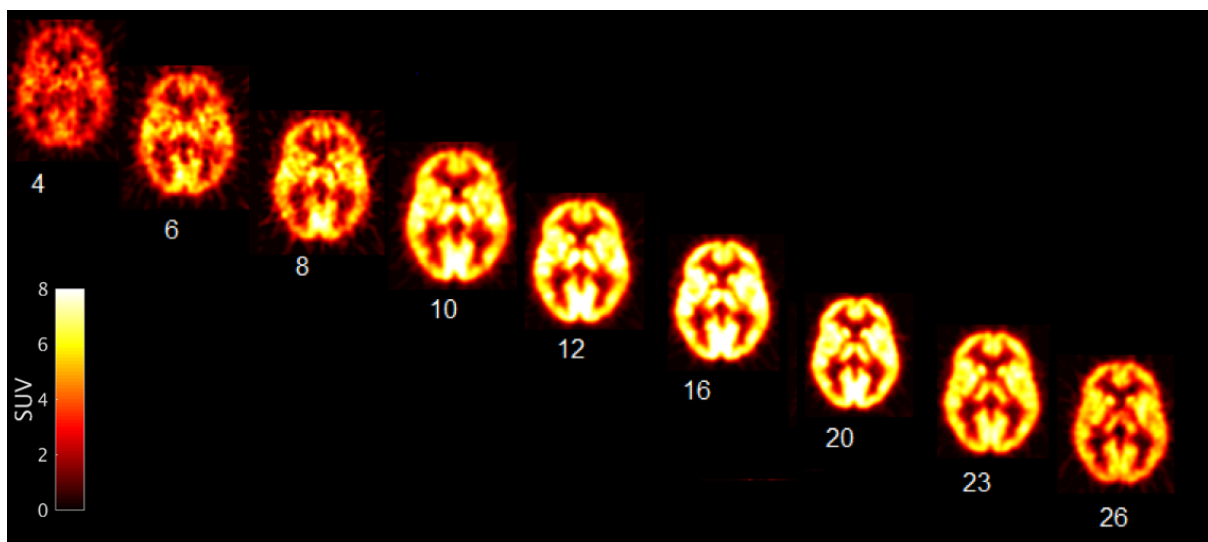


Figure 1.2 Representative dynamic PET series demonstrating time course of tracer uptake over a 90 minute acquisition. The numbers under the images correspond to the frame number (for clarity 9 out of 26 frames shown).

In the case of a dynamic PET scan, multiple frames of varying lengths are sequentially collected to generate time-activity curves (TACs) of radioactivity concentration, with early time frames reflecting tracer delivery and later frames reflecting tracer interaction with biological targets. Information on how tracer uptake varies over time (i.e. the tracer kinetics) can only be derived from a dynamic PET data series. A representative dynamic PET scan is depicted in Figure 1.2. All PET scans acquired and analysed for the thesis were acquired dynamically. Detailed information on the dynamic PET scan acquisition and processing pipelines are covered in Chapter 3. Dynamic PET images provide physiological information about the specific brain tissue being targeted in the form of spatiotemporal distribution of a tracer in the region. However, the spatial resolution of PET is fundamentally limited due to positron range, noncollinearity of annihilation photons, detector size, as well as noise introduced by the sources of measurement error described previously (Saha, 2016). Augmenting PET data with information from a spatially co-registered structural MRI image that has high anatomical detail enables enhanced quantification of PET images with more accurate anatomical localisation of the PET signal.

1.2 Magnetic Resonance Imaging

This section covers the basic principles that govern MRI physics and provides a short introduction to the T1 weighted MRI image.

1.2.1 MRI Physics

The fundamental physical principle behind MRI is the alignment of nuclear “spin” with an external magnetic field (Grover, Tognarelli, Crossey, et al., 2015). The protons belonging to atomic nuclei in the body have a net magnetic moment and direction due to the protons’ spin (Shung, Smith, & Tsui, 1992). When a subject is placed in an external magnetic field (B_0) such

as an MRI scanner, the majority of the spins line up in the same direction as B_0 lowering their state of energy, while some increase their energy state going in the opposite direction to B_0 (Plewes & Kucharczyk, 2012). This results in a net longitudinal magnetization M in the z direction causing the atomic nuclei to rotate around their axes at a velocity equivalent to the Larmor Frequency (Figure 1.3 A, left)(Westbrook, Roth, & Talbot, 2011). During an MRI scan, the nuclei absorb energy upon the application of a radiofrequency (RF) pulse which alters the spins' state of energy (Figure 1.3 A, middle). Subsequently, shutting off the RF pulse relaxes the spins to their original state of equilibrium, giving off energy (Figure 1.3 A, right). The change in energy induces a voltage that is detected and amplified by the coils of an MRI scanner, in turn producing an electrical signal called free induction decay (FID) (Hendee, Ritenour, & Hoffmann, 2003).

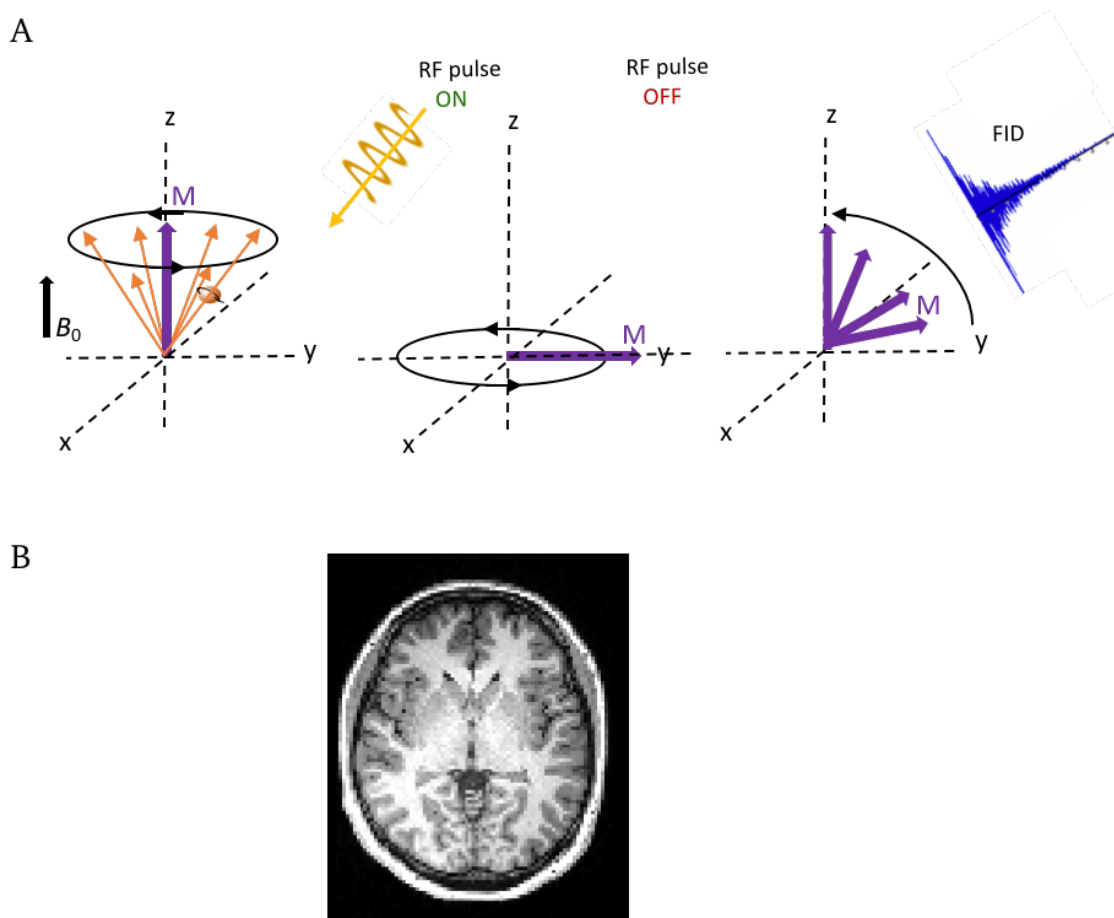


Figure 1.3 **A** The application of an RF pulse alters the protons' spin energy, resulting in the net magnetization (M) to switch from the z axis to the x - y axis. Subsequently shutting off the RF pulse relaxes the spins to their original state. The resulting change in energy is detected by the MRI coils and produces an electrical signal (FID). **B** Axial cross-section of a T1-weighted MRI image.

The localization of a FID signal requires the application of spatially variant gradients in the magnetic field strength of B_0 , which results in faster or slower nuclear precession around the field and therefore higher or lower FID signal. This allows for the detection of multiple FIDs at different positions in space, enabling the reconstruction of a 3D MRI image (Figure 1.3 B) (Grover, Tognarelli, Crossey, et al., 2015; Hendee, Ritenour, & Hoffmann, 2003).

1.2.2 T1 weighted MRI images

As mentioned above, nuclear spins undergo relaxation after they absorb RF energy. The loss of energy in the z direction during this process is described as longitudinal (T1) relaxation, where T1 is a time constant that describes the time it takes for the system to return to 63% of thermal equilibrium following excitation by an RF pulse. T1 depends on the structure and composition of the surroundings of the relaxing protons and can be manipulated by varying the repetition time between RF pulses. Different T1s produce different FID signals which manifest in different intensities in an MRI image. For example, fat has a short T1 value (260 ms) appearing bright, whereas water and cerebrospinal fluid (CSF) have longer T1 values (3000-5000 ms) appearing darker (Möllenhoff, Oros-Peusquens, & Shah, 2012). A T1 weighted image such as the example shown in Figure 1.3 B is an image where the difference in signal intensity in tissues (tissue contrast) is mainly due to the differences in T1 across tissues.

This strong tissue contrast of T1 weighted MRI sequences is the reason it is often used to provide additional neuroanatomical information to aid the analysis of PET scans. All of the PET images acquired in this project were registered to a three-dimensional, T1 weighted, gradient-echo sequence known as MPRAGE in order to define predetermined regions of interest (ROI) and report radiotracer concentrations in those regions.

1.3 Quantification Methods in PET

There are a number of spatial processing steps applied to both a subject's T1 weighted MRI scan and their reconstructed dynamic PET data before any physiologically meaningful parameters can be derived. These include inter-modality image registration, tissue segmentation and motion correction, all of which are covered in the image analysis workflow described in Chapter 3.

This section focuses on the final two steps of PET quantification which are regional TAC generation and the tracer kinetic modelling methods used to derive the final quantitative outcome measures. First TAC and ROI generation are discussed, followed by a basic introduction into some of the pharmacokinetic concepts involved in tracer uptake from blood into brain tissue. Finally, commonly used tracer kinetic modelling methods are introduced and the process of selecting the appropriate model for a given tracer is discussed.

1.3.1 Time-Activity Curve and Region of Interest Generation

The generation of a PET signal and its subsequent reconstruction into a PET image was explained in section 1.1. The radioactivity concentration of a tracer derived from a PET image can be reported either on a voxel-wise or regional basis. A TAC is the radioactivity concentration in tissue over time and is generated using intensities of the voxels (3D pixel) in a given ROI. ROIs are either defined on the subject's structural image manually, or semi-automatically using a standardised brain atlas image. The Hammer's, Clinical Imaging Centre (CIC) and Automated Anatomical Labelling (AAL) brain atlases are three of the most frequently used atlases in the field (Hammers, Allom, Koeppe, et al., 2003; Tziortzi, Searle, Tzimopoulou, et al., 2011; Tzourio-Mazoyer, Landeau, Papathanassiou, et al., 2002). The chosen atlas needs to be spatially aligned with the subject's PET image before ROIs can be defined. This is

accomplished using non-linear image registration techniques that use mathematical transformations to bring different data sets into the same coordinate system. The types of image registration methods specific to the MRI and PET processing pipelines employed in this thesis are detailed in Chapter 3 sections 3.1-3.2.

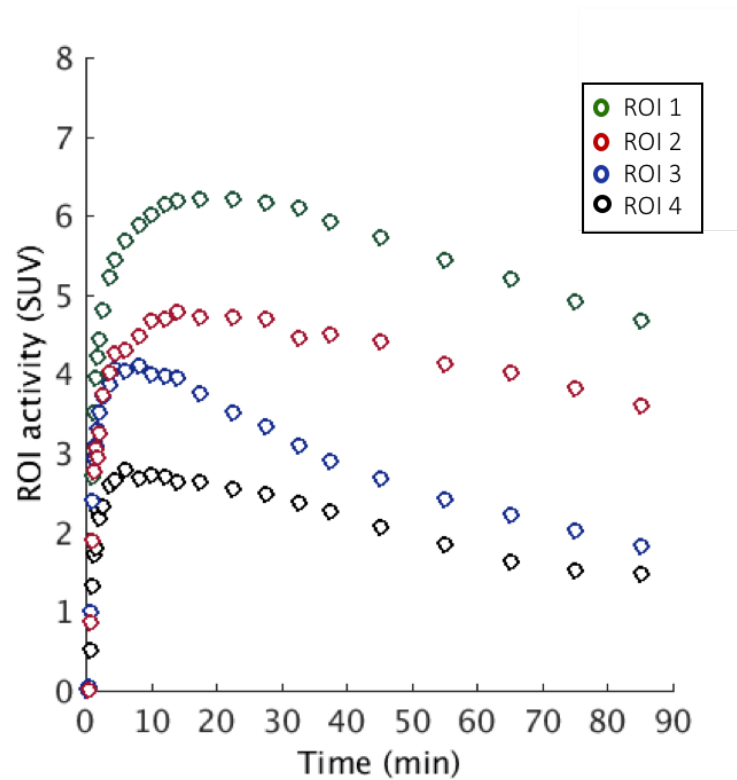


Figure 1.4 TACs for four ROIs representing changing regional radioactivity throughout the course of a 90 minute dynamic PET scan.

A regional TAC is generated by calculating the mean intensity of the voxels in a given ROI in each frame and are plotted against the midframe time for display purposes (some representative TACs are shown in Figure 1.4). Regional radioactivity is reconstructed in quantitative units of kBq/ml and so TACs can be displayed in these units or alternatively converted into standardised uptake values (SUV) by using Equation 1.1.

1.3.2 Basic Pharmacokinetics

The source of radioactivity taken up by the brain during a PET scan is considered to be the concentration of radioactivity in the plasma portion of blood. A tracer entering brain tissue from plasma is required to cross the blood-brain barrier (BBB), which is a selective semipermeable barrier consisting of tightly arranged capillary endothelial cells separating circulating blood from the brain and cerebrospinal fluid (Daneman & Prat, 2015). The delivery of tracer from the capillary into brain tissue is governed by local perfusion (f) and the fraction of the radioligand that is extracted into tissue during a single capillary passage, i.e., extraction fraction (E). Some key pharmacokinetic parameters used to quantify tracer uptake into brain tissue are summarised in Table 1.1.

Parameter	Abbreviation	Unit	Definition
Perfusion	f	ml.100g ⁻¹ .min ⁻¹ or min ⁻¹	Blood flow per unit tissue
Extraction	E	Unitless	Fraction of tracer moving from blood to tissue during a single capillary passage
Plasma to tissue rate constant	K_1	ml.g ⁻¹ .min ⁻¹ or min ⁻¹	Rate constant for transfer from blood to tissue
Permeability	P	cm.min ⁻¹	Permeability of tracer across capillary membrane
Surface area	S	cm ² .g ⁻¹	Capillary surface area per unit mass of tissue
Permeability surface area product	PS	ml.100g ⁻¹ .min ⁻¹	-

The rate constant describing delivery from blood into tissue is referred to as K_1 and is given by

$$K_1 = f \cdot E \quad \text{Equation 1.2}$$

By considering the capillary as a solid cylinder, f , E , P and S can be related using the Renkin-Crone Equation (Crone 1963; Renkin 1954)

$$E = 1 - e^{\frac{-PS}{f}} \quad \text{Equation 1.3}$$

which states that the extraction of a tracer into the brain depends on perfusion, the tracer's permeability across a capillary membrane (P) and the capillary surface area (S). For tracers with a high PS product such as ¹⁵O-water, ¹⁵O-butanol and ¹¹C-Flumazenil, $PS \gg f$, in which

case E will approach 1 resulting in 100% extraction. Substituting this into Equation 1.2 yields $K_1 \cong f$, meaning K_1 will mainly be governed by perfusion. Conversely, for tracers such as ^{18}F -Fluorodopa which have low PS products, i.e. $\text{PS} \ll f$, $E \cong \frac{\text{PS}}{f}$ and therefore $K_1 \cong \text{PS}$.

1.3.3 Compartmental Models

The distribution of a tracer is often described using a compartmental model. The compartments in the model represent the different states in which the tracer exists (for example free or bound to a target), and thus may not be spatially separated. Deriving physiological parameters of interest such as tracer uptake, blood flow, metabolism or receptor concentration requires differentiating between these compartments. Compartmental modelling uses mathematical models to relate the dynamics of a tracer in each compartment to the final composite signal (C_T) observed in a PET image (Carson, 2003).

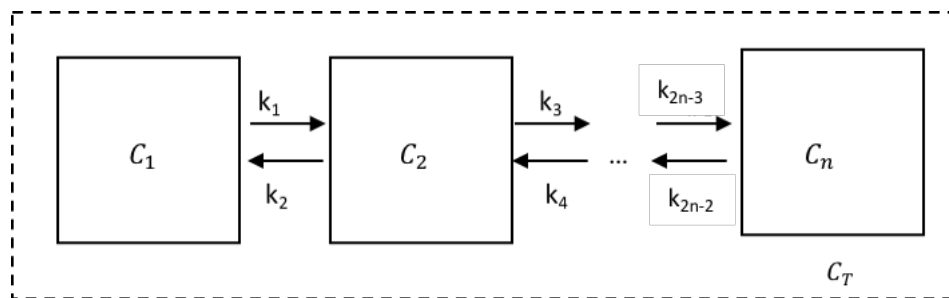


Figure 1.5 Compartmental model configuration for a system with n compartments. Each box represents a compartment and the arrow represent the exchange of radiotracer between compartments.

Figure 1.5 demonstrates a n -compartmental model configuration, where $C_1(t)$, $C_2(t)$, $C_3(t) \dots C_n(t)$ describe the radioactivity concentration in each compartment at time t . The rate of transfer of tracer between the compartments is described by rate constants (microparameters) $k_1, k_2 \dots k_n$, where n represents the number of compartments. Tracers can be described as reversible or irreversible, depending on their binding characteristics. Irreversible tracers are effectively trapped in a particular compartment via binding that does not dissociate during the timescale of the scanning procedure. There are disadvantages

associated with using irreversible tracers to measure target density in the brain such as they may be limited by blood flow into the brain. Unlike irreversible tracers, reversible tracers do not get trapped, and all compartments have non-zero rates of outward flow (Gunn, Gunn, & Cunningham, 2001). A typical example of a tracer with reversible kinetics is ^{11}C -Raclopride, which binds to dopamine receptors (Farde, Eriksson, Blomquist, et al., 1989). All subsequent discussion is limited to reversible tracers.

The two main assumptions that underlie compartmental modelling are that for a given compartment there is no gradient in tracer concentration and that the physiological processes being measured are at 'steady state', i.e., the rate constants of the system are unchanged throughout the duration of the study (Morris, Endres, Schmidt, et al., 2004). These assumptions allow for the transfer rates between compartments to be linearly related to the differences in their radioactivity concentrations (Kety 1951). A compartmental model can therefore be expressed as a system of linear and differential equations that describe the rate of change of tissue radioactivity concentration. Solving for these differential equations allows for the calculation of radioactivity concentration in a given compartment, $C_i(t)$.

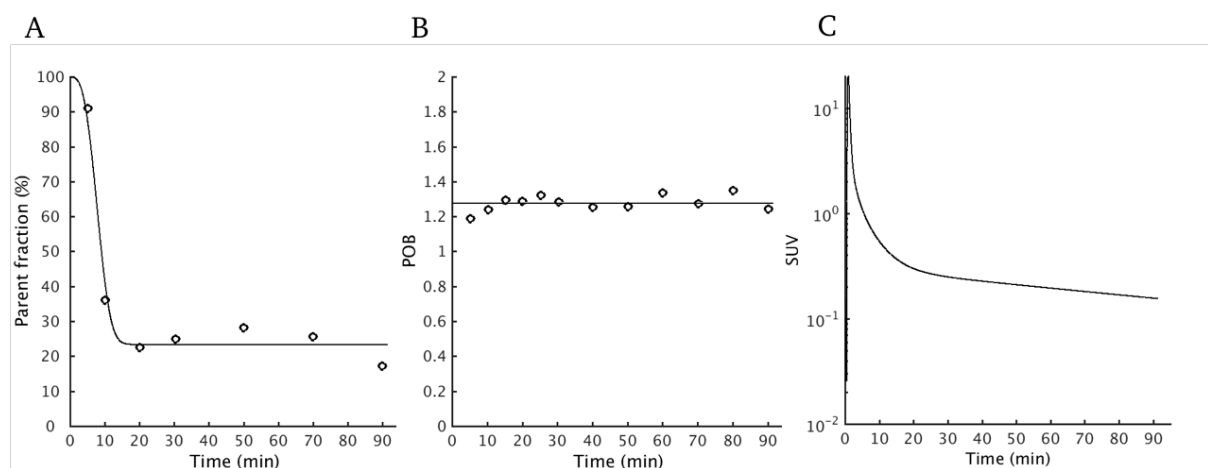


Figure 1.6 **A** A sigmoid parent fraction model fitted to metabolite data where each data point represents the fraction of parent radioligand over the course of a PET scan. **B** A linear plasma over blood model fitted to the ratio of plasma to blood radioactivity over the course of a PET scan. **C** A *PPF* and *POB* corrected arterial input function.

Arterial Input Function

Over the course of a PET scan, there is a constant supply of tracer into a subject's bloodstream that is referred to as the arterial input function (AIF). The AIF describes the concentration of tracer available to cross the BBB into brain tissue. Although it is not strictly a compartment of the model in the mathematical sense because it is measured and not solved for, the AIF is often depicted as a separate compartment (C_A). Most tracers get metabolized and produce radiometabolites which can either cross the BBB, in which case they need to be incorporated into a compartmental model or stay trapped in the blood compartment. The fraction of free parent radiotracer (*PPF*) that contributes to C_A is calculated and accounted for during the kinetic modelling process. Another correction that is applied to the AIF accounts for the ratio between free tracer that is in plasma to that in whole blood, referred to as the plasma over blood (*POB*) ratio. This is done to enable the generation of a total plasma activity curve from the measured blood data which includes both red blood cells and plasma. During a dynamic PET scan acquisition, blood samples are withdrawn and used to estimate *PPF* and *POB*. Empirical models can be fitted to these discrete data samples to obtain continuous and smooth *PPF* and *POB* curves as shown in Figure 1.6 A and B. The final *PPF* and *POB* corrected input function, shown in Figure 1.6 C, can then be used as input for the tissue kinetic modelling steps to follow. The choice of *PPF* model requires careful attention as it can have an impact on outcome parameters derived from tissue kinetic modelling (Tonietto, Veronese, Rizzo, et al., 2015).

Once C_A has been corrected for *PPF* and *POB*, the tissue activity in a given compartment i can be described by

$$C_i(t) = h_i(t) \otimes C_A(t) \quad \text{Equation 1.4}$$

where $h_i(t)$ is the impulse response function describing the response of compartment i to a single bolus input of magnitude of 1, and C_i is the tracer concentration in each compartment.

Equation 1.4 describes the convolution (\otimes) of $C_A(t)$ with impulse response function $h_i(t)$ which is a sum of exponentials.

One-Tissue Compartment Model

The one-tissue compartment (1TC) model is the simplest form of compartmental model consisting of one tissue compartment C_1 which for a radioligand represents a combination of tracer that is free, non-specifically and specifically bound in tissue as shown in Figure 1.7 A. As mentioned in section 1.3.2, the rate constant of tracer delivery from plasma C_A into tissue C_1 is called K_1 . The second rate constant k_2 describes the rate of clearance from tissue back into plasma. This system can be described by the following equations

$$\frac{dC_1(t)}{dt} = K_1 C_A(t) - k_2 C_1(t) \quad \text{Equation 1.5}$$

$$C_T(t) = (1 - V_B)C_1(t) + V_B C_B(t) \quad \text{Equation 1.6}$$

where C_T is the sum of the concentrations in C_1 and in whole blood (C_B), and V_B is the fractional blood volume which is included to account for intra-vascular radioactivity in the ROI. It should be noted that the blood terms V_B and C_B , though accounted for in the kinetic modelling process, are omitted from all subsequent equations for the sake of clarity.

It follows from equation 1.4 that the solution to the system of equations 1.5 and 1.6 is given by

$$C_T(t) = K_1 \exp(-k_2 t) \otimes C_A(t) \quad \text{Equation 1.7}$$

The main parameter of interest derived from the 1TC model is the volume of distribution, V_T , defined as the ratio of the concentration of radiotracer in the tissue (C_T) to that in the plasma (C_A) at equilibrium (Innis et al., 2007). The calculation of V_T from this model is provided in section 1.3.6 (Equation 1.16).

Two-Tissue Compartment Model

Often, the kinetics observed do not fit the 1TC model, in which case a two-tissue compartment (2TC) model is required. The two compartments in this case represent tracer that is non-displaceable (ND) (free + non-specifically bound), and tracer that is specifically bound to the target of interest. As depicted in figure 1.7 B, the 2TC system consists of the blood compartment C_A and two tissue compartments C_1 and C_2 , where C_1 represent the non-displaceable component of the PET signal, and C_2 the concentration of tracer that is specifically bound in tissue, which is often the main compartment of interest (Carson, 2003). The 2TC model requires the estimation of four rate constants K_1 , k_2 , k_3 and k_4 . This is accomplished by solving for the following system of equations

$$\frac{dC_1}{dt} = K_1 C_A(t) - (k_2 + k_3)C_1(t) + k_4 C_2(t) \quad \text{Equation 1.8}$$

$$\frac{dC_2}{dt} = k_3 C_1(t) - k_4 C_2(t) \quad \text{Equation 1.9}$$

$$C_T(t) = C_1(t) + C_2(t) \quad \text{Equation 1.10}$$

where k_3 and k_4 are the rates of transfer between C_1 and C_2 . The solution to this set of equations is given by

$$C_T(t) = (\alpha_1 \exp(\beta_1 t) + \alpha_2 \exp(\beta_2 t)) \otimes C_A(t) \quad \text{Equation 1.11}$$

where α_1 and β_1 are combinations of rate constants connecting the different compartments (Gunn, Gunn, & Cunningham, 2001). The full solution of the 2TC model is outside the scope of this thesis but can be found in Phelps et al 1979 (Phelps, Huang, Hoffman, et al., 1979).

As with the 1TC model, one of the main parameters of interest that can be derived using this model is V_T (see section 1.3.6 Equation 1.17 for details on calculation). A second parameter of interest that can be directly derived from the 2TC model is K_1 , which is the rate constant for transfer from arterial plasma to tissue and is especially important when assessing a new tracer (Innis & Carson, 2007).

1.3.4 Simplified Reference Tissue Model

First introduced by Lammertsma and Hume in 1996 (Adriaan A. Lammertsma & Hume, 1996), the simplified reference tissue model (SRTM) depicted in Figure 1.7 C is a widely used model which relies on the existence of a reference region C_{REF} that is devoid of specific binding and is used as input instead of an AIF. This model assumes that the kinetics of both the reference and target tissues can be described by a 1TC model, that the contribution of signal from whole blood is negligible and that the non-displaceable component of the signal (V_{ND}) in the reference and target tissues are equal.

The total signal in target tissue is given by

$$C_T(t) = R_1 C_{Ref}(t) + \left(k_2 - \frac{R_1 k_2}{BP_{ND}} \right) C_{Ref}(t) \otimes \exp \left(- \frac{k_2}{1 + BP_{ND}} t \right) \quad \text{Equation 1.12}$$

where R_1 represents the ratio of K_1 to tracer delivery to reference region (K'_1), and binding potential (BP_{ND}) is the ratio of specifically bound tracer to nondisplaceable tracer in tissue at equilibrium (Innis et al, 2007). This model obviates the need for arterial blood sampling, therefore reducing the cost and patient discomfort associated with a dynamic PET scan with arterial blood sampling. It is important to make sure that all assumptions of SRTM are met before removing arterial blood acquisition from a study protocol, as violations of the reference region assumptions can lead to biased estimates of the true BP_{ND} (Salinas, Searle, & Gunn, 2015).

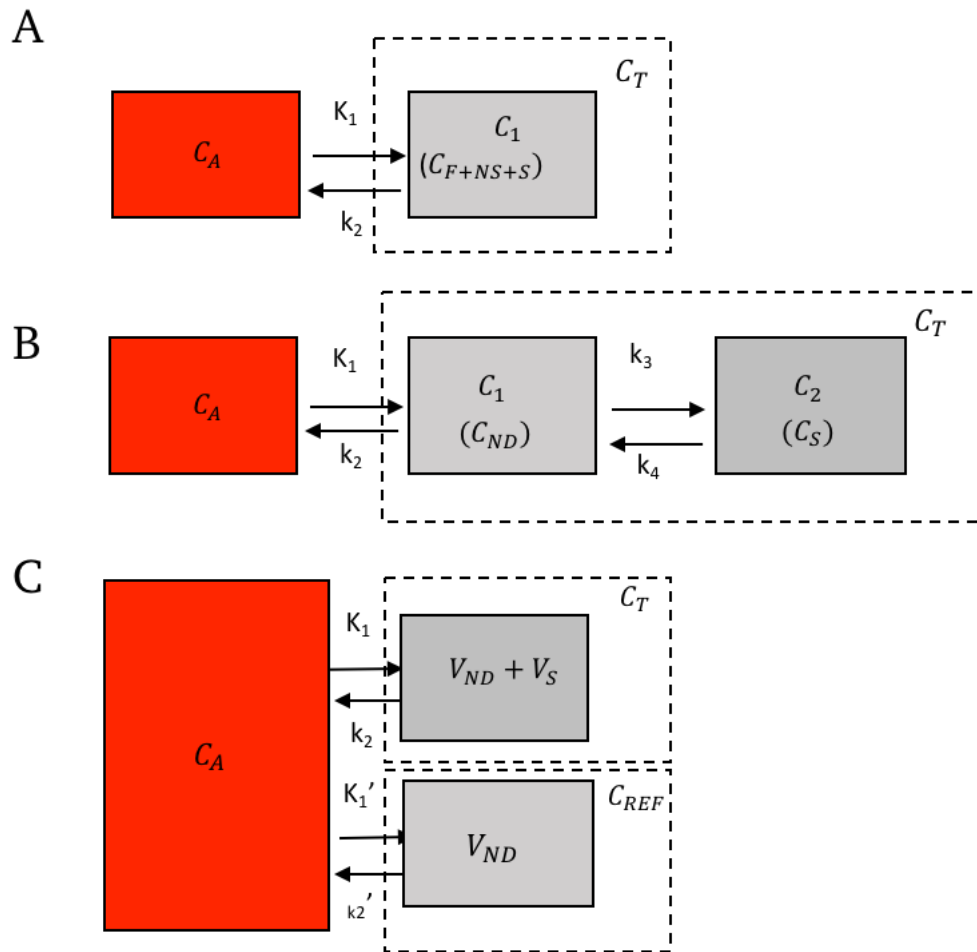


Figure 1.7 A 1TC model configuration. B 2TC model configuration. C SRTM model configuration.

1.3.5 Graphical Analysis

An alternative method to compartmental modelling is graphical analysis which is based on the concept that measured time activity data that describe C_A and C_T can be mathematically transformed into linear equations whose intercept and slopes carry physiological meaning (Carson, 2003). Unlike compartmental models, graphical models do not require a priori knowledge of the underlying model and have the advantage that they can be easily applied on a voxel-by-voxel basis making the generation of parametric images easier.

A widely used graphical method for reversible tracers is the Logan Plot (Logan, Fowler, Volkow, et al., 1990). This method makes use of the state of secular equilibrium reached between plasma and the reversible components of a system after a certain amount of time, t^* . Using a non-iterative linear estimator, the Logan method allows for the derivation of V_T using Equation 1.13

$$\frac{\int_0^t C_T(\tau) d\tau}{C_T(t)} = V_T \times \frac{\int_0^t C_A(\tau) d\tau}{C_T(t)} + b \quad \text{Equation 1.13}$$

where the slope of the linear portion of the resulting transformed data is V_T . T^* must be chosen carefully as it can have an effect on final parameter estimates (Bertoldo, Rizzo, & Veronese, 2014).

It has been shown that statistical noise innate to PET imaging can cause systematic underestimation of V_T by the Logan plot (Carson, 1993; Slifstein & Laruelle, 2000). The process of transforming the data during the generation of a Logan plot introduces statistical error in both the dependent (y) and independent (x) variables. Moreover, the noise in the two variables can become correlated with each other, resulting in further underestimation of V_T when the data are noisy.

A number of strategies have been devised to reduce noise induced bias in graphical analysis. One of such method, multilinear analysis 1 (MA1), is a rearrangement of Equation 1.13 and is more suitable for ordinary least squares regression estimation of V_T (Ichise, Toyama, Innis, et al., 2002). The operational equation for MA1 is given as

$$C_T(t) = -\frac{V_T}{b} \int_0^t C_A(\tau) d\tau + \frac{1}{b} \int_0^t C_T(\tau) d\tau, t > t_0 \quad \text{Equation 1.14}$$

1.3.6 PET Outcome Measures

V_T and BP_{ND} are two primary parameters of interest in PET quantification. In a PET experiment, the total rate of efflux of tracer in each reversible compartment is equal to the total rate of

tracer influx when the system is at equilibrium. As discussed in the previous section, BP_{ND} is the ratio of specifically bound radiotracer to that of nondisplaceable tracer in tissue under these conditions, and can be calculated directly for a reversible 2TC model as

$$BP_{ND} = \frac{k_3}{k_4} = f_{ND} \frac{B_{max}}{K_d} \quad \text{Equation 1.15}$$

where k_3 and k_4 are rate constants describing the exchange of tracer between the nondisplaceable and specific binding compartments (see figure 1.7 B). It is important to note that the direct estimation of k_3 and k_4 is not always reliable, particularly for tracers where the kinetics between the nondisplaceable and specific binding compartments are fast (A. A. Lammertsma, 2012). In *in vitro* receptor binding terms, BP_{ND} is equivalent to the product of the free fraction of ligand in non-displaceable tissue (f_{ND}), receptor density (B_{max}), and receptor affinity ($\frac{1}{K_d}$).

Estimating BP_{ND} directly is not always possible or desirable for these reasons and it is preferable to derive outcome measures from V_T . Solving for the differential equations for the reversible one compartment models (Equation 1.5) at equilibrium, it follows that

$$V_T = \frac{C_T}{C_A} = \frac{K_1}{k_2} \quad \text{Equation 1.16}$$

Similarly, for the 2TC model under equilibrium conditions, solving for Equations 1.8 and 1.9 yields

$$V_T = \left(\frac{K_1}{k_2}\right) \left(1 + \frac{k_3}{k_4}\right) \quad \text{Equation 1.17}$$

In the case that there is a valid reference region, V_T can be used to estimate BP_{ND} indirectly (A A Lammertsma, Bench, Hume, et al., 1996) as

$$BP_{ND} = \frac{V_T^{Target}}{V_T^{Ref}} - 1 \quad \text{Equation 1.18}$$

where $\frac{V_T^{Target}}{V_T^{Ref}}$, or DVR, is the distribution volume ratio and can be used as an outcome measure in its own right (see Figure 1.7 C for graphical representation of target and reference tissues in

SRTM). The indirect calculation of BP_{ND} has been shown to be more robust than the direct calculation given in Equation 1.15 (Parsey, Oquendo, Ogden, et al., 2006). In the absence of a true reference region devoid of specific binding, it may be possible to use a region with low specific binding for normalisation. In this case the region used in the denominator of Equation 1.18 would be referred to as a ‘pseudo reference region’ and the outcome measure would be reported as $DVR - 1$ instead of BP_{ND} , as the small amount of specific binding in the pseudo-reference region will result in biased estimates of the estimated BP_{ND} (Salinas, Searle, & Gunn, 2015).

Another V_T related outcome measure of note is V_T/f_p , which is V_T corrected for the free fraction of tracer in plasma (f_p). V_T/f_p is an important outcome measure to consider in studies where there may be cross sectional differences in f_p .

Finally, one needs to consider semi-quantitative PET measures that can be used to quantify tracer uptake in the brain. Standardized uptake value (SUV) and standardized uptake value ratio (SUVr) are two such measures frequently used in clinical studies as they benefit from the practicality of shorter scan time and a lack of blood sampling. The use of SUV as a quantitative measure in brain PET studies is not encouraged as it is vulnerable to sources of variability including blood perfusion, tracer uptake time and physical imaging factors such as attenuation correction and inaccuracies in cross-calibration of PET instrument which become especially relevant for larger multi-centre PET studies (Boellaard, 2009; Hamberg, Hunter, Alpert, et al., 1994; Laffon, Cazeau, Monet, et al., 2008). SUVr is a way of eliminating some of the variability associated with SUV and involves normalising SUV in a target ROI by that of a ‘reference’ region (see Equation 1.19), provided a true reference region exists for the tracer.

$$SUVr = \frac{SUV_{ROI}}{SUV_{REF}} \quad \text{Equation 1.19}$$

SUVr is calculated over a predetermined time window during which the activity in both the target and reference tissues is relatively constant over time. Semiquantitative measures like

SUVr should be evaluated against full kinetic modelling derived outcome measures before a scanning protocol can be simplified to exclude blood sampling and have shortened scan times.

1.3.7 Parametric images

All of the kinetic analysis methods described so far have discussed quantifying tissue uptake of tracer on a ROI basis. Alternatively, kinetic models can be applied to all of the voxels in a PET image to generate parametric maps of the outcome parameters of interest. Most models that are used in individual TAC analysis can be applied on a voxel basis. For example, for a tracer whose kinetics are well-described by the 1TC model, parametric images of both K_1 and k_2 can be easily generated using basis functions, which can in turn be used to generate a V_T map. Similarly, parametric maps of BP_{ND} , $R_1(=K_1/K'_1)$ and k_2 can be obtained using SRTM. For simplified linear analysis methods such as Logan and MA1, it is possible to generate parametric V_T images with great computational efficiency.

There are several advantages to parametric imaging compared to ROI-based analysis. The use of parametric images allows for whole-image statistical analyses to be performed without any a priori hypotheses regarding the specific location of expected differences or changes, which is important for reducing bias in analysing novel tracer data (Gallezot, Lu, Naganawa, et al., 2019). Another key advantage of parametric images especially relevant for multi-modality imaging studies is the ability to perform statistical analyses combining PET results with other modalities such as fMRI (Gallezot, Lu, Naganawa, et al., 2019). Despite its many advantages, parametric images still require that the appropriate corrections are applied to the original dynamic imaging data from which they were derived (e.g. motion correction), and the measurement of an input function if there is no reference region. Additionally, parametric images often need to undergo some form of noise-reduction due to the high-level noise associated with single-voxel TACs. Parametric imaging can be slow due to the large number of

voxels to fit, thus limiting its application to model forms that can be fitted very quickly (e.g. via linear regression or basis function approaches). Parametrically derived outcome measures should therefore be compared to those estimated using full kinetic modelling for any given tracer.

1.3.8 Parameter Estimation and Model Selection

The optimum estimates of model parameters such as V_T and BP_{ND} are determined by minimising the weighted residual sum of squares (WRSS) between the predicted data and the measured TAC data, referred to in mathematical modelling as the least-squares problem. Iterative algorithms developed to solve nonlinear least-squares problems start by providing initial values of the parameters to be estimated. For each iteration, the change in the WRSS for a given change in model variables is calculated and a new best estimate of a parameter is determined. The process is repeated by updating the estimated parameters at each iteration until no further improvement can be achieved.

An important consideration for solving nonlinear least-squares problems is that reaching the optimal solution is not guaranteed as there is a risk that the algorithm reaches a local solution. Models that are linear in their parameters and have a solution that is in closed form such as MA1 do not run the risk of hitting local minima and are therefore sometimes preferable to compartmental models.

The process of selecting the optimum kinetic model for a tracer involves an initial visual inspection of the model fits which can be used to narrow down the number of models being investigated. The final set of candidate models are then compared on a TAC by TAC basis using statistical tests. Two commonly used methods of model comparison in PET kinetic modelling are the Bayesian information criteria (BIC), also known as the Schwartz method (Schwarz, 1978) and the Akaike information Criteria (AIC)(Akaike, 1973), both of which are information

criteria based on the goodness of fit determined by RSS, and the number of parameters being fitted which increases with increasing model complexity.

Introduced in 1973 by Hirotugu Akaike, AIC attempts to find the model that describes the data with the minimum number of parameters, and is defined as

$$AIC = 2k + n[\ln(RSS)] \quad \text{Equation 1.20}$$

where k is the number of parameters, n is the number of observations (data points) and RSS is the residual sum of squares. A frequently used variation of AIC is AIC_c , which is AIC with a correction included for a small number of samples (Equation 1.21), and is the version used to compare models in this thesis (Wagenmakers & Farrell, 2004).

$$AIC_c = AIC + \frac{2k(k+1)}{n-k-1} \quad \text{Equation 1.21}$$

BIC is closely related to AIC in and is given by

$$BIC = \ln\left(\frac{RSS}{n}\right) + 2\ln(k) \quad \text{Equation 1.22}$$

where the term that penalizes for the number of parameters is larger compared to that of AIC. For both AIC and BIC, the method with the lowest number is considered to be the most parsimonious and therefore the best fit. Importantly, identifying the optimal kinetic model cannot solely rely on these information criteria. Additional investigations such as the test-retest reproducibility of outcome measures and data from cross-sectional studies are also needed to make the most informed choice regarding a method that best describes the kinetics of a given tracer.

1.4 Characteristics of Ideal PET Tracers

Finally, it is important to consider whether a tracer possesses the characteristics that make it useful for quantitative imaging of targets in the brain. An ideal PET tracer should be amenable to labelling with ^{18}F or ^{11}C and have suitably fast brain uptake and washout kinetics. Ideally, the peak uptake in the brain should occur early to enable shorter scanning sessions (W. Pike,

2016). In addition, the tracer should bind to its target reversibly, and possess high enough affinity to provide adequate signal-to-noise and low enough affinity that a secular equilibrium is still be reached within the duration of the scan. The selectivity of the tracer for the target should be high and its binding should be specific, with non-specific binding being kept to a minimum. Further, the metabolism of the tracer should not produce any radiolabelled metabolites that might enter the brain. Very fast tracer metabolism may cause issues both for quantification of the input function (low counts in parent plasma samples especially towards the end of a scan for a C^{11} tracer), and may also limit the distribution of the tracer into the brain tissue, and hence increase noise in the brain TACs. Perhaps most fundamentally, a tracer must be able to penetrate the BBB, which requires a certain level of lipophilicity, a low molecular weight and the absence of efflux transporters for the tracer (Laruelle, Slifstein, & Huang, 2003).

These criteria should be fully evaluated both pre-clinically prior to translation to human studies, as well as clinically in human disease states to guarantee high pathological versus normal (baseline) signal and prove useful in a clinical setting (Narayanaswami, Dahl, Bernard-Gauthier, et al., 2018).

1.5 Conclusion

This chapter introduced the physical principles that underlie PET & MRI imaging, outlining the steps from PET signal generation to the derivation of meaningful outcome measures used in PET studies of the brain. The pharmacokinetic basis of kinetic modelling was discussed, the mathematical modelling methods used to derive outcome measures were explained, and the process of model selection discussed. Finally, the set of criteria that determines a tracer's eligibility for use in human brain PET studies were outlined.

The next chapter provides an introduction to the neurobiology of neurodegeneration and ageing, and reviews a few of the existing PET biomarkers used in the diagnosis and staging of neurodegenerative diseases. The three PET targets that are the focus of this thesis, mitochondrial complex 1 (MC-I), the sigma-1 receptor (S1R) and synaptic vesicle protein 2A (SV2A) and their corresponding tracers ^{18}F -BCPP-EF, ^{11}C -SA-4503 and ^{11}C -UCB-J are introduced, and their potential utility as PET biomarkers of neurodegeneration discussed.

2 PET Biomarkers of Neurodegeneration

The focus of this thesis was to characterise the quantification of 3 PET radiotracers ^{18}F -BCPP- EF , ^{11}C -SA-4503 and ^{11}C -UCB-J in the human brain, to enable their evaluation as potential biomarkers of ageing and neurodegeneration. This chapter provides an overview of the roles of the mitochondria and endoplasmic reticulum (ER), their functions in mediating cellular stress responses, and evidence of their involvement in both ageing and the development of various neurodegenerative disease (NDDs). A brief review of current PET biomarkers of neurodegeneration is given, followed by an introduction to the MIND-MAPS consortium and overview of the 3 tracers in question. The chapter concludes with an outline of the overall aims of this project.

2.1 Pathophysiology of Neurodegeneration

Neurodegeneration can be described as the progressive loss of function and eventual death of neurons in the nervous system. Although the major pathological hallmark of NDDs is the selective loss of synapses and neurons associated with the deposition of altered variants of proteins (Kovacs, 2019), the pathophysiology of neurodegeneration is multifaceted and involves numerous other processes including immune activation and neuroinflammation, activation of the cellular stress responses, mitochondrial and endoplasmic reticulum (ER) dysfunction and synaptic abnormalities. These features and processes (summarised in Figure 2.1) are in large part interdependent and common to a number of NDDs, resulting in clinical manifestations that are both distinct and overlapping depending on the neural pathways affected. Although the precise order in which these phenomena arise is not clear, increasing evidence suggests that mitochondrial, ER and synaptic dysfunction induced by cellular stress is a common denominator across all NDDs.

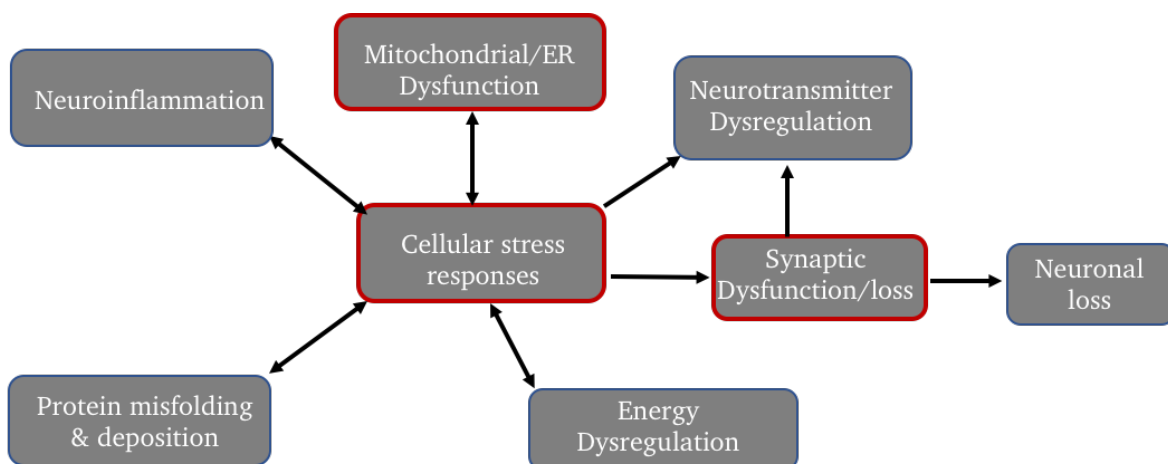


Figure 2.1 Diagram of processes involved in NDD pathophysiology that are linked to dysregulated cellular stress responses. Of these processes, mitochondrial, ER and synaptic axis dysfunction linked to cellular stress (red boxes) are common across all NDDs.

2.1.1 Mitochondrion, endoplasmic reticulum and cellular stress response in NDD

The mitochondrion is a double-membraned organelle found in most eukaryotic cells. Its primary role is to produce energy in the form of adenosine triphosphate (ATP) via oxidative phosphorylation (OXPHOS). OXPHOS involves the flow of electrons through the electron transport chain (ETC) coupled to the pumping of hydrogen atoms across the inner mitochondrial membrane to create an electrochemical gradient used to synthesise ATP (Devine & Kittler, 2018). Neurons carry out a number of high energy demanding processes such as maintaining an electrochemical gradient across their membrane via Ca^{+2} dependent signalling as well as the releasing and recycling of synaptic vesicles, requiring high levels of OXPHOS to produce ATP (Devine & Kittler, 2018). In addition to ATP production, mitochondria also modulate redox signalling. Reactive oxygen species (ROS) produced during OXPHOS, serve as important intracellular signalling molecules at low levels, but can be detrimental at high levels by causing oxidative stress and activating pathways that can result in cell death (Finkel, 2012; Trewin, Berry, & Wojtovich, 2018).

The ER is an intracellular organelle that is physically and biologically associated with the mitochondrion and is mainly responsible for the synthesis, folding, assembly and modification of proteins. A subdomain of the ER, the mitochondria-associated ER membrane (MAM) is critical to functions that occur at the interface of the two organelles including, lipid metabolism, Ca^{+2} transport and apoptosis (Teruo Hayashi, Rizzuto, Hajnoczky, et al., 2009; Saito & Imaizumi, 2018). The ER maintains Ca^{+2} homeostasis together with the mitochondrion and is also involved in promoting the release of synaptic vesicles (Devine & Kittler, 2018; Van Laar & Berman, 2013).

In order to provide the optimal conditions for cellular homeostasis and ultimately neuronal survival, the ER facilitates the activation of coping mechanisms in response to cellular stress.

One such cellular stress response is the unfolded protein response (UPR), which occurs in response to abnormal cellular conditions such as Ca^{2+} depletion, oxidative stress and protein misfolding (Saito & Imaizumi, 2018). In UPR, the accumulation of unfolded and/or misfolded proteins activates stress transducers which signal the induction of protein translation, unfolded protein degradation and chaperone protein expression in an effort to restore homeostasis (Saito & Imaizumi, 2018).

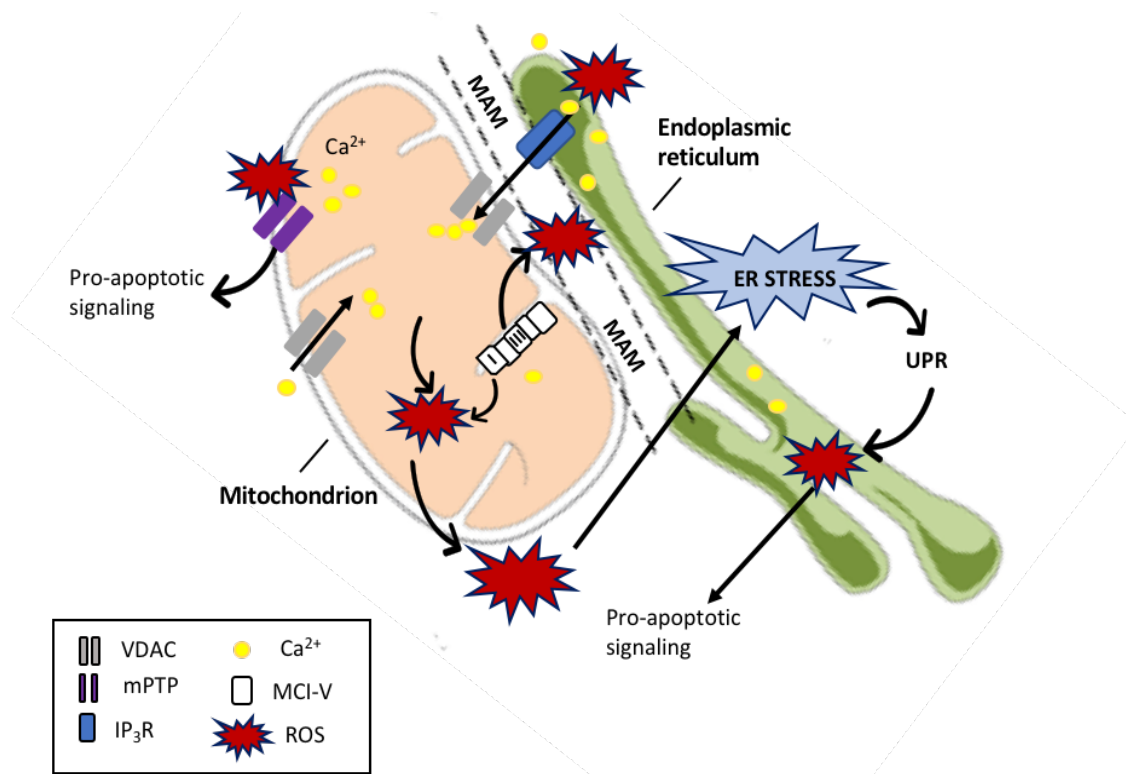


Figure 2.2 Cross-talk between mitochondrion and ER regulates cellular stress response pathways. Ca^{2+} from the ER is released through inositol 1,4,5-trisphosphate receptors (IP_3R) of the MAM and enters the mitochondrion through channels such as the voltage dependent anion channels (VDAC). At high levels, Ca^{2+} can stimulate mitochondrial complexes I and III activity, in turn increasing ROS production. Increased Ca^{2+} and ROS in the mitochondria can open the mitochondrial permeability transition pore (mPTP) and induce apoptotic signaling. ROS can also target Ca^{2+} channels of the ER, increasing Ca^{2+} release and contributing to ER stress. The activation of ER stress pathways activates UPR which can further increase ROS and Ca^{2+} in the ER, resulting in apoptosis.

Though typically considered an adaptive process, the chronic activation of cellular stress pathways due to prolonged stress can be destructive and lead to programmed cell death

(apoptosis). The MAM houses numerous regulators of apoptosis with continuous cross-talk between the two organelles maintaining a delicate balance between cell survival and death (reviewed by S. Grimm, 2012). As demonstrated in Figure 2.2, the detection of increased Ca^{2+} in mitochondria activates the ETC where mitochondrial complexes I and III produce ROS. Increased ROS levels can trigger pro-apoptotic signalling via the mitochondria, and induce ER stress signalling by targeting ER-based Ca^{2+} channels which can activate the UPR, leading to more ROS production and eventual apoptosis (reviewed in Görlach et al. 2015).

Unlike other cells in the body, the majority of neurons are post-mitotic and are therefore especially vulnerable to the detrimental effects of maladaptive stress responses. The prolonged activation of stress pathways has been shown to contribute to neurodegenerative phenotypes such as neuronal death, memory impairment, neuroinflammation and altered amyloidogenic processing (Bond, Lopez-Lloreda, Gannon, et al., 2020). Over the past two decades, there have been numerous findings linking mitochondrial and ER attrition with altered synaptic transmission in Alzheimer's Disease (AD) and Parkinson's Disease (PD) (Cheng, Ulane, & Burke, 2010; Scheff, Price, Schmitt, et al., 2007). There has also been an increased focus on the bidirectional and mutually exacerbating relationships between cellular distress signalling and misfolded proteins in NDDs (Gazit, Vertkin, Shapira, et al., 2016; Hedskog, Pinho, Filadi, et al., 2013; Hsu, Sagara, Arroyo, et al., 2000), making stress responses both the cause and consequence of NDD (Sweeney, Park, Baumann, et al., 2017). Interestingly, the mitochondrial-ER and synaptic events that appear dysregulated both upstream and downstream of unfolded protein accumulation in NDDs such as AD and PD (summarised in Figure 2.3), are also among the key features of ageing.

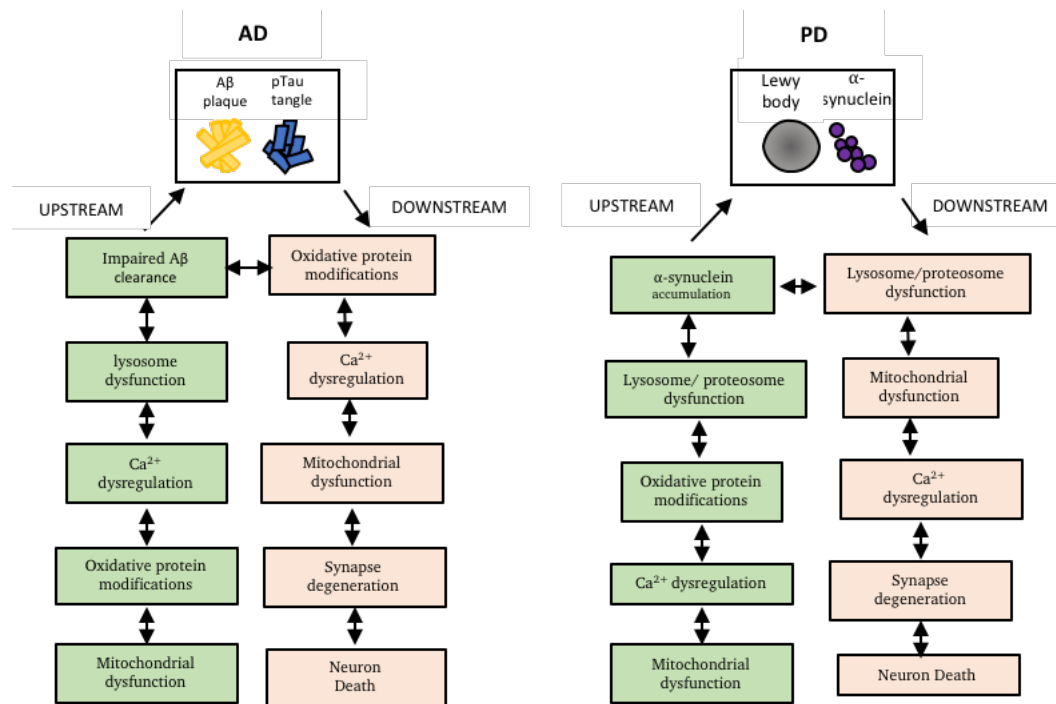


Figure 2.3 Core ageing processes including mitochondrial dysfunction, Ca^{2+} dysregulation, neuron death, oxidative protein modifications and lysosome dysfunction act both downstream and upstream of the accumulation of primary pathological protein aggregates in AD (left) and PD (right). Figure adapted from (Mattson & Arumugam, 2018)

2.1.2 Mitochondrion, Endoplasmic reticulum and Cellular Stress Response in Ageing

Compromised mitochondrial function and impaired cellular stress response systems are considered amongst the primary biological hallmarks of brain ageing (reviewed by Hou et al. 2019; Mattson and Arumugam 2018), while ageing itself is a main risk factor for the development of NDDs (Niccoli & Partridge, 2012). Developing successful interventions for NDDs requires understanding the basic mechanisms that govern ageing and their role in NDD onset and development.

The role of mitochondrial disturbances in ageing has been widely studied, with bioenergetic impairments and disturbances in redox homeostasis shown to increase with age. Age-related reductions in ETC activity were also seen in the hippocampus and frontal cortex in humans

post-mortem (Pandya, Grondin, Yonutas, et al., 2015; Venkateshappa, Harish, Mahadevan, et al., 2012). According to the mitochondrial free radical theory of ageing, first proposed in the 1950s, free radicals produced by mitochondrial activity damage cellular components leading to ageing (D. Harman 1956; Denham Harman 1972). The notion of mitochondrial involvement in the ageing process has been extended to propose that abnormal protein aggregation observed in normal aging is due to reduced energy production as a result of mitochondrial exhaustion (Boccardi, Comanducci, Baroni, et al., 2017). Studies in animals have associated increased age with reduced antioxidant defences, increased oxidative stress and deficits in the mitochondrial OXPHOS system, which culminate in eventual cell death (A. Grimm & Eckert, 2017). Age-related changes are also evident in the ER, with key enzymes required for protein folding being impaired with advancing age (Nuss, Choksi, DeFord, et al., 2008). Furthermore, responses such as UPR and pro-apoptotic signalling which occur in response to ER stress switch from being protective to maladaptive during ageing, resulting in the dampening of responses that are integral to maintaining cellular homeostasis (Brown & Naidoo, 2012).

2.1.3 Synapses in Neurodegeneration and Ageing

The brain is a high energy demanding organ and a disproportionate amount of this energy is used by synapses which are the sites of neurotransmission (Harris, Jolivet, & Attwell, 2012). The releasing and recycling of synaptic vesicles to enable neurotransmission is highly metabolically demanding, requiring high levels of energy in the form of ATP (Devine & Kittler, 2018). It is thus unsurprising that disruptions to the synaptic energy supply leads to neuropathology.

For many NDDs, loss of synapses is the first pathological event that occurs, for example synaptic impairment is evident at presymptomatic stages of AD (Coleman, Federoff, & Kurlan, 2004; Wishart, Parson, & Gillingwater, 2006). There is ample evidence of structural and functional

alterations at the synapse across NDDs including AD, Huntington's disease (HD), Amyotrophic lateral sclerosis (ALS) and PD (Bae & Kim, 2017). Synaptic loss and dysfunction also contribute to the cognitive decline seen in both NDDs and normal ageing (Uylings & de Brabander, 2002; Zhou, Miller, McDaniel, et al., 1998).

Given the importance of the complex interplay between mitochondria, ER and synapses in maintaining a healthy neuron population in the face of both age and disease related brain attrition, studying the molecules involved in these mechanisms could help with the discovery of biomarkers useful for early diagnosis, therapeutic intervention and staging of NDDs. The remainder of this chapter provides an overview of a few existing PET biomarkers for NDDs, followed by a discussion of three promising targets of the mitochondrial-ER-synaptic axis for biomarker research.

2.2 Current PET Biomarkers of Neurodegenerative Disease

Over the past few decades tremendous efforts have been put towards the discovery of biomarkers to enable early detection and in turn early intervention of NDDs. However, there has been minimal success in the use of PET biomarkers molecularly specific enough to improve diagnostic accuracy and tracking of disease progression that would allow quicker screening of drug candidates (Beach, 2017). This section summarises a few of the PET biomarkers that are successfully used as either biomarkers in diagnostic criteria or are considered supportive biomarkers of clinical diagnosis and research.

2.2.1 FDG-PET

PET imaging with ^{18}F -FDG is used as a marker of tissue glucose uptake and glycolysis closely correlated with metabolism. In the brain, FDG-PET scans have been considered to provide indirect correlates of synaptic loss (Márquez & Yassa, 2019). Hypofunction and

hypometabolism of the occipital lobe and parietal cortex derived from an ^{18}F -FDG scan is considered to be a supportive biomarker for Lewy body dementia (McKeith, Boeve, Dickson, et al., 2017; Shimizu, Hirose, Hatanaka, et al., 2018), while frontal hypometabolism is used as a supportive biomarker in the early diagnosis of progressive nuclear palsy (Höglinger, Respondek, Stamelou, et al., 2017). Importantly, a number of studies have indicated the accuracy of FDG-PET for differential diagnosis of AD from other dementias (Tripathi, Tripathi, Damle, et al., 2014).

2.2.2 Amyloid PET

According to the National Institute on Aging and National Institute on Aging and Alzheimer's Association diagnostic guidelines for AD, a positive amyloid PET scan is considered a biomarker of A β protein deposition (Shimizu, Hirose, Hatanaka, et al., 2018) and early diagnosis of AD (Klunk, Engler, Nordberg, et al., 2004; Rowe, Ng, Ackermann, et al., 2007). Amyloid PET has enabled the discovery of increased A β deposition in cognitively normal elderly individuals being linked to abnormal entorhinal activity, and associated with cortical thinning in the frontoparietal brain (Huijbers, Mormino, Wigman, et al., 2014; Villeneuve, Reed, Wirth, et al., 2014). Importantly, amyloid PET imaging has been instrumental in the selection of participants for clinical trials during the asymptomatic phase of AD (Márquez & Yassa, 2019). Currently there are three amyloid PET tracers approved for clinical use: ^{18}F -Florbetapir, ^{18}F -Florbetaben and ^{18}F -Flutemetamol.

2.2.3 Tau PET

Tau is another protein which can accumulate pathologically in cells. Tau deposition as measured by the density of neurofibrillary tangles (NFT) correlates with neurodegeneration and cognitive impairment (Braak & Braak, 1997; Duyckaerts, Brion, Hauw, et al., 1987). Tau PET has made some progress in demonstrating tau deposition being linked to disease

progression in a number of tauopathies including AD, progressive supranuclear palsy and corticobasal degeneration (R. Harada, Okamura, Furumoto, et al., 2018; Sepulcre, Schultz, Sabuncu, et al., 2016). However, a major setback in the development of the first generation of tau PET tracers including ^{18}F -THK5351, ^{18}F -Flortaucipir and ^{11}C -PBB3, has been the presence of off-target binding (Okamura, Harada, Ishiki, et al., 2018). Although the second generation of ligands such as ^{18}F -MK6240 are more selective and have enabled the reliable assessment of tau burden in AD, the long term utility of these agents outside of AD is yet to be demonstrated (Okamura, Harada, Ishiki, et al., 2018).

The development of PET radioligands for other common misfolded proteins including alpha-synuclein, huntingtin and TDP-43 remains a challenge. This is mainly due to the density of these proteins in diseased brains being significantly lower than that of A β and tau in AD brains, which has made it harder to develop ligands that are sufficiently selective (R. Harada, Okamura, Furumoto, et al., 2018).

2.2.4 TSPO Imaging

Besides misfolded proteins, neuroinflammation is also a common feature of a range of NDDs including AD, PD, ALS, and FTD (Werry, Bright, Piguet, et al., 2019). Neuroinflammatory responses involve the activation of microglia which survey their surroundings and react to perturbations in their environment by changing their morphology and migrating to the site of injury to initiate tissue repair and further engage the immune system (Werry, Bright, Piguet, et al., 2019). Microglial activation is therefore a valuable target for detecting neuroinflammation. Translocator protein (TSPO) is implicated in functions relevant to neurodegeneration, and its upregulation has been shown to accompany neuroinflammation in the brain (Banati, 2002; Rojas, Martín, Arranz, et al., 2007). Increases in TSPO PET signal in disease-relevant regions have been shown across a number of NDDs (reviewed by Werry et al.

2019). Although TSPO PET using tracers such as ^{11}C -Ro5-4864, ^{11}C -(R)-PK11195, ^{11}C -PBR28 and ^{18}F -FEPPA has the potential to serve as a clinically useful tool to monitor response to disease modifying therapeutics, the biology of TSPO and its relationship to microglial activation in inflammatory responses is complex and not well understood. Thus, despite the availability of multiple PET radioligands to quantify TSPO density the value of TSPO PET in monitoring NDDs has yet to be demonstrated.

2.2.5 DAT imaging

The dopamine transporter (DAT) is expressed in the terminals of nigrostriatal dopaminergic neurons and enables the re-uptake of dopamine from the synaptic cleft into presynaptic terminals, thus regulating the amount of dopamine available for dopamine stimulation. DAT is involved in a number of brain disorders, making its imaging key for early and differential diagnoses. PET tracers that have been developed for imaging of DAT include ^{11}C -PE2I, ^{18}F -FE-PE2I and more recently, ^{18}F -LBT-999 (Chalon, Vercouillie, Payoux, et al., 2019). So far, DAT imaging has proven most useful in supporting differential diagnosis of PD and other degenerative parkinsonism from vascular and drug-induced parkinsonism, as well as essential tremor (Ikeda, Ebina, Kawabe, et al., 2019).

Despite the wealth of technology and resources that have been put into PET biomarker discovery, the number of robust biomarkers suitable for the detection of disease progression and monitoring the results of disease modifying intervention, is disappointing. Recent discoveries on the role of mitochondrial-ER-synaptic axis pathways in healthy ageing and NDD pathology has opened up a new avenue to pursue in biomarker research. The following section describes the set of three molecular targets identified by the MIND-MAPS consortium as potential markers of ageing and neurodegenerative pathology, as well as the PET tracers that are available to quantify them *in vivo*.

2.3 MIND-MAPS Consortium

The ‘Molecular Imaging of Neurodegenerative Disease: Mitochondria, Associated Proteins & Synapses’ (MIND-MAPS) Consortium is a collaborative project formed to investigate three molecular targets of the mitochondrial/ER/synaptic axis, namely mitochondrial complex-I (MC-I), sigma 1 receptor (S1R) and synaptic vesicle protein 2A (SV2A) (depicted in Figure 2.4) across NDDs in an effort to find markers of disease progression. The functional significance of MC-I, S1R and SV2A are discussed in this section.

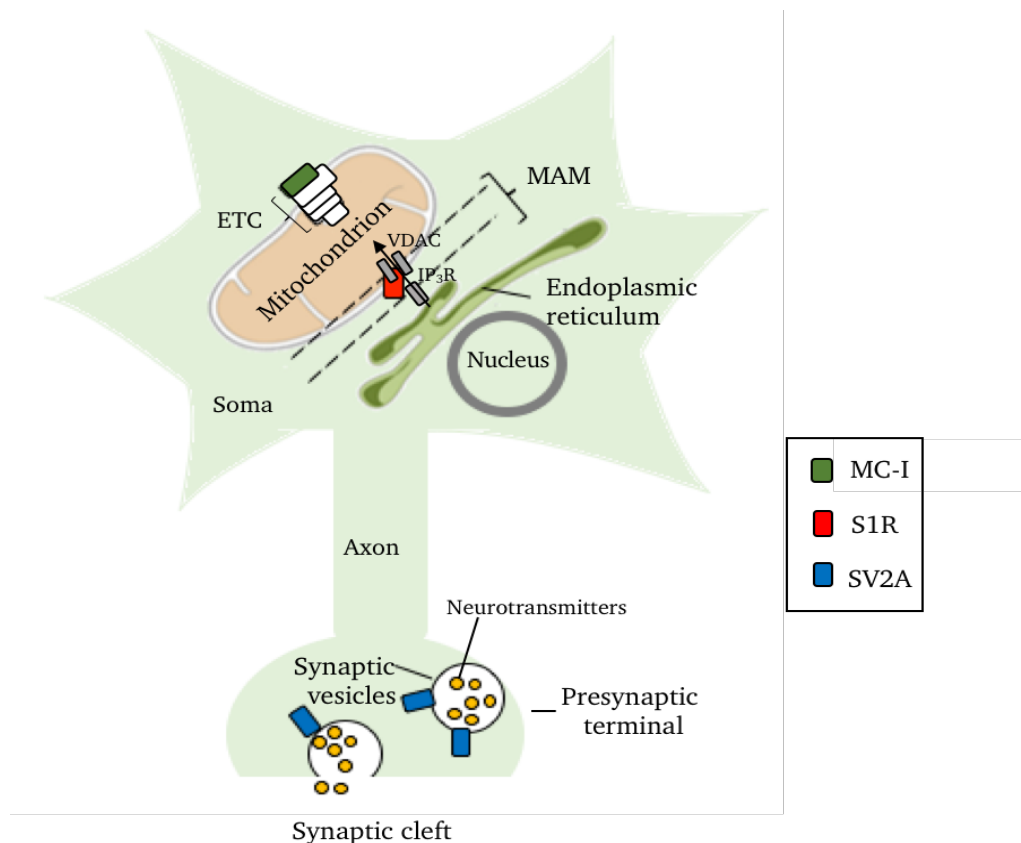


Figure 2.4 The mitochondrial/ER/synaptic axis. MC-I of the ETC enables OXPHOS which results in ATP production, in turn maintaining cellular Ca^{2+} homeostasis, ROS production and apoptosis. S1R of the MAM enables Ca^{2+} flow from the ER to the mitochondrion during OXPHOS, in addition to regulating ER functions critical to neuronal survival. SV2A regulates Ca^{2+} -mediated neurotransmitter release and is essential to neurotransmission. Figure adapted from Mansur et al., 2019.

2.3.1 Mitochondrial complex-I (MC-I)

MC-I is an ETC super-complex where the first step of OXPHOS takes place, and has chief roles in maintaining cellular Ca^{2+} homeostasis, producing reactive oxygen and nitrogen species and regulating apoptosis (A. Grimm & Eckert, 2017; Sazanov, 2015). Altered MC-I function has been associated with cell toxicity, ageing and NDD pathogenesis across diseases (A. Grimm & Eckert, 2017).

Altered MC-I function has been shown in post-mortem analyses of transgenic AD mouse brains which showed impaired MC-I composition that predates the appearance of A β plaques (Gillardon, Rist, Kussmaul, et al., 2007). Similarly, transgenic mice overexpressing Tau show MC-I impairment as well as resulting OXPHOS dysfunction assessed *in vivo* through measurements of mitochondrial membrane potential (Rhein, Song, Wiesner, et al., 2009). MC-I deficiency is also evident post-mortem in the brains of PD patients (Keeney, 2006; Schapira, Cooper, Clark, et al., 1990).

MC-I can be quantified *in vivo* using the PET radioligand ^{18}F -BCPP-EF, developed by Tsukada and colleagues (N. Harada, Nishiyama, Kanazawa, et al., 2013; Hideo Tsukada, 2014). The tracer kinetics of ^{18}F -BCPP-EF have been characterised in the non-human primate (NHP) brain and its suitability for human evaluation confirmed (Hideo Tsukada, 2014; Hideo Tsukada, Ohba, Kanazawa, et al., 2014). A PET study in NHPs has revealed correlations between ^{18}F -BCPP-EF signal and dopamine synthesis in PD, further supporting the potential for this radioligand as useful biomarker of NDD (H. Tsukada, Kanazawa, Ohba, et al., 2016).

2.3.2 Sigma-1 Receptor (S1R)

The sigma 1 receptor (S1R) is a non-opioid receptor located on the MAM. As demonstrated in Figure 2.4, a critical function of S1R is its action as a chaperone protein that stabilises the

inositol 1,4,5-trisphosphate receptor 3 (IP3) in its interaction with the voltage dependent anion channel (VDAC) situated on the outer mitochondrial membrane, to create a channel between the ER and the mitochondrion. (Cárdenas, Miller, Smith, et al., 2010; T Hayashi & Su, 2007). This channel increases Ca^{2+} flow into the mitochondria, enhancing OXPHOS. S1Rs are also involved in ER functions critical to cell survival such as protein sorting and folding, inflammation, lipid synthesis, neuronal plasticity and neuroprotection against oxidative stress induced cell damage and cell death (Giorgi, Missiroli, Patergnani, et al., 2015; T Hayashi & Su, 2007; Matsuno, Nakazawa, Okamoto, et al., 1996; Meunier & Hayashi, 2010; Nguyen, Lucke-Wold, Mookerjee, et al., 2015; Tuerxun, Numakawa, Adachi, et al., 2010).

Altered S1R expression is implicated in an increasing number of NDDs. Immunoblot data obtained from a mouse model of AD has shown increases in S1R predating the appearance of A β plaques (Hedskog, Pinho, Filadi, et al., 2013), highlighting the potential of S1R as an early marker of NDD. Post-mortem data from human patients with various NDDs also demonstrate S1R accumulation in the nuclear inclusions of their neurons (Miki, Mori, Kon, et al., 2014). The *in vivo* quantification of S1R was first made possible by Matsuno et al, who produced a selective PET ligand ^{11}C -SA-4503, which was then used to map S1Rs in the human brain for the first time by Sakata and colleagues (Matsuno, Nakazawa, Okamoto, et al., 1996; Sakata, Kimura, Naganawa, et al., 2007). Preclinical imaging studies have suggested that S1R regulates neuro-restorative mechanisms in a rodent model of PD (Francardo, Bez, Wieloch, et al., 2014), while human PET imaging with ^{11}C -SA-4503 has revealed altered S1R expression in the brains of PD patients (Mishina, Ishiwata, Ishii, et al., 2005).

2.3.3 Synaptic Vesicle protein 2A (SV2A)

The third and final molecular marker, synaptic vesicle protein 2A (SV2A) is a transmembrane glycoprotein expressed ubiquitously throughout the brain on synaptic vesicles (see Figure 2.4)

(Bajjalieh, Frantz, Weimann, et al., 1994). SV2A regulates Ca^{2+} mediated neurotransmitter release and thus is essential to neurotransmission (Chang & Sudhof, 2009; Wan, Zhou, Thakur, et al., 2010). SV2A expression is highly correlated with the expression of established pre-synaptic markers synaptophysin and synaptotagmin, making it an ideal target for monitoring synaptic density (Nowack, Yao, Custer, et al., 2010). SV2A dysfunction has long been associated with abnormal neurotransmission, with post-mortem studies showing reduced synaptic vesicles in AD, PD and HD (Hansen, Daniel, Wilcock, et al., 1998; Honer, Dickson, Gleeson, et al., 1992; Lassmann, Weiler, Fischer, et al., 1992; Sze, Bi, Kleinschmidt-Demasters, et al., 2000).

Synaptic loss is central to all NDDs, with changes to presynaptic structure and function evident in presymptomatic stages of diseases (Milnerwood & Raymond, 2010; Reddy, Tripathi, Troung, et al., 2012; Selkoe, 2002), raising interest in the use of SV2A markers such as ^{11}C -UCB-J which was used to quantify synapses *in vivo* for the first time in the NHP (Nabulsi, Mercier, Holden, et al., 2016). ^{11}C -UCB-J has demonstrated sensitivity to synaptic loss and is a valid alternative to synaptophysin (Finnema, Nabulsi, Eid, et al., 2016). The first *in vivo* quantification of SV2A by ^{11}C -UCB-J in humans was performed by Finnema et al. who characterised ^{11}C -UCB-J as binding specifically to SV2A and possessing ideal PET tracer characteristics with excellent test-retest reproducibility (Finnema, Nabulsi, Mercier, et al., 2017). ^{11}C -UCB-J has since been used to study synaptic loss in NDDs, with recent evidence of reduced ^{11}C -UCB-J signal in both AD and PD (M.-K. Chen, Mecca, Naganawa, et al., 2018; Matuskey, Tinaz, Wilcox, et al., 2020).

2.4 Aims and Outline

The aforementioned findings highlight the potential of MC-I, S1R and SV2A as biomarkers of NDD. Given the complicated interplay between components of the mitochondrial/ER/synaptic axis, studying these molecules in isolation could prove insufficient to elucidate underlying

mechanisms of neurodegeneration. The availability of PET radioligands that enable the quantification of MC1, S1R and SV2A, allows for these molecules to be studied in combination which is a potentially more useful index of mitochondrial/ER/synapse axis function. The MIND-MAPS Consortium has provided the platform to quantify all three targets in disease cohorts with AD, PD, FTD, HD and ALS, as well as in healthy ageing using ^{18}F -BCPP-EF, ^{11}C -SA-4503 and ^{11}C -UCB-J.

^{11}C -SA-4503 and ^{11}C -UCB-J have been evaluated in human studies, but ^{18}F -BCPP-EF imaging has thus far not been conducted in humans, and the tracer kinetics of the ligand in the human brain are not established. ^{11}C -UCB-J kinetics have been successfully validated in humans, however a fully validated kinetic modelling pipeline has yet to be established for human scanning with ^{11}C -SA-4503.

The primary aim of this thesis project was to identify and develop the optimal set of tracer kinetic models and PET image derived outcome measures for each of these radioligands to be implemented across MIND-MAPS cohorts to ensure consistency across analyses (Chapters 3-6). The PET measures derived from the healthy cohort will serve as control data for the cross-sectional studies. A secondary aim was to explore the effects of age and gender on MC-I, S1R and SV2A quantification in humans (Chapter 7).

The following chapter lays out the methodology that was used to develop standardised analysis pipelines for ^{18}F -BCPP-EF, ^{11}C -SA-4503 and ^{11}C -UCB-J.

3 Data Processing Pipelines and Datasets

The first part of this chapter details the pre-processing and analysis workflows that were applied in common to ^{18}F -BCPP-EF, ^{11}C -SA-4403 and ^{11}C -UCB-J scans included in the establishment of standardized analysis pipelines. Any further tracer-specific developmental work has been detailed in chapters 4, 5 and 6 which have been allocated to ^{18}F -BCPP-EF, ^{11}C -SA-4403 and ^{11}C -UCB-J, respectively.

All imaging and ancillary data were processed using Invicro London's in-house PET data quantification tool, MIAKATTM (version 4.3.7) which is implemented in MALTAB (version R2016a; MathWorks Inc.) and uses additional functions from SPM12 (Wellcome Trust Centre for Neuroimaging). The first section of this chapter covers the MRI and PET processing pipelines and their optimisation for each ligand. Tables of subject demographics and ancillary data associated with each scan are provided in the second section of this chapter.

3.1 MRI Data

3.1.1 Image Acquisition and Processing

All subjects received a comprehensive MRI battery including MPRAGE, Fast Grey Matter Acquisition T1 Inversion Recovery, neuromelanin, pulsed arterial spin labelling, diffusion tensor imaging, and resting state fMRI. The scope of this report is limited to the analysis of the T1-weighted structural MRI sequence, MPRAGE, which was used in the analysis of subsequently acquired PET data. This section will summarize the analysis workflow applied to each MRI scan as shown in Figure 3.1.

Each subject received a T1 weighted structural MRI scan acquired on a Siemens 3T Trio clinical MRI scanner (Siemens Healthineers, Erlangen, Germany) with a 32-channel phased-array head coil using a 3D MPRAGE sequence (TE = 2.98 ms, TR = 2300 ms, flip angle of 9°, voxel size = 1.0 mm x 1.0 mm x 1.0 mm).

MRI images were rigid-body aligned to a standard brain template in Montreal Neurological Institute 152 (MNI152) space to create images in Talairach orientation (Grabner, Janke, Budge, et al., 2006; Talairach & Szikla, 1980) and were segmented into grey and white matter probability maps using a unified segmentation algorithm implemented in SMP12 (Ashburner & Friston, 2005). The resulting maps were nonlinearly registered to a standard brain template in MNI152 space using the diffeomorphic nonlinear registration (DARTEL) algorithm, in turn producing a subject specific warp flow-field containing a spatial mapping from subject (T1) space to MNI152 space (Ashburner, 2007). The inverse of the DARTEL flow-fields were then applied to the CIC atlas to produce atlas images in final subject space (Tziortzi, Searle, Tzimopoulou, et al., 2011). As a final step, grey, white and whole structural brain images were resliced to create isotropic versions with a voxel size of 2.0 mm x 2.0 mm x 2.0 mm to be used

in the PET analysis pipeline. Representative images of inputs and outputs of the MRI processing pipeline are provided in Figure 3.1.

The following regions of interest (ROIs) were defined on the structural MRI images: brainstem (BST), substantia nigra (SN), thalamus (THA), ventral striatum (VST), caudate (CAU), putamen (PUT), hippocampus (HIP), insular cortex (INS), temporal lobe (TL), parietal lobe (PL) and frontal cortex (FTCX). The centrum semiovale (CS) region was provided by Takuya Toyonaga and Dr. Richard Carson from the PET Center Department of Radiology and Biomedical Imaging, which was defined in AAL space (Tzourio-Mazoyer, Landeau,

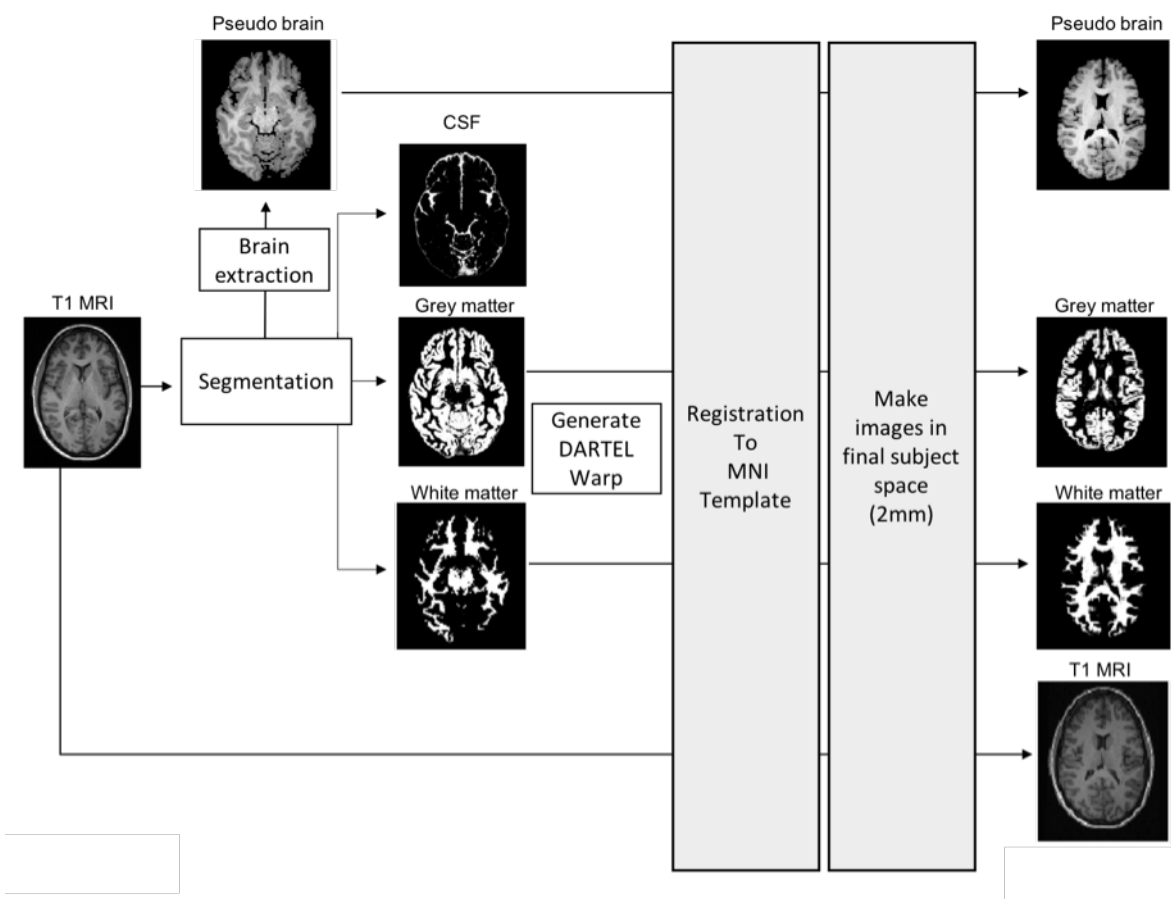


Figure 3.1 MRI data processing pipeline. Each subject's T1-weighted MRI scan was brought into Talairach space and segmented into grey matter, white matter and cerebrospinal fluid (CSF). The segmented images were nonlinearly registered to the MNI standard template to generate DARTEL flow fields. All images were resliced to create isotropic images with 2 mm x 2 mm x 2mm voxel size in final subject space. The inverse of the DARTEL flow fields derived from the nonlinear registration step was applied to the CIC atlas to generate atlas images in final subject space (not shown).

Papathanassiou, et al., 2002) and brought into subject space using the nonlinear registration parameters derived from previous spatial processing steps.

3.2 PET Data

3.2.1 Image acquisition

All PET scans were acquired on either a Siemens Hi-Rez Biograph 6 (FWHM: 7.35 mm, 7.35 mm, 14.4 mm) or Biograph 6 TruePoint PET/CT scanner (FWHM: 7.0 mm, 7.0 mm, 14.4 mm) (Siemens Healthcare, Erlangen, Germany). Although the two scanners used are similar models, the same scanner was used for each subject in order to remove any possibility of scanner differences affecting the test-retest results discussed in Chapter 4. A low-dose CT scan (30 mAs, 130 KeV, 0.55 pitch) was performed immediately before each PET scan in order to estimate attenuation. An intravenous cannula was inserted into a cubital or forearm vein of the subject for radioligand administration, and a second cannula was inserted into the radial artery to enable the collection of arterial blood samples. The radiotracers were administered as a slow bolus (over 20 seconds) in a volume of 20 mL at the start of the PET scan. Injection doses were prepared such that the injected activities would not exceed the maximum recommended injected activity (100 MBq ^{18}F -BCPP-EF, 300 MBq ^{11}C -SA-4503 and 300 MBq ^{11}C -UCB-J). The minimum injected dose was at the physician's discretion. Dynamic emission data were acquired over 90 minutes following radiotracer administration and were reconstructed into 26 frames (frame durations: 8 x 15 s, 3 x 60 s, 5 x 120 s, 5 x 300 s, 5 x 600 s). Corrections were applied to the raw data for attenuation, randoms and scatter.

3.2.2 Image processing

The PET data processing workflow implemented as part of the standard PET analysis pipeline is summarised in Figure 3.2. Following in-scanner pre-processing steps, attenuation corrected

dynamic PET data underwent a standard frame-by-frame motion correction process to account for between-frame motion and improve quantification. Each frame was registered to a reference frame (frame 16 of 26), using rigid body registration (SPM12). The level of motion during a scan was assessed visually as well as via plots of the registration parameters derived from this step. The two registration parameters assessed were translations in the x , y , and z directions and rotations in pitch, roll and yaw (see Figure 3.3 A for a demonstration of translational and rotational parameters assessed). Between-frame changes exceeding 10 mm or 10 degrees in translation and rotation respectively were flagged as ‘severe motion’, resulting in either the removal of the frame in question, or re-reconstruction. Re-reconstruction consisted of first manually dividing the scanning period into segments such that with-in segment motion was minimised, and then moving CT data into the corresponding positions by software registration.

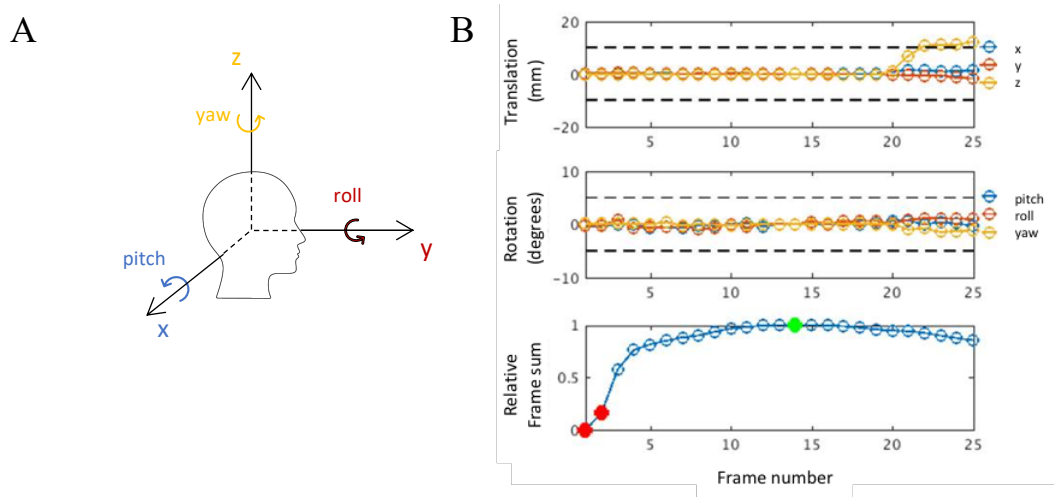


Figure 3.2 Motion correction of PET data. **A** Diagram depicting translational motion in x , y and z directions and rotational motion in pitch, roll and yaw directions. **B** Motion parameters of a subject who exhibited excessive translation motion (top panel), failed QC and whose PET data was subsequently re-reconstructed.

The adjusted CT data was then used to reconstruct the PET data into sections which could subsequently be joined together and analysed as normal. Figure 3.3B shows an example of a subject for which there was excessive translational motion between frames 23 and 26 that had to be re-reconstructed. Finally, motion-corrected dynamic images were rigid body-registered to the subjects' T1-weighted MRI resulting in a motion corrected dynamic image in T1 space (voxel size 2 mm x 2 mm x 2 mm).

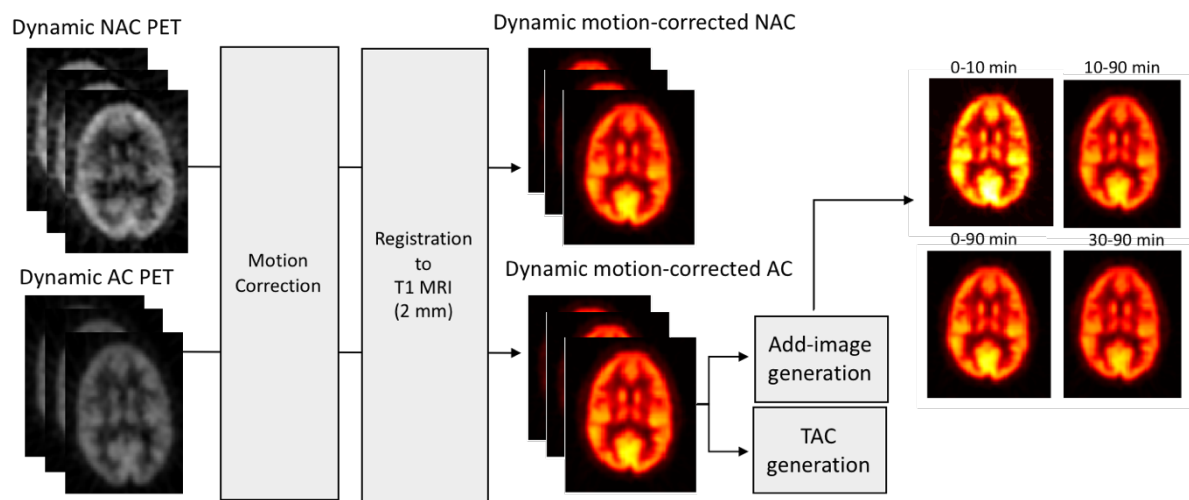


Figure 3.3 PET data processing pipeline. Attenuation corrected (AC) and non-attenuation corrected (NAC) dynamic PET series underwent frame-by-frame motion correction. Upon passing quality control (QC), motion corrected series were co-registered to subjects' MRI image. The final motion-corrected and registered dynamic AC series was used to create 3 sets of TACs (grey, white and no-mask) for each region of the CIC atlas, and used to derive summed images.

Motion corrected dynamic PET images were used to create summed static SUV images (top right Figure 3.2) to enable visualization of tracer distribution over 0-10 minute, 10-30 minute, 30-90 min and 10-90 minute time periods, and enable generation of SUVr data (see Chapter 4 section 4.4.2). Finally, the dynamic motion corrected PET images were used to create regional time activity curves (TACs, process described in Section 1.3.1) for all 125 regions in the CIC atlas. The grey and white tissue probability maps generated from the MRI segmentation step were used to generate TACs for both grey matter and white matter masked ROIs by taking a weighted mean of the voxel intensities for a given ROI and using the tissue probability maps

as a weighting factor. The final set of TACs were generated for non-masked, grey masked and white masked ROIs, which were then used for tracer kinetic modelling along with the arterial input function described in the following section.

3.2.3 Blood data acquisition and arterial input function modelling

As described in Chapter 1, quantification with full kinetic modelling first requires determining an accurate arterial plasma input function. For this, whole blood activity was measured using a continuous automatic blood sampling system (ABSS, Allogg AB, Marlefred, Sweden) for the first 15 minutes of each scan, which was acquired at a rate of 5 mL/min. Additional discrete blood samples were taken manually at 10, 15, 20, 25, 30, 40, 50, 60, 70, 80 and 90 minutes after scan start and total radioactivity concentration was evaluated in both blood and plasma in a Perkin Elmer 1470 10-well gamma counter. For each scan, arterial blood samples taken prior to tracer injection were centrifuged and the plasma free fraction (f_p) was measured by ultrafiltration in triplicate using an arterial blood sample taken prior to tracer injection.

For each ligand, 6 subjects were used to determine the appropriate plasma over blood and parent fraction models to create the optimum metabolite corrected arterial plasma input function. These models were applied to all subsequently acquired scans. Figure 3.4 summarises the steps involved in modelling the arterial input function which are detailed in the following sections.

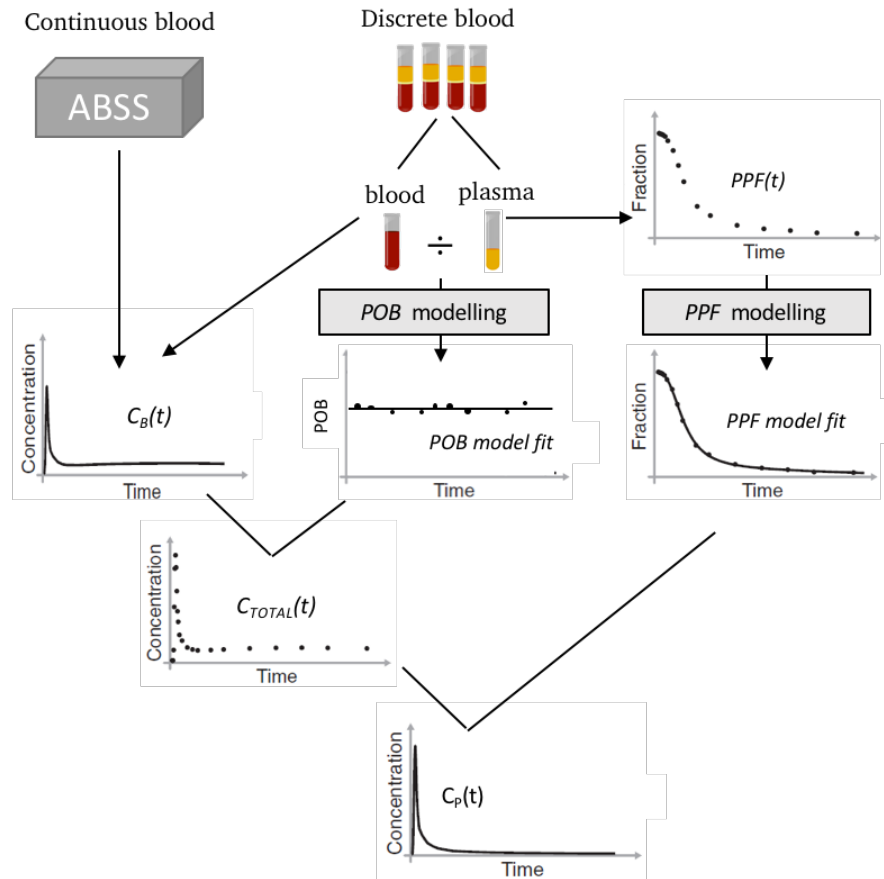


Figure 3.4 Derivation of arterial input function and PET outcome measures. Continuous samples were measured for their radioactivity using a gamma-counter scaled (i.e. calibrated) to match overlapping discrete whole blood samples measured at 5, 10 and 15 minutes, and then merged with the remaining discrete whole blood data to form a whole blood activity curve covering the duration of the scan $C_B(t)$. Activity measurements from the discrete plasma samples were divided by the corresponding whole blood data to form plasma-over-blood (*POB*) data which was fitted with a *POB* model. The resulting fitted *POB* was multiplied with $C_B(t)$ to give a total plasma activity curve, $C_{TOTAL}(t)$. The radioactivity in the plasma was fitted with a *PPF* model to generate a parent fraction curve, which was multiplied by C_{TOTAL} , and smoothed post peak to generate the final metabolite-corrected arterial plasma input function, $C_p(t)$. A time delay was fitted and applied to the input function to account for the separation between blood sample and tissue (not depicted).

Plasma over blood (*POB*) model selection

Discrete blood sample data were fitted with four empirical *POB* models (see Appendix A for full list of models) to determine the ratio of tracer concentration in plasma to that in blood. Akaike Information Criterion (Equation 1.20) was used to select the best model where the lowest AIC value was chosen as the model with the most parsimonious fit. The *POB* ratio resulting from the chosen model fit was applied to the measured whole blood activity curve $C_B(t)$ to generate a total plasma activity curve, $C_{TOTAL}(t)$.

Parent fraction (*PPF*) model selection

Seven discrete blood samples were used to determine the fraction of plasma radioactivity constituted by unchanged parent radioligand (*PPF*) using HPLC analysis. Radiometabolite peaks from chromatogram data were used to calculate the *PPF* for each sample *i*

$$PPF_i = \frac{\sum[\text{cpm}_{par} - \mu(\text{cpm}_{bkg})]}{\sum[\text{cpm}_{par+met} - \mu(\text{cpm}_{bkg})]} \quad \text{Equation 3.1}$$

where cpm is counts per minute, μ is the average, *bkg* is the background window, *par* is the parent metabolite window and *met* is the metabolite window. Figure 3.5 shows an example of chromatograms generated from the first (5 minute) and last (90 minute) metabolite samples acquired during dynamic PET scan, where for illustrative purposes, the parent and metabolite windows have been marked with red and black arrows, respectively. These windows were defined for each ligand based on initial visual inspection of chromatograms from 4-5 PET scans, and cross-checked against elution times defined in the literature, where available.

Background activity was defined as the average of the counts per minute in the background window. The background window was either set individually for each sample by a blood lab technician resulting in windows of varying lengths across scans (referred to in Chapter 5 as the ‘original model’) or defined as part of the analysis process from the average cpm in a wider window fixed to include all non-parent and non-metabolite retention times (referred to in Chapter 5 as the ‘modified model’). *PPF* data were defined using only the parent and metabolite windows under the assumption that with proper background correction, the sum of counts in the background window would sum up to zero.

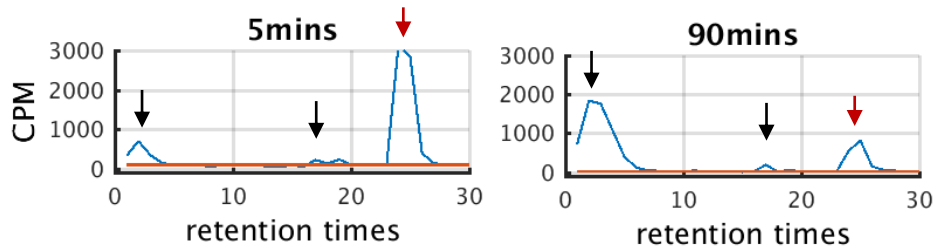


Figure 3.5 Example chromatogram data showing parent and radiometabolite radioactivity measured by HPLC at 5 minutes (left) and 90 minutes (right) post tracer administration. The red and black arrows indicate parent and metabolite windows, respectively.

PPF data defined using Equation 3.1 were used to generate a parent fraction curve describing tracer metabolism in plasma over the duration of the scan. The resulting *PPF* curve was subsequently fitted with 7 empirical *PPF* models (see Appendix B for full list of models used), and AIC was used to select the optimum model. In the case where there was a second or third potential *PPF* model, separate arterial input functions were calculated with each *PPF* model and the remaining modelling steps were run in parallel to obtain PET outcome measures for each case (see Chapter 5, SA4503 metabolite analysis). As a final step, the radioactivity in the plasma was multiplied by the parent fraction estimated from the optimum *PPF* model, $PPF(t)$,

$$C_P(t) = C_{TOTAL}(t) \cdot PPF(t) \quad \text{Equation 3.2}$$

resulting in a metabolite-corrected arterial plasma input function ready to be used as input for tracer kinetic modelling in the brain.

3.2.4 Kinetic Analysis and Model Selection

As an initial assessment of appropriate kinetic models, the TAC data from 6 subjects were fitted with fixed (blood volume = 5%) and fitted blood volume variants of the one and two-tissue compartmental models (1TC & 2TC), the performance of which were assessed using AIC and parameter identifiability based on the percentage standard error (SE) derived from the covariance matrix. TACs were also fitted with graphical method multilinear analysis 1 (MA1) with fitted and fixed blood volume variants as well as varying temporal windows ($t^* = 20, 30$

and 40 min). Prior to fitting, whole blood radioactivity was subtracted from the TAC data. Linear regression coefficient of determinations (r^2) were used to compare performance between the graphical method MA1 and the compartmental models.

The tissue kinetic model selection process described in this section was repeated for all three radioligands. The main outcome measures assessed in common for all three radioligands were volume of distribution (V_T), distribution volume ratio (DVR) and V_T normalised to f_p (V_T/f_p). V_T/f_p was reported to explore its utility in studies where cross-sectional differences in f_p may arise. V_T estimates that were poorly estimated ($SE\% > 10$) were excluded from model comparisons. Semi-quantitative outcome measure SUVr was also reported for ^{18}F -BCPP-EF and ^{11}C -UCB-J.

3.2.5 Time stability analysis

In order to assess the stability of each radiotracer over time, the performance of tracer kinetic models was assessed over varying scan lengths (from a full 90 minute acquisition to 10 minutes) by re-estimating regional V_T for each scan duration. The re-estimated V_T values were expressed as percentages of the V_T estimate derived from the full scan ($V_T^{90\text{min}}$). The distribution of V_T across all subjects and regions was assessed for each scan duration and used as a measure of time stability of the radiotracers in the population.

3.2.6 Parametric map generation

Parametric V_T maps were generated for each ligand in order to generate population mean and standard deviation images. The basis function implementation of 1TC was used to generate parametric images for ^{11}C -UCB-J. MA1 graphical analysis were used to generate individual parametric images for ^{18}F -BCPP-EF and ^{11}C -SA-4503. Individual parametric images were spatially normalized to MNI152 using nonlinear registration to enable the generation of a mean

parametric image for each ligand. Parametrically derived V_T values were compared against those generated from full kinetic modelling using correlation analysis.

3.3 Datasets

This section provides information on the datasets used for the various analyses included in this thesis. The reader is referred to the tables presented here throughout chapters 4-7.

3.3.1 MIND-MAPS Healthy Volunteer Cohort

This cohort consisted of 14 male and 11 female subjects between the ages of 22 and 79 who successfully completed the MIND-MAPS MRI battery and dynamic ^{18}F -BCPP-EF, ^{11}C -SA-4503 and ^{11}C -UCB-J scans with full arterials. One subject withdrew before having their ^{11}C -UCB-J scan (subject 104), reducing the total number of ^{11}C -UCB-J scans to 24. Two subject's ^{11}C -SA-4503 scans were unusable; one of which was due to excessive motion (subject 101) and the other due to a lack of arterial blood samples (subject 120). Both subjects were excluded from the final ^{11}C -SA-4503 analysis. Table 3.1 includes the gender, age, weight, height and body-mass index (BMI) information of the full cohort, all of which were included in the healthy aging analysis (Chapter 7). Table 3.2 includes details of injection parameters and f_p measurements for each scan. All injected activities were under the maximum limit stated in the study protocol. Subjects 101 and 102 were injected with low doses of ^{11}C -UCB-J compared to the mean due to low yield production on the day. The 12 subjects highlighted in grey were included in the quantification of ^{18}F -BCPP-EF, ^{11}C -SA-4503 and ^{11}C -UCB-J in chapters 4, 5 and 6, respectively. The 6 subjects highlighted in bold were used in the preliminary investigations of which arterial plasma input function models and tissue kinetic models to include in the main analysis.

Table 3.1 Demographic Information – MINDMAPS healthy cohort (n=25)

Subject ID	Gender	Age (yrs)	Weight (kg)	Height (cm)	BMI (kg/m ²)
101*	male	29	86.6	180	26.7
102	male	28	80.5	184	23.8
103	male	56	69.9	174	23.1
104†	female	22	59.8	174	19.8
105	male	23	50.1	169	17.5
106	male	75	84.0	176	27.1
107	female	67	62.2	154	26.2
108	female	65	45.0	160	17.6
109	male	46	58.1	176	18.8
110	female	78	55.7	154	23.5
111	male	69	86.1	182	26.0
112	male	68	73.2	180	22.6
113	female	50	87.1	161	33.6
114	female	69	51.1	167	18.3
115	female	75	64.1	154	27.0
116	female	33	69.8	160	27.3
117	male	73	91.8	182	27.7
118	male	64	83.5	182	25.2
119	female	52	67.9	158	27.2
120‡	female	24	79.9	168	28.3
121	male	47	77.9	178	24.6
122	male	74	78.7	177	25.1
123	female	73	88.4	164	32.9
124	male	41	101.0	192	27.4
125	male	36	93.9	178	29.6
Mean ± SD	n/a	53 ± 19	73.9 ± 15.1	171 ± 10	25.1 ± 4.3

* Subject 101 ¹¹C-SA-4503 scan excluded from analysis due to excessive motion

† Subject 104 did not receive a ¹¹C-UCB-J scan

‡ Subject 120 did not receive a ¹¹C-SA-4503 scan

BMI: Body mass index

Table 3.2 Injection parameters and f_p measurements of MIND-MAPS healthy cohort

Subject ID	¹⁸ F-BCPP-EF			¹¹ C-SA-4503			¹¹ C-UCB-J		
	Injected Activity (MBq)	Injected Mass (μg)	f_p	Injected Activity (MBq)	Injected Mass (μg)	f_p	Injected Activity (MBq)	Injected Mass (μg)	f_p
101*	81	0.02	0.091	267	3.86	0.111	90	4.33	0.228
102	86	0.02	0.080	239	1.94	0.094	92	4.48	0.238
103	87	0.03	0.075	257	3.10	0.070	250	3.43	0.273
104†	91	0.06	0.120	249	4.58	0.079	N/A	N/A	N/A
105	89	0.07	0.064	250	2.51	0.071	168	1.22	0.264
106	94	0.04	0.056	281	2.82	0.052	234	1.85	0.205
107	89	0.04	0.086	267	2.29	0.051	176	1.61	0.185
108	97	0.13	0.087	277	5.23	0.072	113	1.45	0.215
109	91	0.07	0.069	244	2.41	0.059	191	2.05	0.247
110	86	0.16	0.083	237	2.58	0.042	182	1.80	0.226
111	87	0.06	0.074	221	2.86	0.058	261	6.26	0.248
112	91	0.05	0.074	234	1.82	0.060	234	1.82	0.208
113	91	0.05	0.061	255	2.01	0.051	230	2.12	0.214
114	96	0.11	0.096	236	1.47	0.064	278	2.23	0.238
115	82	0.09	0.065	268	1.59	0.062	247	2.52	0.253
116	85	0.04	0.074	219	5.43	0.054	249	2.60	0.264
117	82	0.09	0.082	252	3.28	0.099	245	3.53	0.232
118	88	0.12	0.082	277	3.10	0.103	152	2.54	0.249
119	85	0.06	0.125	270	4.77	0.058	282	1.92	0.323
120‡	86	0.15	0.121	n/a	n/a	N/A	208	1.93	0.296
121	88	0.04	0.075	283	7.23	0.044	240	2.85	0.231
122	91	0.07	0.078	271	4.95	0.056	119	0.82	0.230
123	88	0.09	0.072	236	7.78	0.054	141	2.56	0.238
124	92	0.09	0.082	275	2.34	0.069	261	2.30	0.349
125	92	0.12	0.072	269	2.71	0.053	241	2.20	0.230
Mean ± SD	89 ± 4	0.08 ± 0.04	0.082 ± 0.018	256 ± 19	3.44 ± 1.70	0.066 ± 0.019	203 ± 59	2.52 ± 1.19	0.245 ± 0.037

* Subject 101 ¹¹C-SA-4503 scan excluded from analysis due to excessive motion

† Subject 104 did not receive a ¹¹C-UCB-J scan

‡ Subject 120 did not receive a ¹¹C-SA-4503 scan

3.3.2 ¹⁸F-BCPP-EF Test-retest cohort

6 subjects (3 males, 3 females, ages: 24-54) were enrolled in the test-retest variability analysis for ¹⁸F-BCPP-EF, only 5 of which completed both test and retest scans. Subject 002 withdrew following the test visit and was not included the final test-retest analysis. The subject's test scan was, however, included in the assessment of SUV_r as a suitable outcome measure for ¹⁸F-BCPP-

EF (see Chapter 4 section 4.4.2 for analysis). The demographic details of this cohort are provided in Table 3.3, while injection parameters and f_p measurements are given in Table 3.4.

Table 3.3 Demographic Information – ^{18}F -BCPP-EF test-retest cohort (n=6)

Subject ID	Gender	Age (yrs)	Weight (kg)	Height (cm)
001	male	26	81.6	174
002*	male	24	77.8	176
003	female	29	69.7	179
004	female	54	67.3	146
005	female	25	52.3	160
006	male	49	71.0	173
Mean \pm SD	n/a	35 \pm 13	70.0 \pm 10.2	168 \pm 13

*Subject 002 did not receive a retest scan.

Table 3.4 Injection parameters and f_p measurements of ^{18}F -BCPP-EF test-retest cohort

Subject ID	Group	^{18}F -BCPP-EF		f_p
		Injected Activity (MBq)	Injected Mass (μg)	
001	Test	91	0.04	0.068
002*		90	0.07	0.065
003		98	0.05	0.085
004		90	0.12	0.057
005		93	0.08	0.083
006		90	0.1	0.066
Mean \pm SD		92 \pm 3 [†]	0.08 \pm 0.03 [†]	0.072 \pm 0.012 [†]
001	Retest	92	0.11	0.067
003		95	0.08	0.071
004		88	0.05	0.05
005		89	0.09	0.075
006		89	0.09	0.062
Mean \pm SD		91 \pm 3	0.08 \pm 0.02	0.065 \pm 0.010

*Subject 002 did not receive a retest scan.

† Subject 002 not included in mean calculation

4 Quantification and kinetic modelling of ^{18}F -BCPP-EF

Chapter 3 provided an overview of the MRI and dynamic PET processing steps used to generate time activity data for ^{18}F -BCPP-EF, ^{11}C -SA4503 and ^{11}C -UCB-J, as well as blood and tissue kinetic modelling pipelines that were implemented to characterise the three radioligands. In this chapter, the results of the various kinetic modelling approaches evaluated for ^{18}F -BCPP-EF are presented and the optimum tracer kinetic quantification models and outcome measures for this radioligand are established.

4.1 Background and Study Overview

As detailed in Chapter 2, ^{18}F -BCPP-EF is a PET radioligand that targets MC-I in the brain. In their work in NHPs, Tsukada and colleagues demonstrated that ^{18}F -BCPP-EF possessed good lipophilicity and moderate affinity allowing it to readily enter the brain where it displays reversible kinetics (Hideo Tsukada, Ohba, Kanazawa, et al., 2014). ^{18}F -BCPP-EF showed rapid uptake and metabolism in the NHP brain, with polar metabolites that do not cross the BBB (Hideo Tsukada, 2014; Hideo Tsukada, Ohba, Kanazawa, et al., 2014). These findings, along with the specificity of ^{18}F -BCPP-EF for MC-I have paved the way for its successful transition from animal into human studies.

The first part of this study aimed to establish the optimal blood plasma and tissue tracer kinetic quantification approaches and outcome measures for ^{18}F -BCPP-EF in the human brain using data from 12 healthy subjects (Table 3.1, highlighted cohort) (sections 4.2 – 4.3). The second part of the study explored potential reference region approaches to simplify the quantification of ^{18}F -BCPP-EF in clinical studies and included a time stability analysis of the tracer using the full cohort of 30 ^{18}F -BCPP-EF subjects (section 4.4 – 4.5). Finally, the test-retest reproducibility of ^{18}F -BCPP-EF derived binding parameters was assessed (section 4.6).

4.2 Tracer uptake and distribution

^{18}F -BCPP-EF entered the brain readily and demonstrated a heterogeneous distribution (Figure 4.1). Uptake into the brain was fast and peaked at ~5 – 12 minutes post-injection, similar to the time peak tracer uptake was observed in the NHP (~10 minutes post-injection). Peak uptake values ranged from 2.7 g/ml in the centrum semiovale to 6.4 g/ml in the putamen. The high uptake observed in striatal regions was consistent with previously published NHP data (Hideo

Tsukada, Ohba, Kanazawa, et al., 2014). SUV values derived from the centrum semiovale were approximately 50% lower compared to all grey matter regions investigated.

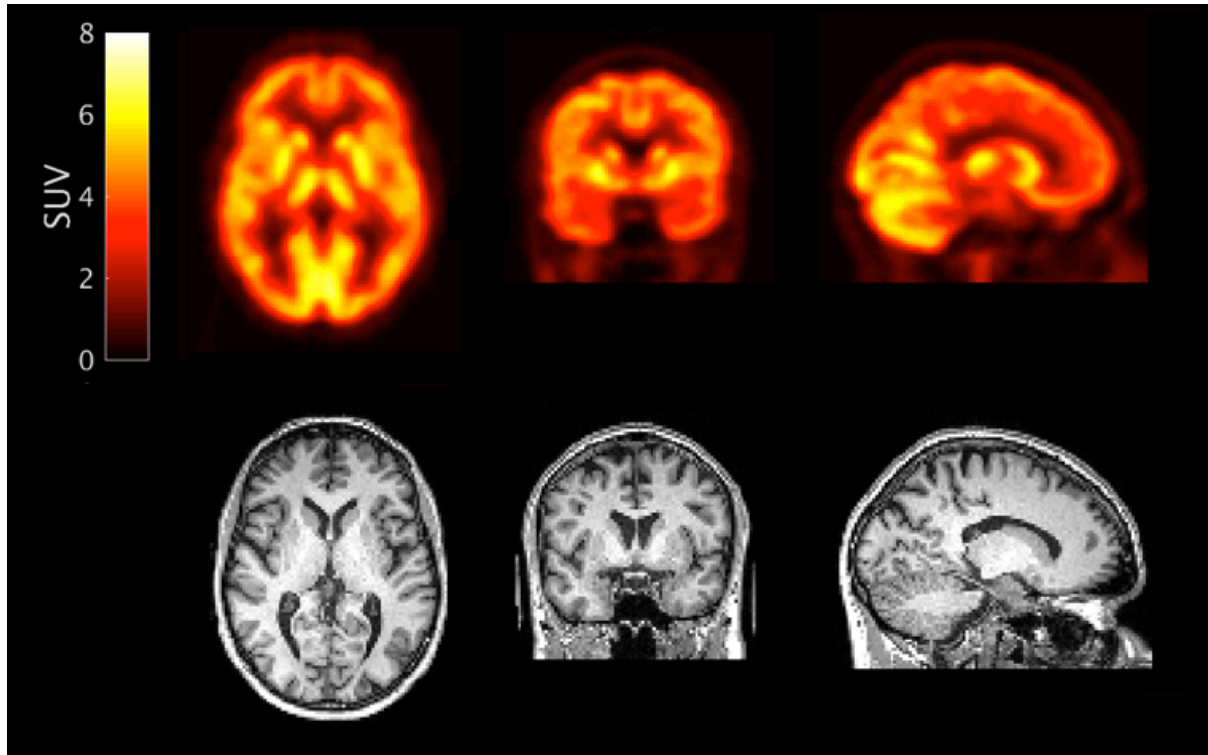


Figure 4.1 Orthogonal cross sections of co-registered ^{18}F -BCPP-EF PET and MR images from a representative subject. PET images are shown as SUV summed from 10-90 minutes.

4.3 Determining the optimum arterial plasma input function

The protocol for the acquisition and processing of arterial blood data acquired during a dynamic PET scan was presented in Chapter 3 (see Figure 3.4). This section includes the results of the modelling process of the concentration of radioligand in plasma over blood (*POB*) and the fraction of parent radioligand free to enter brain tissue (*PPF*), both of which are necessary to create an accurate input function. The models established here were applied to blood data acquired during all subsequent ^{18}F -BCPP-EF scans.

4.3.1 Modelling the plasma over blood (*POB*) data

An initial visual inspection of model fits showed that the ratio of ^{18}F -BCPP-EF concentration in plasma to that in blood (*POB*) was constant over the course of the PET scan (Figure 4.2). Further comparison of 4 empirical *POB* models (see Appendix A for full list of equations) using the AIC confirmed that the ‘constant’ model produced the lowest AIC values and therefore best described the *POB* ratio of ^{18}F -BCPP-EF,

$$POB(t) = c \quad \text{Equation 4.1}$$

where c is the plasma over blood ratio at time t . As seen in Figure 4.2, the *POB* data fitted with the ‘constant’ model produced good fits in all subjects, resulting in a *POB* ratio in the range of 1.25 – 1.40.

4.3.2 Modelling the plasma parent fraction (*PPF*) data

^{18}F -BCPP-EF metabolised fairly rapidly in plasma, with $\sim 20\%$ of unmetabolized radioligand measured at 90 minutes post injection. High pressure liquid chromatography (HPLC) data showed one highly polar radiometabolite with an elution time of 2 minutes and a second one with a longer elution time and less radioactivity eluting between 5-7 minutes.

Of the 7 *PPF* models investigated, the most parsimonious fits to the parent fraction data were provided by a sigmoid function with 3 parameters α , β , and γ ,

$$PPF(t) = \frac{\left(1 - \frac{t^3}{t^3 + 10\alpha}\right)^\beta + \gamma}{1 + \gamma} \quad \text{Equation 4.2}$$

where $PPF(t)$ is the estimated fraction of intact parent radioligand in plasma at time t . The sigmoid model selected produced good fits for all subjects included in the study (Figure 4.3). The *PPF* derived from these fits was estimated at $20 \pm 8\%$ at 90 minutes post injection ($n=12$).

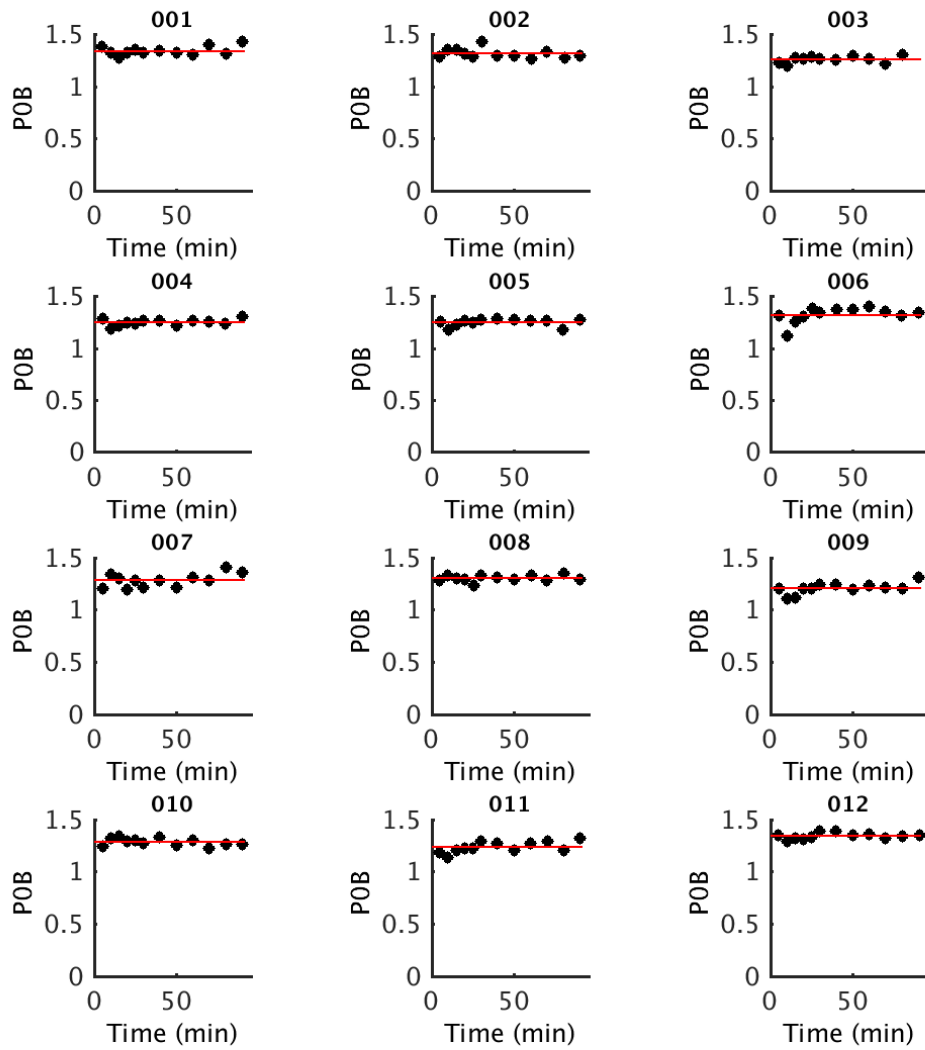


Figure 4.2 Fits of the 'constant' POB model to the blood data from 12 ^{18}F -BCPP-EF scans

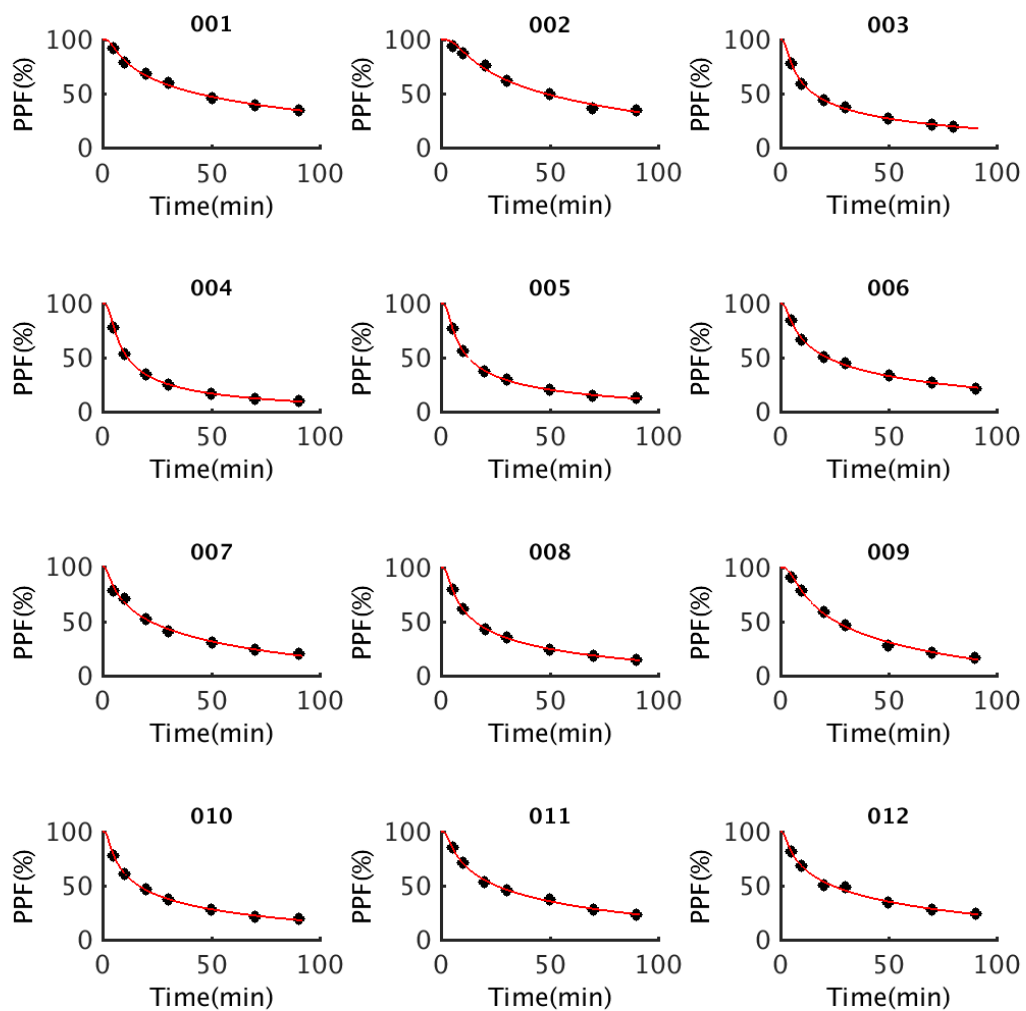


Figure 4.3 Fits of the 'sigmoid' *PPF* model to the metabolite data from 12 ^{18}F -BCPP-EF scans

4.4 Determining the optimum tissue kinetic model for ^{18}F -BCPP-EF

In the comparison of fixed vs. fitted blood volume variants of the kinetic models tested, the fixed variant where blood volume was fixed to 5% produced lower AIC values for all three models. The comparison of the 3 temporal variants of MA1 (t^* 20, 30 and 40 min) to 2TC showed that a t^* of both 20 and 30 minutes produced V_T estimates that were highly correlated with 2TC derived results ($t^* = 20$ min, $r^2=0.99$; $t^* = 30$ min, $r^2=0.99$). The final set of models to be investigated for ^{18}F -BCPP-EF was narrowed down to the following 3; 1TC (fixed BV), 2TC (fixed BV) and MA1 (fixed BV, $t^* = 30$ min).

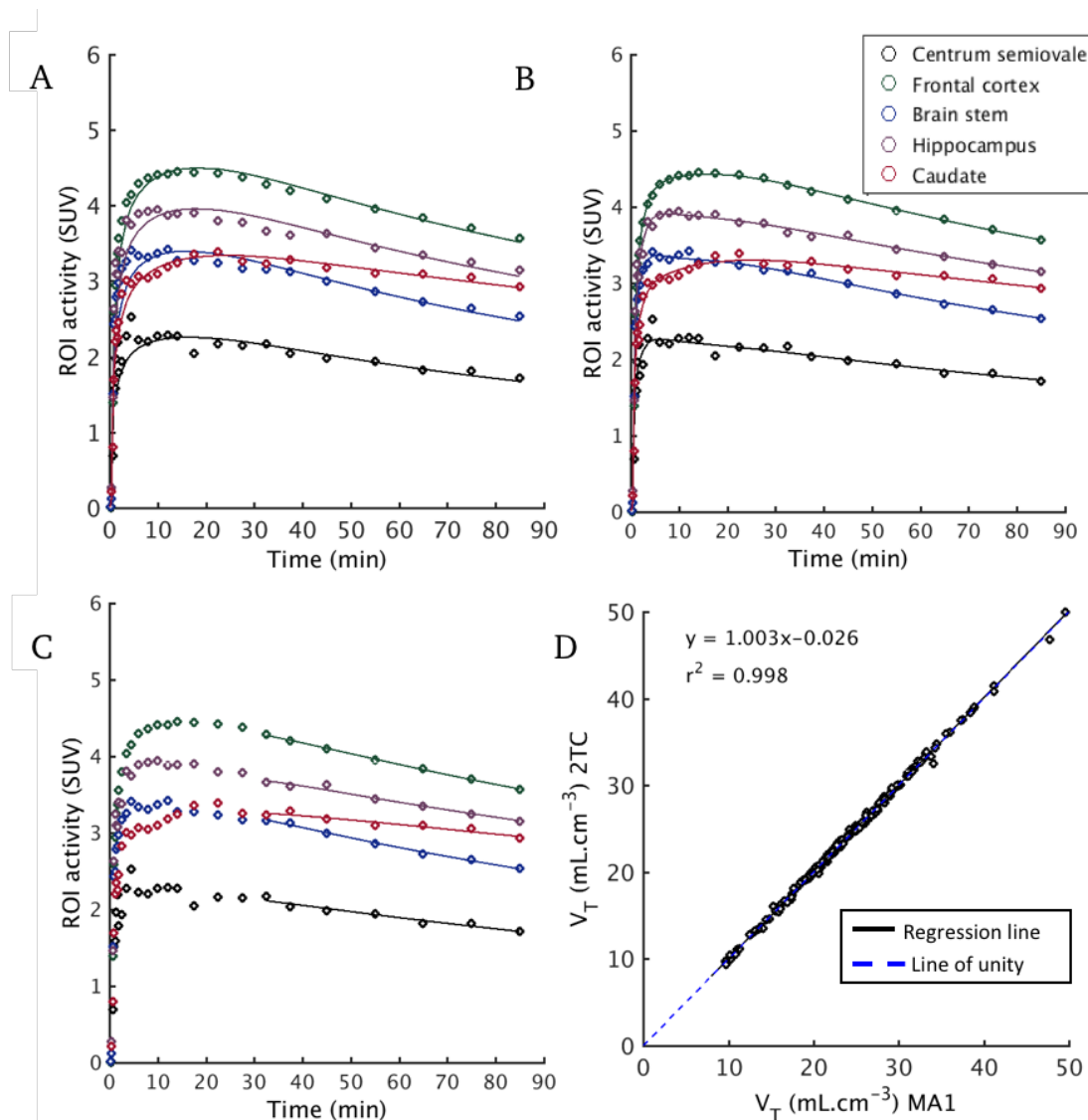


Figure 4.4 ^{18}F -BCPP-EF regional TACs and model fits for a representative subject derived with **A** 1TC, **B** 2TC and **C** MA1. **D** Linear regression plot showing comparison of MA1 vs 2TC derived ^{18}F -BCPP-EF V_T ($n=12$).

^{18}F -BCPP-EF displayed reversible kinetics with all three kinetic models reaching convergence in the regional TAC data (Figure 4.4 A-C). Regional mean V_T , DVR and V_T/f_p estimates derived from the 1TC, 2TC and MA1 are summarised in table 4.1. V_T was robustly estimated in all ROIs explored using both 1TC and 2TC (SE < 10%). AIC values were lower for 2TC over 1TC in all 156/156 cases tested (13 regions x 12 subjects). 2TC and MA1 derived V_T were in excellent agreement ($r^2 = 0.99$) (Figure 4.4 D) and were therefore both chosen as suitable modelling methods for this ligand.

Table 4.1 ^{18}F -BCPP-EF derived regional PET outcome measures

Outcome Kinetic Measure	Kinetic Model	CS	BST	SN	THA	VSTR	CAU	PUT	HIP	INS	TL	PL	FTCX	CER	
V_T (ml.cm ⁻³)	1TC	Mean	10.8	16.2	19.2	21	29.6	19.2	31.9	19.6	24.9	23.1	24.5	23.3	28.5
		COV	19%	17%	14%	21%	21%	32%	20%	19%	18%	18%	21%	19%	17%
	2TC	Mean	11.9	17.5	20.9	22.8	31.6	20.4	34.1	21.6	26.5	24.7	26	24.7	30.6
		COV	17%	17%	14%	20%	20%	32%	18%	18%	17%	17%	20%	18%	16%
	MA1	Mean	11.9	17.5	20.9	22.9	31.6	20.4	34	21.7	26.6	24.8	26.1	24.8	30.6
		COV	17%	17%	14%	20%	20%	32%	19%	18%	17%	17%	20%	19%	16%
V_T/f_p (ml.cm ⁻³)	1TC	Mean	143	214	254	278	391	255	422	259	329	306	323	309	377
		COV	16%	17%	14%	21%	20%	35%	18%	18%	17%	17%	18%	18%	15%
	2TC	Mean	157	232	277	302	418	271	451	286	351	328	343	327	405
		COV	15%	18%	14%	20%	19%	35%	17%	17%	17%	17%	17%	18%	15%
	MA1	Mean	157	232	277	303	419	271	450	287	352	329	344	329	405
		COV	16%	18%	14%	20%	20%	35%	17%	17%	17%	17%	18%	18%	15%
DVR	1TC	Mean	n/a	1.51	1.79	1.95	2.73	1.77	2.96	1.82	2.31	2.15	2.27	2.17	2.65
		COV	n/a	10%	9%	12%	10%	27%	9%	11%	9%	10%	10%	9%	8%
	2TC	Mean	n/a	1.47	1.76	1.92	2.65	1.71	2.86	1.82	2.23	2.08	2.17	2.07	2.58
		COV	n/a	12%	8%	13%	11%	28%	9%	11%	9%	10%	9%	8%	10%
	MA1	Mean	n/a	1.58	1.78	1.93	2.67	1.71	2.87	1.83	2.25	2.10	2.19	2.09	2.59
		COV	n/a	12%	10%	14%	12%	29%	10%	11%	10%	10%	10%	9%	10%

V_T values ranged from 11.9 ± 2.0 ml.cm⁻³ in the centrum semiovale to 34.0 ± 6.6 ml.cm⁻³ in the putamen. The intersubject variability of regional V_T estimates across all regions investigated was calculated as $18 \pm 3\%$. The intersubject variability in DVR results derived using the centrum semiovale as a reference region was reduced, while correcting V_T by f_p had no significant effect on intersubject variability.

4.5 Investigation of the centrum semiovale as a pseudo reference region

MC-I is present in all mitochondria in the human body, making it unfeasible to find a region completely devoid of specific signal. The CS, demonstrated in Figure 4.5, is a small subsection of the white matter which has previously been investigated as a reference region for various radioligands that have shown low or negligible signal in this region compared to grey matter regions (Finnema, Nabulsi, Eid, et al., 2016). Recently, the definition of the region has been optimised such that the risk of signal contamination by partial volume effects from surrounding grey matter have been minimised, therefore offsetting any noise that may arise from the low signal and small size of the region (Finnema, Nabulsi, Eid, et al., 2016). As stated earlier, ^{18}F -BCPP-EF showed $\sim 50\%$ lower uptake in the CS compared to grey matter ROIs in this dataset. Energy consumption in the white matter is approximately 20-25% of that in the grey matter as a result of the markedly high energy cost associated with neuronal signalling which is consistent with the low MC-I related signal seen in this region (Harris & Attwell, 2012; Yu, Herman, Rothman, et al., 2018). Together these suggest that the CS is a good candidate for investigation as a pseudo reference region.



Figure 4.5 Demonstration of centrum semiovale (CS) placement within a white matter mask. CS region kindly provided by Takuya Toyonaga and Dr. Richard Carson from the Yale PET Center.

The validation of a region as a reference region typically requires carrying out a homologous competition study using a target specific blocking agent. However, due to the potentially lethal effects fully blocking MC-I can have on cardiac function, there is no suitable blocking agent available to be used in human studies. In this absence of human blocking data, the suitability of the CS as a possible pseudo reference region was assessed based on previously acquired data provided to us by Professor Hideo Tsukada and colleagues from a study conducted in 4 healthy male rhesus monkeys (*Macaca mulatta*) (age: 3-5 years) scanned with ^{18}F -BCPP-EF at baseline and following pre-administration of 0.1 mg/kg of rotenone (MC-I inhibitor). Although a full dose-escalation was not possible, baseline and post-rotenone competition V_T data was provided for a set of 10 ROIs (Table 4.2). Full details on scanning procedures, rotenone administration and study protocol are provided in the manuscript by Tsukada et al (Hideo Tsukada, Ohba, Kanazawa, et al., 2014).

Table 4.2 V_T data from baseline/ post-rotenone monkey and baseline human ^{18}F -BCPP-EF scans

ROI	MONKEY (n=4)		HUMAN (n=30)
	Baseline	Post-block	-
Centrum semiovale	N/A	N/A	10.9 ± 1.9
Cerebral WM	13.4 ± 3.0	10.6 ± 2	15.5 ± 3.0
Cerebellum	26.2 ± 3.0	16.2 ± 1.4	28.1 ± 4.9
Frontal cortex	26.0 ± 1.0	17.0 ± 0.9	23.6 ± 4.2
Temporal cortex	26.7 ± 1.9	17.1 ± 0.9	23.4 ± 3.8
Occipital cortex	34.4 ± 4.8	20.6 ± 2.7	26.2 ± 4.6
Striatum	30.6 ± 1.9	19.3 ± 3.3	27.4 ± 5.2
Hippocampus	23.4 ± 1.0	15.0 ± 1.2	20.4 ± 3.5
Parietal cortex	28.5 ± 1.7	17.4 ± 0.8	24.4 ± 4.7
Cingulate	27.7 ± 1.8	18.3 ± 0.09	25.4 ± 4.5

Data are mean ± SD with units of $\text{ml}\cdot\text{cm}^{-3}$. Centrum semiovale data was not available for the monkey dataset.

4.5.1 Estimation of ^{18}F -BCPP-EF V_{ND} from NHP data

Regional $V_T^{\text{baseline}} - V_T^{\text{rotenone}}$ data were plotted against V_T^{baseline} data to create an occupancy plot, from which an estimate for the non-displaceable volume of distribution (V_{ND}) in NHP was derived (Cunningham, Rabiner, Slifstein, et al., 2010; Lassen, Bartenstein, Lammertsma, et al.,

1995)(Figure 4.6). A nonlinear least-squares estimator was used to derive fractional brain occupancy of MC-I by rotenone for each monkey, with a shared V_{ND} across all four monkeys.

Given the assumption that BP_{ND} is conserved between NHP and human species ($BP_{ND}^{NHP} \cong BP_{ND}^{Human}$), the following equation holds true,

$$\frac{V_T^{Human}}{V_T^{NHP}} = \frac{V_{ND}^{Human}}{V_{ND}^{NHP}} \quad \text{Equation 4.3}$$

This in turn allows for the translation of V_{ND}^{NHP} to V_{ND}^{Human} by creating an interspecies scaling factor. To do this, the ratio of regional V_T^{NHP} derived from baseline ^{18}F -BCPP-EF scans to regional V_T^{Human} derived from the current ^{18}F -BCPP-EF data set was calculated for the cerebral white matter, cerebellum, frontal cortex, cingulate cortex, temporal cortex, parietal cortex, occipital cortex, striatum and hippocampus. The regional ratios were averaged to create a scaling factor which was applied to the estimated V_{ND}^{NHP} to predict V_{ND}^{Human} . The human BP_{ND} in the cerebral white matter was predicted from the following equation

$$BP_{ND}^{CWM} = \frac{V_T^{CWM}}{V_{ND}} - 1 \quad \text{Equation 4.4}$$

The shared V_{ND} in NHP was estimated as $8.78 \text{ mL}\cdot\text{cm}^{-3}$ from the intercept of the occupancy plots shown in Figure 4.6. The fractional occupancies estimated from these plots were 55.7%, 55.1%, 50.2% and 55.8%, for monkeys 1, 2, 3 and 4, respectively. Dividing average baseline NHP V_T values by corresponding human baseline values produced an interspecies scaling factor of 1.07 ± 0.14 , resulting in an estimated V_{ND}^{HUMAN} of $8.2 \text{ mL}\cdot\text{cm}^{-3}$, which is similar to the mean V_T estimate in the human CS of $10.9 \pm 1.9 \text{ mL}\cdot\text{cm}^{-3}$. Human and NHP baseline V_T data used to derive the interspecies scaling factor are plotted in Figure 4.7. Using Equation 4.4, BP_{ND}^{NHP} in cerebral white matter was calculated as 0.54, which is indicative of a small amount of specific binding.

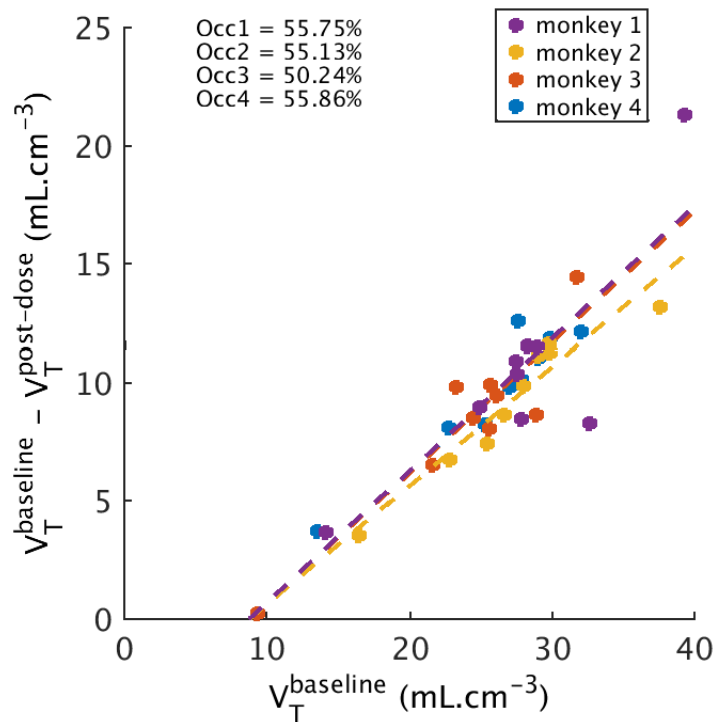


Figure 4.6 Occupancy plots of monkeys 1-4, where V_{ND} is given by the x intercept. (n=4, 9 ROIs). Figure modified from Mansur et al., 2020.

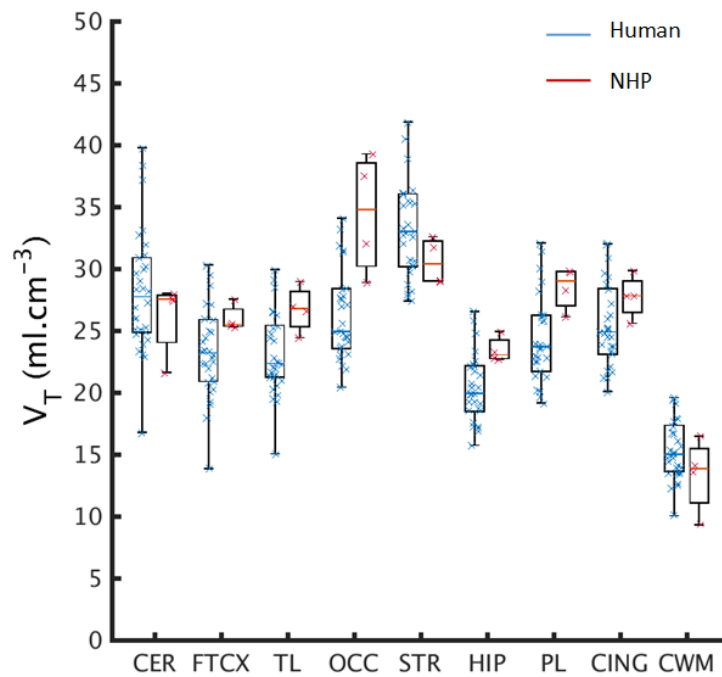


Figure 4.7. Boxplot showing human baseline V_T data (blue, n = 30) and NHP (red, N = 4) V_T data

4.5.2 Assessment of SUVR-1 as an outcome measure

Having established the CS as a useful pseudo reference region for ^{18}F -BCCP-EF, data from 30 healthy subjects were used to derive semiquantitative standardised uptake value ratios (SUVR) to assess a simplified outcome measure and enable comparison to measures derived from full kinetic analysis. All 12 grey matter regions were included in the analysis.

SUVR-1 values were obtained by normalizing the average standardized uptake value (SUV) in a target ROI derived from a 20 minute static image to that of the average SUV in the CS and subtracting 1. The optimum time window to generate SUVR-1 was determined by creating SUVR images for 8 different 20 minute time windows ranging from 0-20 minutes to 70-90 minutes, and evaluating the strength of their correlation with DVR-1 across subjects using least-squares linear regression.

Table 4.3 Summary of regional DVR – 1, SUVR – 1 and K_1 values for ^{18}F -BCCP-EF (n=30)

Outcome Measure		BST	SN	THA	VSTR	CAU	PUT	HIP	INS	TL	PL	FTCX	CER
DVR - 1	mean	0.52	0.82	1.01	1.79	0.89	1.91	0.87	1.34	1.15	1.25	1.17	1.58
	COV	29%	19%	23%	15%	51%	13%	20%	15%	14%	17%	16%	12%
SUVR - 1	mean	0.59	0.86	1.08	1.71	0.88	1.90	0.89	1.42	1.19	1.33	1.27	1.61
	COV	24%	17%	23%	17%	55%	14%	20%	16%	15%	19%	19%	12%
K_1 ($\text{ml}\cdot\text{cm}^{-3}\cdot\text{min}^{-1}$)	mean	0.36	0.43	0.46	0.44	0.49	0.33	0.54	0.58	0.51	0.49	0.51	0.40
	COV	22%	23%	23%	28%	39%	25%	23%	26%	23%	24%	26%	22%

The centrum semiovale was used as a reference region in the derivation of DVR – 1 and SUVR – 1

Regional DVR-1 values ranged from 0.51 in the brainstem to 1.95 in the putamen, while similarly SUVR-1 values ranged from 0.50 in the brainstem to 1.90 in the putamen (Table 4.3). SUVR-1 computed over later time windows between 50 - 90 minutes post injection was in good agreement with DVR-1 (n= 30, Table 4.4). The strongest correlation was found for the 70-90 time window, for which the gradient of correlation obtained from the slope of the linear regression line, was also close to 1 (Figure 4.8).

Table 4.4 Results from linear correlation of SUVr -1 values with DVR – 1 derived for 8 SUVR time windows (12 ROIs, 30 subjects)

SUVR time window (minutes)	r ²	gradient
0-20	0.01	0.92
10-30	0.72	0.90
20-40	0.77	0.92
30-50	0.81	0.94
40-60	0.86	0.96
50-70	0.90	0.97
60-80	0.92	0.96
70-90	0.94	0.95

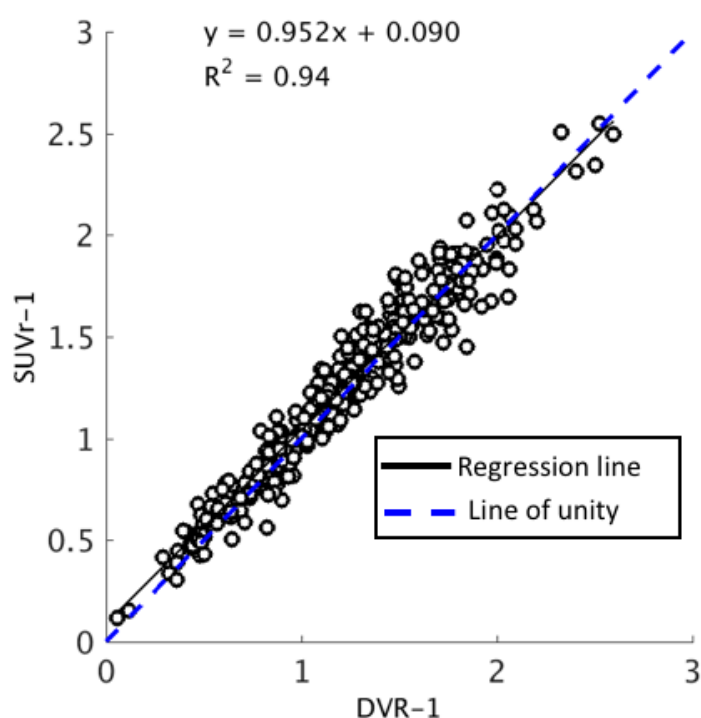


Figure 4.8 Correlation between SUVr-1 and DVR-1 for 30 subjects and 12 ROIs using CS as a pseudo reference region

These results showed that ¹⁸F-BCPP-EF SUVr values obtained between 70 and 90 minutes following ligand administration are in good agreement with DVR derived estimates. It is important to note that the stability of the quantitative outcome measures discussed so far across a 90 minute scan should also come into play in the selection of an optimum time window, as selecting a time window that is earlier than when the system reaches secular equilibrium will affect quantification.

4.5.3 Assessment of tracer delivery effects on SUVR and DVR

The potential sensitivity of binding parameters to tracer delivery is an important factor to consider in the early stages of a new radiotracer. The relationship between changes in tracer delivery rate (K_1) estimates derived under test and retest conditions (ΔK_1) was correlated to that of DVR (ΔDVR) and SUVR ($\Delta SUVR$) to assess if SUVR or DVR were affected by radioligand delivery. K_1 values (provided in Table 4.3) were also compared with DVR and SUVR values directly. K_1 had no effect on either outcome measure when looking at Δ relationships, and the relationship between SUVR and K_1 was very similar to that of DVR and K_1 , increasing confidence that tracer delivery is not a limitation for ^{18}F -BCPP-EF.

4.6 Time stability analysis

In order to assess the stability of ^{18}F -BCPP-EF over time, the performance of both MA1 derived V_T and image-derived $SUVR-1$ was evaluated for varying scan lengths. For V_T , the values estimated for the different scan lengths were expressed as a percentage of the V_T estimated from the full 90 min acquisition ($V_T^{90\text{min}}$), aggregated together over 30 subjects and plotted against time to allow for a population level assessment of time stability, as described previously in Chapter 3.

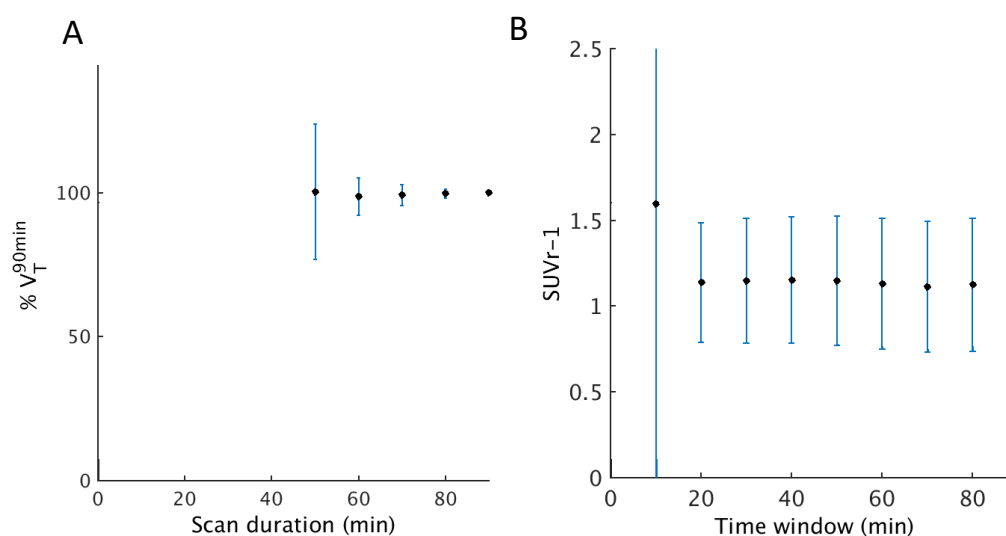


Figure 4.9 Time stability plots of **A** $\%V_T^{90\text{min}}$ and **B** $SUVR-1$ where each data point represents the mean across 360 data points (30 subjects x 12 ROIs). (Data prior to 50 minutes excluded for visual clarity in plot A.)

To assess the stability of SUVr-1, regional values obtained from the time windows specified in section 4.4 were averaged across subjects and plotted against time.

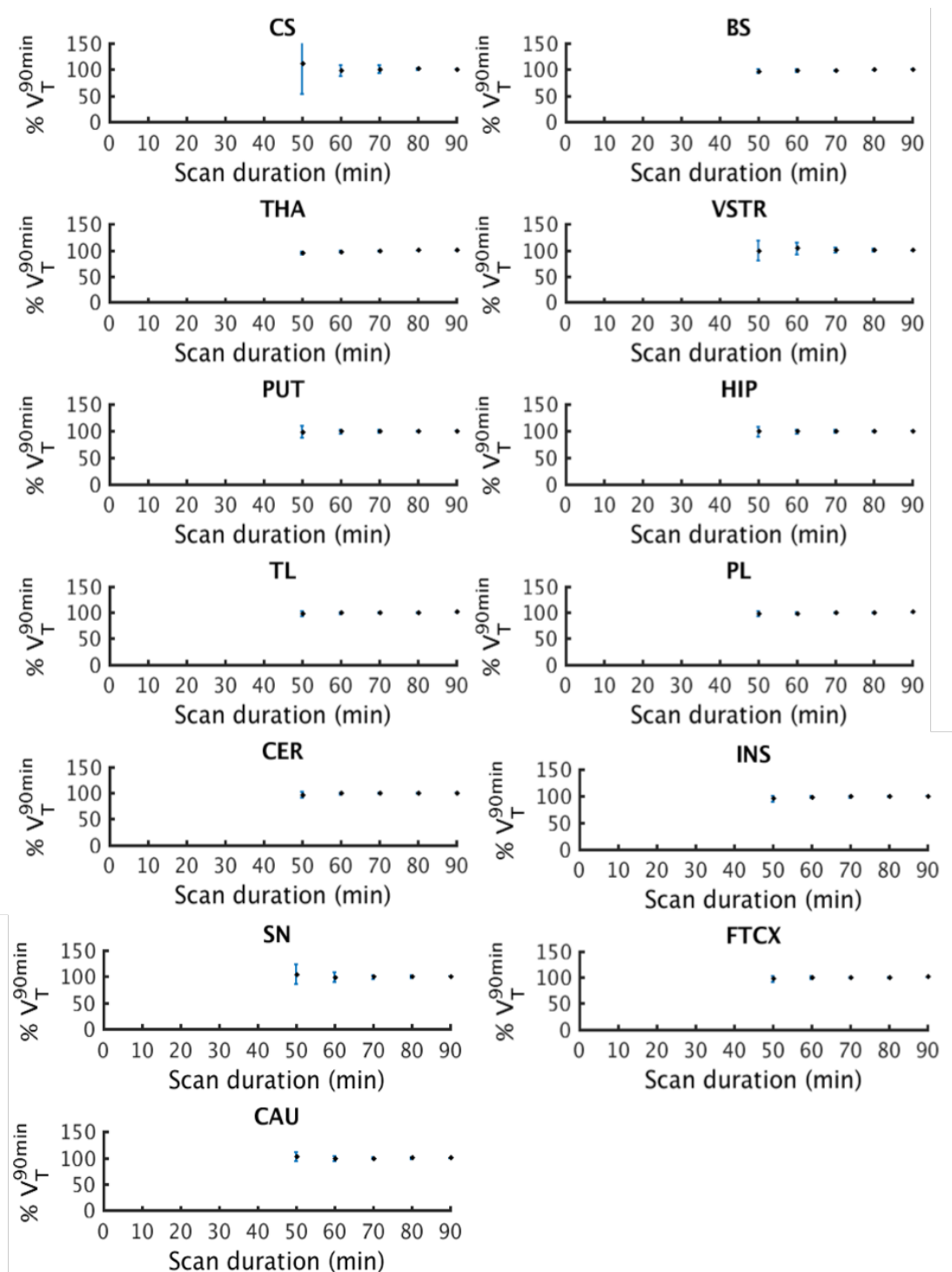


Figure 4.10 Regional time stability plots for ^{18}F -BCPP-EF V_T where each data point represents the mean $\%V_T^{90\text{min}}$ of 30 subjects and the error bars represent standard deviation (SD)

As seen in Figure 4.9 A, 70 minutes of PET data provided good stability of V_T where the resulting V_T was 98.4(6.7)% of the final V_T . The time stability of V_T did not vary greatly across regions (see Figure 4.10 for regional plots).

Though $SUVr - 1$ values started to stabilize as early as 20 minute post ligand administration (Figure 4.9 B), taking into account the excellent correlation between $SUVr-1[70-90]$ and $DVR-1$, 70-90 minutes was selected as the optimum time window from which to reliably estimate $SUVr$ based measures with the increased confidence that the tracer had reached a secular equilibrium. $SUVr - 1$ has the potential to be a non-invasive and simpler measure for ^{18}F -BCPP-EF scans for which a long dynamic scan with full arterials is not feasible. In the case of dynamic ^{18}F -BCPP-EF scans, scan time can reliably be shortened to 70 minutes to confidently quantify V_T in the brain.

4.7 Evaluating the test-retest reliability of ^{18}F -BCPP-EF

In order to further characterise ^{18}F -BCPP-EF signal in the human brain, the test-retest (TRT) reliability of both MA1 and 2TC derived kinetic outcome measures and simplified outcome measure $SUVr-1$ was evaluated. Relative and absolute test-retest variability (TRV, aTRV) and intraclass correlation coefficient (ICC; one-way random effects ANOVA) was calculated for each ROI for 5 subjects (see Table 3.3 for demographic information).

$$TRV(\%) = 200 \times \frac{\text{retest value} - \text{test value}}{(\text{retest value} + \text{test value})} \quad \text{Equation 4.5}$$

$$aTRV(\%) = 200 \times \frac{|\text{retest value} - \text{test value}|}{(\text{retest value} + \text{test value})} \quad \text{Equation 4.6}$$

$$ICC = \frac{BSMSS - WSMSS}{BSMSS + WSMSS} \quad \text{Equation 4.7}$$

where BSMSS is between-subject mean sum of squares and WSMSS is within-subject mean sum of squares. Two-tailed paired t-tests were used in the statistical analysis of test and retest

conditions and linear regression was used to compare outcome measures derived from the two conditions. There were no statistically significant differences between average regional uptake or injection parameters between test and retest conditions (see Table 3.4 for individual radiotracer injection parameters).

Individual SUV images derived from the test and retest conditions and corresponding structural MRI images are shown in Figure 4.11. Peak uptake values (SUV) measured between 5-20 minutes post injection were similar between test and retest conditions. The TRV and aTRV of f_p were $-9.7 \pm 6\%$ and 9.7% , respectively, with an ICC of 0.74. *PPF* measurements were slightly lower for the retest condition than the test condition at the end of the scan ($p < 0.05$).

Test and retest derived V_T values were well correlated ($r^2 = 0.81$), with Bland-Altman plot showing a positive bias of $9\% \pm 2\%$ towards the retest condition (Figure 4.12 A). The raw regional test retest V_T , V_T/f_p , DVR-1 and SUVR-1 values are provided in Table 4.5. The mean regional TRV and aTRV for V_T were $9\% \pm 2\%$ and $13\% \pm 2\%$, respectively (Table 4.6). V_T/f_p values derived from test and retest scans were moderately correlated ($r^2=0.75$), with as a negative mean bias of 18% for the retest condition (Figure 4.12 B). V_T/f_p had poorer TRT variability compared to V_T , with TRV and aTRV of $17\% \pm 2\%$ and $21\% \pm 2\%$, respectively.

Test and retest derived DVR-1 values were well correlated ($r^2 = 0.92$) and showed a negative bias of $\sim 7\%$ for the retest condition (Figure 4.12 C). The global mean TRV and aTRV for DVR-1 were $-9\% \pm 4\%$ and $11\% \pm 4\%$, respectively. As shown in Section 4.4.2, SUVR-1 computed over 70-90 minutes was in good agreement with DVR-1 ($r^2 = 0.94$), with a Bland-Altman plot showing a consistent negative mean bias of $\sim 7\%$ for the retest condition (Figure 4.12 D). SUVR-1 had a global mean TRV of $-8\% \pm 3\%$ and aTRV of $9\% \pm 3\%$.

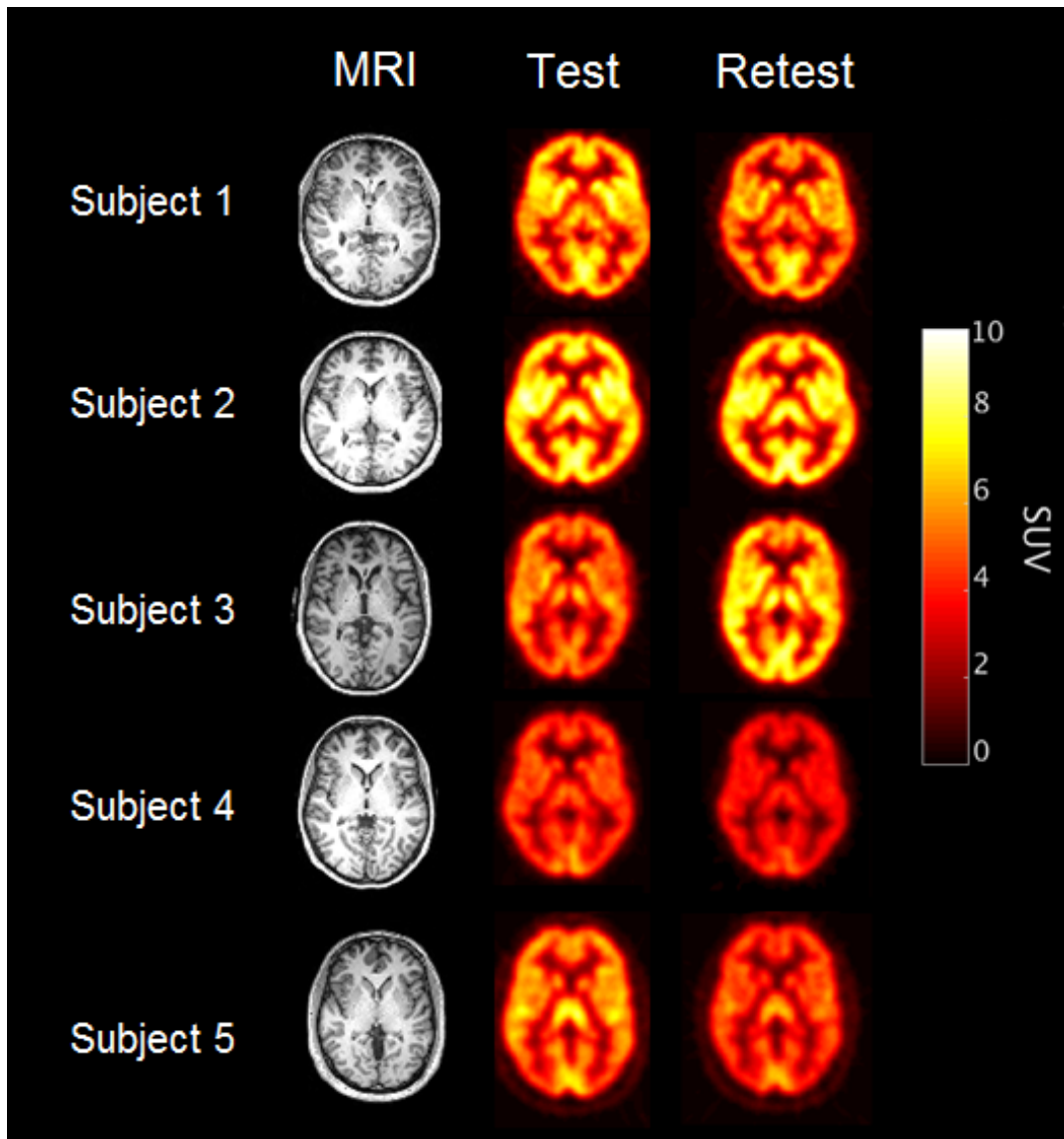


Figure 4.11 Individual MR and SUV Add-images (10-90 min) of ^{18}F -BCPP-EF during test and retest condition. Figure modified from Mansur et al., 2020.

The global mean ICC for V_T , V_T/f_p and DVR-1 remained above 0.60 while for SUV_{r-1} was calculated as 0.89 ± 0.05 . It should be noted that the lowest ICC for V_T was in the CS which overall reduced the reliability of DVR-1 estimates. There were no statistically significant differences between test and retest derived results for any of the outcome measures.

Table 4.5. ¹⁸F-BCPP-EF derived regional test-retest PET outcome measures

Outcome Measure	Kinetic Model	CS	BS	SN	THA	STR	GP	VSTR	CAU	PUT	PC	AC	FL	INS	HIP	AMY	TL	PL	CER	
V_T (ml.cm ⁻³)	test	mean	9.1	13.7	16.7	18.7	23.9	22.5	25.8	19.2	28.3	22.2	21.0	19.5	21.7	17.4	18.6	19.8	20.0	22.3
		COV	16	15	15	20	21	16	17	28	17	21	20	19	17	18	18	15	21	14
	retest	mean	10.3	15.0	18.2	20.3	25.8	24.9	29.0	20.4	30.8	24.7	22.8	21.2	23.5	18.5	19.9	21.6	22.0	24.2
		COV	15	19	20	21	21	17	19	29	17	20	19	19	18	18	17	17	19	19
V_T/f_p (ml.cm ⁻³)	test	mean	127	192	234	261	334	315	361	267	397	310	294	274	304	243	260	278	280	314
		COV	15	13	15	16	18	10	13	27	14	19	17	18	14	15	14	13	18	13
	retest	mean	159	230	281	311	396	382	446	311	474	380	350	326	362	284	307	332	339	373
		COV	14	13	15	15	15	9	13	23	12	16	13	14	12	11	12	12	15	14
DVR-1	test	mean	NAN	0.51	0.84	1.06	1.63	1.50	1.84	1.10	2.13	1.43	1.30	1.15	1.39	0.92	1.05	1.19	1.20	1.47
		COV	NAN	12	7	22	20	18	10	40	13	13	10	17	9	21	11	8	20	12
	retest	mean	NAN	0.45	0.77	0.97	1.50	1.42	1.82	0.96	1.99	1.39	1.22	1.06	1.29	0.80	0.94	1.10	1.14	1.35
		COV	NAN	24	19	23	21	17	17	40	12	14	19	19	16	25	18	14	14	13
SUVr-1	test	mean	NAN	0.55	0.85	1.11	1.60	1.43	1.76	1.08	2.09	1.53	1.37	1.23	1.45	0.93	1.01	1.22	1.27	1.51
		COV	NAN	19	13	28	28	22	16	51	19	19	17	23	15	28	15	13	26	16
	retest	mean	NAN	0.49	0.80	1.02	1.44	1.31	1.65	0.93	1.93	1.51	1.29	1.14	1.34	0.84	0.92	1.14	1.21	1.40
		COV	NAN	27	20	26	26	21	20	48	18	17	21	24	17	27	20	15	20	16

COV is expressed as %, n=5 test, 5 retest

Table 4.6 Test-retest reproducibility of ¹⁸F-BCPP-EF outcome measures

ROI	V_T (mL.cm ⁻³)			V_T/f_p (mL.cm ⁻³)			DVR-1			SUVr-1		
	TRV (%)	aTRV (%)	ICC	TRV (%)	aTRV (%)	ICC	TRV (%)	aTRV (%)	ICC	TRV (%)	aTRV (%)	ICC
CS	13 ± 16	18	0.30	21 ± 21	26	0.39	-	-	-	-	-	-
BS	9 ± 12	13	0.64	17 ± 16	21	0.64	-13 ± 25	18	0.31	-12 ± 14	12	0.83
SN	9 ± 13	12	0.61	17 ± 16	20	0.62	-10 ± 19	17	0.15	-6 ± 9	8	0.86
THA	8 ± 12	13	0.78	16 ± 17	17	0.74	-9 ± 9	11	0.84	-7 ± 5	7	0.94
STR	8 ± 12	13	0.79	16 ± 17	21	0.72	-8 ± 8	9	0.87	-10 ± 5	10	0.91
GP	10 ± 13	14	0.57	18 ± 18	22	0.64	-5 ± 10	9	0.83	-8 ± 6	8	0.89
VSTR	11 ± 14	15	0.54	20 ± 18	23	0.59	-2 ± 9	8	0.81	-7 ± 7	7	0.89
CAU	6 ± 13	12	0.91	14 ± 19	20	0.83	-15 ± 8	15	0.94	-16 ± 7	6	0.94
PUT	8 ± 12	13	0.71	16 ± 18	21	0.69	-7 ± 10	9	0.75	-9 ± 4	9	0.89
PC	11 ± 15	17	0.66	19 ± 20	25	0.58	-2 ± 2	3	0.97	-1 ± 3	3	0.98
AC	8 ± 13	13	0.72	17 ± 17	21	0.64	-8 ± 10	10	0.78	-7 ± 5	7	0.94
FTCX	8 ± 14	14	0.69	16 ± 19	22	0.63	-9 ± 6	9	0.86	-8 ± 2	8	0.94
INS	8 ± 11	12	0.71	16 ± 15	20	0.67	-8 ± 12	11	0.51	-8 ± 6	8	0.86
HIP	6 ± 9	10	0.83	14 ± 14	18	0.77	-15 ± 16	19	0.63	-10 ± 9	11	0.89
AMY	7 ± 12	12	0.71	15 ± 17	20	0.66	-11 ± 12	13	0.57	-10 ± 8	11	0.79
TL	8 ± 11	11	0.67	16 ± 15	19	0.65	-9 ± 15	13	0.16	-7 ± 7	8	0.81
PL	10 ± 15	16	0.67	18 ± 21	24	0.64	-5 ± 6	5	0.88	-3 ± 8	7	0.94
CER	8 ± 11	11	0.71	16 ± 15	20	0.70	-9 ± 14	12	0.31	-8 ± 6	8	0.82
Mean	9	13	0.68	17	21	0.66	-9	11	0.66	-8	9	0.89
SD	2	2	0.13	2	2	0.09	4	4	0.37	3	3	0.05

TRV: Test-retest variability, aTRV: absolute test-retest variability, ICC: intra-class correlation. Data are mean ± SD.CS

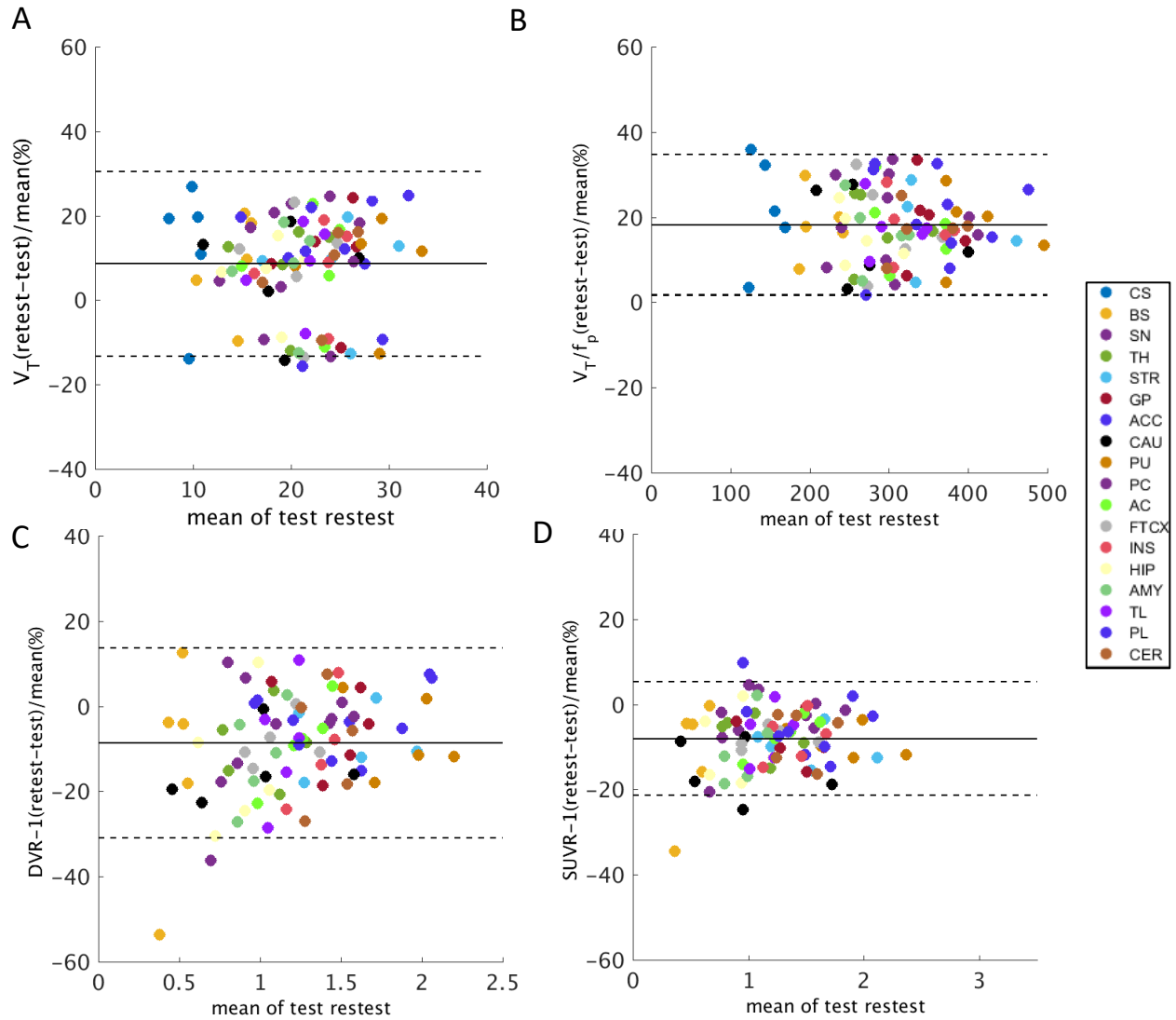


Figure 4.12. Bland-Altman plots for **A** V_T , **B** V_T/f_p , **C** DVR-1, and **D** SUVR-1 derived under test and retest conditions. Values are colour coded by region of interest. Solid line indicates mean and dotted lines indicate ± 1.9 SD. All regions and subjects are included in the plots.

4.8 Parametric V_T Images

In addition to generating TAC based ^{18}F -BCPP-EF V_T values, parametric V_T maps were generated for all ^{18}F -BCPP-EF scans acquired by fitting MA1 (fixed BV, $t^* = 30$ min) on a voxel level. The regional averages of parametric V_T s were calculated to enable comparison to the original TAC derived estimates. As can be seen in Figure 4.13, there was an excellent correlation between the two ($r^2=0.99$).

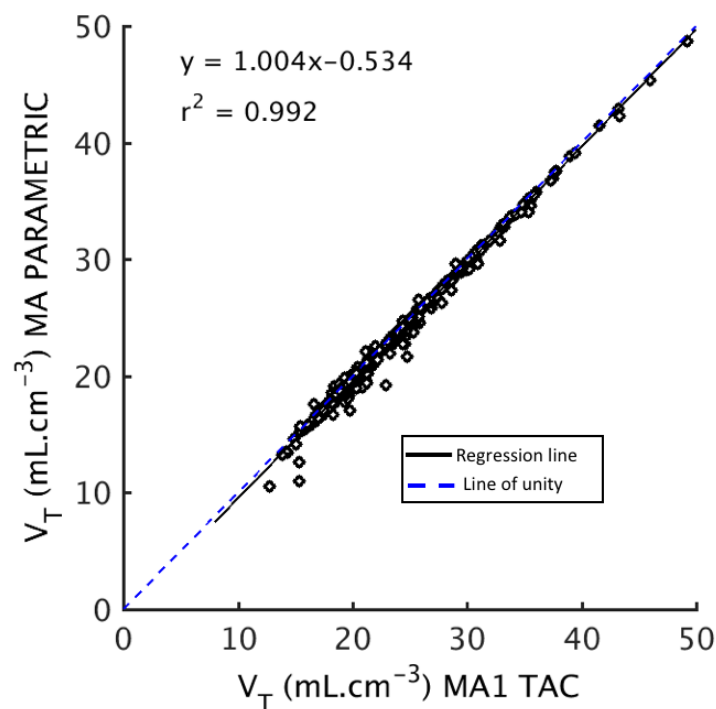


Figure 4.13. Correlation between TAC derived and parametrically derived ^{18}F -BCPP-EF V_T for 30 subjects and 12 ROIs.

Of the parametrically derived V_T estimates, $0.06\% \pm 0.09\%$ of the voxels produced negative values while the percentage of voxels with nonphysiologically high estimates ($V_T > 80$) was $0.008\% \pm 0.01\%$. Further investigation of the time activity curves extracted for these specific voxels revealed that they were very noisy, resulting in poor fits.

V_T images that were initially created in subject space were spatially normalised to MNI52 space by applying the DARTEL flow fields derived previously (see Chapter 3). Flow fields were applied to the parametric V_T images and smoothed using a 4mm x 4mm x 4mm gaussian smoothing kernel. Mean and standard deviation V_T images of ^{18}F -BCPP-EF were created from the 30 healthy subjects by averaging the distribution of intensities in the corresponding voxels (excluding non-physiological estimates) across all subjects (shown in Figure 4.14). As evident from the mean image, the high V_T in the putamen and ventral striatum was consistent across the population, corresponding to average V_T estimates of $33.0 \pm 5.2 \text{ mL}\cdot\text{cm}^{-3}$ and $31.7 \pm 5.5 \text{ mL}\cdot\text{cm}^{-3}$ respectively.

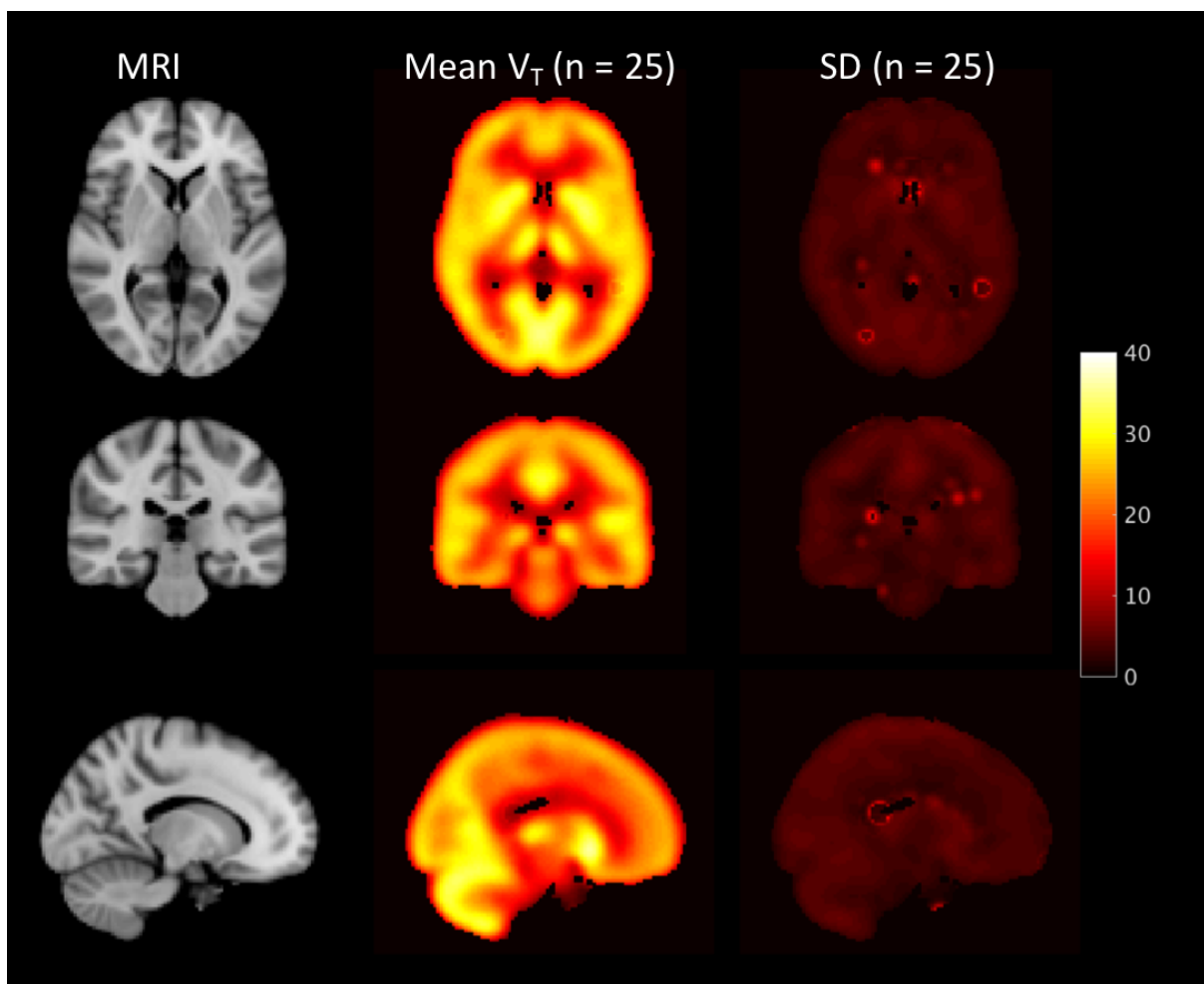


Figure 4.14 Orthogonal cross-sections of MRI (left), mean (middle) and standard deviation (SD) (right) V_T images of ^{18}F -BCPP-EF (n=30).

4.9 Conclusion

The work in this chapter characterised ^{18}F -BCPP-EF for the first time in the human brain. ^{18}F -BCPP-EF kinetics were well described using both MA1 and 2TC models, with all outcome measures investigated showing suitable test-retest variability. Time stability analysis showed that at least 70 minutes of dynamic scanning with ^{18}F -BCPP-EF is sufficient to reliably estimate V_T .

Simplified outcome measure SUVR-1 showed very good correlation with DVR-1 results derived from kinetic modelling, indicating that a static acquisition of 20 minutes acquired between 70-90 minutes post ligand administration could be sufficient to quantify ^{18}F -BCPP-EF. This could prove especially beneficial in larger studies where scan time is limited or in disease cohorts where minimizing patient discomfort needs to be prioritized.

V_{ND} derived from monkey data suggested that the CS could be a useful pseudo reference region for ^{18}F -BCPP-EF, increasing confidence in the suitability of DVR-1 and SUVR-1 as outcome measures for quantifying specific ^{18}F -BCPP-EF signal. It is important to keep in mind that the CS is not a real reference region (not devoid of MC-I) and in the absence of a blocking study in humans there is not sufficient evidence to obviate the need for arterial blood acquisition in a ^{18}F -BCPP-EF scan. Careful consideration should be given when using CS derived outcome measures in cross sectional studies where there could be disease related changes in mitochondria/MC-I function, or where the integrity of the white matter may be compromised. Similarly, caution should be taken before using V_T/f_p as an outcome measure, as this will only likely be appropriate given that there are cross sectional differences in f_p values.

In conclusion, ^{18}F -BCPP-EF possesses suitable characteristics for quantifying MC-I in the human brain.

5 Quantification and kinetic modelling of ¹¹C-SA-4503

Outside of the initial human work performed by Sakata et al., 2007, a reliable and fully validated kinetic modelling pipeline for ¹¹C-SA-4503 has not been fully developed. This chapter evaluates the performance of the kinetic modelling approaches set out in Chapter 3 for ¹¹C-SA-4503 and establishes the optimum tracer kinetic quantification models and outcome measures for this radioligand.

5.1 Background and Study Overview

As reviewed in Chapter 2, the mapping of S1R in the healthy human brain using ^{11}C -SA-4503 was first performed by Sakata and colleagues, whose work showed that ^{11}C -SA-4503 uptake is widespread in the brain, has relatively slow kinetics that are well-described by the 2TC and Logan methods (Sakata, Kimura, Naganawa, et al., 2007), and shows minimal metabolism in plasma.

The work presented here aimed to determine the optimum kinetic methods and suitable outcome measures for quantifying ^{11}C -SA-4503 across the MIND-MAPS cohorts. The distribution of ligand uptake is presented in section 5.2. The process of establishing appropriate blood and plasma models to create a reliable arterial plasma input function are covered in section 5.3, followed by the testing of various tissue kinetic models in section 5.4. Time stability analysis results are presented in section 5.5, and lastly, the performance of voxel-level kinetic modelling is discussed in section 5.6.

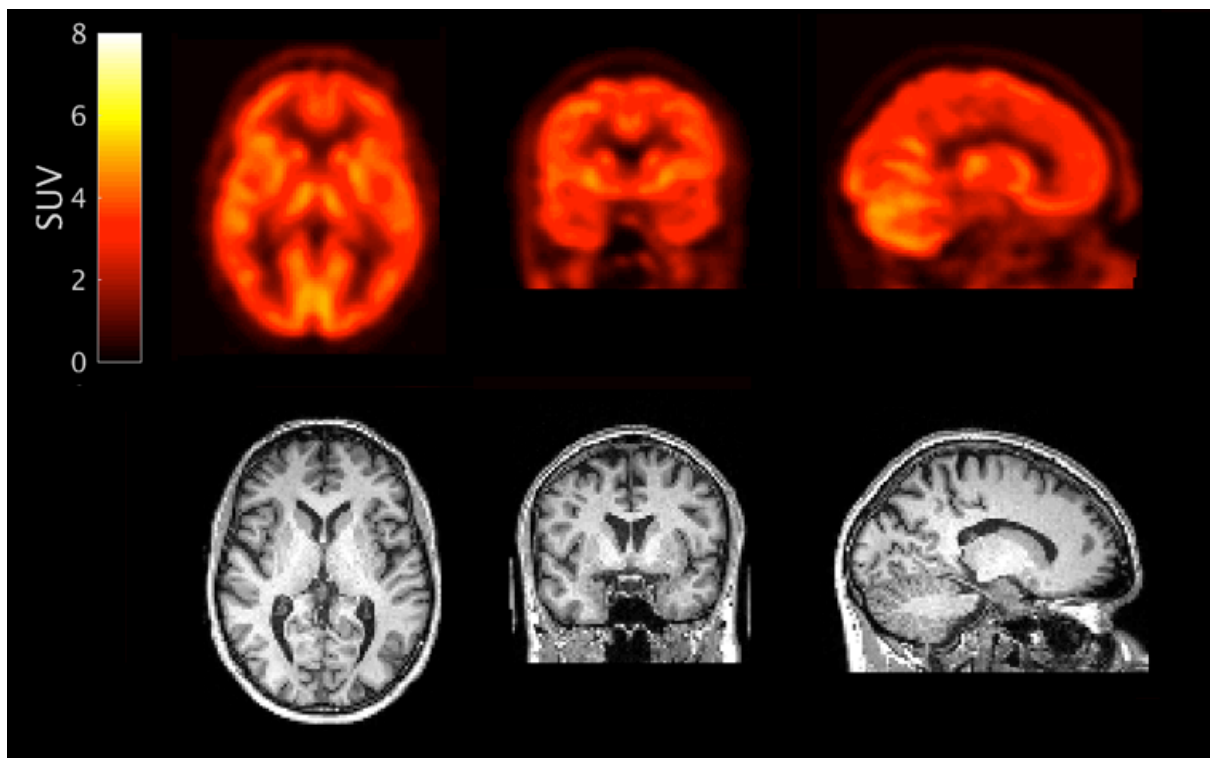


Figure 5.1 Orthogonal cross sections of co-registered ^{11}C -SA-4503 PET and MR images from a representative subject. PET images are shown as SUV summed from 10-90 minutes.

5.2 Tracer uptake and distribution

^{11}C -SA-4503 uptake was slow and reached peak uptake at ~50-60 minutes post-injection in line with previous work in humans (Sakata, Kimura, Naganawa, et al., 2007). Uptake was heterogeneous throughout the brain (Figure 5.1) with the highest SUV values observed in the cerebellum (5 g/ml), followed by the putamen (4.8 g/ml) and insular cortex (4.5) g/ml, and was lowest in the brainstem, caudate and centrum semiovale with SUV values of 3.5 g/ml, 2.9 g/ml and 2.1 g/ml, respectively.

5.3 Determining the optimum arterial plasma input function

The process for the acquisition of arterial blood samples was described in Chapter 3 (Figure 3.4). This section covers the process of selecting the optimum *POB* and *PPF* models. The optimum models established here were then applied to blood data acquired during all subsequent ^{11}C -SA-4503 scans.

5.3.1 Modelling the plasma over blood (*POB*) data

An initial visual inspection of model fits revealed that the ratio of the ^{11}C -SA-4503 concentration in plasma to that in blood (*POB*) started off as an exponential before reaching constant levels over the course of the PET scan (Figure 5.2). Of the 4 *POB* models tested (see Appendix A for full list of models), AIC confirmed that the ‘exponential approach to constant’ (exp-constant) model with 3 parameters a , b and c produced the most parsimonious fits to the ratio of ^{11}C -SA-4503 activity in plasma to blood.

$$POB(t) = a + b(1 - e^{-ct}) \quad \text{Equation 5.1}$$

The *POB* data fitted with this model produced acceptable fits in all 12 subjects, resulting in a *POB* ratio in the range of 0.64 – 0.94 (Figure 5.2).

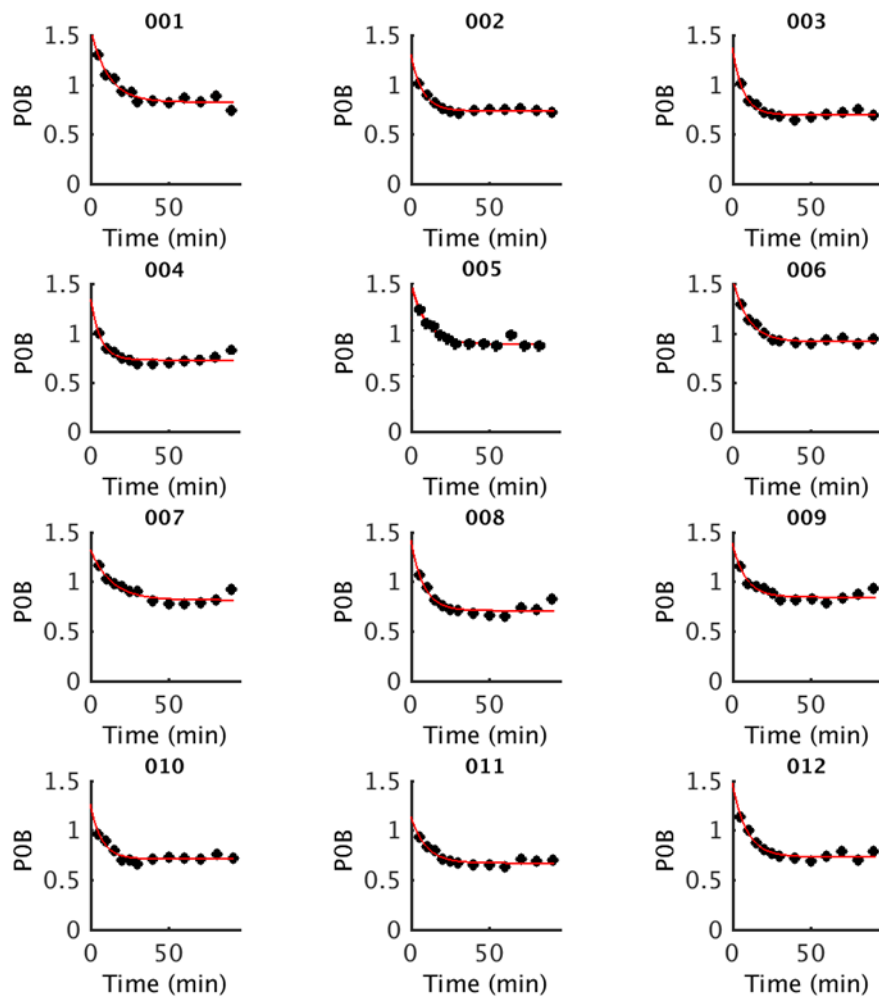


Figure 5.2 Fits of the 'exponential approach to constant' *POB* model to the blood data from 12 ¹¹C-SA-4503 scans

5.3.2 Modelling the plasma parent fraction (PPF) data

^{11}C -SA-4503 metabolism in plasma was slow in line with what has been previously shown by Sakata et al (Sakata, Kimura, Naganawa, et al., 2007). HPLC analysis revealed a single metabolite eluting at between 1st and 7th retention times, and the parent eluting at between 22nd - 27th retention times.

In an initial comparison of 7 PPF models, AIC favoured and ‘exponential + constant’ model given by

$$PPF(t) = e^{-\beta t} + c \quad \text{Equation 5.2}$$

The initial application of this PPF model involved the manual definition of background windows by a blood lab technician (referred to in Chapter 3 and throughout the rest of this chapter as the ‘original model’). This resulted in highly variable parent fraction estimates of between 20% and 70% unmetabolized radioligand remaining intact at 60 minutes most injection (Figure 5.3

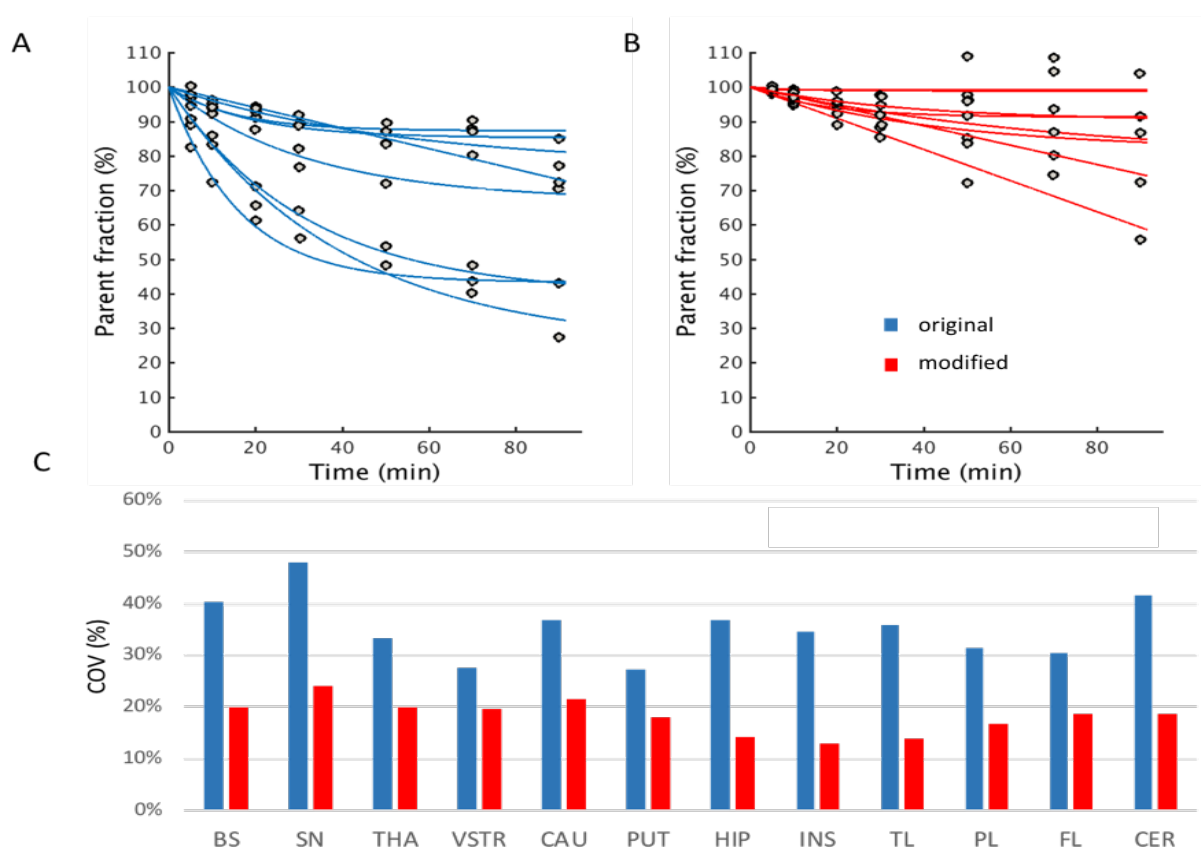


Figure 5.3 PPF model fits derived from fitting the **A** ‘original model’, **B** the ‘modified model’. **C** Inter-subject variability in V_T estimates derived using an input function corrected for metabolites using the ‘original model’ (blue bars) and the ‘modified model’ (red bars) (n=8).

A), which is significantly lower than the literature value of 89%. The intersubject variability in parent fraction estimates resulted in up to 50% variability in V_T estimates derived using the associated input functions (see Figure 5.3 C blue bars).

Modified parent fraction model

As discussed in Section 3.2.3, the background windows used to define the metabolite data in the ‘original model’ were selected manually, sometimes resulting in windows consisting of as little as 1 or 2 retention time points. Moreover, the 70th and 90th minute samples were often excluded from the parent fraction data set due to the high background noise. In order to increase the signal to noise ratio and reduce intersubject variability in PPF and V_T estimates, the definition of the PPF was modified to include a wider background window including all non-parent and non-metabolite retention times. For each sample i , the impact of the background variability on PPF definition was calculated as

$$\Delta Ppf_i = Ppf_i - Ppf_1 \quad \text{Equation 5.3}$$

where

$$Ppf_1 = \frac{\sum [\text{cpm}_{par} - (\mu(\text{cpm}_{bkg}) + SD(\text{cpm}_{bkg}))]}{\sum [\text{cpm}_{par+met} - (\mu(\text{cpm}_{bkg}) + SD(\text{cpm}_{bkg}))]} \quad \text{Equation 5.4}$$

and used to calculate the relative variance σ_i^2

$$\sigma_i^2 \sim (\Delta PPF_i)^2 \quad \text{Equation 5.5}$$

The model fitting was further modified to include a weighting factor equivalent to the inverse of the relative sample variance, which was particularly high in the later time points as demonstrated in Figure 5.4. The fits produced from this modified model are shown in Figure 5.3 B. The new PPF estimate at 60 minutes post- injection was $90\% \pm 7\%$ (range 73% – 100%), and $87\% \pm 10\%$ (range 59% – 100%) at 90 minutes post-injection.

PPF data from 8 subjects was used to compare the performance of the modified PPF model to the original PPF model. As can be seen in Figure 5.3, the inter-subject variability in both the

fraction fits and in V_T estimates were reduced using the modified *PPF* model. As such, the modified *PPF* model was used to derive all subsequent ^{11}C -SA-4503 arterial plasma input function curves.

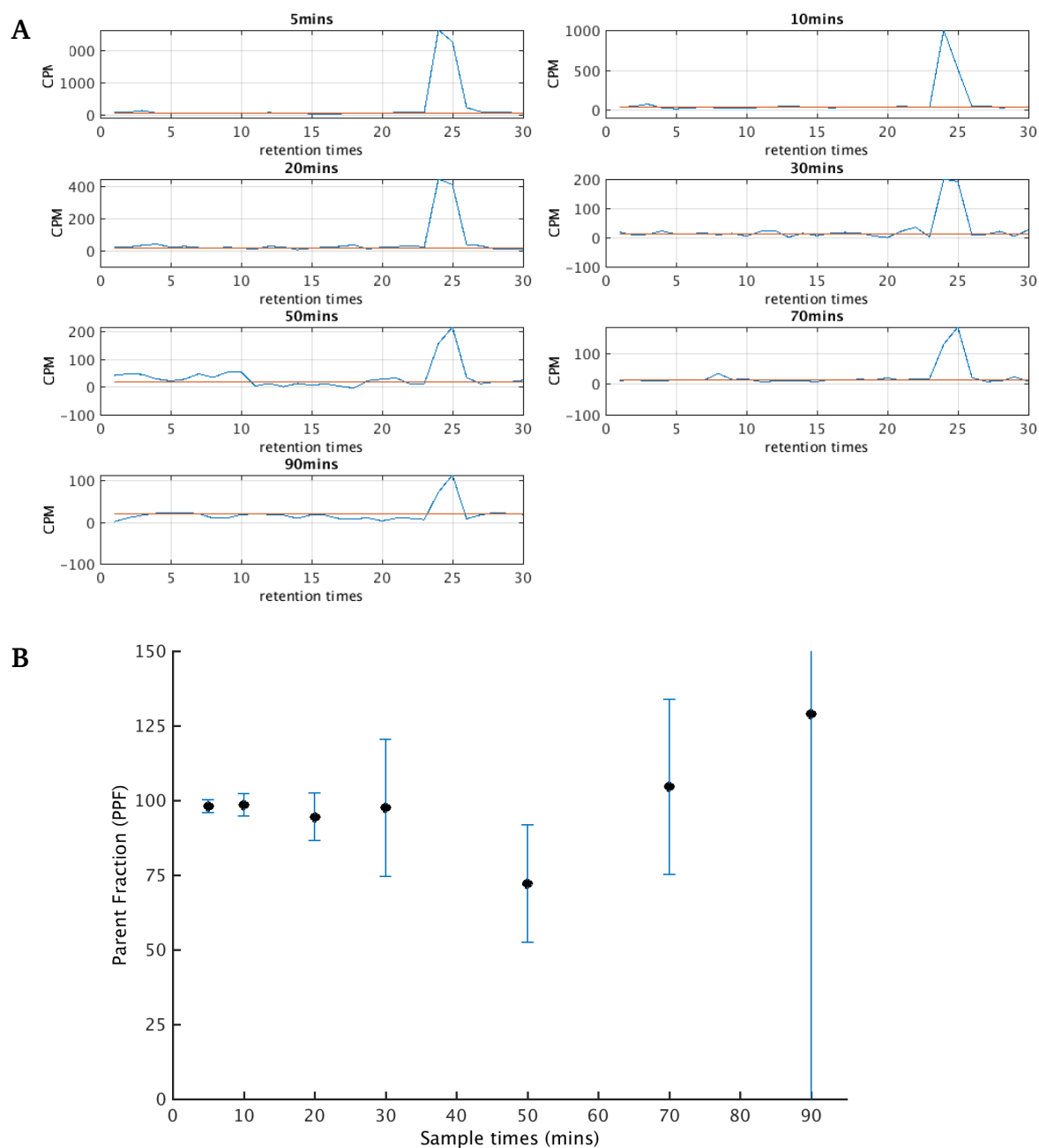


Figure 5.4 **A** ^{11}C -SA-4503 chromatogram data used to calculate *PPF* and **B** the effect of background noise on the variance of *PPF* estimates derived from the ‘exponential + constant’ model for one example subject. Data points in plot **B** represent *PPF* estimates and error bars represent the variance of *PPF* estimates associated with varying the background measurement by one standard deviation.

5.4 Determining the optimum tissue kinetic model for $^{11}\text{C-SA-4503}$

As described in Chapter 3, TAC data were fitted with fixed and fit blood volume variants of the 1TC and 2TC models, as well as 3 MA1 models of varying temporal windows (t^* 20, 30 and 40 min). V_T estimates derived using t^* values of 30 and 40 minutes correlated well with 2TC derived values (MA1³⁰ vs 2TC $r^2 = 0.98$, slope = 0.92; MA1⁴⁰ vs 2TC $r^2 = 0.98$, slope = 1.00). MA1 with a t^* of 30 minutes was chosen as the variant to proceed with. In addition to MA1, 1TC (fixed BV) and 2TC (fixed BV) were also assessed.

Table 5.1 $^{11}\text{C-SA-4503}$ derived regional PET outcome measures

Outcome Measure	Kinetic Model	CS	BST	SN	THA	VSTR	CAU	PUT	HIP	INS	TL	PL	FTCX	CER	
V_T (ml.cm ⁻³)	1TC	mean	22.4	30.7	29.5	27.7	32.9	21.2	36.3	31.4	38.1	34.5	32.1	33.4	40.3
		COV	24%	18%	17%	21%	21%	28%	19%	17%	16%	17%	20%	21%	19%
	2TC	mean	26.6	36.6	34.2	31.7	36.4	28.3	43.2	37.4	45.3	40.5	37.1	38.4	46.8
		COV	27%	21%	19%	22%	18%	22%	20%	16%	19%	16%	22%	24%	20%
	MA1	mean	29.1	36.6	34.6	31.9	37.9	25.1	42.1	37.0	44.7	40.4	36.8	38.5	46.6
		COV	29%	21%	21%	22%	21%	28%	17%	14%	17%	16%	19%	24%	19%

27 values for 2TC estimation were excluded based on V_T of SE% > 10 (n=12)

$^{11}\text{C-SA-4503}$ mean V_T , and V_T/f_p values and the inter-subject coefficient of variation (COV) values derived from the 1TC, 2TC and MA1 models are summarised in Table 5.1. DVR using the CS was not explored as the V_T in this region was not the lowest despite the relatively low uptake in this region. The model fits for 5 representative regions are depicted in Figure 5.5A-C. According to AIC, 2TC produced the most parsimonious fits to TACs in 142/156 of the cases when compared to 1TC; however, 12% of 2TC derived V_T estimates were poorly estimated. This was mainly due to the poor estimation (SE > 10%) of the microparameter k_4 in striatal regions, hippocampus, substantia nigra and the centrum semiovale. MA1 produced good fits to

the TAC data and V_T estimates were in close agreement with those reliably estimated using the 2TC model ($r^2=0.97$) (Figure 5.5 D). Thus, MA1 was chosen as the final model used in all subsequent analyses.

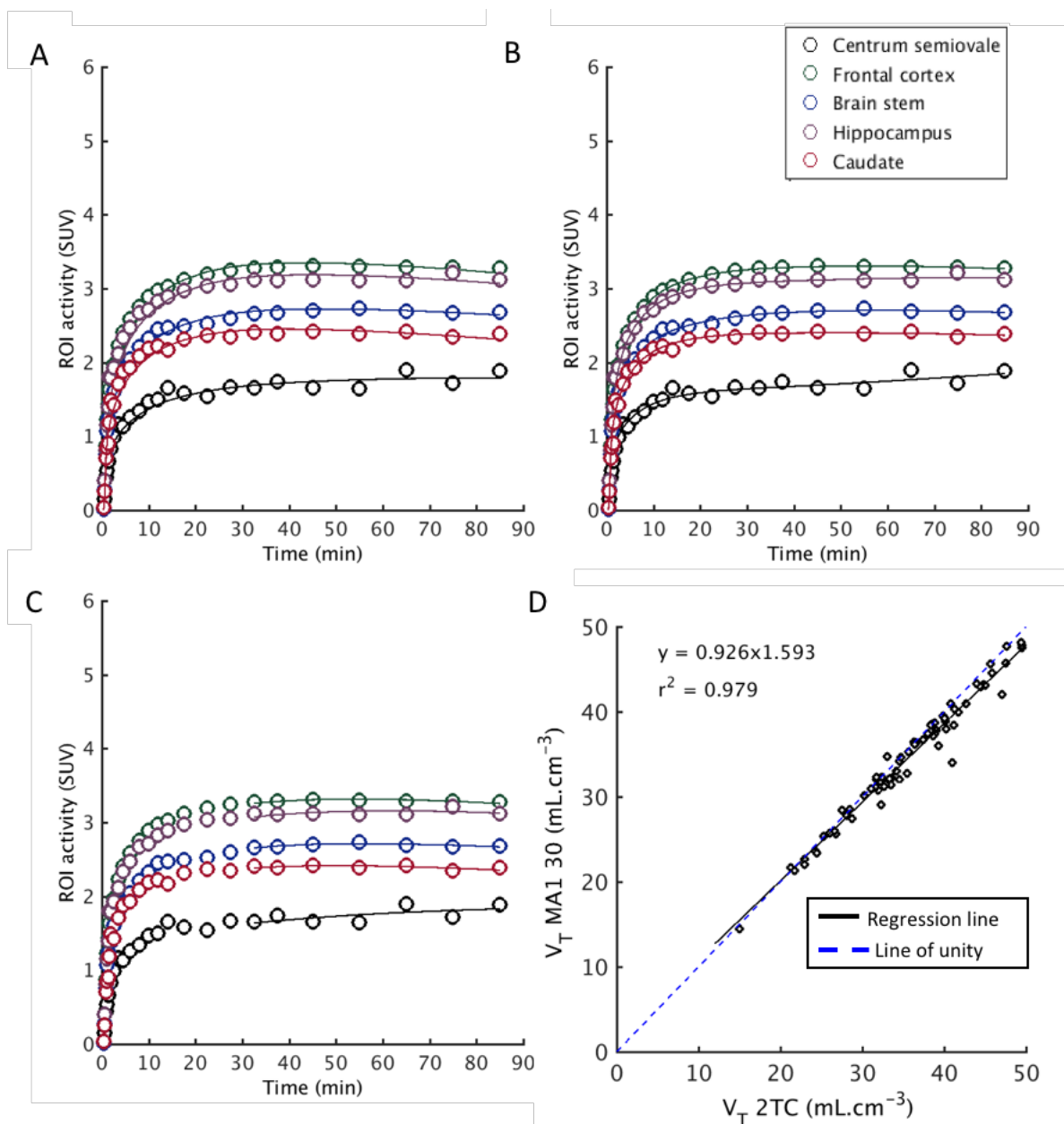


Figure 5.5 ^{11}C -SA-4503 regional TACs and model fits for a representative subject derived with **A** 1TC, **B** 2TC and **C** MA1. **D** Linear regression plot showing comparison of MA1 vs 2TC derived ^{11}C -SA-4503 V_T ($n=12$).

V_T values derived from MA1 ranged from $25.0 \pm 7 \text{ mL}\cdot\text{cm}^{-3}$ in the caudate to $45.9 \pm 7.6 \text{ mL}\cdot\text{cm}^{-3}$ in the cerebellum. The intersubject variability of regional V_T estimates across all regions investigated was calculated as $20 \pm 4\%$. Correcting V_T by f_p increased intersubject variability to $28 \pm 4\%$.

5.4.1 Comparison of metabolite corrected vs. uncorrected results

Different *PPF* models can lead to different PET outcome measure estimates (Tonietto, Veronese, Rizzo, et al., 2015). The accurate description of the parent metabolite fraction via analytical functions is therefore a crucial step for kinetic modelling and subsequent radioligand quantification in tissue.

In their work published in 2007, Sakata et al. estimated a *PPF* of 89% at 60 minutes post-injection in their dataset of 12 healthy volunteers. Based on this result, they explored the potential obviation of metabolite correction, and found a difference of 13% in 2TC-derived binding potentials derived from metabolite corrected and uncorrected input functions. Notably, the binding potentials reported in their study were derived directly from microparameters k_3 and k_4 which has since been shown to be not as robust as indirect estimation from 2TC (Parsey, Oquendo, Ogden, et al., 2006).

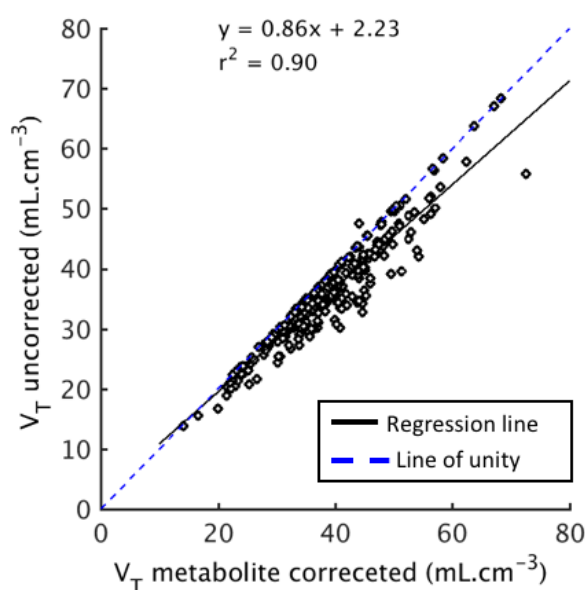


Figure 5.6 Correlation between ^{11}C -SA-4503 V_T estimates derived from metabolite corrected and uncorrected arterial input functions

In order to investigate the impact of metabolite correction on a more robust outcome measure V_T in our dataset, MA1 was rerun with an input function without accounting for metabolites and the results compared to the metabolite-corrected results. The full cohort of 23 healthy volunteers were used in this analysis. The average difference between V_T values derived from metabolite corrected and uncorrected arterial input functions was $\sim 9\%$, which is similar to the difference reported by Sakata et al. However, as shown in Figure 5.6, V_T values derived using the two methods were less correlated ($r^2 = 0.90$) compared to the r^2 of 0.98 reported by Sakata et al. Taken together with the fact that some of the *PPF* estimates for the 60 and 90 minute samples were as low as 60% in our dataset (Figure 5.3B), this suggests that the peripheral metabolism of ^{11}C -SA-4503 is slow but significant enough that correcting for it should not be easily dismissed.

5.5 Time stability analysis of ^{11}C -SA-4503

The performance of MA1 derived V_T was evaluated for varying scan lengths following the time stability methodology laid out in Chapter 3. Time stability data from 23 scans was used to assess time stability of ^{11}C -SA-4503 at a population level.

The minimum time required to produce stable estimates of V_T varied across regions (Figure 5.7), with smaller ROIs such as the hippocampus, substantia nigra, and caudate requiring up to 80 minutes of scan time whereas larger cortical regions reached stability as early as 50 minutes. As shown in Figure 5.8, on average, a minimum of 80 minutes acquisition with ^{11}C -SA-4503 produced reliable V_T estimates that were 98.2(1.2)% of the $V_T^{90\text{min}}$. This gave confidence that despite the slow kinetics of the tracer, scan time can be reliably shortened to 80 minutes.

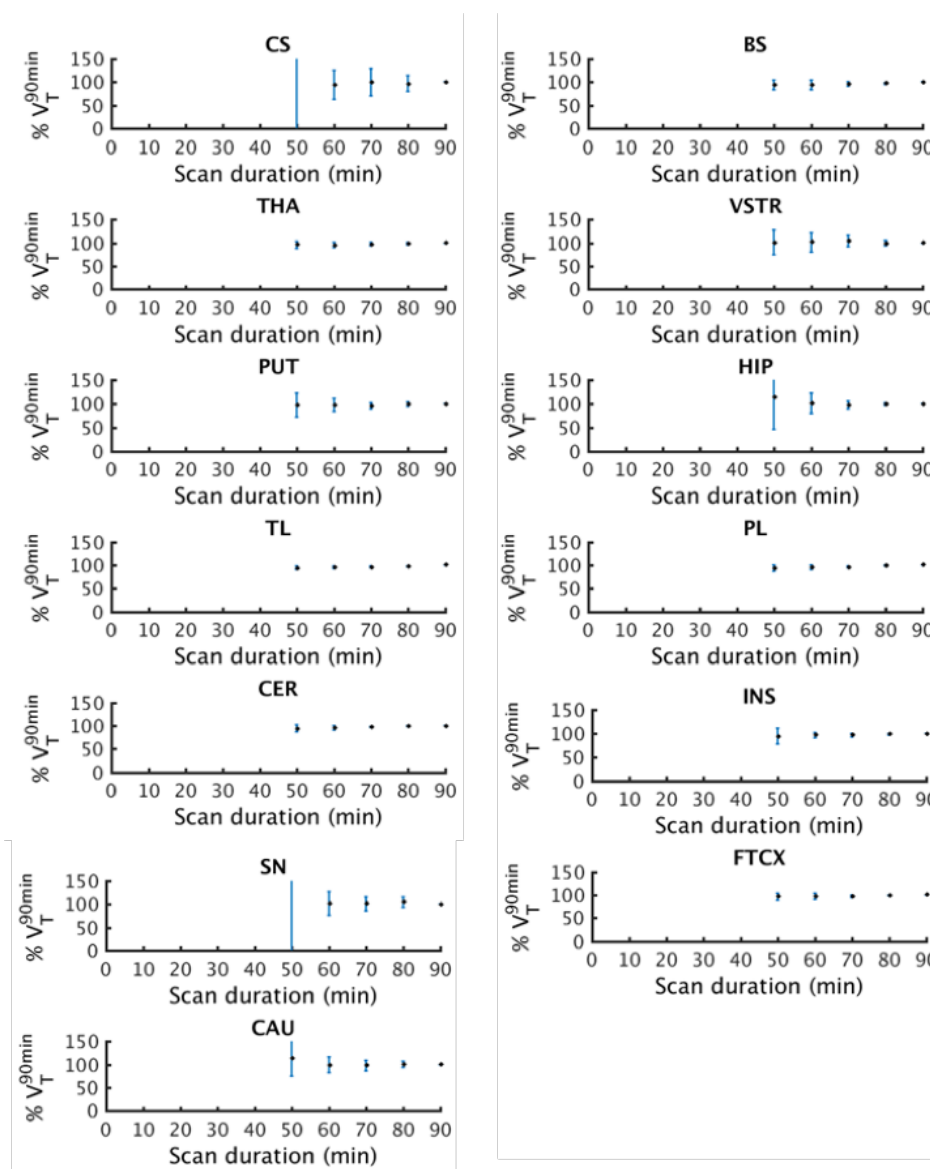


Figure 5.7 Regional time stability plots for ^{11}C -SA-4503 V_T where each data point represents the mean $\%V_T^{90\text{min}}$ of 23 subjects and the error bars represent standard deviation (SD).

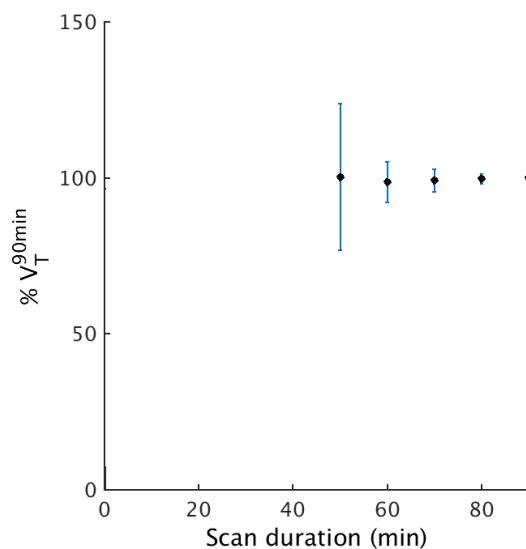


Figure 5.8 Time stability plot of ^{11}C -SA-4503 $\%V_T^{90\text{min}}$ where each data point represents the mean across 256 data points (23 subjects \times 12 ROIs). Data prior to 50 minutes excluded for visual clarity.

5.6 Parametric V_T Images

5.6.1 MA1

Parametric V_T maps were generated for all 23 ^{11}C -SA4503 scans acquired by fitting MA1 at the voxel level. The regional averages of parametric V_T s were correlated with ROI TAC derived estimates, resulting in a moderate correlation ($r^2 = 0.81$), and gradient of 0.74 (Figure 5.9). Of the parametrically derived V_T estimates, $0.52\% \pm 0.41\%$ of the voxels produced negative

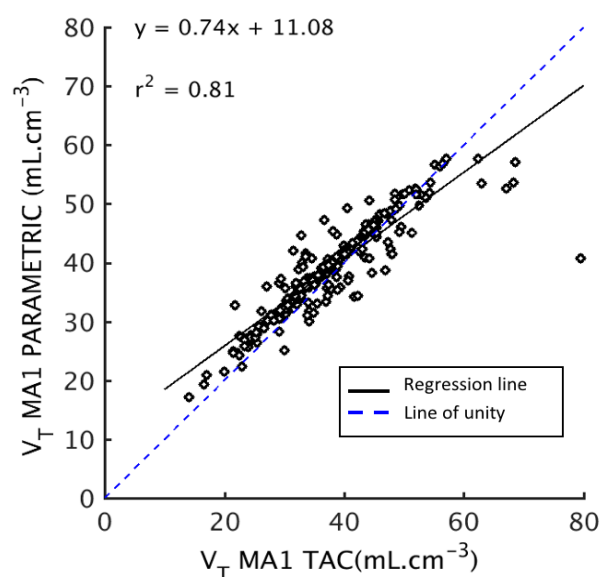


Figure 5.9 Correlation between TAC derived and parametrically derived ^{11}C -SA-4503 V_T for 23 subjects and 12 ROIs.

values while the percentage of voxels with nonphysiologically high estimates ($V_T > 100$) was $0.97\% \pm 0.83\%$.

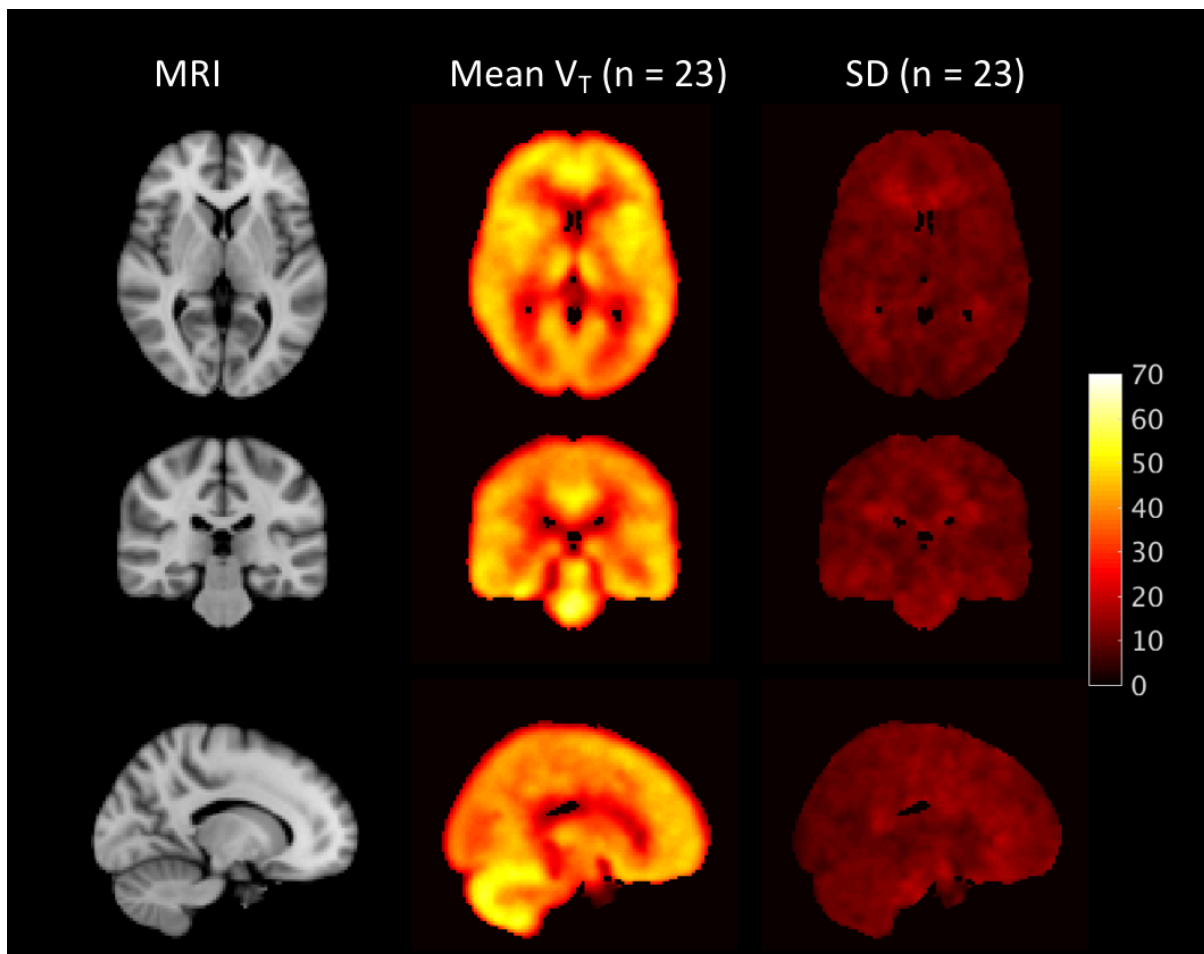
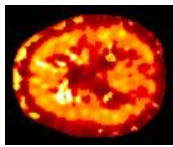
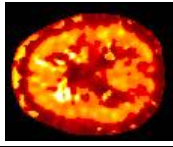
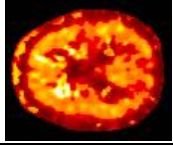
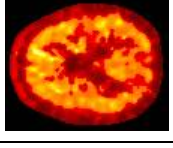


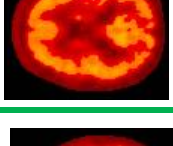



Figure 5.10 Orthogonal cross-sections of MRI (left), mean (middle) and standard deviation (SD) (right) V_T images of ^{11}C -SA-4503 ($n=23$).

Parametric V_T images that were initially created in subject space were spatially normalised to MNI52 space by applying the DARTEL flow fields derived previously (see chapter 3 section 3.5). Flow fields were applied to the images using a $4\text{mm} \times 4\text{mm} \times 4\text{mm}$ smoothing gaussian kernel. Mean and standard deviation V_T images of ^{11}C -SA-4503 were created from the 23 healthy subjects by averaging the distribution of intensities in the corresponding voxels (excluding non-physiological estimates) across all subjects (shown in Figure 5.10). Mean and SD images were further smoothed using a smoothing kernel of $6\text{mm} \times 6\text{mm} \times 6\text{mm}$ for display

purposes. The high V_T observed in the cerebellum and insular cortex was consistent across the population.

Table 5.2 Table showing example 1TC parametric images derived using a range of k_2 min constraints and a comparison of gradients and r^2 from the correlations between parametric 1TC results and with TAC derived MA1 results for each k_2 min

Representative Parametric V_T image								
k_2 min	0.0008	0.0009	0.001	0.002	0.003	0.004	0.005	0.006
% voxels > 100	0.53 0.66	0.45 0.60	0.39±0.55	0.14±0.23	0.02±0.03	4.43e-05 ± 1.40e-04	0	0
gradient	0.95 0.32	0.94 0.31	0.94 0.30	0.89 0.23	0.85 0.19	0.80 ± 0.18	0.74 0.18	0.67 0.18
r^2	0.73 0.14	0.74 0.14	0.74 0.13	0.77 0.12	0.76 0.12	0.75± 0.16	0.71 0.19	0.66 0.22

5.6.2 One TC

As mentioned above, a portion of the voxel-level V_T estimates generated using MA1 were non-physiologically high and needed to be excluded from the correlation with TAC derived results. We therefore explored 1TC to generate more robust parametric ^{11}C -SA-4503 V_T images. 10 ^{11}C -SA-4503 scans were used to generate parametric V_T images using the basis function implementation of 1TC with a range of k_2 min constraints (k_2 min: 0.0008, 0.0009, 0.001, 0.002, 0.003, 0.004, 0.005, 0.006). The resulting sets of V_T estimates were compared in terms of percentage of voxels with non-physiological V_T values, and were correlated with ROI derived MA1 results on a subject by subject basis.

The results of the analysis are summarised in Table 5.2. The percentage of total voxels with $V_T > 100$ was reduced with increasing (faster) k_2 min, reaching nearly 0% at k_2 min=0.004. The comparison of parametrically derived 1TC results with ROI derived MA1 results showed relatively constant r^2 values across the different k_2 min values that were assessed. There was an increase in bias (gradient further away from 1) with increasing k_2 min values, while the group variance decreased and stabilised at k_2 min=0.004. Choosing larger bias over larger variance, I ultimately decided on k_2 min=0.004 as the optimum value for k_2 min and this also allowed for the minimization of voxel loss due to non-physiologically high V_T s.

As a final step, 1TC with k_2 min=0.004 was applied to the whole cohort including 23 ^{11}C -SA-4503 scans. 1TC parametric V_T values were reasonably correlated with TAC derived estimates, with an $r^2 = 0.66$, and gradient of 0.80 (Figure 5.11). This showed that it is feasible to generate parametric images for ^{11}C -SA-4503 using the basis function implementation of 1TC with k_2 min constrained to be 0.004 without having to remove a large number of voxels and sacrificing from image quality, with the caveat that bias correction would be needed.

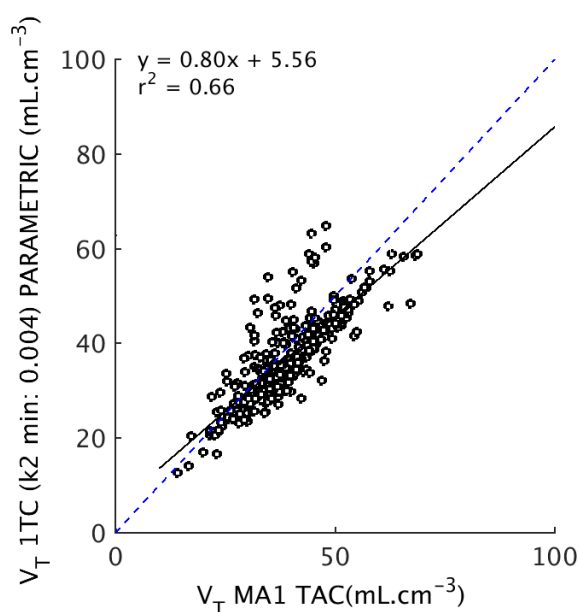


Figure 5.11 Correlation between MA1 TAC derived and 1TC parametrically derived ^{11}C -SA-4503 V_T for 23 subjects and 12 ROIs

5.7 Conclusion

This chapter sought to further characterise ^{11}C -SA-4503 in the human brain by determining the optimum kinetic methods and outcome measures for its quantification across MIND-MAPS cohorts. ^{11}C -SA-4503 uptake into the brain was slow and its kinetics were well described by the graphical analysis method MA1. Kinetic analysis can also be performed on voxel-wise level using MA1 provided non-physiological outliers are removed, and 1TC with the appropriate bias correction. Despite the slow kinetics, a minimum of 80 minute scan time was shown to be sufficient to obtain reliable estimates of V_T .

Despite the successful initial translation of ^{11}C -SA-4503 PET imaging from primate to human and numerous human studies published between 2000-2010, the last decade has been notably lacking in studies with this ligand. The reasons for this stems from some of the limitations of ^{11}C -SA-4503. As shown previously by Sakata and colleagues, there was no region devoid of specific ^{11}C -SA-4503, making the need for arterial blood acquisition unavoidable. The slow

kinetics of the tracer combined with the short half-life of ^{11}C pose limitations on its use in clinical setting as well as cross-sectional studies where certain disease cohorts may be unable to tolerate 80 minutes of dynamic scanning. Importantly, the poor estimation of k_4 microparameters in some regions suggests that ^{11}C -SA-4503 kinetics might approach irreversibility in these regions. Moreover, since the initial translation of ^{11}C -SA-4503 into humans, studies have revealed that ^{11}C -SA-4503 has significant affinity for sigma 2 receptors as well as to vesicular acetylcholine transporters, and lower selectivity to S1R than originally thought (Lan, Bai, Chen, et al., 2019; Shen, James, Andrews, et al., 2015). ^{11}C -SA-4503 therefore fails to meet three of the key requirements of an ideal tracer (reviewed in Chapter 1), i.e. that it has fast tissue kinetics, displays reversible binding and has high affinity and selectivity for its target.

In conclusion, although it does not possess all of the properties of an ideal brain PET radioligand, ^{11}C -SA-4503 has been sufficiently characterised in the healthy human brain and can be applied across the MIND-MAPS consortium to provide an index of S1R concentration.

6 Quantification and kinetic modelling of ^{11}C -UCB-J

The kinetics of ^{11}C -UCB-J have been well-characterised in the rodent, NHP and the human brain (Finnema, Nabulsi, Eid, et al., 2016; Nabulsi, Mercier, Holden, et al., 2016). The work presented in this chapter builds on the existing literature of ^{11}C -UCB-J quantification in humans and sets out to determine an optimal analysis workflow for ^{11}C -UCB-J quantification in to be applied to all MIND-MAPS cohorts.

6.1 Background and Study Overview

^{11}C -UCB-J is a PET radioligand that targets synaptic vesicle protein A (SV2A) which is a transmembrane glycoprotein expressed ubiquitously throughout the brain. Since its discovery in 2014, there has been an ever-increasing effort to demonstrate correlations between ^{11}C -UCB-J signal change and disease progression across a number of neurodegenerative and psychiatric diseases (reviewed in Chapter 2). The popularity of this tracer is in large part due to its favourable imaging characteristics including excellent correlation with the synaptic density marker synaptophysin, high affinity for SV2A, high uptake and fast kinetics (Finnema, Nabulsi, Eid, et al., 2016).

This chapter starts with a brief overview of the literature on ^{11}C -UCB-J quantification methods (section 6.2). The distribution of ligand uptake is presented in section 6.3. The process of establishing appropriate blood and plasma models to create a reliable arterial plasma input function is covered in section 6.4. The optimal tissue kinetic model is established in section 6.5, followed by an assessment of SUVr-1 as an outcome measure and time stability analyses in sections 6.6 and 6.7, respectively. Finally, in section 6.8, voxel-level kinetic modelling results are presented.

6.2 Literature Review of ^{11}C -UCB-J Quantification

Since its first application to humans, ^{11}C -UCB-J kinetics have been studied rigorously. Initial *in vitro* and *in vivo* ^{11}C -UCB-J data confirmed that the tracer is displaceable by SV2A-selective anticonvulsant levetiracetam, displays high uptake and fast kinetics displayed in all grey matter regions and low uptake in white matter regions (Finnema, Nabulsi, Eid, et al., 2016; Nabulsi, Mercier, Holden, et al., 2016). The authors also showed that ^{11}C -UCB-J imaging of SV2A was sensitive to temporal lobe epilepsy induced synaptic loss (Finnema, Nabulsi, Eid, et al., 2016). The same group conducted a further evaluation of ^{11}C -UCB-J kinetics including time stability

analysis and test-retest reproducibility of outcome measures where they showed that the 1TC model is most suitable for estimating the primary outcome measure V_T when applied both on a regional and voxel-wise level with exceptional reproducibility (Finnema, Nabulsi, Mercier, et al., 2017). From their time stability analysis of V_T and K_1 assessed across 120 minutes, scan time was proposed to be shortened to 60 minutes. In 2018, two independent blocking studies by Koole et al and Rossano et al attempted to validate subcortical white matter region centrum semiovale (CS) as a reference tissue ^{11}C -UCB-J (Koole, van Aalst, Devrome, et al., 2018; Rossano, Toyonaga, Finnema, et al., 2019). The first study found no significant effects of blocking on CS binding, while the latter found that CS V_T overestimated V_{ND} by 35–40%. The potential impact of improving CS definition and increasing the number of iterations during iterative reconstruction on the difference between CS V_T and blocking derived V_{ND} have also been investigated and shown to have no significant effect (Rossano, Toyonaga, Finnema, et al., 2019).

Based on the findings that CS may be a biased yet useful estimate of nondisplaceable uptake, an SRTM approach (Y. Wu & Carson, 2002) was also investigated as a potential reference region method for quantifying SV2A (M.-K. Chen, Mecca, Naganawa, et al., 2018; Koole, van Aalst, Devrome, et al., 2018; Mertens, Maguire, Serdons, et al., 2020; Rossano, Toyonaga, Finnema, et al., 2019). The bias of the SRTM approach on SV2A occupancy and density has been shown to be negligible (Koole, van Aalst, Devrome, et al., 2018), and SRTM2 has been used to show significant reductions (41%) in BP_{ND} in the hippocampus of subjects with AD when compared to healthy subjects (M.-K. Chen, Mecca, Naganawa, et al., 2018). The CS has also been used to derive the simplified outcome measure SUV_r , which correlates well with both TAC-based and parametric results derived from full kinetic modelling with 1TC (Koole, van Aalst, Devrome, et al., 2018; Mertens, Maguire, Serdons, et al., 2020).

The remainder of this chapter summarises the results of the kinetic modelling methods that were applied to the ^{11}C -UCB-J scans acquired as part of the MIND-MAPS Consortium. The results are discussed within the context of the published ^{11}C -UCB-J quantification approaches summarised above.

6.3 Tracer Uptake and distribution

^{11}C -UCB-J uptake was heterogeneous and widespread in the brains of 12 healthy volunteers (Table 3.1, highlighted cohort), consistent with the expression of the SV2A in the brain (Figure 6.1). Tracer kinetics were fast, reaching peak values at ~ 7 -21 minutes post injection after which it steadily declined, consistent with previous reports by Finnema and colleagues (Finnema, Nabulsi, Eid, et al., 2016). Uptake values ranged from 3.4 g/ml in the centrum semiovale to highest of 9.6 g/ml in the putamen.

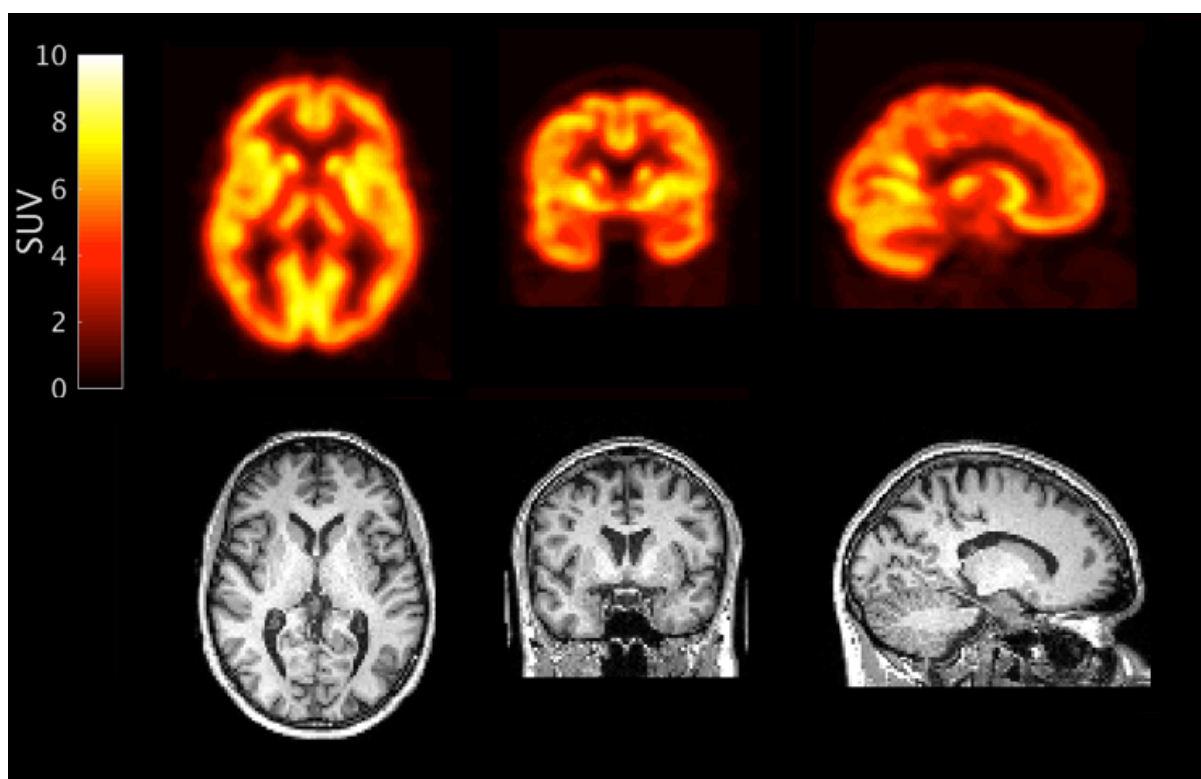


Figure 6.1 Orthogonal cross sections of co-registered ^{11}C -UCB-J PET and MR images from a representative subject. PET images are shown as SUV summed from 10-90 minutes.

6.4 Determining the optimum arterial plasma input function

This section summarises the results of the plasma over blood (*POB*) and parent fraction (*PPF*) models applied to ^{11}C -UCB-J arterial blood data. The models that produced the best fits were in turn applied to blood data acquired during all subsequent ^{11}C -UCB-J scans.

6.4.1 Modelling plasma over blood (*POB*) data

The ratio of ^{11}C -UCB-J concentration in plasma to that in blood stayed at a constant level throughout the 90 minute scan. A comparison of the 4 *POB* models using AIC confirmed that a ‘constant’ model (see Equation 4.1) produced the most parsimonious fits to the *POB* data for ^{11}C -UCB-J. The model produced good fits to all 12 subjects’ data, as can be seen from the model fits shown in Figure 6.2.

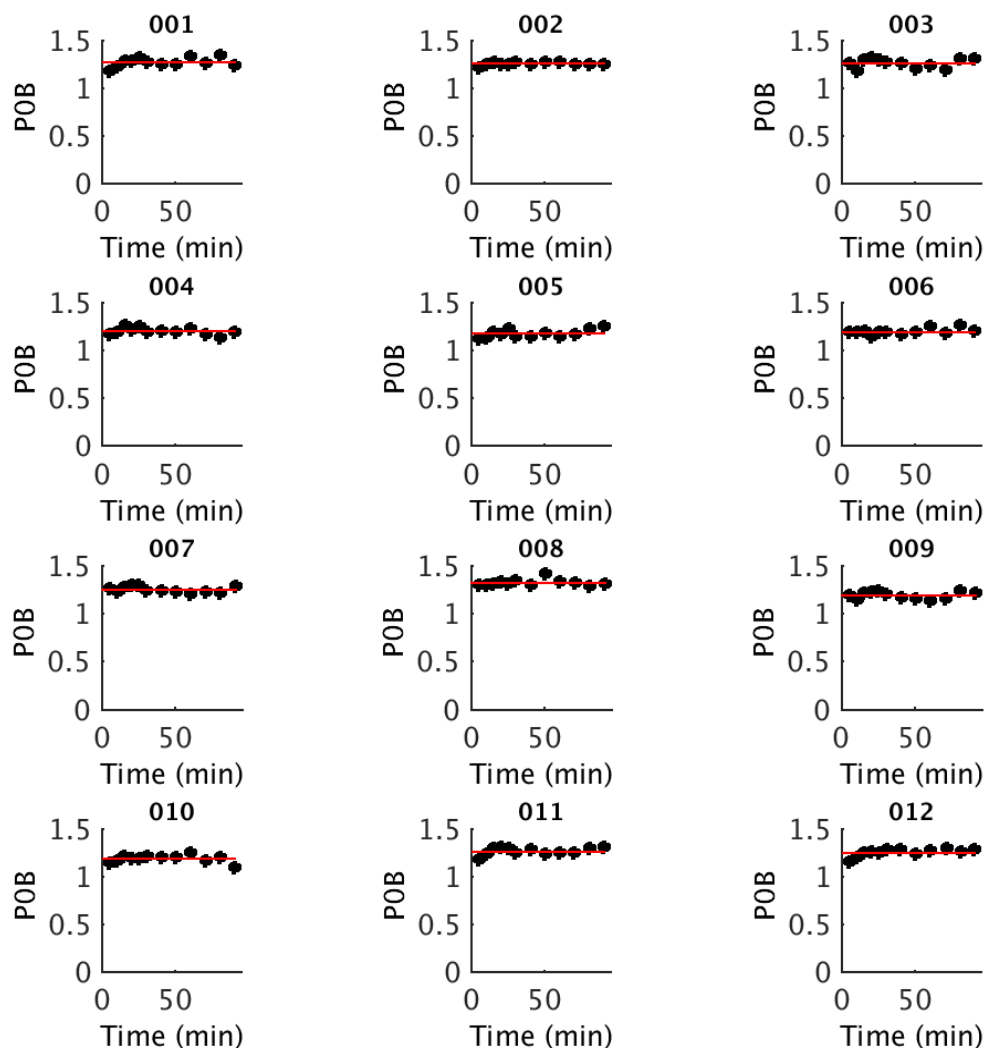


Figure 6.2 Fits of the ‘constant’ *POB* model to the blood data from 12 ^{11}C -UCB-J scans

6.4.2 Modelling plasma parent fraction (PPF) data

^{11}C -UCB-J metabolised quickly in the plasma, with $25 \pm 5\%$ intact tracer remaining at 90 minutes post-injection. HPLC analysis revealed 3 metabolites eluting between 6 and 9 minutes (fractions 18-26), in line with what has been reported previously (Finnema, Nabulsi, Eid, et al., 2016). According to AIC, a sigmoid model with 3 parameters α , β , and γ (Equation 4.2), best described the shape of the parent fraction data over time. This model produced good fits to the parent fraction data of all twelve ^{11}C -UCB-J scans (Figure 6.3).

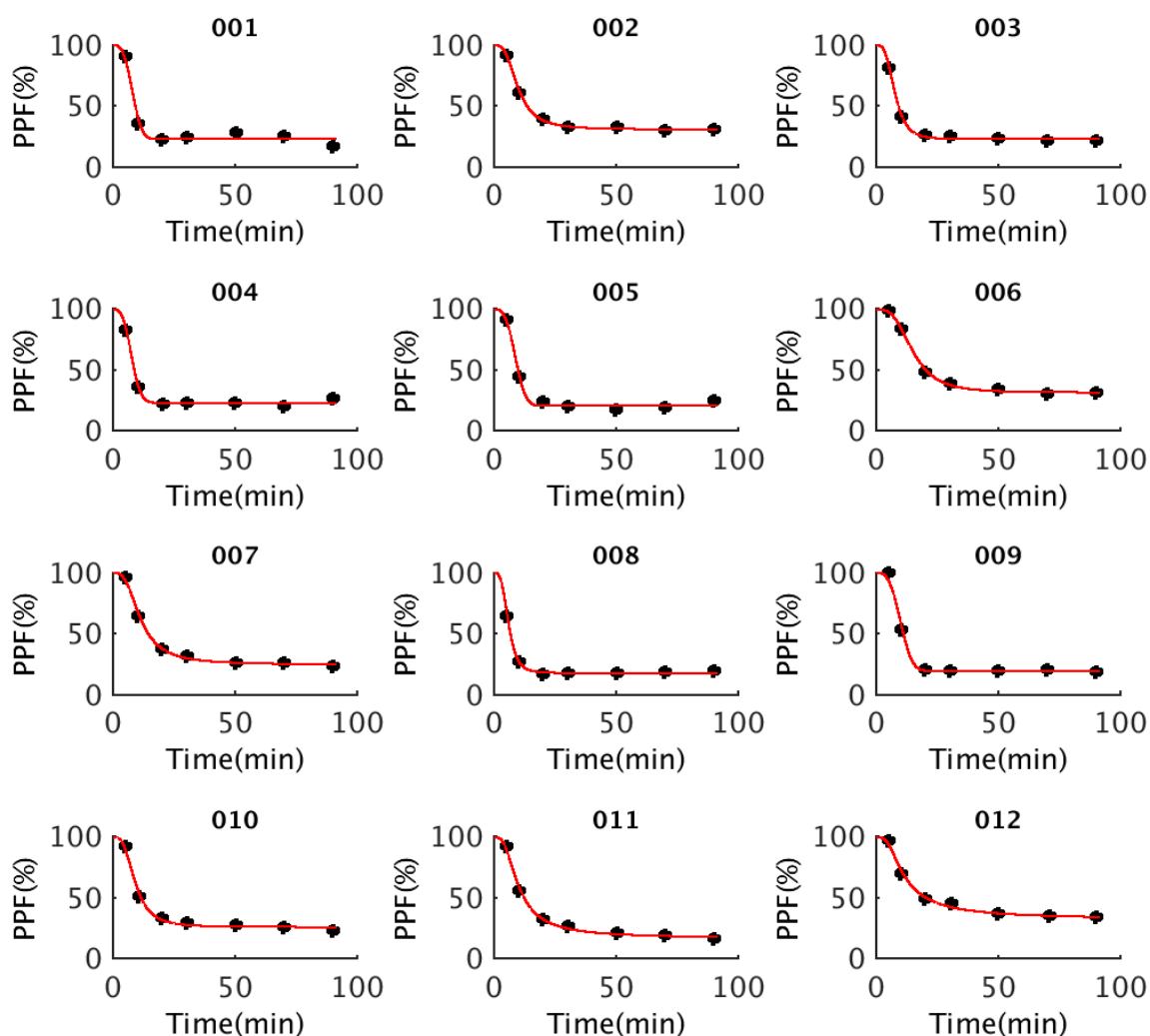


Figure 6.3 Fits of the ‘sigmoid’ *PPF* model to the metabolite data from 12 ^{11}C -UCB-J scans

6.5 Determining the optimum tissue kinetic model for ^{11}C -UCB-J

MA1 ($t^* = 30$ min), 2TC and 1TC models all produced visually acceptable fits to the regional ^{11}C -UCB-J derived TAC data (Figure 6.4 A, B and C). 2TC performed better than 1TC in 10/156 cases according to AIC, however 2TC derived V_T estimates had poorer identifiability ($\text{SE} > 10\%$) in 5/156 cases (regional AIC and SE summarised in Table 6.1), which is in agreement with what has been reported in the literature (Finnema, Nabulsi, Eid, et al., 2016). MA1 results were in excellent agreement with 1TC results ($r^2 = 0.99$). Given the very good agreement between 1TC and gold standard 2TC derived V_T estimates ($r^2=0.99$, Figure 6.4 D), and the ease with which parametric images can be generated using 1TC, this method was chosen as the model of choice to derive final outcome measures.

ROI		CS	BST	SN	THA	VSTR	CAU	PUT	HIP	INS	TL	PL	FTCX	CER	Total
AIC	1TC	3	0	0	0	0	6	0	0	0	0	0	1	0	10
	2TC	9	12	12	12	12	6	12	12	12	12	12	11	12	146
SE>10%	1TC	0	0	0	0	0	0	0	0	0	0	0	0	0	0
	2TC	2	0	1	0	1	0	0	0	0	0	0	0	0	5

The numbers in the top two rows represent the number of times 1TC or 2TC were chosen as the preferred model as assessed by AIC. The numbers in the bottom two rows represent the number of cases for which standard error (SE) associated with 1TC and 2TC derived V_T was larger than 10% .

As covered in section 6.2, the centrum semiovale has been verified as a suitable reference region for ^{11}C -UCB-J and was therefore used to derive DVR and in turn BP_{ND} (DVR-1) as a measure of specific binding. V_T/f_p and K_1 were also assessed as outcome measures for ^{11}C -UCB-J. All outcome measures derived using the 1TC model are provided in Table 6.2.

V_T estimates ranged from 5.7 ± 0.7 ml.cm $^{-3}$ in the CS to 20.9 ± 2.1 ml.cm $^{-3}$ in the putamen, with a mean inter-subject variability across regions at $13\% \pm 5\%$. DVR was highest in the putamen (3.54 ± 0.21) and lowest in the brainstem (1.26 ± 0.21), with intersubject variability slightly reduced to $10\% \pm 5\%$ across regions. Consequently, BP_{ND} was highest in the putamen and lowest in the brainstem. Correction of V_T by f_p had no significant effect on inter-subject variability except for in the centrum semiovale where variability was increased to 18%. Mean

K_1 values ranged from $0.147 \pm 0.019 \text{ mL}\cdot\text{cm}^{-3}\cdot\text{min}^{-1}$ in the CS to $0.382 \pm 0.070 \text{ mL}\cdot\text{cm}^{-3}\cdot\text{min}^{-1}$ in the putamen which was in line with values previously reported in the literature (Finnema, Nabulsi, Mercier, et al., 2017).

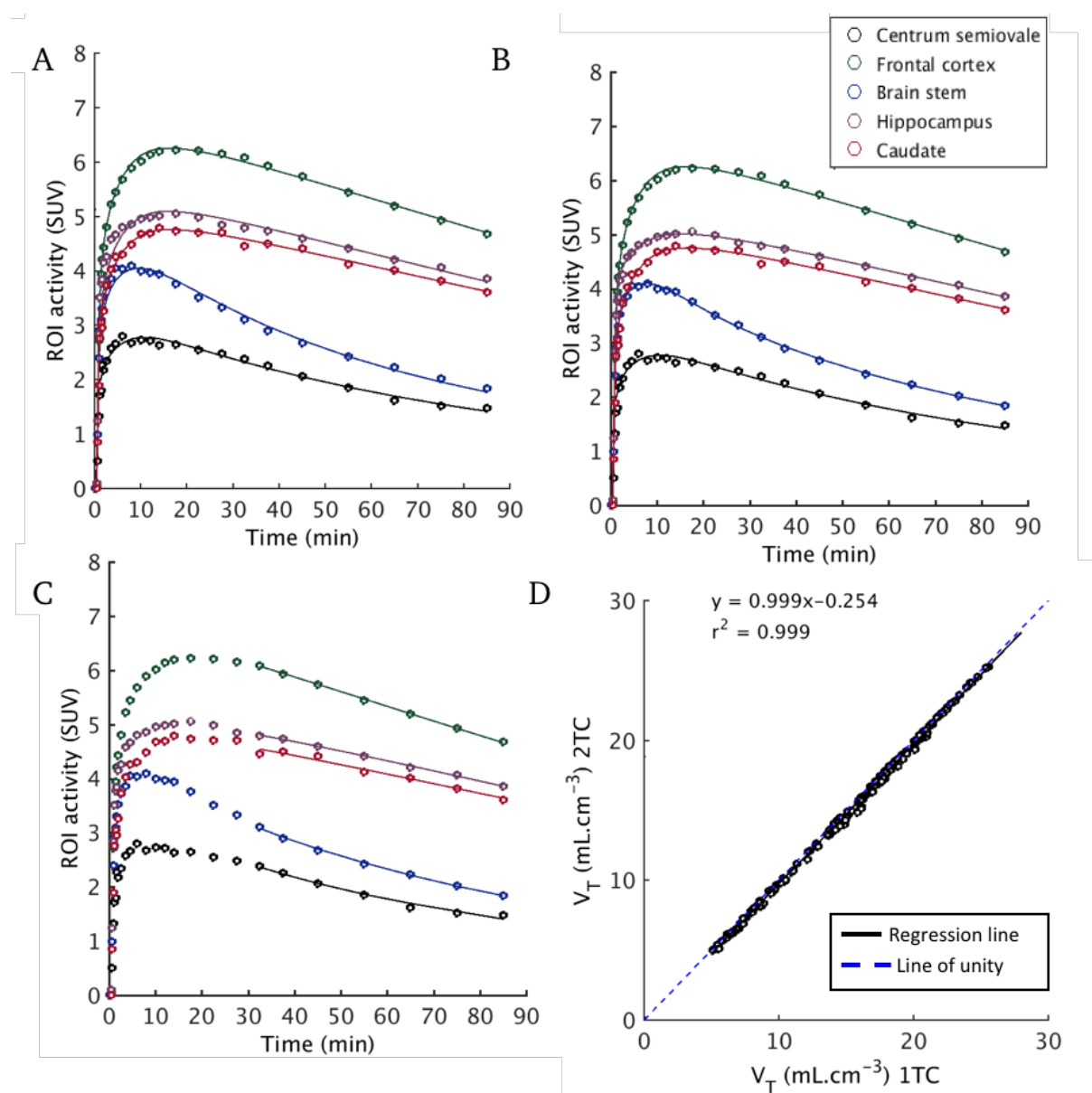


Figure 6.4 ^{11}C -UCB-J regional TACs and model fits for a representative subject derived with **A** 1TC, **B** 2TC and **C** MA1. **D** Linear regression plot showing comparison of 1TC vs 2TC derived ^{11}C -UCB-J V_T ($n=12$).

Table 6.2 ^{11}C -UCB-J derived regional PET outcome measures

Outcome Measure	Kinetic Model	CS	BST	SN	THA	VSTR	CAU	PUT	HIP	INS	TL	PL	FTCX	CER
V_T (mL.cm ⁻³)	1TC	5.7	7.2	8.5	11.2	20.9	12.4	20.9	13.4	20.5	17.6	15.5	14	15.9
		12%	12%	10%	16%	13%	28%	11%	13%	10%	10%	14%	14%	10%
V_T / f_p (mL.cm ⁻³)	1TC	25	31	37	49	91	54	91	62	90	83	77	76	69
		18%	13%	12%	15%	15%	28%	14%	12%	12%	11%	13%	13%	12%
DVR	1TC	n/a	1.26	1.50	1.96	3.66	2.17	3.67	2.50	3.63	3.34	3.11	3.07	2.80
			7%	8%	13%	8%	24%	7%	10%	9%	8%	11%	10%	8%
K_i (mL.cm ⁻³ .min ⁻¹)	1TC	0.147	0.252	0.279	0.309	0.351	0.251	0.397	0.259	0.364	0.312	0.353	0.359	0.368
		14%	15%	14%	19%	20%	32%	18%	18%	20%	17%	18%	20%	16%
BP _{ND}	1TC	n/a	0.26	0.50	0.96	2.66	1.17	2.67	1.50	2.63	2.34	2.12	2.07	1.80
			33%	23%	27%	11%	45%	10%	16%	12%	12%	16%	15%	12%

Data are mean and COV. 5 values for 2TC estimation were excluded based on V_T of SE% > 10. (n=12)

6.6 Assessment of SUVR-1 as an outcome measure

Data from 24 healthy subjects was used to assess SUVR-1 as a simplified outcome measure and enable comparison to BP_{ND} (DVR-1). SUVR values were obtained by normalising SUV values in target ROIs derived from a 20 minute static images to that in the CS. SUVR-1 data was generated for 8 time windows (given in Table 6.3) and compared to BP_{ND} using least-squares linear regression.

Table 6.3 Results from linear correlation of SUVR -1 values with DVR – 1 derived for 8 SUVR time windows (12 ROIs, 24 subjects)

SUVR time window (minutes)	r ²	gradient
0-20	0.19	0.34
10-30	0.73	0.55
20-40	0.86	0.67
30-50	0.90	0.78
40-60	0.95	0.85
50-70	0.97	0.90
60-80	0.97	0.95
70-90	0.96	0.97

As previously demonstrated by Mertens and colleagues (Mertens, Maguire, Serdons, et al., 2020), highly significant correlations were observed between BP_{ND} and SUVR-1 values for 40 - 60, 50 - 70, 60 – 80 and 70 - 90 min post-injection, with 40-60 and 50-70 time intervals showing increased bias compared to the later time intervals where the slope was close to zero (Figure 6.5A-B).

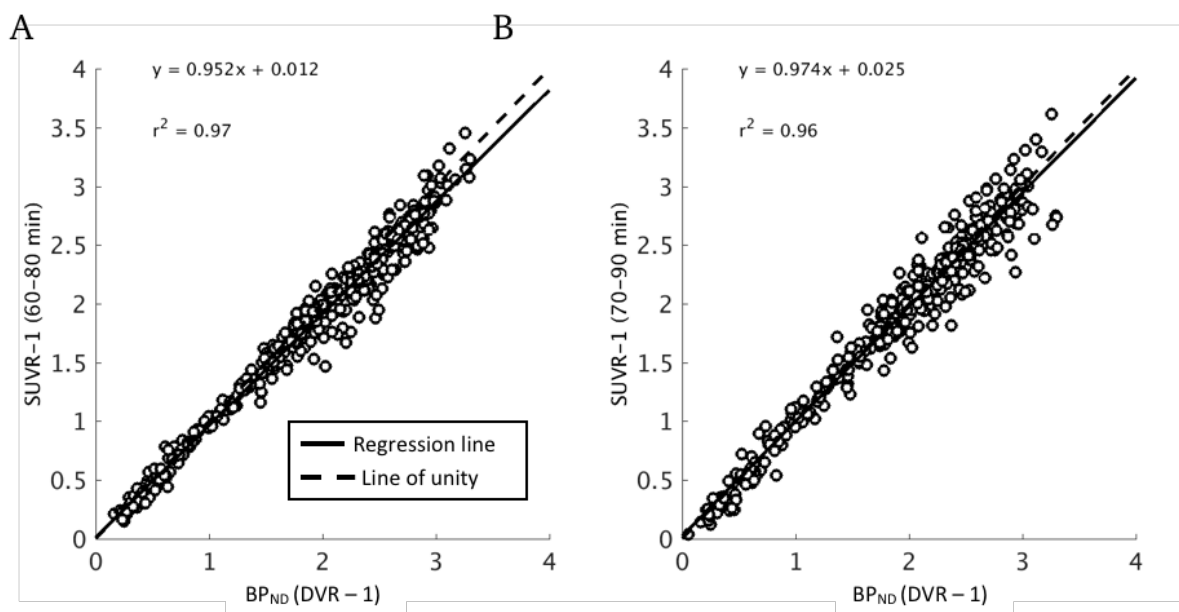


Figure 6.5 Correlation between **A** SUV_r-1 (60-80) and DVR-1, and **B** SUV_r-1 (70-90) and DVR-1 for 24 subjects and 12 ROIs

6.7 Time stability analysis

The time stability of ¹¹C-UCB-J was evaluated by exploring the performance of 1TC derived V_T and K_1 as well as SUV_r-1 derived from the 8 time intervals provided in Table 6.3. The V_T and K_1 values estimated for the different scan lengths were expressed as a percentage of V_T and K_1 estimated from the full 90 min acquisition ($V_T^{90\text{min}}$, $K_1^{90\text{min}}$), aggregated together over 24 subjects and plotted against time as described in Chapter 3.

¹¹C-UCB-J V_T estimates stabilised as early as 60 minutes, yielding a V_T 98.0 ± 1.8 % of $V_T^{90\text{min}}$ (Figure 6.6 A). Similarly, K_1 estimates reached stability at 60 minutes post injection at a value 101.1 ± 1.1 % of $K_1^{90\text{min}}$ (Figure 6.6 B). There were no significant differences in time stability across regions for either V_T or K_1 (regional plots not included). SUV_r - 1 values started to stabilise after 60 minutes (Figure 6.6C), reaching a final mean value of 1.74 ± 0.80 at 70 minutes post-injection.

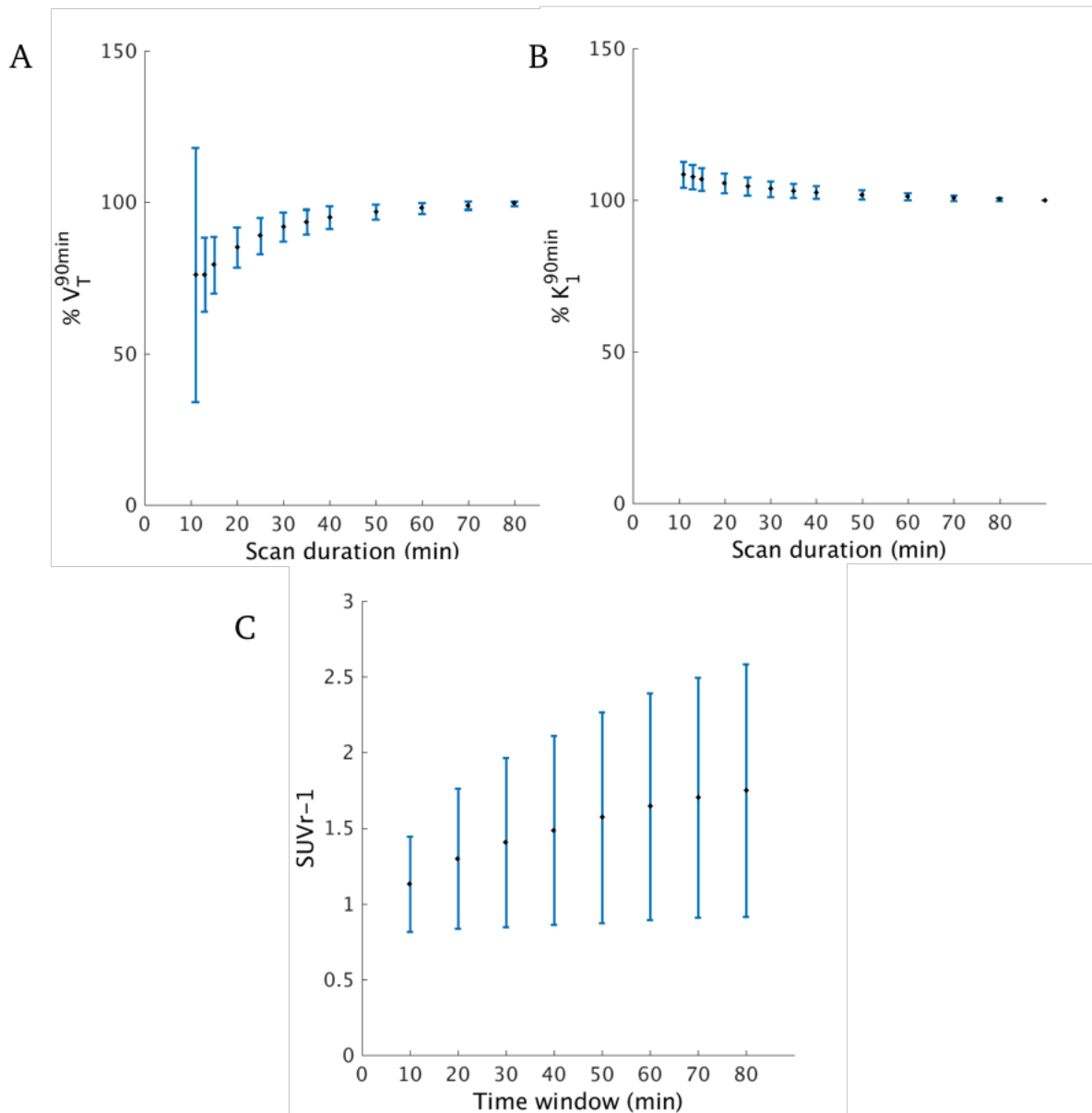


Figure 6.6 Time stability plots of **A** $\% V_T^{90min}$ and **B** $\% K_1^{90min}$ and **C** $SUVr-1$ where each data point represents the mean across 288 data points (24 subjects x 12 ROIs).

The time stability results reported here are in agreement with what has been reported by Finnema and colleagues, who suggested that scan time can be shortened to 60 minutes for both TAC-level and voxel-level quantification of ^{11}C -UCB-J V_T and K_1 (Finnema, Nabulsi, Mercier, et al., 2017). Our assessment of $SUVr-1$ as an outcome measure suggests the $SUVr$ images generated from a 20 minute static ^{11}C -UCB-J acquisition at least 60 minutes post-injection may serve as a good proxy for BP_{ND} . This result supports recent findings by both Koole

et al and Mertens et al who showed that SUVr -1 values derived from 30 minutes static PET scan acquired between 50 and 90 minutes post-injection are highly correlated with DVR – 1 (Koole, van Aalst, Devrome, et al., 2018; Mertens, Maguire, Serdons, et al., 2020).

6.8 Parametric V_T Images

Voxel-based parametric maps of V_T and K_1 were generated for 24 ^{11}C -UCB-J scans using a basis function implementation of 1TC. Parametric V_T images that were initially created in subject space were spatially normalised to MNI52 space by applying the DARTEL flow fields derived previously (see chapter 3 section 3.5). Flow fields were applied to the images using a 4mm x 4mm x 4mm smoothing gaussian kernel.

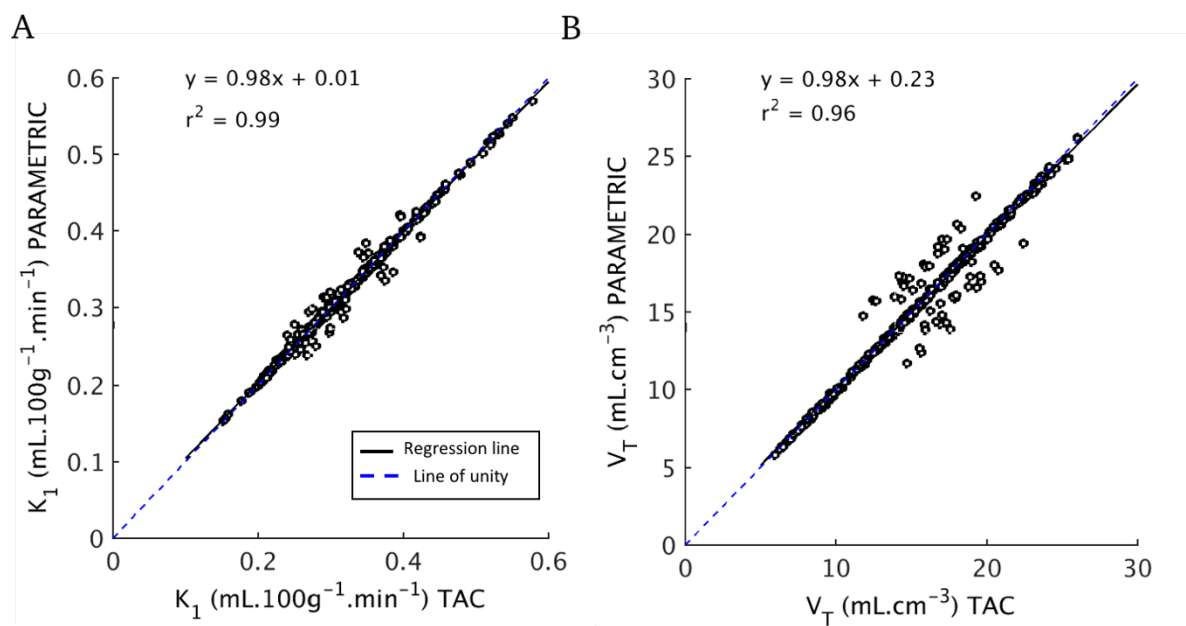


Figure 6.7 Correlation between **A** TAC derived and parametric K_1 **B** TAC derived and parametric V_T for 24 subjects and 12 ROIs

Parametrically derived V_T and K_1 estimates were in excellent agreement with TAC derived results (Figure 6.7), with r^2 values 0.99 and 0.96 obtained for K_1 and V_T , respectively.

Following the normalisation of parametric images from subject space to MNI152 space as described in chapter 3 section 3.5, voxel intensities were averaged across subjects ($n=24$) to create the mean and standard deviation V_T images shown in figure 6.8.

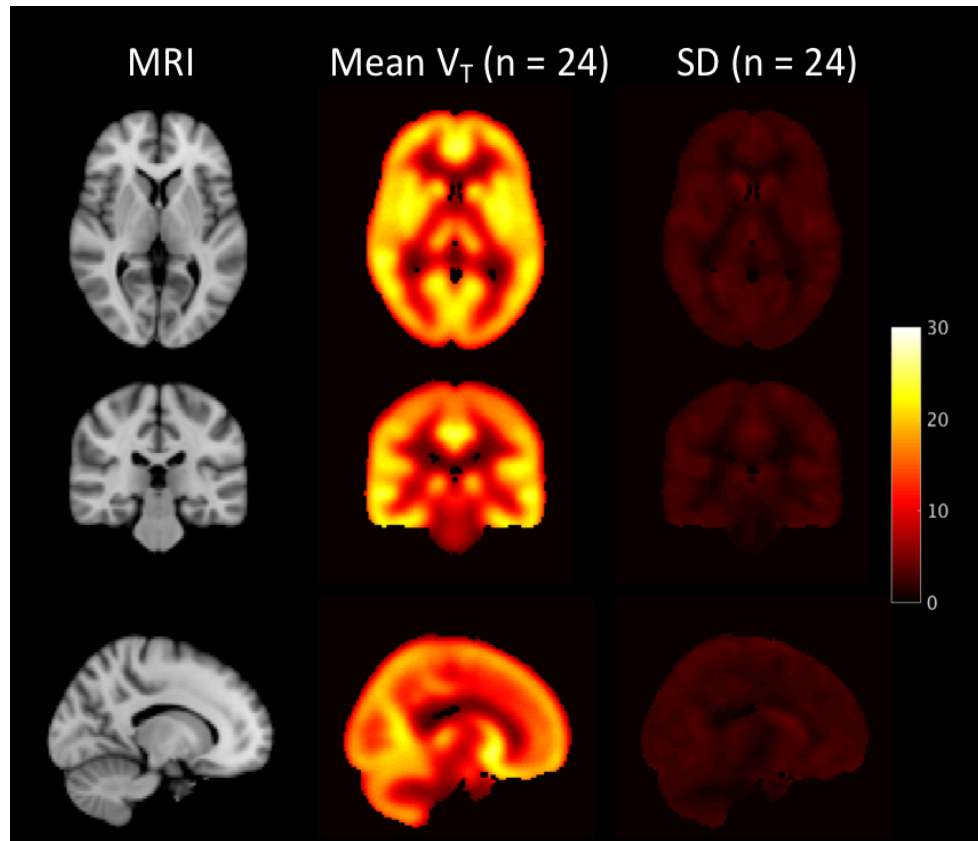


Figure 6.8 Orthogonal cross-sections of MRI (left), mean (middle) and standard deviation (SD) (right) V_T images of ^{11}C -UCB-J ($n=24$).

6.9 Conclusion

^{11}C -UCB-J uptake was widespread and displayed fast kinetics. The 1TC method was chosen as the optimal model to estimate V_T and K_1 , with time stability results showing that at least 60 minutes of dynamic scanning is required to reliably estimate both these outcome measures.

SUVr-1 obtained from a 20 minute static scan acquired at least 60 minutes post-injection produced results that were highly correlated with 1TC derived BP_{ND} results, thus can be reliably

used as a non-invasive measure of binding in situations where arterial blood sampling is not possible and scan time needs to be shortened to accommodate patient comfort. Although a simplified reference region approach such as SRTM2 was not applied to this particular dataset, recently published data suggests it may be used, provided centrum semiovale physiology and kinetics are unchanged due to disease and any potential bias in BP_{ND} that is expected to arise when compared with 1TC results is sufficiently accounted for.

All of the results derived for this particular healthy cohort were in line with what has been previously reported in the literature, adding further confidence that ^{11}C -UCB-J imaging is an excellent method for quantifying SV2A in vivo and will prove useful in the diagnosis and monitoring of brain diseases involving loss of synapses.

7 Assessment of Healthy Ageing Effects on MC-I, S1R and SV2A quantification

The analysis pipelines for quantifying MC-I, S1R and SV2A using ^{18}F -BCPP-EF, ^{11}C -SA-4503 and ^{11}C -UCB-J, respectively, were established in the last 3 chapters. The work in this chapter utilises these pipelines to generate quantitative outcome measures for the full MIND-MAPS healthy volunteer cohort and investigates their relationship with age and gender.

7.1 Background

As detailed in Chapter 2 section 2.12, mitochondrial and ER related dysfunction and related synaptic loss are key aspects of ageing and are thought to contribute to the pathology of NDDs. The mitochondrial theory of ageing associates increasing age with decreased mitochondrial functionality, where the ETC and in particular MC-I are impaired (Pollard, Craig, & Chakrabarti, 2016). Decreased MC-I activity and ROS production correlate with increased age in rats, and MC-I density as measured by ^{18}F -BCPP-EF is reduced with age in monkeys in all brain regions (Hideo Tsukada, 2014). Interestingly, the age dependant reduction in ^{18}F -BCPP-EF signal in healthy aged monkeys has been shown to correlate negatively with A β deposition (Hideo Tsukada, 2014). Human post-mortem data has also shown decreased MC-I activity with age, where the greatest reductions are found in the frontal cortex, temporal cortex cerebellum and putamen (Ojaimi, Masters, Opeskin, et al., 1999).

The involvement of increased ER stress in ageing and the criticality of S1Rs to ER function and neuronal protection have prompted the evaluation of the effect of age on S1Rs in the brain. However, *in vitro* and *in vivo* experiments have produced somewhat conflicting results. S1R expression was preserved in aged rats and mice as measured using immunohistochemistry (Phan, Urani, Sandillon, et al., 2003), whereas human post-mortem autoradiography showed decreased S1R in the frontal cortex in the aged brain PET studies also provide mixed results, with evidence of reduced ^{11}C -SA-4503 binding with increasing age in selective brain regions of rodents (Ramakrishnan, Visser, Rybczynska, et al., 2016), as well increases in ^{11}C -SA-4503 binding with age in the rodent and NHP brain (Ishiwata, Kobayashi, Kawamura, et al., 2003; Kawamura, Kimura, Tsukada, et al., 2003; Wallace, Mactutus, & Booze, 2000). Upregulation of S1R binding sites in response to age-related reductions in endogenous S1R agonists (e.g. neurosteroids) and reduced dopaminergic and glutamatergic signalling, known to be modulated

by S1R, has been proposed as an explanation for increased S1R signal. Evidence of ER stress induced upregulation of S1Rs provides a further mechanism for the age-related increases seen (Mitsuda, Omi, Tanimukai, et al., 2011).

Normal brain ageing is characterized by the selective loss of discrete populations of dendritic spines and synapses (Graham, Naldrett, Kohama, et al., 2019). Age-related functional impairments are likely to be linked to disturbed synaptic maintenance, with hippocampal synapses appearing to be especially vulnerable to age related loss (Canas, Duarte, Rodrigues, et al., 2009; Hof & Morrison, 2004). In humans, an early post-mortem study by Masliah et al showed a reduced number of presynaptic terminals in aged dementia-free subjects compared to younger subjects (Masliah, Mallory, Hansen, et al., 1993). Reduced synaptic density with age in the human brain, particularly in the caudate and thalamus, is also consistent with the preliminary work using ^{11}C -UCB-J PET (Carson, Naganawa, Matuskey, et al., 2018).

Gender is increasingly recognised as a contributing factor to the risk of developing of NDD's. Several studies have suggested two-fold increase in the risk of developing PD in men compared to women (Gillies et al., 2014; Labandeira-Garcia et al., 2016), whereas the prevalence of AD in women is significantly higher than in men (Niu, Álvarez-Álvarez, Guillén-Grima, et al., 2017; Wortmann, 2015). There is therefore an increasing urgency to understand sexual dimorphisms in the healthy as well as injured brain to develop therapies that work for both genders.

Differences in energy metabolism and mitochondrial function are thought to underlie some of the gender differences in vulnerabilities to developing neurodegenerative disease. *In vitro* data from mice has shown female mice to have higher levels of antioxidant enzymes, and be more resistant to MC-1 inhibition by ROS compared to males (Demarest & McCarthy, 2014; Kander, Cui, & Liu, 2017). MC-1 activity measured by metabolic imaging of the brain has been shown

to be higher in the female human brain compared to males (Silaidos, Pilatus, Grewal, et al., 2018).

7.2 Study Overview

Based on the above evidence, the effect of healthy ageing on MC-I, S1R and SV2A binding was investigated. The effect of gender on PET outcome measures was also explored. MC-I, S1R and SV2A were quantified using the kinetic methods established in Chapters 4, 5 and 6, respectively. A preliminary analysis of age effects on MC-I, S1R and SV2A assessed by ^{18}F -BCPP-EF, ^{11}C -SA-4503 and ^{11}C -UCB-J has been published using data from a subset ($n=12$) of the cohort presented here (Mansur, Rabiner, Comley, et al., 2019). This chapter builds on the published work by including the full cohort of subjects and accounting for partial volume effects.

7.2.1 Hypotheses

In light of the mitochondrial theory of ageing, post-mortem evidence of decreased MC-I in ageing humans and findings of reduced ^{18}F -BCPP-EF signal in nonhuman primates, we hypothesised that ^{18}F -BCPP-EF signal would be reduced with age in humans. The involvement of age-related reductions of endogenous S1 agonists and the link between increased ER stress in S1R upregulation, combined with *in vivo* evidence of increased ^{11}C -SA-4503 signal in rats and monkeys led to the hypothesis that ^{11}C -SA-4503 will increase with age in humans. Lastly, because the loss of synapses is a natural consequence of age-related neurodegeneration along with post-mortem and *in vivo* evidence of reduced SV2A in the brain, we hypothesised that ^{11}C -UCB-J signal will be reduced with healthy ageing.

Based on preclinical work showing increased vulnerability of males to oxidative stress induced MC-I damage as well as more recent evidence of increased MC-I function in the healthy human

brains of females compared to males, we hypothesised that there would be higher ^{18}F -BCPP-EF signal in females compared to males. Given the shortage of literature on gender differences in S1R and SV2A expression, no specific hypotheses were formed with regards to the relationship between gender and ^{11}C -SA-4503 and ^{11}C -UCB-J signal.

7.3 Methods

The full MIND-MAPS healthy volunteer cohort was included in this study, resulting in data from a total of 30 ^{18}F -BCPP-EF (25 scans from MIN-DMAPS healthy volunteer cohort + 5 baseline scans from test-retest cohort), 23 ^{11}C -SA-4503 and 24 ^{11}C -UCB-J dynamic PET scans with arterial lines being included in the assessment of the effect of age and gender on MC1, S1R and SV2A density. The age range of subjects included in this study was 22 - 78 for ^{18}F -BCPP-EF, 23 - 78 for ^{11}C -SA-4503 and 22 - 78 for ^{11}C -UCB-J. A summary of demographic information and injection parameters is provided in Table 7.1, whilst demographic information and injection parameters for individual subjects can be found in Tables 3.1 - 3.4. The reader is referred to Chapter 3 sections 3.1 - 3.2 for the scanning protocols and image processing pipelines used.

Table 7.1 MINDMAPS Healthy Ageing Cohort – Summary of Demographic Information, Injection Parameters and f_p

Ligand	Age (yrs)	Weight (kg)	Height (cm)	BMI (kg/m ²)	Injected Activity (MBq)	Injected Mass (μg)	f_p
^{18}F -BCPP-EF (n = 30 16M/14F)	51 ± 19	72.9 ± 14.4	171 ± 11	25.0 ± 4.2	89 ± 4	0.08 ± 0.04	0.080 ± 0.017
^{11}C -SA-4503 (n = 23 13M/10F)	56 ± 18	73.0 ± 15.4	171 ± 11	24.9 ± 4.4	255 ± 19	3.43 ± 1.74	0.064 ± 0.016
^{11}C -UCB-J (n = 24 14M/10F)	55 ± 18	74.4 ± 15.1	171 ± 11	25.3 ± 4.2	204 ± 59	2.52 ± 1.19	0.245 ± 0.037

Data are mean ± SD. M: Male, F: Females, BMI, Body-mass Index

7.3.1 Derivation of PET outcome measures

The decision of which outcome measures to assess for each tracer was based on the work presented in chapters 4, 5 and 6 where the appropriate parameters for quantifying ^{18}F -BCPP-EF, ^{11}C -SA-4503 and ^{11}C -UCB-J in the healthy brain were established.

30 ^{18}F -BCPP-EF scans were used to generate parametric V_T maps using MA1 (fixed BV, $t^* = 30$ min). V_T/f_p and DVR were calculated from the parametric V_T estimates. 23 ^{11}C -SA-4503 scans were analysed to obtain regional V_T and V_T/f_p estimates. Due to the low signal to noise ratio of the ^{11}C -SA-4503 derived parametric images, V_T and V_T/f_p were estimated from regional TACs using MA1 (fixed BV, $t^* = 30$ min). V_T , V_T/f_p and BP_{ND} (DVR -1) were used as outcome measures for 24 ^{11}C -UCB-J scans and were derived by applying a 1TC model on a voxel-wise basis. The term BP_{ND} is used throughout the rest of this chapter instead of DVR-1 despite the small amount of specific binding in the centrum semiovale region in order to be consistent with previous ^{11}C -UCB-J literature. The input function generation steps for ^{18}F -BCPP-EF, ^{11}C -SA-4503 and ^{11}C -UCB-J, have been detailed in chapters 4, 5 and 6, respectively. The ROIs included in the analysis were the centrum semiovale, brainstem, substantia nigra thalamus, globus pallidus, ventral striatum, caudate, putamen, frontal lobe, hippocampus, amygdala, insular cortex, temporal lobe, parietal lobe and cerebellum. These ROIs were chosen to represent major brain areas and were defined as described in Chapter 3, Section 3.3.

7.3.2 Evaluation of age and gender effects

Age effects were evaluated by performing regional Pearson's correlations between age and PET outcome measures as well as between age and regional volumes (Vol_{roi}) that have been normalised to whole brain volumes as

$$\%Vol_{roi} = 100 \times \frac{Vol_{roi}}{Vol_{brain}} \quad \text{Equation 7.1}$$

where Vol_{roi} is the grey matter volume for a given ROI and Vol_{brain} is the whole brain volume. The age vs. volume and age vs. PET outcome measure data were fitted with a linear regression as there was no evidence that a higher dimensional curve was required to describe the data.

Percent rates of change per year in outcome parameters were then calculated as,

$$\% \text{ change/year} = 100 \times \left(\frac{\Delta \text{Parameter}}{\Delta \text{Age}} \right) / \text{Parameter}_{\text{mean}} \quad \text{Equation 7.2}$$

Pearson's correlation coefficient, r , and the associated p values were used to assess the strength of the relationship between age and outcome measures. The statistical significance of Pearson's correlations were tested against a Bonferroni-adjusted p value of 0.003 (0.05/16 regions).

The effect of gender was assessed for V_T estimates derived for each ligand in an exploratory analysis by separating the males and females into two groups and running unpaired t -tests. No corrections for multiple comparisons were applied.

7.3.3 Correcting for partial volume effects

In order to separate the effects of age on MC-I, S1R and SV2A density from the effects of age related volume loss, a partial volume correction (PVC) algorithm (Müller-Gärtner, Links, Prince, et al., 1992) was applied to all three datasets. For ^{18}F -BCPP-EF and ^{11}C -UCB-J, the correction was applied to parametric V_T images, while for ^{11}C -SA-4503, PVC was applied to the dynamic images on a frame by frame basis. The Müller-Gärtner PVC method relies on grey matter (GM) and white matter (WM) segmentations of an MRI image. As demonstrated in the simplified depiction in Figure 7.1, a binary WM map is scaled to an estimate of the true mean WM value, is convolved with the scanner's point-spread function (PSF) and subtracted from the measured PET data (original PET image). The resulting image is then divided by the GM map convolved with the PSF to correct for spill-out effects from grey matter. PVC was not

applied to the substantia nigra as the Müller-Gärtner method has yet to be validated for such small regions.

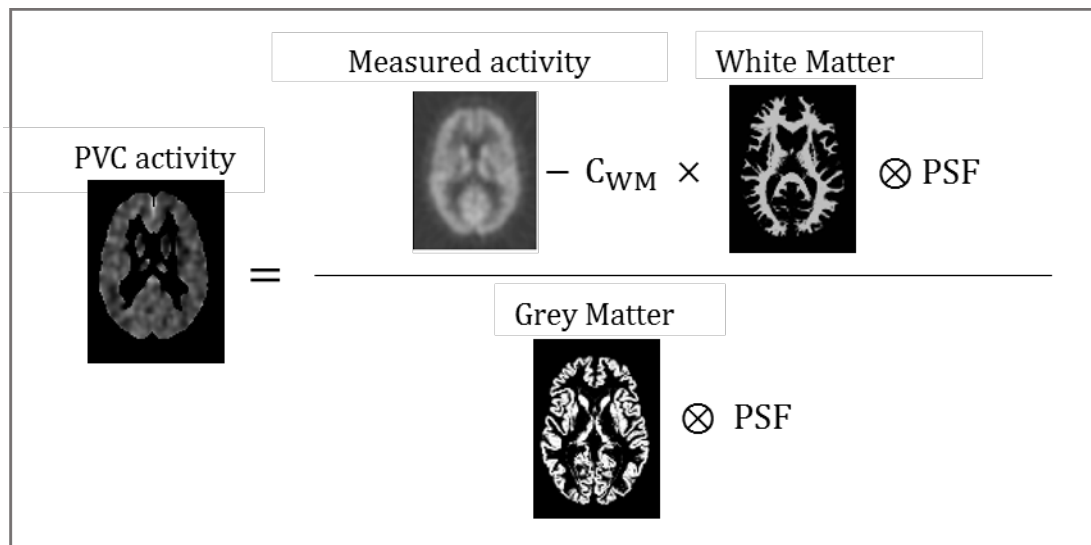


Figure 7.1 Application of the Muller-Gartner PVC method to PET data. A binary WM mask was convolved with the scanner's PSF and scaled to the true white matter activity. This was then subtracted from the activity measured by the PET scanner and divided by a GM map which had been convolved with the scanner's PSF.

7.4 Results

The mean and coefficient of variation (COV) of PET outcome measures derived for the full cohort of MIND-MAPS healthy volunteer subjects for all three ligands and the regional volume data that were used in the linear regressions with age are provided in Table 7.2. The results of the correlation analyses between age and PET outcome measures is limited to V_T , V_T/f_p and DVR for ^{18}F -BCPP-EF, V_T , V_T/f_p for ^{11}C -SA-4503 and V_T , V_T/f_p and BP_{ND} for ^{11}C -UCB-J. Gender effects are discussed for V_T only.

Table 7.2. Summary of regional volumetric and PET outcome measures

Radioligand	Outcome measures	ROI															
		CS	BS	SN	THA	GP	VSTR	CAU	PUT	FL	INS	HIP	AMY	PL	TL	CER	
¹⁸ F-BCPP-EF	V_T	11.5	16.5	19.8	21.8	27.0	31.0	22.3	33.7	23.5	25.3	20.3	21.6	24.5	23.3	28.1	
	(mL.cm ⁻³)	17%	17%	16%	18%	18%	18%	22%	17%	18%	16%	17%	17%	19%	16%	18%	
	V_T/f_p	140	210	252	278	345	395	284	431	300	323	259	275	311	298	358	
	(mL.cm ⁻³)	18%	18%	16%	19%	19%	18%	24%	19%	19%	17%	19%	18%	19%	18%	18%	
DVR	NAN		1.5	1.8	1.9	2.4	2.7	1.9	2.8	1.9	2.2	1.8	1.9	2.0	2.0	2.3	
			10%	9%	11%	9%	19%	18%	9%	7%	8%	9%	8%	7%	8%	8%	
¹¹ C-SA-4503	V_T	29.7	37.8	38.0	33.7	38.7	39.2	28.0	44.7	40.6	46.1	40.7	45.6	38.4	41.8	48.0	
		36%	18%	26%	19%	19%	18%	21%	20%	20%	16%	31%	17%	16%	14%	20%	
	V_T/f_p	486	623	619	552	633	642	459	732	666	756	667	750	630	688	792	
		39%	27%	30%	27%	25%	25%	27%	26%	27%	25%	35%	26%	25%	24%	29%	
¹¹ C-UCB-J	V_T	5.7	7.4	8.8	11.5	15.3	21.7	14.5	22.4	17.9	21.0	14.3	17.4	18.0	19.3	16.2	
	(mL.cm ⁻³)	11%	12%	12%	15%	11%	11%	19%	10%	12%	11%	12%	10%	13%	11%	10%	
	V_T/f_p	24	31	36	48	63	90	60	93	74	87	59	72	74	80	67	
	(mL.cm ⁻³)	17%	15%	14%	17%	15%	16%	20%	15%	15%	14%	15%	14%	15%	15%	15%	
	DVR	NAN		1.55	2.02	2.69	3.81	2.53	3.94	3.57	3.69	2.52	3.07	3.16	3.39	2.84	1.30
				9%	12%	10%	8%	15%	8%	9%	9%	10%	9%	10%	8%	8%	7%
BP _{ND}	NAN		0.55	1.02	1.69	2.81	1.53	2.94	2.57	2.69	1.52	2.07	2.16	2.39	1.84	0.30	
			24%	24%	15%	11%	25%	11%	12%	12%	17%	13%	15%	12%	12%	30%	
Volume (%)		0.12	2.31	0.06	1.37	0.23	0.14	0.33	0.45	5.73	0.87	0.52	0.25	6.60	8.28	6.67	
		10%	5%	7%	5%	6%	9%	13%	11%	10%	10%	8%	8%	10%	8%	7%	

Data are mean and COV. $n_{BCPP-EF} = 30$, $n_{SA-4503} = 23$, $n_{UCB-J} = 24$

7.4.1 Age effects on volume

Regional volumes decreased significantly with age in all regions investigated except for in the brainstem and thalamus. The greatest loss of volume was observed in the caudate, insular cortex, frontal cortex, and parietal lobe with yearly reductions of 0.45%, 0.41%, 0.40% and 0.40%, respectively (correlation results provided in Table 7.3). There were no gender differences in regional volumes in any of the regions examined.

Table 7.3. Age effect on regional volumes (Vol_{ROI})

ROI	r	p	Δ/yr
CS	-0.22	0.23	-0.12
BS	0.38	0.04	0.09
SN	-0.20	0.29	-0.07
THA	0.20	0.29	0.05
GP	-0.25	0.19	-0.08
VSTR	-0.67	0.0001*	-0.31
CAU	-0.69	< 0.0001*	-0.45
PUT	-0.62	< 0.0001*	-0.34
FL	-0.76	< 0.0001*	-0.40
INS	-0.76	< 0.0001*	-0.41
HIP	-0.56	0.001	-0.24
AMY	-0.57	0.001	-0.24
PL	-0.84	< 0.0001*	-0.41
TL	-0.84	< 0.0001*	-0.34
CER	-0.58	0.001	-0.22

*Statistically significant following Bonferroni correction ($p < 0.003$)

Table 7.4. Age effect on ^{18}F -BCPP-EF PET outcome measures

ROIS	V_T			V_T/f_p			DVR		
	r	p	Δ/yr	r	p	Δ/yr	r	p	Δ/yr
CS	0.20	0.30	0.17	0.46	0.01	0.43	NAN	NAN	NAN
BS	0.04	0.83	0.04	0.22	0.25	0.20	-0.30	0.11	-0.15
SN	0.07	0.71	0.06	0.34	0.06	0.27	-0.27	0.15	-0.13
THA	-0.12	0.53	-0.11	0.04	0.83	0.04	-0.55	0.001	-0.30
GP	0.23	0.23	0.21	0.38	0.04	0.37	0.02	0.93	0.01
VSTR	-0.06	0.75	-0.06	0.16	0.41	0.15	-0.49	0.01	-0.25
CAU	-0.39	0.03	-0.46	-0.21	0.27	-0.27	-0.68	0.0003*	-0.65
PUT	0.11	0.55	0.11	0.29	0.12	0.28	-0.21	0.26	-0.10
FL	0.06	0.75	0.06	0.25	0.19	0.24	-0.36	0.05	-0.13
INS	-0.08	0.67	-0.07	0.15	0.42	0.13	-0.59	0.001	-0.26
HIP	-0.01	0.95	-0.01	0.18	0.33	0.17	-0.42	0.02	-0.21
AMY	0.08	0.68	0.07	0.29	0.12	0.27	-0.30	0.11	-0.12
PL	0.06	0.74	0.05	0.27	0.14	0.25	-0.36	0.05	-0.14
TL	0.04	0.83	0.04	0.23	0.23	0.22	-0.37	0.04	-0.15
CER	0.19	0.32	0.17	0.42	0.02	0.38	-0.06	0.77	-0.02

*Statistically significant following Bonferroni correction ($p < 0.003$)

7.4.2 Age and gender effects on ^{18}F -BCPP-EF

The results of the correlation analysis between age and ^{18}F -BCPP-EF PET measures from 30 subjects (16 M, 14 F) are summarised in Table 7.4. Regional V_T was mostly unchanged with age. The only noteworthy change with age was observed in the caudate where there was a 0.46% yearly reduction in V_T though the correlation did not survive following Bonferroni correction (Figure 7.2 A, $r = -0.39$, $p = 0.03$, shown in black). PVC further dampened the

negative trend between age and V_T in the caudate (Figure 7.2 A , $r = -0.16$, $p > 0.05$ shown in red).

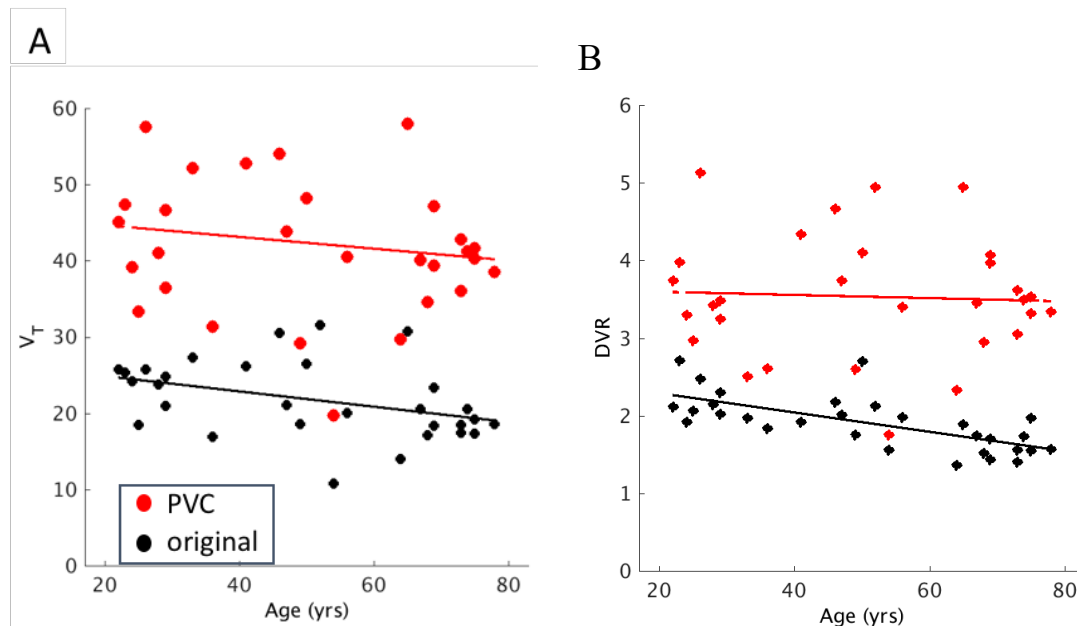


Figure 7.2 Correlation between ^{18}F -BCPP-EF outcome measures and age. **A** V_T and age were negatively correlated in the caudate, **B** DVR and age were negatively correlated in the caudate. Neither of these correlations remained statistically significant following PVC.

There were no significant correlations between age and V_T/f_p , while DVR was reduced in a number of grey matter regions including in the thalamus, ventral striatum, caudate, insular cortex and hippocampus. The only statistically significant reduction in DVR was observed in the caudate (Figure 7.2B, $r = -0.68$, $p < 0.003$) at 0.65% per year; however, this effect was eliminated following the application of PVC (shown in red in Figure 7.2B).

The results of the comparison of V_T estimates in males ($n = 16$) with that in females ($n = 14$) are summarised in Table 7.5 Overall, ^{18}F -BCPP-EF V_T estimates were on average $7.9\% \pm 1.9\%$ higher in females compared to males though none of the differences reached statistical significance. The largest difference between genders was found in the ventral striatum ($\Delta (\%) = 12$, $p = 0.08$).

Table 7.5 Gender differences in ^{18}F -BCPP-EF PET outcome measures

Gender		Age (yrs)	ROI V_T (ml.cm $^{-3}$)														
			CS	BS	SN	THA	GP	VSTR	CAU	PUT	FL	INS	HIP	AMY	PL	TL	CER
MALE (n=16)	Mean	50	11.3	15.9	19.5	21.1	25.8	29.3	21.3	32.3	22.8	24.6	19.5	20.6	23.5	22.4	27.0
	COV	37%	13%	13%	10%	14%	13%	13%	22%	12%	13%	11%	12%	12%	12%	11%	12%
FEMALE (n=14)	Mean	51	11.7	17.2	20.2	22.6	28.4	32.9	23.4	35.3	24.4	26.2	21.3	22.6	25.5	24.4	29.4
	COV	41%	21%	20%	20%	22%	21%	21%	23%	21%	22%	20%	20%	20%	24%	20%	21%
	Δ (%)	2	4	7	4	7	10	12	9	9	7	7	9	9	8	8	8
	p value	0.90	0.59	0.25	0.54	0.29	0.15	0.08	0.27	0.17	0.30	0.27	0.15	0.14	0.25	0.16	0.21

Male age range: 23 – 75; Female age range: 22 - 78

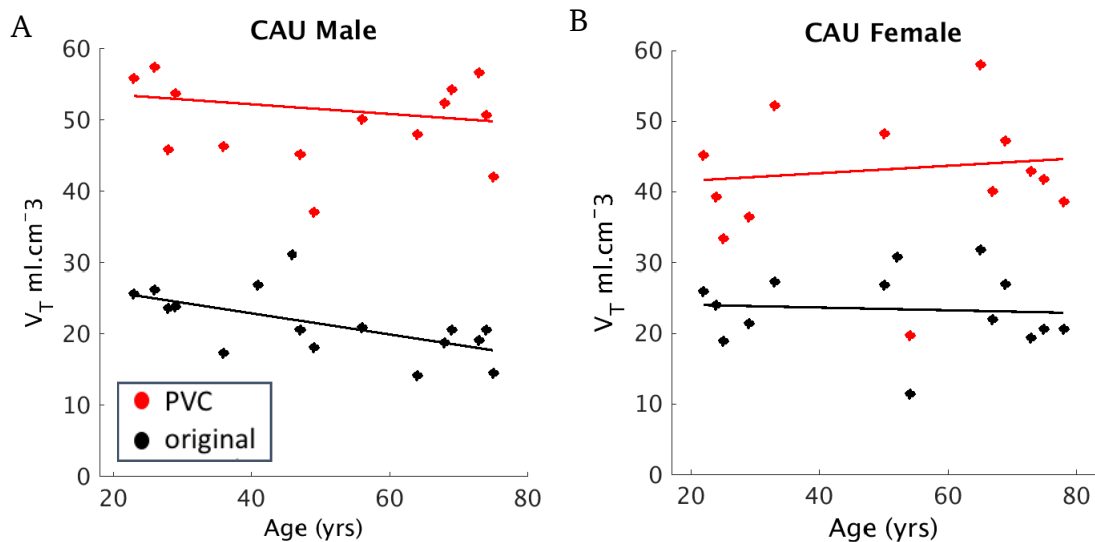


Figure 7.3 Gender differences in age effect on ^{18}F -BCPP-EF V_T in the caudate. **A** V_T and age were negatively correlated in the male caudate. **B** There was no correlation between V_T and age in the female caudate.

Given the overall decreasing trend seen in caudate for all three outcome measures with age, the effect of age in this region was also investigated separately in males and females. As shown in Figure 7.3, the effect of age on caudate V_T was more marked in males (Figure 7.3 A) than in females (Figure 7.3 B), with the male with a yearly reduction rate of 0.7 % per year (PVC uncorrected, $p < 0.05$).

7.4.3 Age and gender effects on ^{11}C -SA-4503

^{11}C -SA-4503 V_T was unchanged with age in the brain (Table 7.6), with the exception of the substantia nigra where there was a yearly reduction rate of 0.69 % ($r = -0.47$, $p = 0.03$) (Figure 7.4). Following normalisation of V_T by f_p , the effect of age in the nigra was suppressed to 0.33% per year ($r = -0.20$, $p = 0.36$). None of the correlations were statistically significant following correction for multiple comparisons.

Table 7.6. Age effects on ^{11}C -SA-4503 PET outcome measures

ROI	V_T			V_T/f_p		
	r	p	Δ/yr	r	p	Δ/yr
CS	0.21	0.35	0.42	0.32	0.15	0.69
BS	-0.28	0.21	-0.29	-0.01	0.96	-0.02
SN	-0.47	0.03	-0.69	-0.24	0.27	-0.41
THA	-0.10	0.67	-0.10	0.10	0.66	0.15
GP	0.13	0.58	0.13	0.27	0.23	0.37
VSTR	-0.09	0.69	-0.09	0.11	0.63	0.15
CAU	-0.20	0.37	-0.24	0.03	0.89	0.05
PUT	-0.04	0.87	-0.04	0.15	0.51	0.21
FL	-0.19	0.40	-0.21	0.04	0.85	0.06
INS	-0.26	0.25	-0.22	0.04	0.87	0.05
HIP	0.17	0.45	0.29	0.28	0.21	0.55
AMY	-0.36	0.10	-0.33	-0.01	0.97	-0.01
PL	-0.15	0.50	-0.14	0.09	0.70	0.12
TL	-0.29	0.20	-0.22	0.04	0.87	0.05
CER	-0.26	0.24	-0.29	-0.01	0.95	-0.02

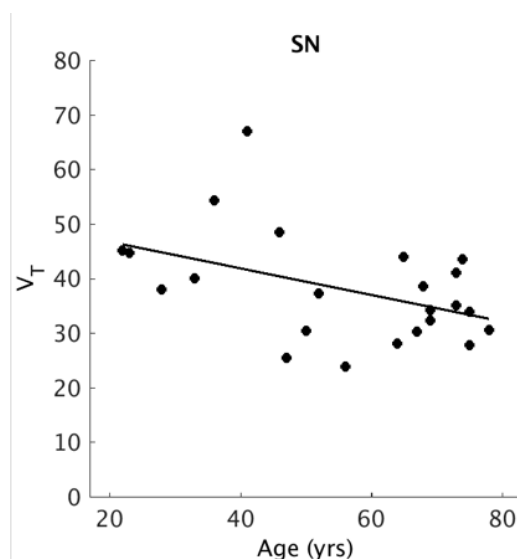


Figure 7.4 Correlation between ^{11}C -SA-4503 V_T and age

The effect of gender on V_T was varied across regions with the largest difference observed in the substantia nigra where the mean V_T in females was 6.2% lower in females compared to males. None of the differences reached statistical significance. Group statistics are presented in Table 7.7.

Table 7.7 Gender differences in ^{11}C -SA-4503 PET outcome measures

Gender	Age (yrs)	ROI V_T (ml.cm ⁻³)															
		CS	BS	SN	THA	GP	VSTR	CAU	PUT	FL	INS	HIP	AMY	PL	TL	CER	
MALE (n=12)	Mean	51.7	29.4	37.3	39.0	33.2	39.2	39.1	28.5	45.1	40.0	46.2	38.4	44.9	37.6	41.8	47.9
	COV	35%	36%	21%	32%	24%	21%	19%	26%	23%	25%	19%	16%	19%	19%	16%	22%
FEMALE (n=11)	Mean	49.9	30.0	38.4	36.7	34.2	38.0	39.3	27.3	44.2	41.4	45.9	38.2*	46.6	39.5	41.9	48.2
	COV	40%	37%	14%	15%	12%	17%	16%	15%	16%	14%	11%	11%	16%	12%	12%	17%
	Δ (%)	-3.5	1.8	2.9	-6.2	3.0	-3.2	0.8	-4.4	-1.2	3.5	-0.7	-0.7	3.7	4.8	0.2	0.6
	p value	0.80	0.91	0.72	0.59	0.72	0.71	0.95	0.65	0.83	0.69	0.91	0.91	0.62	0.49	0.98	0.94

Male age range: 23 – 75; Female age range: 22 – 78 *subject 115 hippocampus V_T outlier - excluded.

7.4.4 Age and gender effects on ^{11}C -UCB-J

V_T was reduced in all grey matter regions and in the CS, with the highest reductions seen in caudate and thalamus, followed by the brainstem, substantia nigra, frontal lobe and parietal lobe (summarised in Table 7.8). The reductions in V_T were statistically significant in the nigra, thalamus, caudate and insular cortex ($p < 0.003$). The only region to survive PVC was the

caudate showing 0.37% yearly reduction ($r = -0.43$, $p = 0.04$). Thalamic V_T was still reduced with age, but the correlation was no longer statistically significant following PVC.

Table 7.8. Age effects on ^{11}C -UCB-J PET outcome measures

ROIS	V_T			V_T/f_p			BP_{ND}		
	r	p	Δ/yr	r	p	Δ/yr	r	p	Δ/yr
CS	-0.40	0.01	-0.28	0.05	0.81	0.05	NAN	NAN	NAN
BS	-0.65	0.001	-0.49	-0.21	0.33	-0.17	-0.65	0.0006*	-1.2
SN	-0.70	0.0001*	-0.44	-0.17	0.44	-0.13	-0.35	0.09	-0.46
THA	-0.72	0.0001*	-0.57	-0.35	0.09	-0.33	-0.72	0.0001*	-1.02
GP	-0.16	0.46	-0.09	0.21	0.32	0.17	-0.16	0.46	-0.15
VSTR	-0.58	0.003	-0.38	-0.09	0.69	-0.08	-0.58	0.003	-0.50
CAU	-0.71	0.0001*	-0.84	-0.45	0.03	-0.54	-0.71	0.0001*	-1.65
PUT	-0.30	0.15	-0.17	0.16	0.45	0.13	-0.30	0.15	-0.24
FL	-0.50	0.01	-0.32	-0.02	0.92	-0.02	-0.50	0.01	-0.49
INS	-0.64	0.0007*	-0.39	-0.12	0.58	-0.09	-0.64	0.0007*	-0.52
HIP	-0.50	0.01	-0.34	-0.05	0.82	-0.04	-0.50	0.01	-0.53
AMY	-0.47	0.02	-0.26	0.06	0.80	0.04	-0.47	0.02	-0.43
PL	-0.58	0.003	-0.32	-0.03	0.89	-0.02	-0.58	0.003*	-0.44
TL	-0.44	0.03	-0.29	0.01	0.99	0.201	-0.44	0.03	-0.46
CER	-0.52	0.01	-0.29	0.01	0.97	0.01	-0.52	0.01	-0.48

*Statistically significant following Bonferroni correction ($p < 0.003$)

The reductions with age in the thalamus, caudate, brainstem and insular cortex were statistically significant for non-PVC corrected BP_{ND} (DVR-1) ($p < 0.003$). Following the application of PVC, only caudate BP_{ND} remained reduced with age ($p < 0.05$) but did not survive Bonferroni correction. Figure 7.5 includes the correlation plots for V_T and BP_{ND} in the brainstem, thalamus and caudate with and without PVC applied.

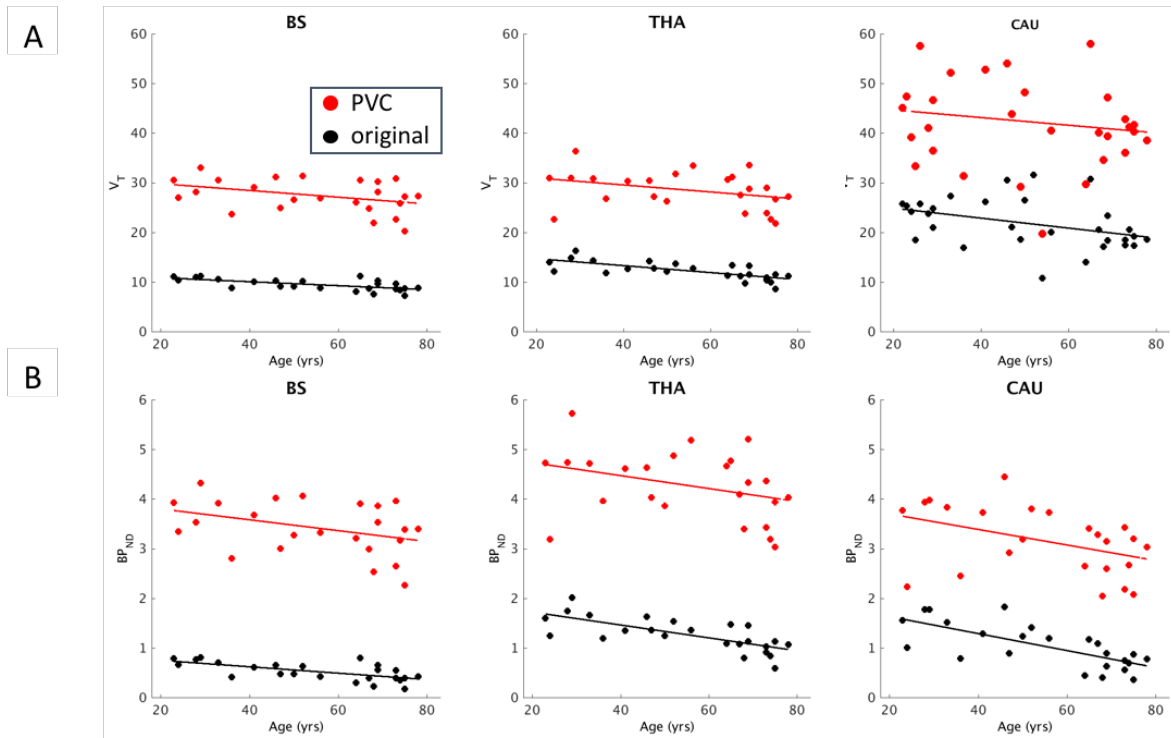


Figure 7.5 Correlation of ^{11}C -UCB-J V_T and BP_{ND} with age. **A** V_T and **B** BP_{ND} were negatively correlated with age in the brainstem, thalamus and caudate.

Table 7.9 Gender differences in ^{11}C -UCB-J outcome PET outcome measures

Gender	Age (yrs)	ROI V_T (ml.cm ⁻³)															
		CS	BS	SN	THA	GP	VSTR	CAU	PUT	FL	INS	HIP	AMY	PL	TL	CER	
MALE (n=12)	Mean	50	5.6	7.4	8.9	11.5	15.1	21.4	14.3	22.2	17.9	21.2	14.1	17.2	17.8	19.3	16.2
	COV	37%	10%	14%	13%	18%	11%	14%	24%	11%	15%	13%	14%	12%	15%	13%	12%
FEMALE (n=11)	Mean	53	5.9	7.4	8.8	11.6	15.6	22.2	14.7	22.7	17.8	20.7	14.6	17.8	18.3	19.2	16.2
	COV	37%	12%	10%	10%	11%	10%	6%	9%	8%	8%	7%	8%	8%	10%	7%	8%
	Δ (%)	6	5.0	0.3	-0.8	0.4	3.5	3.3	3.2	2.0	-0.6	-2.1	3.3	3.2	3.0	-0.7	-0.3
	p value	0.66	0.26	0.95	0.87	0.95	0.44	0.48	0.68	0.63	0.91	0.65	0.51	0.45	0.58	0.87	0.94

Male age range: 23 – 75; Female age range: 22 – 78 n = 24

As summarised in Table 7.9, there was no obvious effect of gender on ^{11}C -UCB-J V_T estimates.

7.5 Discussion

The work presented here assessed the effect of healthy ageing and gender on PET outcome measures derived from ^{18}F -BCPP-EF, ^{11}C -SA-4503 and ^{11}C -UCB-J scans in a healthy volunteer cohort aged between 22 and 78.

7.5.1 Choice of outcome parameters

A number of different outcome measures were assessed in relation to age, each of which have their own assumptions built in. V_T assumes the fraction of free tracer in plasma (f_p) that is available to enter the brain is constant across subjects. V_T/f_p corrects for this, however, introduces further variability due to measurement variability associated with f_p . In the absence of a true reference region, as is the case with both ^{11}C -UCB-J and ^{81}F -BCPP-EF, the use of DVR instead of V_T eliminates the variability associated with arterial input functions, but also introduces bias if there is a specific binding component present in the pseudo-reference region.

Using different outcome measures allows us to test the various assumptions inherent in them – so a result that is consistent across all methods is likely to be most robust.

7.5.2 Age Effects

Regional ^{18}F -BCPP-EF V_T estimates were mostly unaffected by age except for in the caudate where there was a decrease of $\sim 0.46\%$ per year with age ($p = 0.03$); however, this reduction was minimal and not significant following the application of PVC. Though reductions in ^{18}F -BCPP-EF V_T have been shown in the non-human primate cerebellum, frontal and temporal cortex, striatum, hippocampus and most significantly occipital and parietal lobe (Hideo Tsukada, 2014), the only reduction seen in human V_T was in the caudate, which could be explained by the lack of PVC application to the NHP data, as well as by interspecies differences in age-related changes to MC-I function. V_T/f_p was unchanged with age in all regions including the caudate, likely as a result of a 0.24% reduction per year in f_p . Age had an effect on ^{18}F -BCPP-EF derived DVR values, with reductions observed in a number of grey matter regions ($p < 0.05$, non-PVC corrected). The only statistically significant reduction following the application of Bonferroni correction was observed for DVR in the caudate, however this did not hold true for the PVC-corrected data. The loss of statistical significance in the relationship

between age and both V_T and DVR in the caudate could be the result of increased variability of in V_T and DVR estimates following PVC. Given that the caudate has been shown to be particularly vulnerable to age related atrophy (Gunning-Dixon, Head, McQuain, et al., 1998; Raz, Rodrigue, Kennedy, et al., 2003), it is not clear whether the reductions observed in DVR and V_T was the result of age or volume loss. Nevertheless, the significant reduction seen in non-PVC corrected ^{18}F -BCPP-EF DVR in the caudate with increasing age is supportive of age-related decrease in MC-I in this region.

Despite preclinical reports of age-related increases in ^{11}C -SA-4503 signal, no such increases were observed in this human cohort in any of the regions investigated. Contrary to the initial hypothesis, decreases in V_T with age were observed in one brain region, with other regions showing little or no change. V_T/f_p was unchanged in all regions, which was not due to any age-related change in f_p . The only significant finding for this ligand was the 0.64% yearly reduction rate in V_T in the substantia nigra; however this correlation did not survive correction for multiple comparisons. Although PVC was not applied to the SN, the lack of substantial volumetric loss in this region gives confidence that the reduction in this region may be a real effect. This result is in agreement with the age related reductions in ^{11}C -SA-4503 signal reported in the aged rodent midbrain compared to young animals (Ramakrishnan 2016). The same study also reported significant reductions in the pons, medulla thalamus and hypothalamus in aged rodents. Although the pons, medulla and hypothalamus were not included in the original set of ROIs, post-hoc analysis of age of effects in these regions showed yearly reductions with age of 19% ($r = -0.19$, $p > 0.1$), 0.59 % ($r = -0.41$, $p = 0.05$) and 0.49 % ($r = -0.37$, $p = 0.08$), respectively. However, the reductions with age in these three regions were not preserved following the application of PVC.

Reductions in ^{11}C -SA-4503 signal have been found in the brains of PD patients (Mishina, Ohyama, Ishii, et al., 2008). The reduced density and activity of S1Rs has been associated with

increased sensitivity to apoptotic signalling and reduced viability of neurons (Hedskog, Pinho, Filadi, et al., 2013). S1R stimulation by agonists has been shown to recover dopaminergic fibre density and causes overall neuro-restoration in the nigrostriatal pathway in an animal model of PD (Francardo, Bez, Wieloch, et al., 2014). Considering the role of S1R in promoting cell survival and neuroprotection, age induced decreases in nigral S1R could potentially increase the vulnerability of this region to age-related neurodegenerative diseases where the nigra is particularly affected.

Consistent with recent reports of age effects on ^{11}C -UCB-J binding, we observed age-related reductions in ^{11}C -UCB-J V_T and BP_{ND} in nearly all grey matter regions tested, with significant reductions in the caudate and thalamus ($p < 0.003$). These negative correlations with age did not remain statistically significant following the application of PVC which substantially weakened the effect of age induced reductions in ^{11}C -UCB-J signal in all regions. Interestingly, the thalamus and brainstem were among the few regions for which there was no significant loss of volume with age; therefore the lack of reduced age effect in the partial volume corrected results for these regions could be explained by the increased noise in the post-PVC data that is an inherent consequence of PVC. Our results in the caudate and thalamus agreed with the recent preliminary findings by Toyonaga and colleagues (Toyonaga, Lu, Naganawa, et al., 2019); however our results did not survive PVC. One reason for this discrepancy could be the different PVC method employed, as the choice of PVC method has also been shown to lead to different conclusions in PET studies of ageing in the brain due to different sensitivities to scanner PSF, brain mask size, PET reconstruction algorithms and thresholding parameters (Greve, Salat, Bowen, et al., 2016). Although the functional significance of the largest reduction in SV2A being observed in the caudate is not clear, the combined reductions in the caudate and thalamus is suggestive of these regions being particularly vulnerable to synaptic loss.

Interestingly, brain regions where moderate negative linear correlations ($-0.36 < r < -0.68$, $p < 0.05$) were observed between age and non-PVC corrected ^{18}F -BCPP-EF DVR also showed moderate negative linear correlations between age and non-PVC corrected ^{11}C -UCB-J BP_{ND} . Similarly, the regions unaffected by age including the putamen, pallidum, cerebellum and nigra were conserved across these two ligands. The fact that the two ligands showed a similar pattern of regional loss with age was not unexpected. The pre-synaptic terminals are known to be very rich in mitochondria, hence a loss of these terminals can be expected to result in a loss of MC1 as well. Conversely, a disruption in energy production due to reduced MC-I would cause reduced synaptic transmission and synaptic loss, manifesting as decreased ^{11}C -UCB-J signal.

Finally, it is important to acknowledge some of the caveats associated with this study. Firstly, the upper end of the age range of subjects included was 78, which may be considered too low given that approximately 32% of individuals aged 85 or older suffer from age-related dementia, (L.E., J., P.A., et al., 2013). A second caveat to address is that given the present subject numbers and associated within group variability, linear regression was identified as the most viable model to assess age-related changes, although a more complex relationship is biologically more plausible. Future studies with greater subject numbers may be able to explore this further. Lastly, the method used to correct for multiple comparisons was the Bonferroni correction, which is acknowledged as being conservative, especially when hypotheses are highly correlated (S. Y. Chen, Feng, & Yi, 2017). The Bonferroni corrected results should therefore be interpreted with caution. Future analyses of the effect of age on these ligands could use a more lenient correction method such as a false discovery rate.

7.5.3 Gender Effects

There were no statistically significant gender differences observed for regional V_T for any of the ligands, ^{18}F -BCPP-EF derived V_T estimates were globally higher in females compared to males, with female estimates being nearly twice as variable across subjects. Ageing also affected V_T differentially between females and males in the caudate, with this particular cohort of females not showing any reduction in caudate V_T as opposed to the significant reduction seen in males. It is thought that females might be better equipped for dealing with oxidative stress under physiological conditions (Kander, Cui, & Liu, 2017). Female mice have been shown to be resistant to ROS induced inhibition of MC-I activity (Diwakar et al. 2007; Kenchappa et al. 2004), and show higher levels of antioxidant enzymes (Vina, Gambini, Lopez-Gruesso, et al., 2012). Additionally, oestrogen is thought to provide women with additional neuroprotection which increases their energetic capacity (Demarest & McCarthy, 2014). These findings combined could partially explain the suppression of age effects in female ^{18}F -BCPP-EF signal in caudate.

7.6 Conclusion

All three ligands analysed showed reductions in signal with age, although the extent and regional distribution of reductions differed depending on the radiotracer. ^{18}F -BCPP-EF signal was reduced with age in the caudate when assessed by V_T and DVR as an outcome measure, though this could be indicative of volumetric loss rather than reduced MC-I activity. Interestingly, the effect of age in the caudate was mostly driven by males, with females showing no changes with age. ^{18}F -BCPP-EF was more significantly and globally decreased with age when assessed using DVR as an outcome measure. It is important that all the age effects we observed for this ligand be interpreted with caution given loss of statistical significant correlations following the application of PVC. ^{11}C -SA-4503 signal was mostly unchanged in the regions

analysed, except for in the substantia nigra where there was a yearly reduction in V_T . However, the result in the nigra should be interpreted with caution due to the lack of suitable PVC method to apply to this region. Lastly, non-PVC corrected ^{11}C -UCB-J signal was most strikingly reduced in the caudate and thalamus, confirming recent reports of these regions being particularly susceptible to age-related synaptic loss.

There were no prominent gender differences in ^{11}C -SA-4503 or ^{11}C -UCB-J V_T , while ^{18}F -BCPP- EF signal was between 4% - 12% higher in females compared to males across all regions investigated. Although the differences were not statistically significant, these results may indicate increased vulnerability of males to MC-I loss and resultant dysfunction that is potentially exacerbated with age.

Altogether, the results presented here are indicative of loss of MC-I and SV2A in healthy ageing. The picture with S1R is less clear and its expression may well be stable over age in a healthy population. Further work is needed to uncover the exact nature and functional relevance of any changes mentioned above before MC-I, S1R and SV2A can be considered useful biomarkers of the ageing mitochondrial/ER/synaptic axis.

8 Conclusions, Limitations and Future Work

The identification of molecular targets that are altered early on in neurodegenerative diseases and the existence of PET tracers to accurately quantify these targets allows for the discovery of robust and sensitive outcome measures to be used as biomarkers that are critical to the development of disease modifying therapeutics and preventative strategies. The work in this thesis culminated in the characterisation of three PET tracers, ^{18}F -BCPP-EF, ^{11}C -SA-4503 and ^{11}C -UCB-J, in the healthy human brain, and in the establishment of the optimal kinetic modelling pipelines and outcome measures (summarised in Table 8.1) that will enable their evaluation as biomarkers across neurodegenerative diseases for potential early diagnosis, patient stratification and monitoring disease progression.

Table 8.1 Optimal blood and tissue kinetic modelling methods and outcome measures

Analysis Methods	^{18}F -BCPP-EF	^{11}C -SA-4503	^{11}C -UCB-J
<i>PPF</i> Model	Sigmoid	Exponential plus constant	Sigmoid
<i>POB</i> Model	Constant	Exponential approaches to constant	Constant
Tissue Kinetic Model	2TC (fixed BV) MA1 (fixed BV, t^* : 30 min)	MA1 (fixed BV, t^* : 30 min)	1TC (fixed BV)
Outcome Measure	V_T , V_T/f_p † DVR/DVR-1* SUVr-1*	V_T , V_T/f_p †	V_T , V_T/f_p † DVR/DVR-1* SUVr-1*
Scan Time	70 min	80 min	60 min

*Use of reference region based outcome measures requires caution for both ^{18}F -BCPP-EF and ^{11}C -UCB-J as centrum semiovale is not devoid of specific binding and cross-sectional differences in centrum semiovale anatomy and/or binding may occur.

† V_T/f_p is a suitable outcome measure provided there are cross-sectional differences in f_p .

-Blood volume (BV) fixed to 5%

The tracer kinetics of ^{18}F -BCPP-EF were characterised in the human brain for the first time in Chapter 4. It was concluded that ^{18}F -BCPP-EF can be characterised using V_T derived either from the MA1 or 2TC model applied regionally or MA1 applied on a voxel-wise basis. Future studies

using this ligand may reduce their scan time to 70 minutes and still reliably estimate V_T . Importantly, the successful derivation of V_{ND} from the blocking data in monkeys supports the use of the centrum semiovale as a pseudo reference region for this ligand, increasing confidence in the use of reference based outcome measure DVR-1 in cases where arterial blood sampling is not possible. Additionally, SUVr-1 derived from a 20 minute static acquisition at 70 minutes following injection may be used as a proxy for DVR-1 in situations where blood sampling is not possible and scan time is limited. Importantly, the work presented here is not sufficient to conclude that the centrum semiovale is a good enough reference region to obviate the need for arterial blood acquisition ^{18}F -BCPP-EF scan. Centrum semiovale derived outcome measures should therefore be used and interpreted with caution, particularly in cross-sectional studies where changes in white matter may arise due to disease. Similar caution is advised before using V_T/f_p as an outcome measure, as there may be cross sectional difference in f_p values.

The work presented in Chapter 5 showed that ^{11}C -SA-4503 can be quantified on region-wise or voxel-wise level using MA1 as a model. The quality of the parametric images generated was not ideal and post-smoothing as well as removal of a large number of noisy voxels may be necessary to derive meaningful V_T estimates. Despite the relatively slow kinetics, a reduced scan time of 80 minutes still allowed for the reliable estimation of V_T . ^{11}C -SA-4503 V_T was significantly variable across subjects, in part due to the large variability in metabolite profiles across subjects. A drawback of ^{11}C -SA-4503 appeared to be the reliability of metabolite measurements due to high background noise, as well variability in metabolite profile across subjects ranging from negligible metabolism to up to 60% metabolism. Given these mixed results it is hard to draw any solid general conclusion with regards to metabolite correction of ^{11}C -SA-4503; however, an arterial input function that has been corrected for metabolites with a weighting factor that accounts for measurement error reduced the variability in the results of this particular cohort. Although the lack of a potential reference region, difficulty in metabolite measurements and slow kinetics make this ligand less amenable for regular use in a clinical

setting as a future biomarker, I believe the work sufficiently characterised ^{11}C -SA-4503 kinetics in the healthy human brain and produced an analysis pipeline that can be applied across the MIND-MAPS consortium to explore potential changes in S1R with neurodegeneration.

The work presented in Chapter 6 on the characterisation of ^{11}C -UCB-J confirmed what has been shown in recent literature, namely that it possesses excellent imaging characteristics including high uptake and fast kinetics. The 1TC model was the optimal compartmental model to estimate V_T with time stability results raising the possibility of scan time to be reduced to 60 minutes. The results showed that SUV_T -1 obtained from a 20 minute static scan acquired at least 60 minutes post-injection can be reliably used as a non-invasive measure of binding in situations where arterial blood sampling is not possible and scan time needs to be shortened to accommodate patient comfort. Given the existence of human blocking data in the literature, the centrum semiovale derived outcome measure DVR -1 (BP_{ND}) can be used to quantify ^{11}C -UCB-J, provided there are no disease related cross sectional or longitudinal changes in the centrum semiovale. Altogether, this work added further confidence to the excellence of ^{11}C -UCB-J as a method for quantifying SV2A.

The application of the optimised analysis pipelines to the larger MIND-MAPS cohort in Chapter 7 allowed for the investigation of the three tracers as potential biomarkers of healthy ageing. Despite observations of reduced signal with age in all three tracers, following the application of a PVC algorithm to the data the only definitive result was a reduction of ^{11}C -UCB-J V_T and BP_{ND} with age in the caudate and thalamus, emphasising the impact PVC can have on studies of the effects age related changes in the brain. Another interesting preliminary finding was the gender difference in the relationship between age and ^{18}F -BCPP-EF V_T in the caudate. Given the known role of sex steroids in gender differences in mitochondrial function (Demarest & McCarthy, 2014; Gaignard, Savouroux, Liere, et al., 2015), future work should compare ^{18}F -

BCPP-EF in both pre- and postmenopausal women with men of the same ages to draw any reliable conclusions.

These results summarised above provide some initial evidence for the effects of age on MC-I and SV2A. The data here can be used to generate hypotheses to be tested in future fully powered studies. In particular, it would be important to investigate whether a combination of ligands can provide more robust markers of clinical relevance than single measures. Future longitudinal studies that investigate changes in PET signal combined with clinical measures such as MMSE scores will be necessary to elucidate the biomarker potential of these tracers in normal and pathological aging. ^{18}F -BCPP-EF lacks a valid reference region combined with the unfeasibility of conducting a full blockade of the target due to the toxicity of compounds targeting the ubiquinone binding site on MC-I, presents certain challenges for widespread use of this ligand. Although the simplified pseudo-reference region derived measure SUVr-1 explored holds promise as a practical marker of target density, more work is will be necessary to evaluate its appropriateness in various disease cohorts. The structural and neurochemical integrity of the centrum semiovale in various disease conditions, as well any changes in peripheral metabolism of ^{18}F -BCPP-EF have to be elucidated. Another point that needs investigation, is whether change in ^{18}F -BCPP-EF signal correlates to loss of MC-I density or alterations in MC-I function. One way to address this issue would be for future studies to combine ^{18}F -BCPP-EF signal quantification with *in vivo* measurements of MC-I function such measurements of respiration and activity such as MC-I and ATP levels in peripheral bloods cells and quantification of brain energy metabolites using ^1H -magnetic resonance spectroscopy (MRS) as recently implemented by Silaidos and colleagues (Silaidos, Pilatus, Grewal, et al., 2018).

.

^{11}C -UCB-J derived PET measures hold promise as useful biomarkers that may be sensitive to age-related changes in SV2A density. Recent evidence of altered BP_{ND} in brain regions of interest in cognitively normal AD subjects underscores the potential of ^{11}C -UCB-J PET as a biomarker for clinical trials of disease-modifying therapies targeting the restoration of synaptic loss (M.-K. Chen, Mecca, Naganawa, et al., 2018). The work done in characterising the centrum semiovale as a useful reference region should help to obviate the need for arterial blood sampling, although this needs to be confirmed for all new disease cohorts. Evidence of the suitability of SUVr -1 derived from a short static image as a good proxy for ^{11}C -UCB-J BP_{ND} makes the tracer all the more likely to succeed in the world of clinical biomarker development, where the requirement for complex kinetic modelling to derive outcome measures is often a hindrance to a tracer's routine use in clinical trials. As is true for any PET tracer being investigated as a potential biomarker, any changes in ^{11}C -UCB-J signal that may arise in future cross sectional studies in disease cohorts will have to have a large enough effect size and outcome measures specific and sensitive enough to be able to accurately detect the presence of disease on an individual level, which has remained a challenging aspect of clinically useful PET biomarkers development (First, Drevets, Carter, et al., 2018).

Future cross-sectional studies using disease cohorts and the current healthy volunteer dataset may provide some clue as to whether ^{11}C -SA4503 has the potential to be a biomarker of disease related changes in S1R; however, given the caveats discussed earlier, these studies may benefit more from replacing the tracer with one possessing more favourable imaging properties. ^{11}C -HCC0929 has been proposed as an improved candidate, though this ligand has not yet been quantified in humans (Lan, Bai, Chen, et al., 2019).

Finally, this work did not make use of the multi-tracer nature of the dataset which would allow for the application of more complex multidimensional analyses of how MC-I, S1R and SV2A might interact in healthy individuals as well as in ageing. Future work should leverage this to

explore the integrity of the mitochondrial/ER/synaptic axis as a whole, potentially elucidating information that might not be apparent from studying the three targets in isolation.

Despite its limitations, this thesis produced an optimal set of analytical pipelines and outcome measures for ^{18}F -BCPP-EF, ^{11}C -SA-4503 and ^{11}C -UCB-J, that can now be implemented across the MIND-MAPS disease cohorts, ensuring consistency in methodology and enabling the robust study of potential changes to the mitochondrial/ER/synaptic axis across neurodegenerative diseases.

Bibliography

- Akaike, H. (1973). Information Theory and an Extension of the Maximum Likelihood Principle. *International Symposium on Information Theory, 1973*, 267–281.
<https://doi.org/10.1007/978-1-4612-1694-0>
- Ashburner, J. (2007). A fast diffeomorphic image registration algorithm. *NeuroImage*, 38(1), 95–113. <https://doi.org/10.1016/j.neuroimage.2007.07.007>
- Ashburner, J., & Friston, K. J. (2005). Unified segmentation. *NeuroImage*, 26(3), 839–851.
<https://doi.org/10.1016/j.neuroimage.2005.02.018>
- Bae, J. R., & Kim, S. H. (2017). Synapses in neurodegenerative diseases. *BMB Reports*, 50(5), 237–246. <https://doi.org/10.5483/bmbrep.2017.50.5.038>
- Bajjalieh, S. M., Frantz, G. D., Weimann, J. M., McConnell, S. K., & Scheller, R. H. (1994). Differential expression of synaptic vesicle protein 2 (SV2) isoforms. *The Journal of Neuroscience : The Official Journal of the Society for Neuroscience*, 14(9), 5223–5235.
<https://doi.org/10.1523/jneurosci.4781-09.2010>
- Banati, R. B. (2002). Visualising microglial activation in vivo. *Glia*, 40(2), 206–217.
<https://doi.org/10.1002/glia.10144>
- Beach, T. G. (2017). A Review of Biomarkers for Neurodegenerative Disease: Will They Swing Us Across the Valley? In *Neurology and Therapy*, 6(Suppl 1), 5–13.
<https://doi.org/10.1007/s40120-017-0072-x>
- Bertoldo, A., Rizzo, G., & Veronese, M. (2014). Deriving physiological information from PET images: From SUV to compartmental modelling. In *Clinical and Translational Imaging*, 2, 239–251. <https://doi.org/10.1007/s40336-014-0067-x>
- Boccardi, V., Comanducci, C., Baroni, M., & Mecocci, P. (2017). Of energy and entropy: The ineluctable impact of aging in old age dementia. In *International Journal of Molecular Science*, 18(12), 2672. <https://doi.org/10.3390/ijms18122672>
- Boellaard, R. (2009). Standards for PET image acquisition and quantitative data analysis. *Journal of Nuclear Medicine*, 50(Suppl 1), 11S–20S.
<https://doi.org/10.2967/jnumed.108.057182>
- Bond, S., Lopez-Lloreda, C., Gannon, P. J., Akay-Espinoza, C., & Jordan-Sciutto, K. L. (2020). The Integrated Stress Response and Phosphorylated Eukaryotic Initiation Factor 2 α in Neurodegeneration. *Journal of Neuropathology and Experimental Neurology*, 79(2), 123–143. <https://doi.org/10.1093/jnen/nlz129>

- Braak, H., & Braak, E. (1997). Frequency of stages of Alzheimer-related lesions in different age categories. *Neurobiology of Aging*, *18*(4), 351–357. [https://doi.org/10.1016/S0197-4580\(97\)00056-0](https://doi.org/10.1016/S0197-4580(97)00056-0)
- Brown, M. K., & Naidoo, N. (2012). The endoplasmic reticulum stress response in aging and age-related diseases. In *Frontiers in Physiology*, *3*, 263. <https://doi.org/10.3389/fphys.2012.00263>
- Canas, P. M., Duarte, J. M. N., Rodrigues, R. J., Köfalvi, A., & Cunha, R. A. (2009). Modification upon aging of the density of presynaptic modulation systems in the hippocampus. *Neurobiology of Aging*, *30*(11), 1877–1884. <https://doi.org/10.1016/j.neurobiolaging.2008.01.003>
- Cárdenas, C., Miller, R. A., Smith, I., Bui, T., Molgó, J., Müller, M., Vais, H., Cheung, K. H., Yang, J., Parker, I., Thompson, C. B., Birnbaum, M. J., Hallows, K. R., & Foskett, J. K. (2010). Essential Regulation of Cell Bioenergetics by Constitutive InsP3 Receptor Ca²⁺ Transfer to Mitochondria. *Cell*, *142*(2), 270–283. <https://doi.org/10.1016/j.cell.2010.06.007>
- Carson, R. E. (1993). PET parameter estimation using linear integration methods: Bias and variability considerations. *Annals of Nuclear Medicine*.
- Carson, R.E., Naganawa, M., Matuskey, D., Mecca, A., Pittman, B., Toyonaga, T., Lu, Y., Dias, M., Nabulsi, N., Finnema, S., Chen, M.-K., Malison, R., Esterlis, I., van Dyck, C., & Huang, Y. (2018). Age and sex effects on synaptic density in healthy humans as assessed with SV2A PET. *Journal of Nuclear Medicine*, *59*(Suppl 1), 541.
- Carson, Richard E. (2003). 6 Tracer Kinetic Modeling in PET *. *Positron Emission Tomography: Basic Science*, 147–179. <https://doi.org/10.1016/j.cpet.2007.08.003>
- Chalon, S., Vercouillie, J., Payoux, P., Deloye, J.-B., Malherbe, C., Le Jeune, F., Arlicot, N., Salabert, A.-S., Guilloteau, D., Emond, P., & Ribeiro, M.-J. (2019). The Story of the Dopamine Transporter PET Tracer LBT-999: From Conception to Clinical Use. In *Frontiers in Medicine*, *6*, 90. <https://www.frontiersin.org/article/10.3389/fmed.2019.00090>
- Chang, W.-P., & Sudhof, T. C. (2009). SV2 Renders Primed Synaptic Vesicles Competent for Ca²⁺-Induced Exocytosis. *Journal of Neuroscience*, *29*(4), 883–897. <https://doi.org/10.1523/JNEUROSCI.4521-08.2009>
- Chen, M-K., Mecca, A. P., Naganawa, M., Finnema, S. J., Toyonaga, T., Lin, S., Najafzadeh, S., Ropchan, J., Lu, Y., McDonald, J. W., Michalak, H. R., Nabulsi, N. B., Arnsten, A. F. T., Huang, Y., Carson, R. E., & van Dyck, C. H. (2018). Assessing Synaptic Density

- in Alzheimer Disease With Synaptic Vesicle Glycoprotein 2A Positron Emission Tomographic Imaging. *JAMA Neurology*, 75(10), 1215–1224.
<https://doi.org/10.1001/jamaneurol.2018.1836>
- Chen, S. Y., Feng, Z., & Yi, X. (2017). A general introduction to adjustment for multiple comparisons. *Journal of Thoracic Disease*, 9(6), 1725–1729.
<https://doi.org/10.21037/jtd.2017.05.34>
- Cheng, H. C., Ulane, C. M., & Burke, R. E. (2010). Clinical progression in Parkinson disease and the neurobiology of axons. In *Annals of Neurology* 67(6), 715–725.
<https://doi.org/10.1002/ana.21995>
- Coleman, P., Federoff, H., & Kurlan, R. (2004). A focus on the synapse for neuroprotection in Alzheimer disease and other dementias. *Neurology*, 63(7), 1155 LP – 1162.
<https://doi.org/10.1212/01.WNL.0000140626.48118.0A>
- Crone, C. (1963). The Permeability of Capillaries in Various Organs as Determined by Use of the ‘Indicator Diffusion’ Method. *Acta Physiologica Scandinavica*, 58, 292-305.
<https://doi.org/10.1111/j.1748-1716.1963.tb02652.x>
- Cunningham, V. J., Rabiner, E. A., Slifstein, M., Laruelle, M., & Gunn, R. N. (2010). Measuring drug occupancy in the absence of a reference region: The Lassen plot revisited. *Journal of Cerebral Blood Flow and Metabolism*, 30(1), 46–50.
<https://doi.org/10.1038/jcbfm.2009.190>
- Daneman, R., & Prat, A. (2015). The blood–brain barrier. *Cold Spring Harbor Perspectives in Biology*, 7(1), a020412. <https://doi.org/10.1101/cshperspect.a020412>
- Demarest, T. G., & McCarthy, M. M. (2014). Sex differences in mitochondrial (dys)function: Implications for neuroprotection. In *Journal of Bioenergetics and Biomembranes*, 47(1-2), 173–188. <https://doi.org/10.1007/s10863-014-9583-7>
- Devine, M. J., & Kittler, J. T. (2018). Mitochondria at the neuronal presynapse in health and disease. In *Nature Reviews Neuroscience*, 19(2), 63–80.
<https://doi.org/10.1038/nrn.2017.170>
- Diwakar, L., Kenchappa, R. S., Annepu, J., & Ravindranath, V. (2007). Downregulation of glutaredoxin but not glutathione loss leads to mitochondrial dysfunction in female mice CNS: Implications in excitotoxicity. *Neurochemistry International*, 51(1), 37–46.
<https://doi.org/10.1016/j.neuint.2007.03.008>
- Duyckaerts, C., Brion, J. P., Hauw, J. J., & Flament-Durand, J. (1987). Quantitative assessment of the density of neurofibrillary tangles and senile plaques in senile dementia of the Alzheimer type. Comparison of immunocytochemistry with a specific antibody

- and Bodian's protargol method. *Acta Neuropathologica*, 73(2), 167–170.
<https://doi.org/10.1007/BF00693783>
- Erlandsson, K., Buvat, I., Pretorius, P. H., Thomas, B. A., & Hutton, B. F. (2012). A review of partial volume correction techniques for emission tomography and their applications in neurology, cardiology and oncology. In *Physics in Medicine and Biology*, 57(21), R119–159. <https://doi.org/10.1088/0031-9155/57/21/R119>
- Farde, L., Eriksson, L., Blomquist, G., & Halldin, C. (1989). Kinetic Analysis of Central [11C]Raclopride Binding to D2-Dopamine Receptors Studied by PET—A Comparison to the Equilibrium Analysis. *Journal of Cerebral Blood Flow & Metabolism*, 9(5), 696–708. <https://doi.org/10.1038/jcbfm.1989.98>
- Finkel, T. (2012). Signal transduction by mitochondrial oxidants. In *Journal of Biological Chemistry*, 287(7), 4434–4440. <https://doi.org/10.1074/jbc.R111.271999>
- Finnema, S. J., Nabulsi, N. B., Eid, T., Detyniecki, K., Lin, S. F., Chen, M. K., Dhaher, R., Matuskey, D., Baum, E., Holden, D., Spencer, D. D., Mercier, J., Hannestad, J., Huang, Y., & Carson, R. E. (2016). Imaging synaptic density in the living human brain. *Science Translational Medicine*, 8(348), 38ra96. <https://doi.org/10.1126/scitranslmed.aaf6667>
- Finnema, S. J., Nabulsi, N. B., Mercier, J., Lin, S., Chen, M.-K., Matuskey, D., Gallezot, J.-D., Henry, S., Hannestad, J., Huang, Y., & Carson, R. E. (2017). Kinetic evaluation and test–retest reproducibility of [¹¹C]UCB-J, a novel radioligand for positron emission tomography imaging of synaptic vesicle glycoprotein 2A in humans. *Journal of Cerebral Blood Flow & Metabolism*, 38(11), 2041–2052.
<https://doi.org/10.1177/0271678X17724947>
- First, M. B., Drevets, W. C., Carter, C., Dickstein, D. P., Kasoff, L., Kim, K. L., McConathy, J., Rauch, S., Saad, Z. S., Savitz, J., Seymour, K. E., Sheline, Y. I., & Zubieta, J.-K. (2018). Clinical Applications of Neuroimaging in Psychiatric Disorders. *The American Journal of Psychiatry*, 175(9), 915–916. <https://doi.org/10.1176/appi.ajp.2018.1750701>
- Francardo, V., Bez, F., Wieloch, T., Nissbrandt, H., Ruscher, K., & Cenci, M. A. (2014). Pharmacological stimulation of sigma-1 receptors has neurorestorative effects in experimental parkinsonism. *Brain*, 137(7), 1998–2014.
<https://doi.org/10.1093/brain/awu107>
- Gaignard, P., Savouroux, S., Liere, P., Pianos, A., Théron, P., Schumacher, M., Slama, A., & Guennoun, R. (2015). Effect of sex differences on brain mitochondrial function and its suppression by ovariectomy and in aged mice. *Endocrinology*, 156(8), 2893–2904.
<https://doi.org/10.1210/en.2014-1913>

- Gallezot, J.-D., Lu, Y., Naganawa, M., & Carson, R. E. (2019). Parametric Imaging With PET and SPECT. *IEEE Transactions on Radiation and Plasma Medical Sciences*, *4*(1), 1–23. <https://doi.org/10.1109/trpms.2019.2908633>
- Gazit, N., Vertkin, I., Shapira, I., Helm, M., Slomowitz, E., Sheiba, M., Mor, Y., Rizzoli, S., & Slutsky, I. (2016). IGF-1 Receptor Differentially Regulates Spontaneous and Evoked Transmission via Mitochondria at Hippocampal Synapses. *Neuron*, *89*(3), 583–597. <https://doi.org/10.1016/j.neuron.2015.12.034>
- Gillardot, F., Rist, W., Kussmaul, L., Vogel, J., Berg, M., Danzer, K., Kraut, N., & Hengerer, B. (2007). Proteomic and functional alterations in brain mitochondria from Tg2576 mice occur before amyloid plaque deposition. *Proteomics*, *7*(4), 605–616. <https://doi.org/10.1002/pmic.200600728>
- Giorgi, C., Missiroli, S., Patergnani, S., Duszyński, J., Wieckowski, M. R., & Pinton, P. (2015). Mitochondria-Associated Membranes: Composition, Molecular Mechanisms, and Physiopathological Implications. *Antioxidants & Redox Signaling*, *22*(12), 995–1019. <https://doi.org/10.1089/ars.2014.6223>
- Görlach, A., Bertram, K., Hudecova, S., & Krizanova, O. (2015). Calcium and ROS: A mutual interplay. In *Redox Biology*, *6*, 260–271. <https://doi.org/10.1016/j.redox.2015.08.010>
- Grabner, G., Janke, A. L., Budge, M. M., Smith, D., Pruessner, J., & Collins, D. L. (2006). Symmetric atlas and model based segmentation: an application to the hippocampus in older adults. *Medical Image Computing and Computer-Assisted Intervention : MICCAI ... International Conference on Medical Image Computing and Computer-Assisted Intervention, Volume Part II*, 58–66.
- Graham, L. C., Naldrett, M. J., Kohama, S. G., Smith, C., Lamont, D. J., McColl, B. W., Gillingwater, T. H., Skehel, P., Urbanski, H. F., & Wishart, T. M. (2019). Regional Molecular Mapping of Primate Synapses during Normal Healthy Aging. *Cell Reports*, *27*(4), 1018–1026. <https://doi.org/10.1016/j.celrep.2019.03.096>
- Greve, D. N., Salat, D. H., Bowen, S. L., Izquierdo-Garcia, D., Schultz, A. P., Catana, C., Becker, J. A., Svarer, C., Knudsen, G. M., Sperling, R. A., & Johnson, K. A. (2016). Different partial volume correction methods lead to different conclusions: An 18F-FDG-PET study of aging. *NeuroImage*, *132*, 334–343. <https://doi.org/10.1016/j.neuroimage.2016.02.042>
- Grimm, A., & Eckert, A. (2017). Brain aging and neurodegeneration: from a mitochondrial point of view. In *Journal of Neurochemistry*, *143*(4), 418–431.

<https://doi.org/10.1111/jnc.14037>

- Grimm, S. (2012). The ER-mitochondria interface: The social network of cell death. In *Biochimica et Biophysica Acta - Molecular Cell Research*, 1823(2), 327–334. <https://doi.org/10.1016/j.bbamcr.2011.11.018>
- Grover, V. P. B., Tognarelli, J. M., Crossey, M. M. E., Cox, I. J., Taylor-Robinson, S. D., & McPhail, M. J. W. (2015). Magnetic Resonance Imaging: Principles and Techniques: Lessons for Clinicians. In *Journal of Clinical and Experimental Hepatology*, 5(3), 246–255. <https://doi.org/10.1016/j.jceh.2015.08.001>
- Gunn, R. N., Gunn, S. R., & Cunningham, V. J. (2001). Positron emission tomography compartmental models. *Journal of Cerebral Blood Flow and Metabolism*, 21(6), 635–652. <https://doi.org/10.1097/00004647-200106000-00002>
- Gunn, R. N., Sargent, P. A., Bench, C. J., Rabiner, E. A., Osman, S., Pike, V. W., Hume, S. P., Grasby, P. M., & Lammertsma, A. A. (1998). Tracer kinetic modeling of the 5-HT(1A) receptor ligand [carbonyl-11C]WAY-100635 for PET. *NeuroImage*, 8(4), 426–440. <https://doi.org/10.1006/nimg.1998.0379>
- Gunning-Dixon, F. M., Head, D., McQuain, J., Acker, J. D., & Raz, N. (1998). Differential aging of the human striatum: A prospective MR imaging study. *American Journal of Neuroradiology*, 19(8), 1501–1507.
- Hamberg, L. M., Hunter, G. J., Alpert, N. M., Choi, N. C., Babich, J. W., & Fischman, A. J. (1994). The dose uptake ratio as an index of glucose metabolism: Useful parameter or oversimplification? *Journal of Nuclear Medicine*, 35(8), 1308–1312.
- Hammers, A., Allom, R., Koepp, M. J., Free, S. L., Myers, R., Lemieux, L., Mitchell, T. N., Brooks, D. J., & Duncan, J. S. (2003). Three-dimensional maximum probability atlas of the human brain, with particular reference to the temporal lobe. *Human Brain Mapping*, 19(4), 224–247. <https://doi.org/10.1002/hbm.10123>
- Hansen, L. A., Daniel, S. E., Wilcock, G. K., & Love, S. (1998). Frontal cortical synaptophysin in Lewy body diseases: relation to Alzheimer's disease and dementia. *J Neurol Neurosurg Psychiatry*, 64(5), 653–656. <https://doi.org/10.1136/jnnp.64.5.653>
- Harada, N., Nishiyama, S., Kanazawa, M., & Tsukada, H. (2013). Development of novel PET probes, [18F]BCPP-EF, [18F]BCPP-BF, and [11C]BCPP-EM for mitochondrial complex 1 imaging in the living brain. *Journal of Labelled Compounds and Radiopharmaceuticals*, 56(11), 553–561. <https://doi.org/10.1002/jlcr.3056>
- Harada, R., Okamura, N., Furumoto, S., & Yanai, K. (2018). Imaging Protein Misfolding in the Brain Using β -Sheet Ligands. In *Frontiers in Neuroscience*, 12, 585.

- <https://www.frontiersin.org/article/10.3389/fnins.2018.00585>
- Harman, D. (1956). Aging: a theory based on free radical and radiation chemistry. *Journal of Gerontology*, *11*(3), 298–300. <https://doi.org/10.1093/geronj/11.3.298>
- Harman, D. (1972). The Biologic Clock: The Mitochondria? *Journal of the American Geriatrics Society*, *20*(4), 145–147. <https://doi.org/10.1111/j.1532-5415.1972.tb00787.x>
- Harris, J. J., & Attwell, D. (2012). The energetics of CNS white matter. *Journal of Neuroscience*, *32*(1), 356–371. <https://doi.org/10.1523/JNEUROSCI.3430-11.2012>
- Harris, J. J., Jolivet, R., & Attwell, D. (2012). Synaptic Energy Use and Supply. *Neuron*, *75*(5), 762–777. <https://doi.org/10.1016/j.neuron.2012.08.019>
- Hayashi, T., & Su, T. P. (2007). Sigma-1 receptor chaperones at the ER-mitochondrion interface regulate Ca(2+) signaling and cell survival. *Cell*, *131*(3), 596–610. [https://doi.org/S0092-8674\(07\)01099-9](https://doi.org/S0092-8674(07)01099-9) [pii]r10.1016/j.cell.2007.08.036
- Hayashi, Teruo, Rizzuto, R., Hajnoczky, G., & Su, T. P. (2009). MAM: more than just a housekeeper. In *Trends in Cell Biology*, *19*(2), 81–88. <https://doi.org/10.1016/j.tcb.2008.12.002>
- Hebert, L. E., Weuve, J., Scherr, P.A., & Evans, D. A. (2013). Alzheimer disease in the United States (2010-2050) estimated using the 2010 census. *Neurology*, *80*(19), 1778–1783. <https://doi.org/10.1212/WNL.0b013e31828726f5>
- Hedskog, L., Pinho, C. M., Filadi, R., Ronnback, A., Hertwig, L., Wiehager, B., Larssen, P., Gellhaar, S., Sandebring, A., Westerlund, M., Graff, C., Winblad, B., Galter, D., Behbahani, H., Pizzo, P., Glaser, E., & Ankarcrona, M. (2013). Modulation of the endoplasmic reticulum-mitochondria interface in Alzheimer’s disease and related models. *Proceedings of the National Academy of Sciences*, *110*(19), 7916–7921. <https://doi.org/10.1073/pnas.1300677110>
- Hendee, W. R., Ritenour, E. R., & Hoffmann, K. R. (2003). Medical Imaging Physics, Fourth Edition. *Medical Physics*. <https://doi.org/10.1118/1.1563664>
- Hinz, R., Bhagwagar, Z., Cowen, P. J., Cunningham, V. J., & Grasby, P. M. (2007). Validation of a tracer kinetic model for the quantification of 5-HT_{2A} receptors in human brain with [¹¹C]MDL 100,907. *Journal of Cerebral Blood Flow and Metabolism*, *27*(1), 161–172. <https://doi.org/10.1038/sj.jcbfm.9600323>
- Hirsch, G. V, Bauer, C. M., & Merabet, L. B. (2015). Using structural and functional brain imaging to uncover how the brain adapts to blindness. *Journal of Psychiatry and Brain Functions*, *2*, 5. <https://doi.org/10.7243/2055-3447-2-7>
- Hof, P. R., & Morrison, J. H. (2004). The aging brain: Morphomolecular senescence of

- cortical circuits. In *Trends in Neurosciences*, 27(10), 607–613.
<https://doi.org/10.1016/j.tins.2004.07.013>
- Hoffman, E. J., Huang, S. C., & Phelps, M. E. (1979). Quantitation in positron emission computed tomography: 1. effect of object size. *Journal of Computer Assisted Tomography*, 3(3), 299–308. <https://doi.org/10.1097/00004728-197906000-00001>
- Höglinger, G. U., Respondek, G., Stamelou, M., Kurz, C., Josephs, K. A., Lang, A. E., Mollenhauer, B., Müller, U., Nilsson, C., Whitwell, J. L., Arzberger, T., Englund, E., Gelpi, E., Giese, A., Irwin, D. J., Meissner, W. G., Pantelyat, A., Rajput, A., van Swieten, J. C., ... Bordelon, Y. (2017). Clinical diagnosis of progressive supranuclear palsy: The movement disorder society criteria. *Movement Disorders*, 32(6), 853–864. <https://doi.org/10.1002/mds.26987>
- Honer, W. G., Dickson, D. W., Gleeson, J., & Davies, P. (1992). Regional synaptic pathology in Alzheimer's disease. *Neurobiology of Aging*, 13(3), 375–382. [https://doi.org/10.1016/0197-4580\(92\)90111-A](https://doi.org/10.1016/0197-4580(92)90111-A)
- Hou, Y., Dan, X., Babbar, M., Wei, Y., Hasselbalch, S. G., Croteau, D. L., & Bohr, V. A. (2019). Ageing as a risk factor for neurodegenerative disease. In *Nature Reviews Neurology*, 15(10), 565–581. <https://doi.org/10.1038/s41582-019-0244-7>
- Hsu, L. J., Sagara, Y., Arroyo, A., Rockenstein, E., Sisk, A., Mallory, M., Wong, J., Takenouchi, T., Hashimoto, M., & Masliah, E. (2000). α -synuclein promotes mitochondrial deficit and oxidative stress. *American Journal of Pathology*, 157(2), 401–410. [https://doi.org/10.1016/S0002-9440\(10\)64553-1](https://doi.org/10.1016/S0002-9440(10)64553-1)
- Huijbers, W., Mormino, E. C., Wigman, S. E., Ward, A. M., Vannini, P., McLaren, D. G., Becker, J. A., Schultz, A. P., Hedden, T., Johnson, K. A., & Sperling, R. A. (2014). Amyloid deposition is linked to aberrant entorhinal activity among cognitively normal older adults. *Journal of Neuroscience*, 34(15), 5200–5210. <https://doi.org/10.1523/JNEUROSCI.3579-13.2014>
- Ichise, M., Toyama, H., Innis, R. B., & Carson, R. E. (2002). Strategies to improve neuroreceptor parameter estimation by linear regression analysis. *Journal of Cerebral Blood Flow and Metabolism*, 22(10), 1271–1281. <https://doi.org/10.1097/01.WCB.0000038000.34930.4E>
- Ikeda, K., Ebina, J., Kawabe, K., & Iwasaki, Y. (2019). Dopamine Transporter Imaging in Parkinson Disease: Progressive Changes and Therapeutic Modification after Anti-parkinsonian Medications. *Internal Medicine (Tokyo, Japan)*, 58(12), 1665–1672. <https://doi.org/10.2169/internalmedicine.2489-18>

- Innis, R. B., & Carson, R. (2007). Consensus nomenclature: Its time has come. *European Journal of Nuclear Medicine and Molecular Imaging*, 34(8), 1239. <https://doi.org/10.1007/s00259-007-0481-7>
- Ishiwata, K., Kobayashi, T., Kawamura, K., & Matsuno, K. (2003). Age-related changes of the binding of [3h]SA4503 to sigma1 receptors in the rat brain. *Annals of Nuclear Medicine*, 17(1), 73–77. <http://www.ncbi.nlm.nih.gov/pubmed/12691135>
- Jomaa, H., Mabrouk, R., & Khelifa, N. (2018). Post-reconstruction-based partial volume correction methods: A comprehensive review. In *Biomedical Signal Processing and Control*, 46, 131–144. <https://doi.org/10.1016/j.bspc.2018.05.029>
- Kander, M. C., Cui, Y., & Liu, Z. (2017). Gender difference in oxidative stress: a new look at the mechanisms for cardiovascular diseases. In *Journal of Cellular and Molecular Medicine*, 21(5), 1024–1032. <https://doi.org/10.1111/jcmm.13038>
- Kawamura, K., Kimura, Y., Tsukada, H., Kobayashi, T., Nishiyama, S., Kakiuchi, T., Ohba, H., Harada, N., Matsuno, K., Ishii, K., & Ishiwata, K. (2003). An increase of sigma receptors in the aged monkey brain. *Neurobiology of Aging*, 24, 745–752. [https://doi.org/10.1016/S0197-4580\(02\)00152-5](https://doi.org/10.1016/S0197-4580(02)00152-5)
- Keeney, P. M. (2006). Parkinson's Disease Brain Mitochondrial Complex I Has Oxidatively Damaged Subunits and Is Functionally Impaired and Misassembled. *Journal of Neuroscience*, 26(19), 5256–5264. <https://doi.org/10.1523/JNEUROSCI.0984-06.2006>
- Kenchappa, R. S., Diwakar, L., Annepu, J., & Ravindranath, V. (2004). Estrogen and neuroprotection: higher constitutive expression of glutaredoxin in female mice offers protection against MPTP-mediated neurodegeneration. *The FASEB Journal*, 18(10), 1102–1104. <https://doi.org/10.1096/fj.03-1075fje>
- Kety S. S. (1951). The theory and applications of the exchange of inert gas at the lungs. *Pharmacological Reviews*, 3(1), 1-41.
- Klunk, W. E., Engler, H., Nordberg, A., Wang, Y., Blomqvist, G., Holt, D. P., Bergström, M., Savitcheva, I., Huang, G. F., Estrada, S., Ausén, B., Debnath, M. L., Barletta, J., Price, J. C., Sandell, J., Lopresti, B. J., Wall, A., Koivisto, P., Antoni, G., ... Långström, B. (2004). Imaging Brain Amyloid in Alzheimer's Disease with Pittsburgh Compound-B. *Annals of Neurology*, 55(3), 306–319. <https://doi.org/10.1002/ana.20009>
- Koole, M., van Aalst, J., Devrome, M., Mertens, N., Serdons, K., Lacroix, B., Mercier, J., Sciberras, D., Maguire, P., & Van Laere, K. (2018). Quantifying SV2A density and drug occupancy in the human brain using [11C]UCB-J PET imaging and subcortical white matter as reference tissue. *European Journal of Nuclear Medicine and Molecular*

- Imaging*, 46(2), 396–406. <https://doi.org/10.1007/s00259-018-4119-8>
- Kovacs, G. G. (2019). Molecular pathology of neurodegenerative diseases: Principles and practice. In *Journal of Clinical Pathology*, 72(11), 725–735.
<https://doi.org/10.1136/jclinpath-2019-205952>
- Laffon, E., Cazeau, A. L., Monet, A., De Clermont, H., Fernandez, P., Marthan, R., & Ducassou, D. (2008). The effect of renal failure on 18F-FDG uptake: A theoretic assessment. *Journal of Nuclear Medicine Technology*, 36(4), 200–202.
<https://doi.org/10.2967/jnmt.107.049627>
- Lammertsma, A A, Bench, C. J., Hume, S. P., Osman, S., Gunn, K., Brooks, D. J., & Frackowiak, R. S. (1996). Comparison of methods for analysis of clinical [11C]raclopride studies. *J Cereb Blood Flow Metab*, 16(1), 42–52.
<https://doi.org/10.1097/00004647-199601000-00005>
- Lammertsma, Adriaan A. (2012). Compartmental modeling in emission tomography. In *Handbook of Particle Detection and Imaging*. https://doi.org/10.1007/978-3-642-13271-1_42
- Lammertsma, Adriaan A., & Hume, S. P. (1996). Simplified reference tissue model for PET receptor studies. *NeuroImage*, 4(3), 153–158. <https://doi.org/10.1006/nimg.1996.0066>
- Lan, Y., Bai, P., Chen, Z., Neelamegam, R., Placzek, M. S., Wang, H., Fiedler, S. A., Yang, J., Yuan, G., Qu, X., Schmidt, H. R., Song, J., Normandin, M. D., Ran, C., & Wang, C. (2019). Novel radioligands for imaging sigma-1 receptor in brain using positron emission tomography (PET). *Acta Pharmaceutica Sinica. B*, 9(6), 1204–1215.
<https://doi.org/10.1016/j.apsb.2019.07.002>
- Laruelle, M., Slifstein, M., & Huang, Y. (2003). Relationships between radiotracer properties and image quality in molecular imaging of the brain with positron emission tomography. *Molecular Imaging and Biology*, 5(6), 363–375.
<https://doi.org/10.1016/j.mibio.2003.09.009>
- Lassen, N. A., Bartenstein, P. A., Lammertsma, A. A., Prevett, M. C., Turton, D. R., Luthra, S. K., Osman, S., Bloomfield, P. M., Jones, T., Patsalos, P. N., O'Connell, M. T., Duncan, J. S., & Vanggaard Andersen, J. (1995). Benzodiazepine receptor quantification in vivo in humans using [11C]flumazenil and PET: Application of the steady-state principle. *Journal of Cerebral Blood Flow and Metabolism*, 15(1), 152–165.
<https://doi.org/10.1038/jcbfm.1995.17>
- Lassmann, H., Weiler, R., Fischer, P., Bancher, C., Jellinger, K., Floor, E., Danielczyk, W., Seitelberger, F., & Winkler, H. (1992). Synaptic pathology in alzheimer's disease:

- Immunological data for markers of synaptic and large dense-core vesicles. *Neuroscience*, 46(1), 1–8. [https://doi.org/10.1016/0306-4522\(92\)90003-K](https://doi.org/10.1016/0306-4522(92)90003-K)
- Logan, J., Fowler, J. S., Volkow, N. D., Wolf, A. P., Dewey, S. L., Schlyer, D. J., MacGregor, R. R., Hitzemann, R., Bendriem, B., John Gatley, S., & Christman, D. R. (1990). Graphical analysis of reversible radioligand binding from time-activity measurements applied to [N-11C-methyl]-(-)-cocaine PET studies in human subjects. *Journal of Cerebral Blood Flow and Metabolism*, 10(5), 740–747. <https://doi.org/10.1038/jcbfm.1990.127>
- Mansur, A., Rabiner, E. A., Comley, R. A., Lewis, Y., Middleton, L. T., Huiban, M., Passchier, J., Tsukada, H., & Gunn, R. N. (2019). Characterization of 3 PET tracers for Quantification of Mitochondrial and Synaptic function in Healthy Human Brain: 18 F-BCPP-EF, 11 C-SA-4503, 11 C-UCB-J. *Journal of Nuclear Medicine*, 61(1), 96–103. <https://doi.org/10.2967/jnumed.119.228080>
- Mansur, A., Rabiner, E. A., Tsukada, H., Comley, R. A., Lewis, Y., Huiban, M., Passchier, J., & Gunn, R. N. (2020). Test–retest variability and reference region-based quantification of 18F-BCPP-EF for imaging mitochondrial complex I in the human brain. *Journal of Cerebral Blood Flow and Metabolism*, 34, 708–714. <https://doi.org/10.1177/0271678X20928149>
- Márquez, F., & Yassa, M. A. (2019). Neuroimaging Biomarkers for Alzheimer’s Disease. In *Molecular Neurodegeneration*, 14(1), 21. <https://doi.org/10.1186/s13024-019-0325-5>
- Masliah, E., Mallory, M., Hansen, L., DeTeresa, R., & Terry, R. D. (1993). Quantitative synaptic alterations in the human neocortex during normal aging. *Neurology*, 43(1), 192–197. https://doi.org/10.1212/wnl.43.1_part_1.192
- Matsuno, K., Nakazawa, M., Okamoto, K., Kawashima, Y., & Mita, S. (1996). Binding properties of SA4503, a novel and selective sigma 1 receptor agonist. *European Journal of Pharmacology*, 306(1–3), 271–279. <http://www.ncbi.nlm.nih.gov/pubmed/8813641>
- Mattson, M. P., & Arumugam, T. V. (2018). Hallmarks of Brain Aging: Adaptive and Pathological Modification by Metabolic States. In *Cell Metabolism*, 27(6), 1176–1199. <https://doi.org/10.1016/j.cmet.2018.05.011>
- Matuskey, D., Tinaz, S., Wilcox, K. C., Naganawa, M., Toyonaga, T., Dias, M., Henry, S., Pittman, B., Ropchan, J., Nabulsi, N., Suridjan, I., Comley, R. A., Huang, Y., Finnema, S. J., & Carson, R. E. (2020). Synaptic Changes in Parkinson Disease Assessed with in vivo Imaging. *Annals of Neurology*, 87(3), 329–338. <https://doi.org/10.1002/ana.25682>
- McKeith, I. G., Boeve, B. F., Dickson, D. W., Halliday, G., Taylor, J. P., Weintraub, D.,

- Aarsland, D., Galvin, J., Attems, J., Ballard, C. G., Bayston, A., Beach, T. G., Blanc, F., Bohnen, N., Bonanni, L., Bras, J., Brundin, P., Burn, D., Chen-Plotkin, A., ... Kosaka, K. (2017). Diagnosis and management of dementia with Lewy bodies. In *Neurology*, 89(1), 88–100. <https://doi.org/10.1212/WNL.0000000000004058>
- Mertens, N., Maguire, R. P., Serdons, K., Lacroix, B., Mercier, J., Sciberras, D., Van Laere, K., & Koole, M. (2020). Validation of Parametric Methods for [¹¹C]UCB-J PET Imaging Using Subcortical White Matter as Reference Tissue. *Molecular Imaging and Biology*, 22(2), 444–452. <https://doi.org/10.1007/s11307-019-01387-6>
- Meunier, J., & Hayashi, T. (2010). Sigma-1 receptors regulate Bcl-2 expression by reactive oxygen species-dependent transcriptional regulation of nuclear factor κB. *Journal of Pharmacology and Experimental*, 332(2), 388–397. <https://doi.org/10.1124/jpet.109.160960.membranes>
- Meyer, P. T., Bhagwagar, Z., Cowen, P. J., Cunningham, V. J., Grasby, P. M., & Hinz, R. (2010). Simplified quantification of 5-HT_{2A} receptors in the human brain with [¹¹C]MDL 100,907 PET and non-invasive kinetic analyses. *NeuroImage*, 50(3), 984–993. <https://doi.org/10.1016/j.neuroimage.2010.01.037>
- Miki, Y., Mori, F., Kon, T., Tanji, K., Toyoshima, Y., Yoshida, M., Sasaki, H., Kakita, A., Takahashi, H., & Wakabayashi, K. (2014). Accumulation of the sigma-1 receptor is common to neuronal nuclear inclusions in various neurodegenerative diseases. *Neuropathology*, 34(2), 148–158. <https://doi.org/10.1111/neup.12080>
- Milnerwood, A. J., & Raymond, L. A. (2010). Early synaptic pathophysiology in neurodegeneration: Insights from Huntington's disease. In *Trends in Neurosciences*, 33(11), 513–523. <https://doi.org/10.1016/j.tins.2010.08.002>
- Mishina, M., Ishiwata, K., Ishii, K., Kitamura, S., Kimura, Y., Kawamura, K., Oda, K., Sasaki, T., Sakayori, O., Hamamoto, M., Kobayashi, S., & Katayama, Y. (2005). Function of sigma1 receptors in Parkinson's disease. *Acta Neurologica Scandinavica*, 112, 103–107. <https://doi.org/10.1111/j.1600-0404.2005.00432.x>
- Mishina, M., Ohyama, M., Ishii, K., Kitamura, S., Kimura, Y., Oda, K. I., Kawamura, K., Sasaki, T., Kobayashi, S., Katayama, Y., & Ishiwata, K. (2008). Low density of sigma1 receptors in early Alzheimer's disease. *Annals of Nuclear Medicine*, 22(3), 151–156. <https://doi.org/10.1007/s12149-007-0094-z>
- Mitsuda, T., Omi, T., Tanimukai, H., Sakagami, Y., Tagami, S., Okochi, M., Kudo, T., & Takeda, M. (2011). Sigma-1Rs are upregulated via PERK/eIF2 α /ATF4 pathway and execute protective function in ER stress. *Biochemical and Biophysical Research*

- Communications*, 415(3), 519–525. <https://doi.org/10.1016/j.bbrc.2011.10.113>
- Möllenhoff, K., Oros-Peusquens, A. M., & Shah, N. J. (2012). Introduction to the basics of magnetic resonance imaging. *NeuroMethods*, 71, 75–98. <https://doi.org/10.1007/7657-2012-56>
- Morris, E. D., Endres, C. J., Schmidt, K. C., Christian, B. T., Muzic, R. F., & Fisher, R. E. (2004). Kinetic Modeling in Positron Emission Tomography. In *Emission Tomography: The Fundamentals of PET and SPECT*. <https://doi.org/10.1016/B978-012744482-6.50026-0>
- Müller-Gärtner, H. W., Links, J. M., Prince, J. L., Bryan, R. N., McVeigh, E., Leal, J. P., Davatzikos, C., & Frost, J. J. (1992). Measurement of radiotracer concentration in brain gray matter using positron emission tomography: MRI-based correction for partial volume effects. *Journal of Cerebral Blood Flow and Metabolism*, 12(4), 571–583. <https://doi.org/10.1038/jcbfm.1992.81>
- Nabulsi, N. B., Mercier, J., Holden, D., Carre, S., Najafzadeh, S., Vandergeten, M.-C., Lin, S.-f., Deo, A., Price, N., Wood, M., Lara-Jaime, T., Montel, F., Laruelle, M., Carson, R. E., Hannestad, J., & Huang, Y. (2016). Synthesis and Preclinical Evaluation of ¹¹C-UCB-J as a PET Tracer for Imaging the Synaptic Vesicle Glycoprotein 2A in the Brain. *Journal of Nuclear Medicine*, 57(5), 777–784. <https://doi.org/10.2967/jnumed.115.168179>
- Narayanaswami, V., Dahl, K., Bernard-Gauthier, V., Josephson, L., Cumming, P., & Vasdev, N. (2018). Emerging PET Radiotracers and Targets for Imaging of Neuroinflammation in Neurodegenerative Diseases: Outlook Beyond TSPO. In *Molecular Imaging*, 17, 1536012118792317. <https://doi.org/10.1177/1536012118792317>
- Nguyen, L., Lucke-Wold, B. P., Mookerjee, S. A., Cavendish, J. Z., Robson, M. J., Scandinaro, A. L., & Matsumoto, R. R. (2015). Role of sigma-1 receptors in neurodegenerative diseases. In *Journal of Pharmacological Sciences*, 127(1), 17–29. <https://doi.org/10.1016/j.jphs.2014.12.005>
- Niccoli, T., & Partridge, L. (2012). Ageing as a risk factor for disease. In *Current Biology*, 22(17), R741–752. <https://doi.org/10.1016/j.cub.2012.07.024>
- Niu, H., Álvarez-Álvarez, I., Guillén-Grima, F., & Aguinaga-Ontoso, I. (2017). Prevalence and incidence of Alzheimer's disease in Europe: A meta-analysis. *Neurología (English Edition)*, 32(8), 523–532 <https://doi.org/10.1016/j.nrleng.2016.02.009>
- Nowack, A., Yao, J., Custer, K. L., & Bajjalieh, S. M. (2010). SV2 regulates neurotransmitter release via multiple mechanisms. *AJP: Cell Physiology*, 299(5), C960–C967.

<https://doi.org/10.1152/ajpcell.00259.2010>

- Nuss, J. E., Choksi, K. B., DeFord, J. H., & Papaconstantinou, J. (2008). Decreased enzyme activities of chaperones PDI and BiP in aged mouse livers. *Biochemical and Biophysical Research Communications*, *365*(2), 355–361. <https://doi.org/10.1016/j.bbrc.2007.10.194>
- Ojaimi, J., Masters, C. L., Opeskin, K., McKelvie, P., & Byrne, E. (1999). Mitochondrial respiratory chain activity in the human brain as a function of age. *Mechanisms of Ageing and Development*, *111*(1), 39–47. [https://doi.org/10.1016/S0047-6374\(99\)00071-8](https://doi.org/10.1016/S0047-6374(99)00071-8)
- Okamura, N., Harada, R., Ishiki, A., Kikuchi, A., Nakamura, T., & Kudo, Y. (2018). The development and validation of tau PET tracers: current status and future directions. In *Clinical and Translational Imaging*, *6*(4), 305–316. <https://doi.org/10.1007/s40336-018-0290-y>
- Pandya, J. D., Grondin, R., Yonutas, H. M., Haghazadeh, H., Gash, D. M., Zhang, Z., & Sullivan, P. G. (2015). Decreased mitochondrial bioenergetics and calcium buffering capacity in the basal ganglia correlates with motor deficits in a nonhuman primate model of aging. *Neurobiology of Aging*, *36*(5), 1903–1913. <https://doi.org/10.1016/j.neurobiolaging.2015.01.018>
- Parsey, R. V., Oquendo, M. A., Ogden, R. T., Olvet, D. M., Simpson, N., Huang, Y., Van Heertum, R. L., Arango, V., & Mann, J. J. (2006). Altered Serotonin 1A Binding in Major Depression: A [carbonyl-C-11]WAY100635 Positron Emission Tomography Study. *Biological Psychiatry*, *59*(2), 106–113. <https://doi.org/10.1016/j.biopsych.2005.06.016>
- Phan, V. L., Urani, A., Sandillon, F., Privat, A., & Maurice, T. (2003). Preserved sigma1 (σ 1) receptor expression and behavioral efficacy in the aged C57BL/6 mouse. *Neurobiology of Aging*, *24*(6), 865–881. [https://doi.org/10.1016/S0197-4580\(02\)00231-2](https://doi.org/10.1016/S0197-4580(02)00231-2)
- Phelps, M. E., Huang, S. C., Hoffman, E. J., Selin, C., Sokoloff, L., & Kuhl, D. E. (1979). Tomographic measurement of local cerebral glucose metabolic rate in humans with (F-18)2-fluoro-2-deoxy-D-glucose: Validation of method. *Annals of Neurology*, *6*(5), 371–388. <https://doi.org/10.1002/ana.410060502>
- Plewes, D. B., & Kucharczyk, W. (2012). Physics of MRI: A primer. In *Journal of Magnetic Resonance Imaging*, *35*(5), 1038–1054. <https://doi.org/10.1002/jmri.23642>
- Pollard, A. K., Craig, E. L., & Chakrabarti, L. (2016). Mitochondrial complex 1 activity measured by spectrophotometry is reduced across all brain regions in ageing and more specifically in neurodegeneration. *PLoS ONE*, *11*(6), e01577405. <https://doi.org/10.1371/journal.pone.0157405>

- Ramakrishnan, N. K., Visser, A. K. D., Rybczynska, A. A., Nyakas, C. J., Luiten, P. G. M., Kwizera, C., Sijbesma, J. W. A., Elsinga, P. H., Ishiwata, K., Dierckx, R. A. J. O., & van Waarde, A. (2016). Sigma-1 Agonist Binding in the Aging Rat Brain: a MicroPET Study with [(11)C]SA4503. *Molecular Imaging and Biology*, *18*(4), 588–597.
<https://doi.org/10.1007/s11307-015-0917-6>
- Raz, N., Rodrigue, K. M., Kennedy, K. M., Head, D., Gunning-Dixon, F., & Acker, J. D. (2003). Differential Aging of the Human Striatum: Longitudinal Evidence. *American Journal of Neuroradiology*, *24*(9), 1849–1856.
- Reddy, P. H., Tripathi, R., Troung, Q., Tirumala, K., Reddy, T. P., Anekonda, V., Shirendeb, U. P., Calkins, M. J., Reddy, A. P., Mao, P., & Manczak, M. (2012). Abnormal mitochondrial dynamics and synaptic degeneration as early events in Alzheimer's disease: Implications to mitochondria-targeted antioxidant therapeutics. In *Biochimica et Biophysica Acta - Molecular Basis of Disease*, *1822*(5), 639–649.
<https://doi.org/10.1016/j.bbadis.2011.10.011>
- Renkin, E. M. (1954). Filtration, diffusion, and molecular sieving through porous cellulose membranes. *The Journal of General Physiology*, *38*(2), 225–243.
<https://doi.org/10.1085/jgp.38.2.225>
- Rhein, V., Song, X., Wiesner, A., Ittner, L. M., Baysang, G., Meier, F., Ozmen, L., Bluethmann, H., Dröse, S., Brandt, U., Savaskan, E., Czech, C., Götz, J., & Eckert, A. (2009). Amyloid- β and tau synergistically impair the oxidative phosphorylation system in triple transgenic Alzheimer's disease mice. *Proceedings of the National Academy of Sciences of the United States of America*, *106*(47), 20057–20062.
<https://doi.org/10.1073/pnas.0905529106>
- Rojas, S., Martín, A., Arranz, M. J., Pareto, D., Purroy, J., Verdager, E., Llop, J., Gómez, V., Gisbert, J. D., Milián, O., Chamorro, Á., & Planas, A. M. (2007). Imaging Brain Inflammation with [11C]PK11195 by PET and Induction of the Peripheral-Type Benzodiazepine Receptor after Transient Focal Ischemia in Rats. *Journal of Cerebral Blood Flow & Metabolism*, *27*(12), 1975–1986.
<https://doi.org/10.1038/sj.jcbfm.9600500>
- Rossano, S., Toyonaga, T., Finnema, S. J., Naganawa, M., Lu, Y., Nabulsi, N., Ropchan, J., De Bruyn, S., Otoul, C., Stockis, A., Nicolas, J. M., Martin, P., Mercier, J., Huang, Y., Maguire, R. P., & Carson, R. E. (2019). Assessment of a white matter reference region for 11C-UCB-J PET quantification. *Journal of Cerebral Blood Flow and Metabolism*, *40*(9), 1890–1901 <https://doi.org/10.1177/0271678X19879230>

- Rowe, C. C., Ng, S., Ackermann, U., Gong, S. J., Pike, K., Savage, G., Cowie, T. F., Dickinson, K. L., Maruff, P., Darby, D., Smith, C., Woodward, M., Merory, J., Tochon-Danguy, H., O'Keefe, G., Klunk, W. E., Mathis, C. A., Price, J. C., Masters, C. L., & Villemagne, V. L. (2007). Imaging β -amyloid burden in aging and dementia. *Neurology*, 68(20), 1718–1725 <https://doi.org/10.1212/01.wnl.0000261919.22630.ea>
- Saha, G. B. (2016). Basics of PET imaging: Physics, chemistry, and regulations, third edition. In *Basics of PET Imaging: Physics, Chemistry, and Regulations, Third Edition*. <https://doi.org/10.1007/978-3-319-16423-6>
- Saito, A., & Imaizumi, K. (2018). Unfolded protein response-dependent communication and contact among endoplasmic reticulum, mitochondria, and plasma membrane. In *International Journal of Molecular Sciences*, 19(10), 3215. <https://doi.org/10.3390/ijms19103215>
- Sakata, M., Kimura, Y., Naganawa, M., Oda, K., Ishii, K., Chihara, K., & Ishiwata, K. (2007). Mapping of human cerebral sigma1 receptors using positron emission tomography and [¹¹C]SA4503. *NeuroImage*, 35(1), 1–8. <https://doi.org/10.1016/j.neuroimage.2006.11.055>
- Salinas, C. A., Searle, G. E., & Gunn, R. N. (2015). The simplified reference tissue model: Model assumption violations and their impact on binding potential. *Journal of Cerebral Blood Flow and Metabolism*, 35(2), 304–311 <https://doi.org/10.1038/jcbfm.2014.202>
- Sazanov, L. A. (2015). A giant molecular proton pump: structure and mechanism of respiratory complex I. *Nature Reviews Molecular Cell Biology*, 16(6), 375–388. <https://doi.org/10.1038/nrm3997>
- Schapira, A. H. V., Cooper, T. S. J. M., Clark, J. B., Jenner, P., & Marsden, T. C. D. (1990). Mitochondrial Complex I Deficiency in Parkinson 's Disease. *Journal of Neurochemistry*, 54, 823–827.
- Scheff, S. W., Price, D. A., Schmitt, F. A., Dekosky, S. T., & Mufson, E. J. (2007). Synaptic alterations in CA1 in mild Alzheimer disease and mild cognitive impairment. *Neurology*, 68(12), 1501–1508. <https://doi.org/10.1212/01.wnl.0000260698.46517.8f>
- Schwarz, G. (1978). JSTOR: The Annals of Statistics, Vol. 6, No. 2 (Mar., 1978), pp. 461-464. *The Annals of Statistics*.
- Selkoe, D. J. (2002). Alzheimer's disease is a synaptic failure. In *Science*, 298(5594), 789–791. <https://doi.org/10.1126/science.1074069>
- Sepulcre, J., Schultz, A. P., Sabuncu, M., Gomez-Isla, T., Chhatwal, J., Becker, A., Sperling, R., & Johnson, K. A. (2016). In vivo tau, amyloid, and gray matter profiles in the aging

- brain. *Journal of Neuroscience*, 36(28), 7364–7374.
<https://doi.org/10.1523/JNEUROSCI.0639-16.2016>
- Shen, B., James, M. L., Andrews, L., Lau, C., Chen, S., Palner, M., Miao, Z., Arksey, N. C., Shuhendler, A. J., Scatliffe, S., Kaneshige, K., Parsons, S. M., McCurdy, C. R., Salehi, A., Gambhir, S. S., & Chin, F. T. (2015). Further validation to support clinical translation of [(18)F]FTC-146 for imaging sigma-1 receptors. *EJNMMI Research*, 5(1), 49. <https://doi.org/10.1186/s13550-015-0122-2>
- Shimizu, S., Hirose, D., Hatanaka, H., Takenoshita, N., Kaneko, Y., Ogawa, Y., Sakurai, H., & Hanyu, H. (2018). Role of neuroimaging as a biomarker for neurodegenerative diseases. In *Frontiers in Neurology*, 9, 265. <https://doi.org/10.3389/fneur.2018.00265>
- Shung, K. K., Smith, M. B., & Tsui, B. M. W. (1992). *CHAPTER 4 - Magnetic Resonance Imaging* (K. K. Shung, M. B. Smith, & B. M. W. B. T.-P. of M. I. Tsui (eds.), 213–271. Academic Press. <https://doi.org/https://doi.org/10.1016/B978-0-12-640970-3.50009-0>
- Silaidos, C., Pilatus, U., Grewal, R., Matura, S., Lienerth, B., Pantel, J., & Eckert, G. P. (2018). Sex-associated differences in mitochondrial function in human peripheral blood mononuclear cells (PBMCs) and brain. *Biology of Sex Differences*, 9(1), 34. <https://doi.org/10.1186/s13293-018-0193-7>
- Slifstein, M., & Laruelle, M. (2000). Effects of statistical noise on graphic analysis of PET neuroreceptor studies. *Journal of Nuclear Medicine*, 41(12), 2083–2088.
- Sweeney, P., Park, H., Baumann, M., Dunlop, J., Frydman, J., Kopito, R., McCampbell, A., Leblanc, G., Venkateswaran, A., Nurmi, A., & Hodgson, R. (2017). Protein misfolding in neurodegenerative diseases: Implications and strategies. *Translational Neurodegeneration*, 6, 6. <https://doi.org/10.1186/s40035-017-0077-5>
- Sze, C. I., Bi, H., Kleinschmidt-Demasters, B. K., Filley, C. M., & Martin, L. J. (2000). Selective regional loss of exocytotic presynaptic vesicle proteins in Alzheimer's disease brains. *Journal of the Neurological Sciences*, 175(2), 81–90. [https://doi.org/10.1016/S0022-510X\(00\)00285-9](https://doi.org/10.1016/S0022-510X(00)00285-9)
- Talairach, J., & Szikla, G. (1980). Application of stereotactic concepts to the surgery of epilepsy. *Acta Neurochirurgica, Supplement*, 30, 35–54. https://doi.org/10.1007/978-3-7091-8592-6_5
- Tonietto, M., Veronese, M., Rizzo, G., Zanotti-Fregonara, P., Lohith, T. G., Fujita, M., Zoghbi, S. S., & Bertoldo, A. (2015). Improved models for plasma radiometabolite correction and their impact on kinetic quantification in PET studies. *Journal of Cerebral Blood Flow and Metabolism*, 35(9), 1462–1469. <https://doi.org/10.1038/jcbfm.2015.61>

- Toyonaga, T., Lu, Y., Naganawa, M., Matuskey, D., Mecca, A., Pittman, B., Nabulsi, N., Finnema, S., Chen, M.-K., Malison, R., Esterlis, I., Dyck, C. Van, Huang, Y., & Carson, R. (2019). Relationship of Age and Synaptic Density: A 11C-UCB-J PET Study in Healthy Controls with Partial Volume Correction. *Journal of Nuclear Medicine*, *60*(Suppl 1), 423–423.
http://jnm.snmjournals.org/cgi/content/short/60/supplement_1/423
- Trewin, A. J., Berry, B. J., & Wojtovich, A. P. (2018). Exercise and mitochondrial dynamics: Keeping in shape with ROS and AMPK. In *Antioxidants*, *7*(1), 7.
<https://doi.org/10.3390/antiox7010007>
- Tripathi, M., Tripathi, M., Damle, N., Kushwaha, S., Jaimini, A., D'Souza, M. M., Sharma, R., Saw, S., & Mondal, A. (2014). Differential diagnosis of neurodegenerative dementias using metabolic phenotypes on F-18 FDG PET/CT. *Neuroradiology Journal*, *27*(1), 13–21.
<https://doi.org/10.15274/NRJ-2014-10002>
- Tsukada, H., Kanazawa, M., Ohba, H., Nishiyama, S., Harada, N., & Kakiuchi, T. (2016). PET Imaging of Mitochondrial Complex I with 18F-BCPP-EF in the Brains of MPTP-Treated Monkeys. *Journal of Nuclear Medicine*, *57*(6), 950–953.
<https://doi.org/10.2967/jnumed.115.169615>
- Tsukada, Hideo. (2014). The use of 18F-BCPP-EF as a PET probe for complex i activity in the brain. *Methods in Enzymology*, *547*(C), 417–431. <https://doi.org/10.1016/B978-0-12-801415-8.00020-5>
- Tsukada, Hideo, Ohba, H., Kanazawa, M., Kakiuchi, T., & Harada, N. (2014). Evaluation of 18F-BCPP-EF for mitochondrial complex I imaging in the brain of conscious monkeys using PET. *European Journal of Nuclear Medicine and Molecular Imaging*, *41*(4), 755–763. <https://doi.org/10.1007/s00259-013-2628-z>
- Tuerxun, T., Numakawa, T., Adachi, N., Kumamaru, E., Kitazawa, H., Kudo, M., & Kunugi, H. (2010). SA4503, a sigma-1 receptor agonist, prevents cultured cortical neurons from oxidative stress-induced cell death via suppression of MAPK pathway activation and glutamate receptor expression. *Neuroscience Letters*, *469*(3), 303–308.
<https://doi.org/10.1016/j.neulet.2009.12.013>
- Tziortzi, A. C., Searle, G. E., Tzimopoulou, S., Salinas, C., Beaver, J. D., Jenkinson, M., Laruelle, M., Rabiner, E. A., & Gunn, R. N. (2011). Imaging dopamine receptors in humans with [11C]-(+)-PHNO: Dissection of D3 signal and anatomy. *NeuroImage*, *54*(1), 264–277. <https://doi.org/10.1016/j.neuroimage.2010.06.044>

- Tzourio-Mazoyer, N., Landeau, B., Papathanassiou, D., Crivello, F., Etard, O., Delcroix, N., Mazoyer, B., & Joliot, M. (2002). Automated anatomical labeling of activations in SPM using a macroscopic anatomical parcellation of the MNI MRI single-subject brain. *NeuroImage*, *15*(1), 273–289 <https://doi.org/10.1006/nimg.2001.0978>
- Uylings, H. B. M., & de Brabander, J. M. (2002). Neuronal Changes in Normal Human Aging and Alzheimer's Disease. *Brain and Cognition*, *49*(3), 268–276. <https://doi.org/https://doi.org/10.1006/brcg.2001.1500>
- Van Laar, V. S., & Berman, S. B. (2013). The interplay of neuronal mitochondrial dynamics and bioenergetics: Implications for Parkinson's disease. In *Neurobiology of Disease*, *51*, 43–55 <https://doi.org/10.1016/j.nbd.2012.05.015>
- Venkateshappa, C., Harish, G., Mahadevan, A., Srinivas Bharath, M. M., & Shankar, S. K. (2012). Elevated oxidative stress and decreased antioxidant function in the human hippocampus and frontal cortex with increasing age: Implications for neurodegeneration in Alzheimer's disease. *Neurochemical Research*, *37*(8), 1601–1614. <https://doi.org/10.1007/s11064-012-0755-8>
- Villeneuve, S., Reed, B. R., Wirth, M., Haase, C. M., Madison, C. M., Ayakta, N., Mack, W., Mungas, D., Chui, H. C., DeCarli, C., Weiner, M. W., & Jagust, W. J. (2014). Cortical thickness mediates the effect of β -amyloid on episodic memory. *Neurology*, *82*(9), 761–767. <https://doi.org/10.1212/WNL.0000000000000170>
- Vina, J., Gambini, J., Lopez-Grueso, R., M. Abdelaziz, K., Jove, M., & Borras, C. (2012). Females Live Longer than Males: Role of Oxidative Stress. *Current Pharmaceutical Design*. *17*(36), 3959–3965. <https://doi.org/10.2174/138161211798764942>
- W. Pike, V. (2016). Considerations in the Development of Reversibly Binding PET Radioligands for Brain Imaging. *Current Medicinal Chemistry*, *23*(18), 1818–1869. <https://doi.org/10.2174/0929867323666160418114826>
- Wagenmakers, E. J., & Farrell, S. (2004). AIC model selection using Akaike weights. In *Psychonomic Bulletin and Review*, *11*(1), 192–196. <https://doi.org/10.3758/BF03206482>
- Wallace, D. R., Mactutus, C. F., & Booze, R. M. (2000). Sigma binding sites identified by [3H] DTG are elevated in aged Fischer-344 \times Brown Norway (F1) rats. *Synapse*, *35*(4), 311–313. [https://doi.org/10.1002/\(SICI\)1098-2396\(20000315\)35:4<311::AID-SYN9>3.0.CO;2-5](https://doi.org/10.1002/(SICI)1098-2396(20000315)35:4<311::AID-SYN9>3.0.CO;2-5)
- Wan, Q. F., Zhou, Z. Y., Thakur, P., Vila, A., Sherry, D. M., Janz, R., & Heidelberger, R. (2010). SV2 Acts via Presynaptic Calcium to Regulate Neurotransmitter Release. *Neuron*, *66*(6), 884–895. <https://doi.org/10.1016/j.neuron.2010.05.010>

- Watabe, H., Endres, C. J., Breier, a, Schmall, B., Eckelman, W. C., & Carson, R. E. (2000). Measurement of dopamine release with continuous infusion of [¹¹C]raclopride: optimization and signal-to-noise considerations. *Journal of Nuclear Medicine : Official Publication, Society of Nuclear Medicine*, 41(3), 522–530.
- Werry, E. L., Bright, F. M., Piguët, O., Ittner, L. M., Halliday, G. M., Hodges, J. R., Kiernan, M. C., Loy, C. T., Kril, J. J., & Kassiou, M. (2019). Recent developments in TSPO PET imaging as a biomarker of neuroinflammation in neurodegenerative disorders. In *International Journal of Molecular Sciences*, 20(13), 3161. <https://doi.org/10.3390/ijms20133161>
- Westbrook, C., Roth, C. K., & Talbot, J. (2011). MRI in Practice 4th. In *Journal of Chemical Information and Modeling*. <https://doi.org/10.1017/CBO9781107415324.004>
- Wishart, T. M., Parson, S. H., & Gillingwater, T. H. (2006). Synaptic Vulnerability in Neurodegenerative Disease. *Journal of Neuropathology & Experimental Neurology*, 65(8), 733–739. <https://doi.org/10.1097/01.jnen.0000228202.35163.c4>
- Wortmann, M. (2015). P4-151: World Alzheimer report 2014: Dementia and risk reduction. *Alzheimer's & Dementia*, 11(7S), 837. <https://doi.org/10.1016/j.jalz.2015.06.1858>
- Wu, M., & Shu, J. (2018). Multimodal Molecular Imaging: Current Status and Future Directions. In *Contrast Media and Molecular Imaging*, 2018, 1382183. <https://doi.org/10.1155/2018/1382183>
- Wu, Y., & Carson, R. E. (2002). Noise reduction in the simplified reference tissue model for neuroreceptor functional imaging. *Journal of Cerebral Blood Flow and Metabolism*, 22(12), 1440–1452. <https://doi.org/10.1097/01.WCB.0000033967.83623.34>
- Yu, Y., Herman, P., Rothman, D. L., Agarwal, D., & Hyder, F. (2018). Evaluating the gray and white matter energy budgets of human brain function. *Journal of Cerebral Blood Flow and Metabolism*, 38(8), 1339–1353. <https://doi.org/10.1177/0271678X17708691>
- Zaidi, H., & Montandon, M. L. (2007). Scatter Compensation Techniques in PET. In *PET Clinics*. <https://doi.org/10.1016/j.cpet.2007.10.003>
- Zhan, S. S., Beyreuther, K., & Schmitt, H. P. (1993). Quantitative assessment of the synaptophysin immuno-reactivity of the cortical neuropil in various neurodegenerative disorders with dementia. *Dementia*, 4(1013–7424), 66–74. <https://doi.org/10.1159/000107299>
- Zhou, L., Miller, B. L., McDaniel, C. H., Kelly, L., Kim, O. J., & Miller, C. A. (1998). Frontotemporal dementia: Neuropil spheroids and presynaptic terminal degeneration.

Annals of Neurology, 44(1), 99–109. <https://doi.org/10.1002/ana.410440116>

Appendix A

POB Models

- $y = \alpha x + \beta$ (Linear)
- $y = \alpha + \beta(1 - e^{-\gamma x})$ (Exponential approaches to constant)
- $y = \alpha + \beta(1 - e^{-\gamma x})$ (Exponential approaches to constant
 α, β, γ constrained)
- $y = \alpha$ (Constant)

Appendix B

PPF Models

- $y = e^{-\beta x}$ (One exponential $\alpha = 1$)
- $y = \alpha e^{-\beta x}$ (One exponential)
- $y = \alpha e^{-\beta x} + 1 - \alpha$ (Exponential + constant)
- $y = \alpha e^{-\beta x} + (1 - \alpha)e^{-\gamma x}$ (Two exponential $\alpha = 1$)
- $y = \alpha e^{-\beta x} + \gamma e^{-\delta x}$ (Two exponential)
- $y = \left(1 - \frac{x^3}{x^3 + 10\alpha}\right)\beta + \gamma^2$ (Sigmoid 1)
- $y = \frac{\left(1 - \frac{x^3}{x^3 + 10\alpha}\right)^\beta + \gamma}{1 + \gamma}$ (Sigmoid 2)

Appendix C

Figure Permissions

Figure	Source	Copyright Holder	Permission
2.4	(Mansur, Rabiner, Comley, et al., 2019)	SNMMI	Granted under Open access non-commercial use

